A RAMAN SPECTROSCOPIC INVESTIGATION OF THE MURINE OOCYTE

Bryony Kathryn Davidson

PhD

The University of Edinburgh

2010

Declaration

I declare that this thesis has been composed solely by myself and has not been submitted for any previous degree. The work contained within this thesis is my own and all work of other authors is duly acknowledged. Furthermore, the assistance provided to me during the course of this work has also been acknowledged.

Bryony Kathryn Davidson

Abstract

Over recent years, the application of assisted reproductive techniques in the treatment of infertility has increased exponentially, yet these methodologies still remain inherently inefficient. It has long been established that the single greatest obstacle to improving the success of these treatments is determining the quality of the oocytes used. However, currently the methods available for oocyte assessment are mainly qualitative, and suffer due to a lack of standardisation. As such, the efficiency of fertility treatments could benefit from the introduction of a rigorous quantitative measure of oocyte quality and maturation.

The principal aim of this thesis was to determine the potential of Raman spectroscopy when applied to the field of oocyte biology. Consequently, this thesis addressed three main areas of investigation: **I. the intra-oocyte biochemical variation**; **II. the biochemistry of oocyte maturation**; and finally, **III. the effect of environment on the mature oocyte *in vivo* and *in vitro*.**

I. To investigate the presence of intra-oocyte biochemical variation, oocytes from various stages of development were analysed using high resolution Raman mapping, in combination with univariate and multivariate analysis. Images revealed variation between the germinal vesicle and ooplasm in immature oocytes, as well as intra-ooplasmic variation in all oocytes.

II. The spectral analysis of oocytes derived from pre-antral and *in vitro* cultured follicles revealed significant variation: It was found that Raman spectroscopy could successfully discriminate between immature and mature oocytes.

III. Finally, the spectral analysis of oocytes derived from unstimulated and stimulated ovulation cycles, as well as those derived from *in vitro* follicle cultures, revealed that although biochemically similar, *in vitro* matured oocytes demonstrated reduced protein content. Furthermore, greater spectral variation was observed in superovulated oocytes, which was found to describe the corresponding morphological quality.

In conclusion, this thesis has demonstrated the effective application of Raman spectroscopy to the study of fixed murine oocytes. Raman mapping experiments have demonstrated this technique for the visualisation of biochemical variation which exists within the oocyte. Furthermore, using Raman spectroscopy, the identification of the biochemical variation resulting from different maturation mechanisms has been achieved, as has the discrimination of immature and mature oocytes. These results indicate that Raman spectroscopy holds promise as a quantitative analysis method in the field of fertility treatment.

Assistance

The experimental work and data analysis presented in this thesis was conducted solely by myself with the following exceptions:

Chapters 4, 5 and 7 - The injections for the superovulation protocol were performed by personnel based at the animal house.

Chapters 6 and 7 - Alison Murray assisted with the dissection of pre-antral follicles.

Acknowledgements

I would like to acknowledge my supervisor, Alistair Elfick, for his continual support throughout the duration of my studies. His encouragement and advice has enabled me to take advantage of numerous opportunities, not least of which was a research visit to the University of Michigan. I would also like to thank my second supervisor, Norah Spears, for her unlimited patience which enabled my transition from engineer to semi-competent biologist; her advice and guidance throughout has been invaluable.

Special thanks must also go to Alison Murray who spent many an hour guiding me through the minefield of tissue culture and for always being on hand to answer my questions. I would also like to thank Wojtek Krzanowski for his advice on where to start with the mountain that is multivariate statistics. Thanks must also go to my research group at the University of Edinburgh and the Morris group at the University of Michigan for their advice and assistance. Ross Moffat and Craig Warren deserve a mention for always being there for a coffee and a moan.

A special thank you goes to my parents, Forbes and Gill, for quickly learning not to ask the question “how is it going?” and, in general, for their unflagging support throughout my seemingly unending academic career. Finally, I must express my eternal gratitude to Jonny who has been there every step of the way, even when that meant a 3am trip to the lab (sorry about that!).

Table of Contents

List of Figures

List of Tables

List of Equations

Abbreviations

AFM	atomic force microscopy
AMH	anti-Müllerian hormone
ART	assisted reproductive techniques
BSA	bovine serum albumin
CARS	coherent anti-stokes Raman scattering
CCD	charge coupled device
COC	cumulus-oocyte-complex
CV	canonical variate
CVA	canonical variate analysis
DNA	deoxyribonucleic acid
dpc	days post coitus
EGF	epidermal growth factor
FBS	foetal bovine serum
FSH	follicle stimulating hormone
FTIR	Fourier transform infrared
GDF-9	growth differentiation factor 9
GUI	graphical user interface
GV	germinal vesicle
GVBD	germinal vesicle breakdown
hCG	human chorionic gonadotrophin
ICSI	intra-cytoplasmic sperm injection
IGF	insulin-like growth factor
IR	infrared
IU	international units
IVF	*in vitro* fertilisation
IVM	*in vitro* maturation
KL	kit ligand
LH	luteinising hormone
MEM	modified Eagle’s medium
MI	metaphase I
MII	metaphase II
MSC	multiplicative signal correction

MTOC	microtubule organising centre
NIR	near infrared
OHSS	ovarian hyper-stimulation syndrome
OLS	ordinary least squares
PB	polar body
PBB	polar body biopsy
PBS	phosphate buffered saline
PC	principal component
PCA	principal component analysis
PCOS	polycystic ovarian syndrome
PGC	primordial germ cell
PMSG	pregnant mare serum gonadotrophin
r-FSH	recombinant follicle stimulating hormone
RNA	ribonucleic acid
SERS	surface-enhanced Raman scattering
SNR	signal to noise ratio
SO	superovulation
SORS	spatially offset Raman scattering
SV	singular value
SVD	singular value decomposition
TERS	tip-enhanced Raman scattering
TGF	transforming growth factor
USO	unstimulated ovulation

Chapter 1

Literature Review: The Oocyte

It has been established that the single greatest obstacle to improving the success of in vitro *fertilisation is determining the quality of the oocytes used. As such, this literature review will introduce the subject of oogenesis and the growth and maturation of the murine oocyte and its associated follicle. Following this, a critical review of current methodology for assessing oocyte and embryo quality will be presented.*

1.1 Infertility and Its Treatment

The UK's Human Fertilisation and Embryology Authority (HFEA) report that 1 in 7 couples have problems conceiving. Whilst many couples can improve their chance of conception by following simple medical advice relating to nutrition, alcohol consumption and stress reduction, for others there exists some physiological problem which affect their fertility, and ultimately their ability to conceive. These problems are normally grouped into the following categories of infertility; male factor, female factor, combination factor and unidentified. Male factor infertility accounts for approximately 30 % of all infertility, and can include problems such as low sperm counts or motility. Similarly, 28 % of all infertility results from female factor infertility[1]. Conditions affecting the uterus, endometriosis, ovulation problems, or most commonly, blocked or damaged fallopian tubes can be the cause in these cases. Until relatively recently, couples who experienced the aforementioned problems would have been unable to conceive. However, since the advent of assisted reproductive techniques (ARTs) in the mid-1970s many of these couples now have that opportunity.

1.1.1 Application of ARTs in the Treatment of Infertility

In vitro fertilisation (IVF) involves the laparoscopic collection of female germ cells, called oocytes, which are then fertilised and cultured in the laboratory for several days, before the embryo is finally implanted in the uterus. This method was developed in the mid-1970s and in 1978 lead to the first live birth using ARTs. Since this milestone, there has been significant growth in both the number of treatment options and the uptake of fertility treatments, with a reported 3 million babies having been born worldwide using ARTs. Conventional IVF remains the most popular treatment option in the UK, with around 18,500 women undergoing this treatment in 2006[2]. However, intra-cytoplasmic sperm injection (ICSI) which was introduced in 1991[3] , whereby a single sperm is injected directly into the oocyte, now accounts for 48 % of all fertility treatments performed in the UK[1].

Over the last two decades, advancements in the understanding of infertility and an increase in demand for more specialised treatment options, has led to the development of numerous new techniques, each of which aims to address a specific clinical need. For example, *in vitro* maturation of oocytes, which involves the collection and culture of immature oocytes, was primarily introduced as a treatment option for women, such as those with polycystic ovarian syndrome (PCOS), who were at risk of ovarian hyper-stimulation syndrome (OHSS) during ordinary IVF cycles. Similarly, cryopreservation protocols for the long-term storage of both oocytes and embryos have been developed in an effort to preserve the fertility of women undergoing treatment for other conditions, such as cancer.

1.1.2 Existing Issues Surrounding ARTs

Although significant progress has been made in the field of fertility treatment, much about the growth and development of gametes and embryos *in vivo* is still not fully understood. As such, there have been questions raised about the safety and developmental implications of some of the treatment protocols. The use of ovarian stimulation, by administration of gonadotrophins which exceed physiological levels, is routinely used to increase the number of oocytes recruited for maturation in the ovary. However, aside from the risk of inducing OHSS, the implications of this treatment in the selection and subsequent developmental competence of oocytes is still in question. Similarly, the impact of *in vitro* culture on the highly orchestrated processes of oocyte maturation and embryo development is far from resolved. The poor efficiencies observed in treatments using frozen oocytes also suggest that the impact of the cryopreservation process on developmental competence needs to be addressed. Perhaps, more significantly, the impact on the long term development and health of offspring born through the application of ARTs needs to be monitored, as an increase in the incidence of some congenital disorders has been reported in children born using these methodologies[4-6].

1.2 The Ovary

1.2.1 The Formation and Structure of the Ovary

During foetal development in the mouse, sexual differentiation of the sexual organs, or gonads, does not occur until around 10.5 -12.5 days *post-coitus* (dpc), when the expression of the *Sry* gene initiates the formation of male gonads, or testes. In the absence of *Sry* expression, the female gonads, or ovaries, form through the differentiation of the bipotential gonads[7]. The ovary is the location of the formation, growth and maturation of female germ cells, termed oocytes. As the oocytes develop, they are encapsulated by somatic cells (granulosa cells), in units known as ovarian follicles. In the mouse, the ultrastructure and organisation of the ovary changes significantly after birth. The follicle-encapsulated oocytes are separated by highly vascularised connective tissue, called stroma, and each follicle is surrounded by a basement membrane, as illustrated in Figure 1.1. At any one time, only a small proportion of the available follicles will be actively growing, with the rest being held in a suspended state awaiting recruitment to the growing pool.

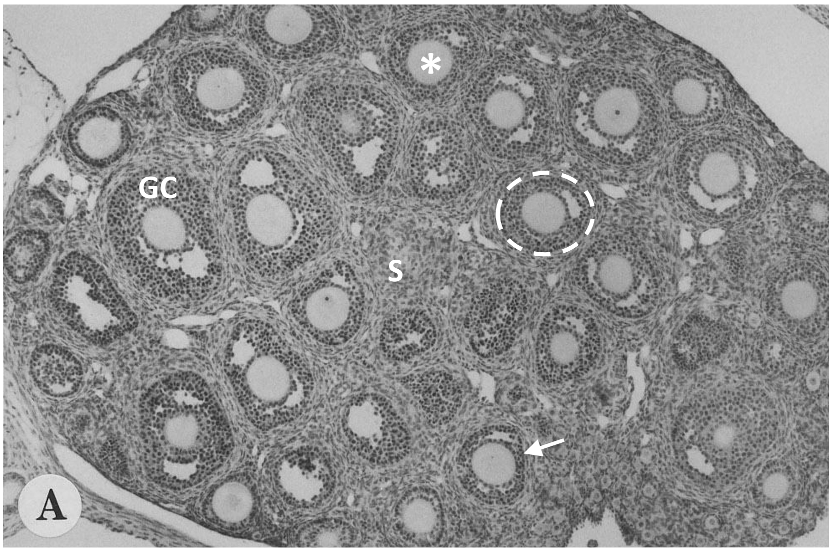

Figure 1.1 – Illustration of the ultrastructure of an ovary from a 14 day-old mouse, showing the localisation of oocytes(asterisk);granulosa cells (GC); basement membranes (arrow); follicles (dashed circle); and stroma (S). Image adapted from [8].

1.2.2 The Ovarian Reserve

Unlike the male germ line which is continuously produced throughout life, there exists from birth a fixed ovarian reserve of oocytes. Although, it should be noted that recent publications have reported the possible existence of germ-line stem cells in the mammalian ovary which may be capable of subsequent oocyte production[9-11], but these publications remain highly controversial. In the mouse, the ovary contains approximately 8000 oocytes at birth[12]. However, approximately 75 % of these will be lost to apoptosis or expelled from the ovary during the first few weeks *post-partum*[13]. Throughout reproductive life, the remaining oocytes and their associated ovarian follicles will be continuously recruited to the growing pool. However, only a small proportion of those recruited will reach ovulation; the others will undergo apoptosis and degrade, which in the ovary is termed atresia.

1.3 The Follicle and Folliculogenesis

The ovarian follicle is essential to the successful growth and maturation of competent oocytes. It has been observed that oocytes with no associated follicle ultimately undergo atresia. The purpose of the follicle is to nourish and control the development of the oocyte[14]. Yet, the role of the oocyte in follicular development is not passive; it has been shown that the oocyte plays a significant role in the regulation of follicular, and thus its own, development by secreting oocyte-specific factors. As such, this section will discuss the structure, development and recruitment of the ovarian follicle following which, attention will be turned to the oocyte and its development in Section 1.4.

1.3.1 The Structure of the Ovarian Follicle

At birth, in the mouse ovary, almost all oocytes are completely nude of somatic cells[13] and exit as germ cell clusters within the ovary[15]. Shortly after birth, these germ cell clusters break down, resulting in significant oocyte loss. The remaining oocytes, which are held in meiotic arrest, each become associated with a few flattened somatic, or pre-granulosa, cells and are enclosed by a basement membrane. This process represents the first stage of folliculogenesis, and marks the formation of primordial follicles. This population of primordial follicles represents the ovarian reserve of the individual, only a small proportion of which will eventually be ovulated.

Upon formation, primordial follicles enter a quiescent phase, which in some cases will persist until near the end of the reproductive life span. However, a small number of primordial follicles are continuously recruited to enter into the pre-antral growth phase. The first visible signs of follicle recruitment are an increase in the number and shape of granulosa cells[16]. The presence of a single layer of cuboidal granulosa cells surrounding the oocyte indicates entry into the growing pool and signifies the transition from primordial to primary follicle (Figure 1.2a). Upon entering into the slow pre-antral growth phase, the granulosa cells which comprise the primary follicle undergo extensive proliferation. Additionally, vascularised layers of thecal cells are formed outside of the basement membrane from the interstitial stroma cells. The appearance of two or more layers of granulosa cells signifies the formation of the pre-antral follicle (Figure 1.2b). In the mouse, the pre-antral follicle will reach approximately 200 μm in diameter by the end of the pre-antral growth phase[17].

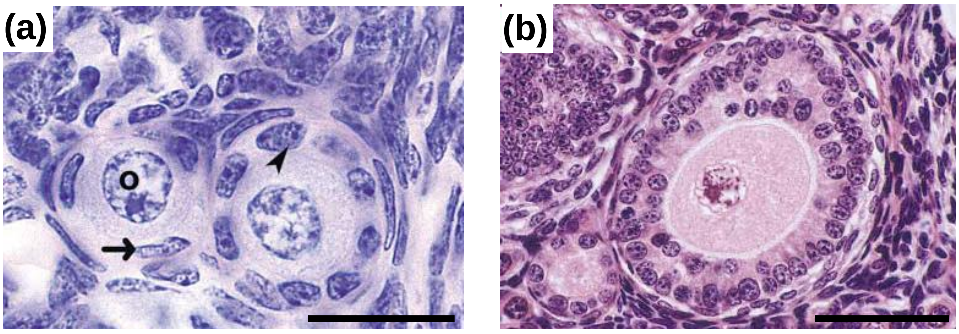

Figure 1.2 – Examples of (a) primordial, primary and (b) early pre-antral follicles in a murine ovary. Primordial follicles comprise an oocyte (o), surrounded by flattened granulosa cells (arrow) while primary follicles display cuboidal granulosa cells (arrowhead); scale bar represents 20 μm. Pre-antral follicles display more than one complete layer of cuboidal granulosa cells and an emerging thecal layer; scale bar represents 50 μm (images recreated from [18]).

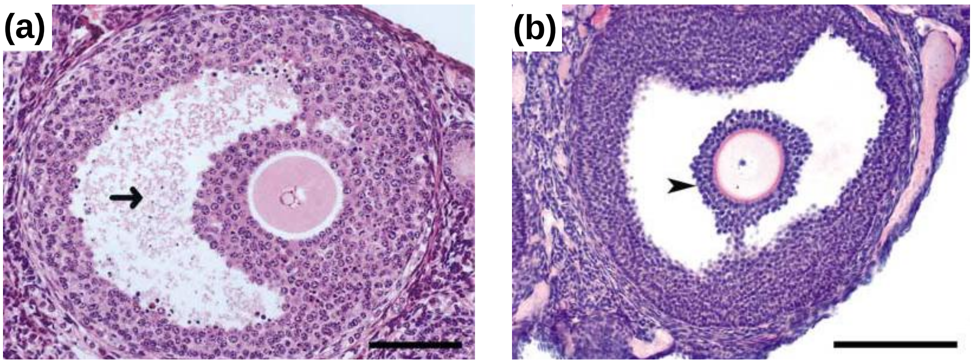

Figure 1.3 – Examples of (a) antral and (b) Graafian follicles in a murine ovary. Antral follicles are characterised by the formation of a fluid filled cavity (arrow); scale bar represents 100 μm. Graafian follicles display a distinct cumulus granulosa cell layer around the oocyte (arrowhead); scale bar represents 200 μm (images recreated from [18]).

Although most of the follicles which are recruited to the growing pool reach the late pre-antral stage, only those which are advanced in their growth, and highly vascularised, will make the transition to antral formation. Regardless of species, the transition from pre-antral to antral follicle occurs when approximately 2000 – 3000 granulosa cells comprise the follicle. At this point, fluid begins to accumulate in the small spaces between granulosa cells, eventually coalescing to form a large fluid filled antral cavity (Figure 1.3a)[19]. Concurrently, the granulosa cells undergo rapid proliferation and differentiation to form two populations; the cumulus cells which enclose the oocyte and the mural cells which remain adjacent to the basement membrane.

Of the follicles which enter the antral growth phase, only a species-specific number will ultimately reach ovulation while the others, termed subordinate follicles, undergo atresia. The selection of the follicles destined for ovulation is achieved through the establishment of follicular dominance, one characteristic of which is a higher level of vascularisation. In the dominant follicle, rapid expansion of the antral cavity occurs, separating the two populations of granulosa cells. The cumulus-enclosed oocyte becomes fully enveloped by the expanding follicular fluid, and only remains connected to the mural cells, on the basement membrane, by a thin stalk of cells (Figure 1.3b). This characteristic follicle is termed the Graafian, or pre-ovulatory, follicle and it contains an oocyte which is fully competent to resume meiosis.

1.3.2 Regulation of Follicle Recruitment and Growth

As has been previously discussed, the development of oocytes and their associated ovarian follicles is a bidirectional process. During folliculogenesis, communication between the oocyte and the surrounding granulosa cells is enabled by the formation of gap junctions in the oocyte membrane. These facilitate the transport of non-soluble nutrients, metabolic precursors and other molecules, from the outset of folliculogenesis.

Upon recruitment, follicles are committed to the process of continual growth, and consequently will either be selected for ovulation or undergo atresia. As such, the control of follicle recruitment is essential to the maintenance of ovarian reserves throughout reproductive life. The process by which primordial follicles are selected to enter the growing pool remains unclear. However, it is generally recognised that primordial follicle activation is regulated by a balance between inhibitory and stimulatory factors, while being independent of gonadotrophin stimulation. Amongst others, the granulosa cell derived anti-Müllerian hormone (AMH)[20] and kit ligand (KL)[21, 22] and the oocyte-specific PTEN[23] have all been implicated in the control of primordial follicle transition in the mouse (Figure 1.4).

Progression through the pre-antral phase of follicular growth is reported to occur in the absence of direct extra-ovarian hormonal stimuli[24], instead resulting from the direct interaction of the oocyte and surrounding granulosa cells[25]. In particular, research has shown growth differentiation factor 9 (GDF9), an oocyte-specific member of the transforming growth factor-beta (TGF-β) superfamily to be essential to the regulation of granulosa cell function and follicular development[26].

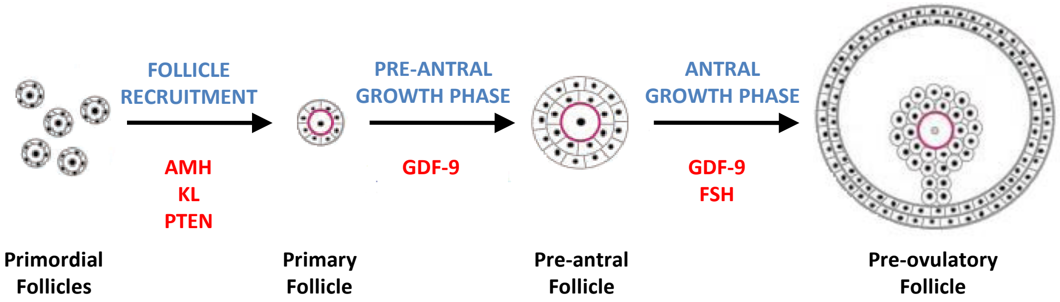

Figure 1.4 –The factors (detailed in red) which have been identified to play a significant role in the progression of murine folliculogenesis are illustrated (image adapted from[25]).

In contrast to the earlier stages of follicular development, progression from the pre-antral to antral growth phase and beyond is dependent upon the secretion of the pituitary hormones follicle stimulating hormone (FSH) and luteinising hormone (LH). Most of the follicles which are selected to enter the pre-antral growth phase will reach the latter stages, with only a few being lost to atresia. However, only a selection of these follicles is capable of responding to the gonadotrophin signals, and thus entering into the antral stage of follicular growth.

1.4 The Oocyte and Oogenesis

1.4.1 Meiosis: Creation of the Germline

The oogonia, which are the precursors of the oocyte, contain one maternal and one paternal copy of each chromosome, which together are referred to as a homologous pair. As a result, the oogonium is classified as being a diploid cell. However, in order to maintain the correct chromosomal complement upon fertilisation, the number of chromosomes in both the male and female germ cells must be reduced by half, so they only contain one copy of each chromosome. The process by which this is achieved is termed meiosis and the resulting germ cell is classified as a haploid cell. In the female, meiosis involves two nuclear divisions, and results in the formation of one diploid and two haploid daughter cells, as illustrated in Figure 1.5.

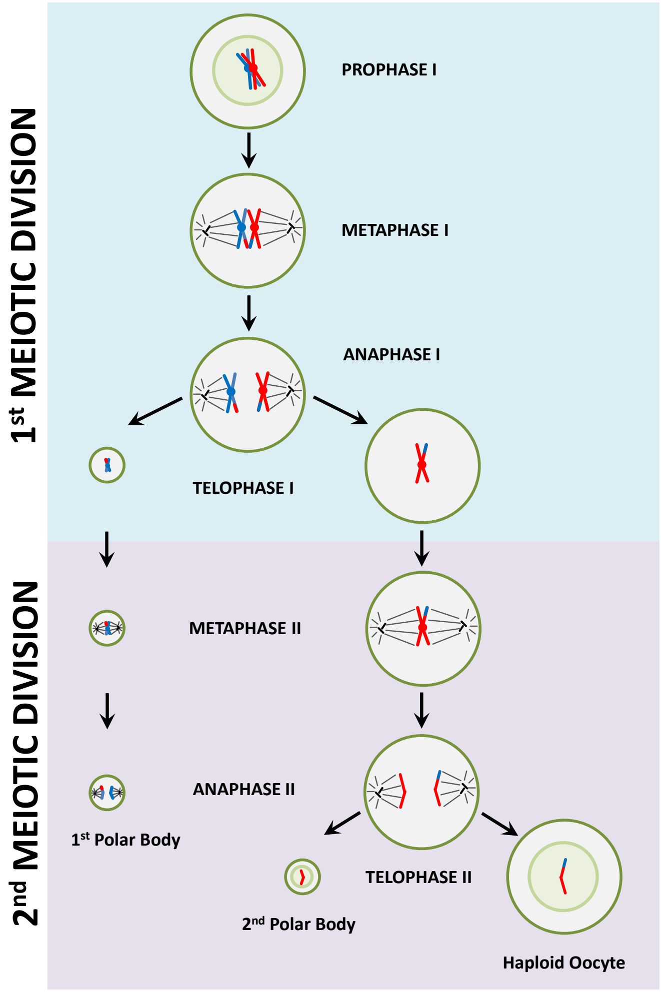

Figure 1.5 – Illustration of the progression of meiosis in the oocyte. For simplicity, the reduction in chromosomal complement and cellular division are shown for a single homologous pair.

Prior to the initiation of meiosis DNA replication occurs, such that each chromosome is duplicated. The two identical chromosomes are known as sister chromatids and behave as a unit during meiosis. Each of the two meiotic divisions consists of four primary stages; prophase, metaphase, anaphase and telophase. Prophase I is the longest and most complex stage of meiosis in the female germ line, and is generally regarded as consisting of five distinct stages; leptotene, zygotene, pachytene, diplotene and diakinesis.

The initiation of meiosis is characterised by the condensation of the replicated DNA during the leptotene stage. Following this, at the zygotene stage of the first prophase, the homologous chromosomes become associated with one another, in a process called synapsis, to form pairs of chromosomes called bivalents. Crossing over, whereby genetic material is exchanged between homologous chromosomes, occurs during pachytene and finally, during the diplotene and diakinesis stages of the meiotic prophase, the homologous chromosomes begin to separate once more. Late in diakinesis the nuclear membrane, or germinal vesicle (GV) as it is termed in the oocyte, begins to breakdown. Concurrently, meiotic spindles form at the poles of the oogonium and begin to attach to the chromosomes.

Metaphase I is characterised by the alignment of the chromosomes in the centre of the cytoplasm between the poles, followed by the attachment of the meiotic spindles to the chromosomes. The separation and migration of the homologous pairs indicates progression to anaphase I, with the formation of two diploid daughter cells occurring upon completion of telophase I, and thus the first meiotic division. The progression of the second meiotic division is analogous to the first. However, as no DNA replication occurs prior to initiation of prophase II the resulting daughter cells are haploid. In the case of female germ cells, the separation of the cytoplasm during telophase I and II is not equal. Instead, one of the daughter cells, the oocyte, is much larger than the other two, which are referred to as polar bodies.

1.4.2 Establishment of Germ Cell Population

Oogenesis initiates from the primordial germ cell (PGC), which is the precursor of both female and male gametes. In the mouse, the PGCs are first detectable at 7-8 dpc near the base of the allantois[27]. Subsequently, over several days the PGCs migrate towards the genital ridge, a process thought to be controlled by chemotaxis. During migration their numbers increase from approximately 100[28] to 5000[29]. Around 12 dpc the PGCs present at the developing gonad are distinguishable from the surrounding epithelial cells. In the female, once established at the developing ovary, the PGCs undergo differentiation and lose their motility. At this point the PGCs are reclassified as oogonia[30].

1.4.3 Oogenesis in the Mouse

The oogonia proceed through a phase of extensive mitotic proliferation which is completed by 13.5 dpc[31]. From day 12 post fertilisation, oogonia begin entering the first meiotic prophase and by day 16 almost all oogonia are in the pachytene stage of meiosis I[32]. The oogonium becomes a primary oocyte upon initiation of meiosis and the oocyte progresses through the leptotene, zygotene and pachytene stages of the first meiotic division before arresting at the diplotene stage of meiotic prophase I[17]. In the mouse by day 5 post partum, all primary oocytes have reached the diplotene stage of the first meiotic prophase and enter into a period of meiotic arrest which will persist until shortly before they are ovulated or undergo atresia. At this stage, the primary oocyte is approximately 15μm in diameter[33] and is contained within a primordial follicle unit.

Upon recruitment of the primordial follicle to the pre-antral growth phase, the associated oocyte undergoes a period of extensive growth lasting approximately 2 weeks, in the mouse. During this time, the oocyte increases in size from 15 μm to 80 μm[19], which represents a 150 fold increase in volume. Upon entering the antral follicular growth phase, the oocyte ceases to grow, and enters a period of maturation, during which alterations that are necessary for successful fertilisation and subsequent embryonic development occur. This acquisition of competence occurs sequentially and, as such, only mature Graafian follicles contain oocytes competent to undergo successful embryonic development (Table 1.1).

	GVBD	MII	2-cell	Blastocyst	Implantation
Primordial	x	x	x	x	x
Pre-antral	√	x	x	x	x
Early Antral	√	√	√	x	x
Graafian	√	√	√	√	√

Table 1.1 – Details of the step-wise acquisition of competence during folliculogenesis.

1.4.4 Cytoplasmic Maturation

Throughout development, the oocyte undergoes significant ultrastructural reorganisation of the cytoplasm and, concurrently, molecules which are necessary for successful fertilisation and embryo development are sequentially acquired. These alterations comprise the cytoplasmic maturation of the oocyte, an overview of which will now be presented.

One of the most striking changes which occur during oocyte development is the formation of a glycoprotein coat, known as the zona pellucida, which surrounds the oocyte. The zona pellucida is comprised of the structural glycoproteins ZP1, ZP2 and ZP3, which are exclusively secreted by the oocyte into the perivitelline space between the oocyte and the primordial follicle, upon recruitment to the growing pool. Structurally, the zona pellucida is a 10 μm thick coat consisting of long filaments of ZP2-ZP3 dimers which are covalently linked by ZP1 molecules[34]. Aside from acting as a barrier to its surrounding environment and maintaining structural integrity, the zona pellucida has two primary functions; facilitation of fertilisation through sperm binding and prevention of polyspermy, whereby multiple sperm fertilise the oocyte. ZP3 molecules are the site for sperm binding during fertilisation while ZP2 molecules facilitate sperm penetration. Subsequently, the sperm block is achieved through the enzymatic modification of the zona pellucida upon sperm penetration[30].

Throughout the period of maturation, the oocyte sequentially acquires new organelles and their distribution within the cytoplasm undergoes extensive change (Figure 1.6). The fidelity of the process of organelle replication is of vital importance to subsequent embryonic development, as the zygote inherits its cytoplasm, and thus organelles, almost exclusively from the oocyte[30]. In particular, the role of mitochondria in oocyte development and competence has attracted significant attention. During maturation, the morphology and

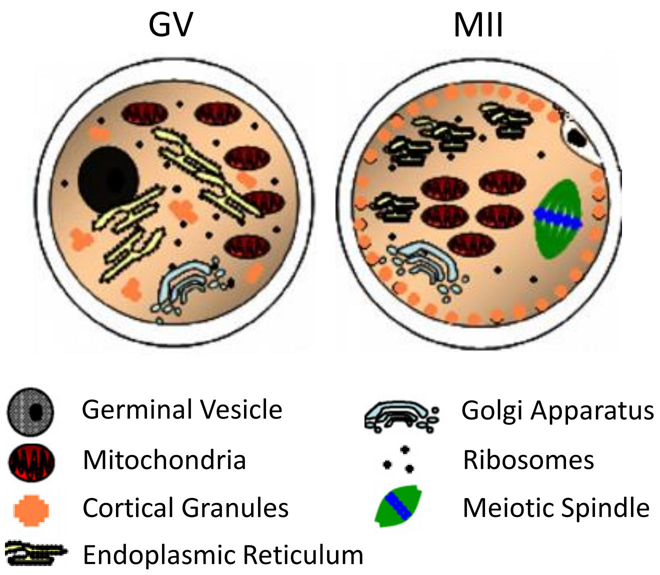

Figure 1.6 – Illustration of the cytoplasmic reorganisation which occurs during oocyte maturation (image adapted from [35]).

distribution of these organelles changes: Mitochondria in growing oocytes are reported to be homogeneously distributed throughout the cortical cytoplasm[36], often becoming closely associated with the endoplasmic reticulum, and display an elongated or arched morphology with vacuolated cristae[37]. In contrast to those found in the growing oocyte, the mitochondria in the mature oocyte display a spherical morphology[38] and are distributed evenly throughout the cytoplasm[39]. Furthermore, the mature metaphase II oocyte contains significantly more mitochondria, at approximately 100,000 [33]. A dramatic increase in ribosome numbers is also observed during cytoplasmic maturation; the mature murine oocyte contains approximately 100 million ribosomes[33]. This increase is consistent with the increase in RNA and protein synthesis which is observed during maturation. Conversely, a decrease in the quantity of endoplasmic reticulum is observed during cytoplasmic maturation.

Early in the maturation process, the Golgi apparatus migrates to the oocyte cortex and breaks up to form multiple units; this transformation is thought to occur in preparation of cortical granules production[40]. Cortical granules are oocyte-specific secretory vesicles which comprise a membrane bound mixture of glycoproteins and enzymes which are essential in the sperm block reaction. Initially, they are found to continuously occupy the cortical region, with some forming clusters. However, upon resumption of meiosis, cortical granules become more closely associated with the oolemma and are found to be absent from the animal pole upon migration of the meiotic spindle[41]. Another structure unique to the oocyte of rodents is the fibrous lattices. These proteinaceous structures become more abundant during maturation, and are thought to act as a “mammalian yolk” providing energy during embryonic development[33].

In addition to organelle proliferation, during cytoplasmic maturation the oocyte accumulates a large number of membrane-bound vesicles, glycogen granules, lipid droplets and multivesicular bodies which are required for energy storage and molecular transport between the oocyte and follicular domains[17].

Throughout its development, the oocyte synthesises and absorbs macromolecules. These substances are required, not only for the successful growth and maturation of the oocyte, but are also stored for subsequent deployment during early embryonic development. The most marked macromolecular changes results from the rapid increase in transcription and translation during oocyte growth. RNA synthesis increases 300-fold to around 15 $fgmin^{-1}$ during oocyte growth, with the fully grown oocyte containing approximately 0.3 - 0.5 ng of RNA *in toto*[42]. RNA transcription ceases at this point and will not resume until the 2-cell stage of embryonic development. In the interim, the maternal RNA is degraded such that 70 % of the total RNA reserve will be lost, with 20% being lost between the resumption of meiosis and ovulation[43]. Similarly, protein synthesis increases from around 1 to 40 pgh^{-1} during oocyte growth, with the fully grown oocyte containing approximately 30 ng of protein *in toto*, 4.5 ng of which comprises the zona pellucida[32].

1.4.5 Nuclear Maturation

The final preparatory stages prior to ovulation involve the nuclear maturation of the oocyte which resumes approximately 12 hours prior to ovulation. This process occurs in response to the pre-ovulatory luteinising hormone (LH) surge, and its initiation can be identified by the breakdown of the germinal vesicle (GVBD). The oocyte completes meiosis I, extruding a polar body, before progressing to the metaphase of the second meiotic division whereby it encounters its second meiotic block. The oocyte, now termed a MII oocyte, remains arrested at this stage until fertilised, upon which it will complete the second round of meiosis and extrude the second polar body[44].

Around the time of the resumption of meiosis, the gap junctions, which exist in the oolemma, are terminated preventing further communication between the cumulus cells and enclosed oocyte[30]. Indeed, it has been postulated that the termination may remove the inhibitory effect which has maintained meiotic arrest. Additionally, the cumulus cells which surround the oocyte undergo “cumulus expansion” during which the cells become more loosely packed. Simultaneously, these cumulus cells start secreting hyaluron which produces a muco-elastic extracellular matrix that aids oocyte pick-up by the fimbria, at the entry to the fallopian tube[45].

1.4.6 The Implications of Manipulating Oogenesis

The preceding sections have demonstrated the complex and highly orchestrated processes which comprise the establishment, maintenance and development of the oocyte and its associated follicle. Despite the significant advances in the understanding of ovarian biology, there is still much which remains unclear. Specifically, the regulation and control of follicular recruitment, dominance and oocyte maturation are still not fully understood. Consequently, the application and impact of ARTs which involve the manipulation of the process of natural selection through the recruitment of follicles which are destined for atresia, the intra-cytoplasmic injection of sperm and the *in vitro* manipulation of oocytes and embryos is still not fully understood. However, it is clear that the assessment of oocyte competence and quality are vital to furthering understanding in this field.

1.5 The Assessment of Oocyte Maturity and Quality

At present, the process by which the dominant and subordinate follicle populations are established is unclear. However, it has been postulated that follicular atresia is a method of disposing of oocytes and follicles which have an impaired developmental potential. Many of the protocols implemented in clinical ARTs involve ovarian stimulation. In these cycles, many of the follicles which were destined for, and may have already started to undergo, atresia are instead recruited for ovulation. As such, it is unsurprising that the effective assessment of oocyte quality and maturity remains a significant hurdle to improving the efficiency of these techniques.

Currently, morphological assessment is the primary method used for quality assessment. However, although some would argue that morphological assessment of oocytes prior to fertilisation provides some indication of the developmental outcome of the treatment, it is certainly not a definitive science. Firstly, this process is highly subjective and therefore prone to human error. Furthermore, many of the studies which have investigated the relationship between oocyte morphology and developmental potential have been conducted by different groups using different protocols, chemicals, media and most importantly a different cohort of patients. As such, it is very hard to ascertain the true value of morphological assessment and its implementation in IVF labs has most probably persisted due to the lack of suitable alternatives. The purpose of this section is to provide an overview of the current methods available for identification of oocyte maturity and quality, both in a clinical setting and the research laboratory.

1.5.1 The Current Gold Standard: Oocyte Morphology

Morphological assessment is still used as one of the main methods of quality assessment in IVF labs. However, the extent to which it can prove useful depends upon the type of ART procedure to be implemented and the experience of the embryologist[46].

Cumulus-Oocyte-Complex Assessment

In standard IVF cycles the cumulus cells are not removed, making morphological scoring of the oocyte difficult. In such cases, scoring is based upon the appearance and expansion of the cumulus-oocyte-complex (COC). During unstimulated cycles, the extent of cumulus expansion has been reported to be indicative of oocyte maturity[47]. Similarly, in stimulated cycles, despite the asynchronicity of nuclear maturation and cumulus expansion[48, 49], increased fertilisation rates have been reported for COCs which are assessed as morphological mature[50-53].

Extracytoplasmic Assessment

Although not possible in ordinary IVF cycles, techniques which involve denudation enable direct morphological assessment of the oocyte using light microscopy. Several studies have investigated the influence of morphological characteristics external to the oolemma on oocyte quality. In one such study, oocytes displaying a large perivitelline space were reported to have reduced capacity for fertilisation and resulted in lower embryo quality[54]. Conversely, other researchers have found that no relationship exists between extracytoplasmic abnormalities, including large perivitelline space, dark zona pellucida and shape, and fertilisation rate[55, 56].

Cytoplasmic Assessment

For cycles in which oocytes are denuded, considerable attention has been paid to the correlation of ooplasm morphology and developmental competence. Early studies reported no significant effect on fertilisation rate and embryo development in oocytes displaying abnormal ooplasm morphology[55-57], although a reduction in implantation was observed in one of these studies[57]. In contrast, the presence of inclusions[54], vacuoles[58] and aggregated smooth endoplasmic reticulum[59] in the ooplasm have been reported to have a negative impact on fertilisation rates. Furthermore, it has been reported that embryos derived from oocytes displaying multiple ooplasm abnormalities are of poorer quality and experience delayed cleavage[60].

Polar Body Assessment

The presence of the first polar body (PB) is generally regarded as an indication that an oocyte is meiotically mature. As such, the assessment of PB morphology has long been proposed as an indicator of oocyte quality. In an early study, PB fragmentation was found to be negatively correlated with embryo quality[54]. Subsequently, a series of studies found that the morphology of the first PB was positively correlated with embryo quality, fertilisation, implantation and pregnancy rates[61-63]. Although, recent work has indicated that first PB morphology is not indicative of developmental outcome[64-66].

Summary

These findings suggest that morphological assessment can provide some indication of oocyte developmental competence. However, it remains that there exist numerous conflicting reports as to the efficacy of these methodologies. It is possible that many of these conflicts arise as a result of cumulative effects; for example, the presence of cytoplasmic inclusions and large perivitelline spaces has been reported to have a higher incidence in older females, who as a population are more likely to present other abnormalities, such as spindle disruption. As such, the contribution of a specific morphological abnormality to the developmental competence of an oocyte is difficult to elucidate.

1.5.2 Emerging Non-Invasive Techniques

Birefringence Imaging

Birefringence is the decomposition of a ray of light into an ordinary and extraordinary component upon passing through a highly ordered crystalline substance which shows directional dependence, or anisotropy. These two components travel at different speeds through the material, and as such, anisotropic materials possess two different indices of refraction. The difference between these refractive indices is equal to the magnitude of birefringence, otherwise known as retardance. The application of birefringence imaging was first reported in 2000 for meiotic spindle visualisation (Figure 1.7a) in mammalian oocytes[67]. Since then, many studies have reported significantly higher rates of fertilisation and embryo development for oocytes which display a birefringent spindle when compared to those in which the spindle does not display birefringence[68-72] . In particular, this technique has attracted significant attention in the field of cryopreservation[73-76], as it is known that the freeze-thaw cycle can disrupt the meiotic spindle. This technique, however, is only capable of providing information regarding nuclear maturation; it is not indicative of cytoplasmic maturation, and as such should not be applied as the solitary means of selection.

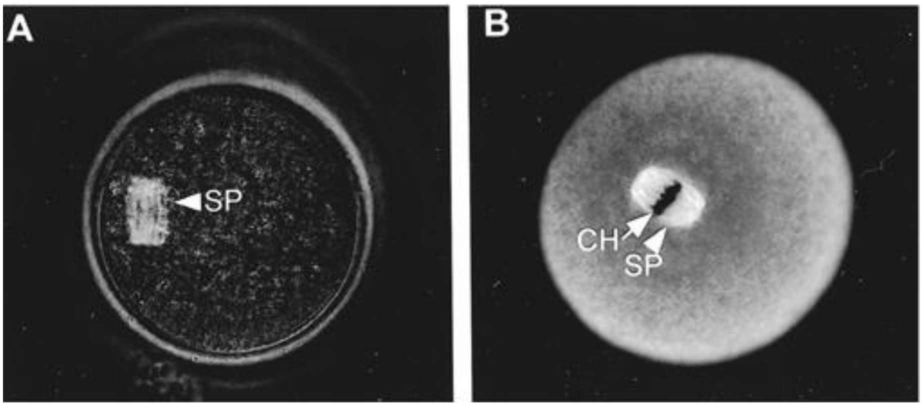

Figure 1.7 – Comparison of (A) birefringent and (B) fluorescence spindle visualisation in a MII mouse oocyte[77]. SP and CH denote the meiotic spindle and chromosomes, respectively.

Analysis of Follicular Fluid

Analysis of follicular fluid derived from large and small antral follicles using Fourier-transform infrared spectroscopy (FTIR) revealed that the biochemical profiles of large follicles were more tightly clustered than those of small follicles[78], indicating that the biochemical profile of follicular fluid may be related to oocyte maturity and quality.

Some researchers have reported a relationship between the concentration of certain hormones, including 17β-oestradiol[79, 80], progesterone[81], prolactin[82] and luteinising hormone[83], and oocyte developmental competence. Similarly, significant attention has been paid to the effect of follicular fluid growth factor concentrations on oocyte quality. The intrafollicular concentrations of selected insulin-like growth factors (IGF) have been identified as markers for oocyte maturity and quality[84-86]. The levels of BMP-15[87] and AMH[88] in follicular fluid have also been suggested for the determination of oocyte quality and developmental potential. Furthermore, results obtained from the proteomic profiling of follicular fluid have indicated that the concentration of lactoferrin[89], leptin[90-92] and free amino acids[93] affect oocyte developmental potential. More recently, metabolomics has been used to investigate the temporal changes in follicular fluid composition during maturation[78, 94].

The analysis of follicular fluids provides an appealing alternative to current methods of oocyte selection. It is entirely non-invasive, as the analysis is performed on material which would otherwise be discarded. However, care would have to be taken not to contaminate the fluid during aspiration, as it has been shown that even small quantities of contaminants, such as blood, can alter the profile of follicular fluids[95]. Furthermore, as it has been demonstrated that ovarian stimulation protocols can affect the composition of follicular fluid[96-98], research into the robustness in light of different stimulation protocols would have to be completed.

Analysis of Culture Media

A viable alternative to follicular fluid analysis is the investigation of culture media. To date, these methods have been mostly applied to embryo cultures. Amino acid profiling of spent embryo culture media, using HPLC, has shown the profiles of specific amino acids to be predictive of embryo development and clinical pregnancy outcome[99-101]. Similarly, the near-infrared (NIR) and Raman spectroscopic profiles of spent day 3 and 5 embryo culture media have been shown to predict embryo development potential and implantation rates with greater success than morphological assessment alone[102-104]. Most recently, NIR spectroscopy has been applied to the investigation of oocyte culture media, collected after 4 hours, for the assessment of maturity and developmental potential[105]. This work reported significantly different spectral profiles from MII and MI oocytes and the developmental potential of oocytes was predicted with good sensitivity and specificity. Although significant spectral variation was observed within each group, this technique still shows significant promise.

1.5.3 A Stage Further: Genetic Profiling

It has long been established that cumulus cells play a critical role in the support of oocyte growth and maturation. As such, the alteration of gene expression during this process has been suggested as a method for determining oocyte quality and developmental competence. In particular, the cumulus expression of the hyaluronan synthase 2 (HAS2), gremlin1 (GREM1), cyclooxygenase 2 (COX2; PTGS2)[106, 107], pentraxin 3 (PTX3)[108], cathepsin[109] and progesterone receptor s (PGR) [110] have all attracted attention. However, to date the number of samples included in these studies has not been large enough to indicate a true predictive outcome.

Another technique which addresses the issue of genetic abnormalities in the gamete is that of polar body biopsy (PBB). This method involves the removal and genetic profiling of the first and/or second PB. Its most common application is that of aneuploidy testing but it has also been used in the screening of specific autosomal dominant[111] and X-linked disorders[112]. However, this method only really provides information regarding the genetic quality of the oocyte; it provides no information regarding the paternal genetic contribution[113].

1.6 Raman Spectroscopy for Oocyte Analysis?

It has been established that the process of oocyte growth and maturation involves a series of highly orchestrated biochemical and ultrastructural modifications. At present, there exist many methods to investigate the localisation and quantisation of specific molecules and organelles within the oocyte. However, in many cases, these techniques require extensive sample preparation and can compromise the integrity of the sample, thus preventing further investigation. Conversely, Raman spectroscopy, which is a technique that detects the vibrations of the functional groups within molecules, provides a method for the investigation of biochemical modifications without the need for complicated sample preparation. Furthermore, this technique has attracted significant attention in the field of bioanalysis due, in part, to its ability to provide a biochemical “fingerprint” of all the macromolecules present at a specific location and relatively high spatial resolution (< 1 μm).

1.7 Conclusions

Over recent years, the application of ARTs in the treatment of infertility has increased exponentially, yet these methodologies still remain inherently inefficient. It has long been established that the single greatest obstacle to improving the success of these treatments is determining the quality of the oocytes used. Currently, morphological assessment is routinely used for quality assessment, but this method is highly subjective. Undoubtedly, the efficiency of fertility treatments could benefit from the introduction of a rigorous quantitative measure of oocyte quality and maturation. The strong research effort to identify alternative methods has lead to some promising techniques, although in many cases more extensive studies, incorporating larger patient cohorts, are required.

The principal aim of this thesis was to determine the potential of Raman spectroscopy when applied to the field of oocyte biology. Consequently, the primary goals of this work were:

I. To establish if Raman spectroscopic mapping could be used to elucidate the intra-cytoplasmic biochemical variation at different stages of oocyte and embryo development and, as such, provide a method to further ovarian research.

II. To ascertain if Raman spectroscopy could be used to monitor the changes which occur during oocyte maturation *in vivo* and *in vitro*, with a view to developing a quantitative method for assessment of oocyte maturation.

Chapter 2

The Theory and Application of Raman Spectroscopy in the Field of Bioanalysis

Raman spectroscopy, although now widely applied to the study of biological samples, is still one of the less well recognised spectroscopic techniques. As such, the purpose of this chapter is to introduce the reader to the theory of molecular vibrations, light scattering and Raman spectroscopy. Furthermore, current and past applications in the fields of biology and medicine will also be discussed in order to demonstrate its potential and limitations as a diagnostic technique.

2.1 Introduction

In order to further the understanding of oocyte biology, and ultimately improve the efficiency of ARTs, it is necessary to explore the application of techniques which enable the non-invasive analysis of both morphological and biochemical characteristics of the oocyte. Whilst histological methods and immunoassays remain essential, they require significant sample preparation and often are not practical for time lapse analyses. Rapid advances in image processing methods and optical elements have led to high resolution microscopic imaging methods. However, in the absence of fluorophores, they are capable of providing little chemical information. Although, there are techniques, such as the birefringence imaging discussed in the previous chapter, which are capable of providing more detailed information non-invasively, many only allow investigation of particular components within the oocyte. Conversely, Raman spectroscopy, which has been routinely applied to the analysis of biological specimens, is a minimally-invasive technique which is capable of providing a complete “biochemical fingerprint” of a sample.

Firstly, this chapter will provide a brief introduction to the theory and principles of Raman micro-spectroscopy; for a more in depth consideration of this technique a number of comprehensive texts are available [114-116]. Secondly, in an effort to illustrate the potential of this technique in the analysis of biological specimens, an overview of the application of Raman spectroscopy in the field of bioanalysis will be given.

2.2 The Theory of Raman Spectroscopy

When a sample is illuminated, the incident photons can interact with the sample in a number of ways: The photons may be absorbed, transmitted, reflected, or scattered. There exist several types of scattering process. On a fundamental level, scattering describes photons which are deflected along a path which differs from the incident path. There exist two types of scattering: elastic and inelastic. Elastic, or Rayleigh, scattering refers to photons which are scattered without any significant exchange of energy. Conversely, inelastic scattering occurs when there is a transfer of energy between the photon and the material upon which the illumination falls. It is this inelastic scattering which is measured in the Raman process. However, the process of Raman scattering is inherently weak; of the incident photons, approximately 1 in 1000 will be Rayleigh scattered, whilst only 1 in 10,000,000 photons will be Raman scattered. The process of scattering can be described by considering the interaction of the incident photons with the molecules which comprise the sample.

2.2.1 Molecular Quantum Mechanics

To fully appreciate the process of Raman scattering, we must first understand the quantised nature of the molecules' energy levels. Every molecule consists of a number of electronic states, each of which contains a finite number of vibrational and rotational states which can only take values that are equivalent to the energy required to induce a stable vibration or rotation in that molecule. The energy which is associated with a single vibration between two intramolecular atoms is a function of the internuclear separation of the two atoms: As this separation increases, so does the associated energy of vibration, until a point is reached at which the atoms are essentially free of one another. Conversely, as the internuclear separation decreases, the associated energy decreases until the nuclei become too close that they are repelled by one another.

The Morse curve, as illustrated by Figure 2.1, pictorially describes the energy associated with the change in internuclear separation for a single electronic state of a given molecule. In Figure 2.1, the horizontal lines represent the possible vibrational states for an electronic state of a given molecule. The ground vibration state, in which no vibration is taking place, is denoted by ν_0.

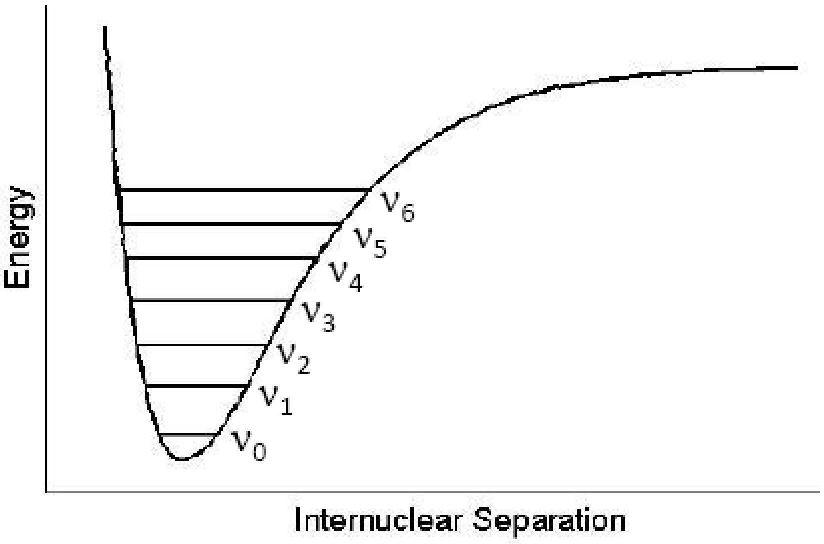

Figure 2.1 – Morse curve showing the change in energy associated with increasing internuclear separation between vibrational energy level. The curve describes the change in energy which is associated with increasing internuclear separation during bond vibration.

2.2.2 Qualitative Description of Raman Scattering

In order to understand the process of scattering, it is necessary to recognise that the energy of a photon is a function of its frequency: If an incident photon has frequency ν_0, then it is possible to define its energy using Equation 2.1, where the energy of the photon, E, is the product of the photon's frequency, ν, and Plank's constant, h.

$$E = hv_0$$

Equation 2.1

Fundamentally, the interaction of a photon and molecule may be considered as an unstable transitory, or virtual, complex formed between the incident photon and the distorted energy levels of the molecule. Upon illumination, the interaction between the incident photons and the molecules, which comprise the sample, can result in the distortion of the electron clouds which surrounds the nuclei. This distortion results in the polarisation of the electron cloud and is a short-lived phenomenon whereby the molecule is raised to a higher energy, or virtual, state. At this specific point in time, the energy of the photon can be said to have be transferred to the molecule. However, this virtual complex is unstable and as such, leads to the rapid release, or scattering, of energy in the form of a photon.

In the case of Rayleigh scattering, upon breakdown of the virtual complex no nuclear movement is induced and so the incident photon's energy is conserved. Consequently, the photon released has the same energy, and therefore frequency, as the incident photon, and the molecule returns to its original vibrational level which is most often the ground state. Conversely, in the case of Raman scattering, upon breakdown of the virtual complex nuclear movement is induced, which in turn leads to a bond vibration. In such cases, a significant energy transfer will take place between the photon and molecule, resulting in a frequency shift of the scattered photon.

Most commonly, the energy is transferred from the photon to the molecule. In such cases, upon release of the photon, the molecule returns to an excited vibrational level and the released photon has a new energy equal to that of the incident photon less the energy required to induce the bond vibration. Thus, the scattered photon has a lower frequency. This type of scattering process is termed Stokes Raman scattering. The reverse, however, is possible whereby the molecule is already in an excited state before complex formation and the transfer of energy is to the scattered photon. Upon release of the photon, the molecule is returned to a lower vibrational level and the photon released has a higher energy. This type of scattering, which leads to the release of a photon with a higher frequency, is termed anti-Stokes Raman scattering.

A simpler form of the Morse curve, known as a Jablonski diagram, can be used to represent the process of scattering in a more accessible form, thus enabling a direct comparison of the three scattering processes. As an illustrative example, Figure 2.2 depicts a Jablonski diagram for the vibrational energy levels required to induce a single arbitrary bond vibration in a molecule.

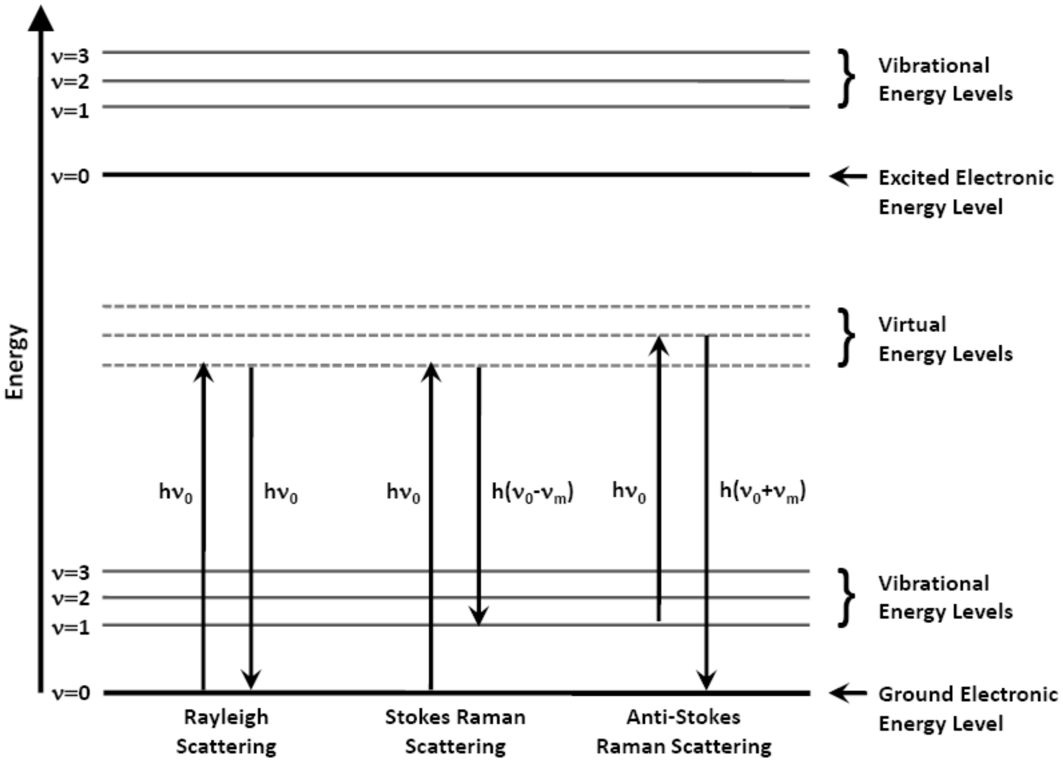

Figure 2.2 – Jablonski diagram which illustrates the transfer of energy during Rayleigh, Stokes and anti-Stokes Raman scattering. It should be noted that the scale of this diagram has been altered for clarity; the energy between the electronic states is far greater than is suggested by this diagram.

In the case of Raman scattering, the same vibrational energy levels are involved whether the scattering is Stokes or anti-Stokes. As such, the energy transferred from a photon in Stokes Raman scattering is equal to the energy transferred to the photon in anti-Stokes Raman scattering, giving rise to a symmetrical spectrum about the Rayleigh line, as illustrated by Figure 2.3 . However, at ambient temperature, the intensities of the anti-Stokes lines are less than their Stokes equivalents. This is true because anti-Stokes Raman scattering requires the molecule to exist in an excited vibrational state, an event which is less common at ambient temperature.

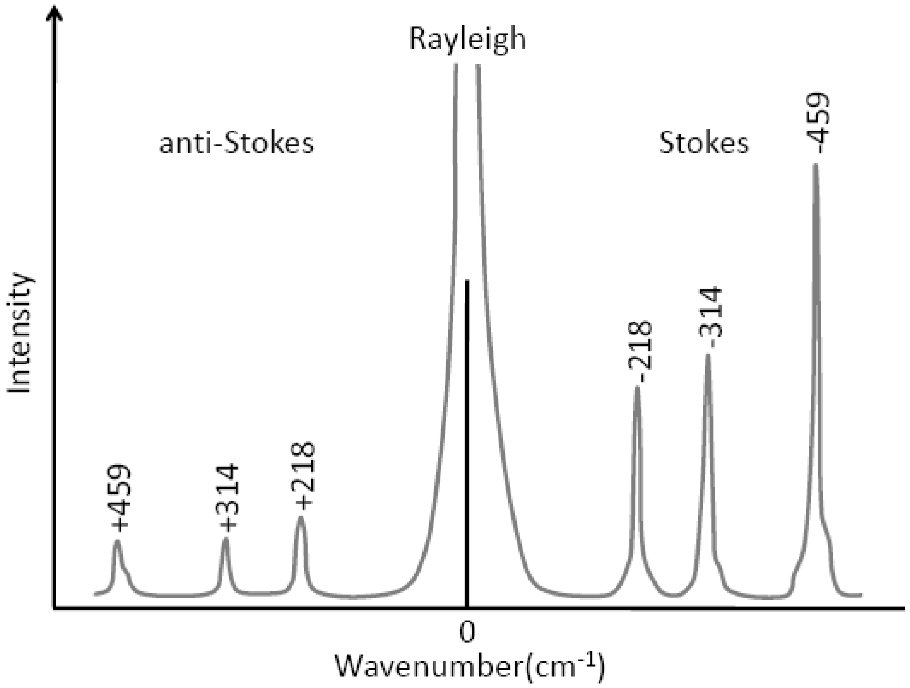

Figure 2.3 – Illustration of the symmetrical nature of Stokes and anti-Stokes Raman scattering about the Rayleigh, or zero shift, line. Note the anti-Stokes scattering has lower intensity than its Stokes counterpart due to the ground vibrational state being more highly populated at room temperature.

It is possible to use the Boltzmann equation, as defined by Equation 2.2, to determine the ratio of the intensities of Stokes to anti-Stokes Raman scattering.

$$\frac{N_n}{N_m} = \frac{g_n}{g_m} exp\left[\frac{-(E_n - E_m)}{kT}\right]$$

Equation 2.2

Here N_n and N_m are the number of molecules which exist in the excited and ground vibrational energy levels, respectively. Whilst g_n and g_m denote the degeneracy, and E_n and E_m the energy, of the excited and ground vibrational states. The Boltzmann constant, k, and the temperature, T, complete this equation.

Ordinarily, only the Stokes Raman scattering is measured due to the lower intensity of the anti-Stokes scattering. As such, from here on in, the use of the term Raman will refer only to that of Stokes Raman scattering.

2.2.3 The Mathematical Theorem of Raman Spectroscopy

Before we can begin to understand the physical process behind the Raman phenomenon, we must first consider the laser source which is used to illuminate the sample. A wave of polarised electromagnetic radiation, such as a laser, travelling along the z-axis consists of an electric component and a magnetic component, which operate perpendicular to one another. Only the electric component is of interest in the Raman phenomenon. The electric field strength, E, of a laser beam fluctuates with time and can be described by Equation 2.3, where E_0 denotes the vibrational amplitude of the laser and ν the frequency of the laser at time, t.

$$E = E_0 cos 2\pi \upsilon t$$

Equation 2.3

When linearly polarised light, such as that produced by a diode laser, interacts with a molecule it can result in the distortion of the electron cloud and therefore induce a dipole moment in the molecule. The extent to which the electron cloud distorts is related to the polarisability of the molecule. Ordinarily the electron clouds of larger molecules are more easily distorted. The electric dipole which is induced as a result of this interaction is expressed in its simplest form by Equation 2.4, where the induced dipole is denoted by μ and the polarisability and electric field strength of the laser by α and E respectively.

$$\mu(t) = \alpha(t)E(t)$$

Equation 2.4

However, the polarisability of a molecule describes the shape and volume of the electron cloud at a given time. Therefore, in order to be adequately described, it must be represented as a tensor in all three Cartesian coordinates. Similarly, the polarisation of the incident light may be in any plane. As such, the induced molecular dipole may occur in any plane and therefore must be expressed in all three Cartesian coordinates as described by Equation 2.5.

$$\begin{bmatrix}\mu_x\\ \mu_y\\ \mu_z\end{bmatrix} = \begin{bmatrix}\alpha_{xx} & \alpha_{xy} & \alpha_{xz}\\ \alpha_{yx} & \alpha_{yy} & \alpha_{yz}\\ \alpha_{zx} & \alpha_{zy} & \alpha_{zz}\end{bmatrix}\begin{bmatrix}E_x\\ E_y\\ E_z\end{bmatrix}$$

Equation 2.5

If the molecule vibrates upon interaction with the incident light, the time dependant induced nuclear displacement from the equilibrium position, q, can be described in terms of the amplitude, q_0, and frequency, ν_m, of the molecular vibration using Equation 2.6.

$$q = q_0 cos 2\pi \upsilon_m t$$

Equation 2.6

Furthermore, the polarisability of the molecule is dependent upon its environmental state and events such as nuclear vibrations will alter the polarisability of the molecule. Consequently, it is possible to describe the polarisability of the molecule in terms of nuclear movement using an expanded Taylor's series. However, for small molecular vibrations the polarisability is a linear function of nuclear movement, and therefore can be adequately expressed by Equation 2.7 where α_0 denotes the polarisability of the molecule at equilibrium position.

$$\alpha = \alpha_0 + \left(\frac{\partial \alpha}{\partial q}\right)_0 q_0 + \ldots$$

Equation 2.7

Combining the aforementioned equations provides an expression (Equation 2.8) which describes the induced dipole moment which occurs during the scattering process.

$$\begin{aligned}\mu &= \alpha E_0 cos 2\pi \upsilon_0 t\\ &= \alpha_0 E_0 cos 2\pi \upsilon_0 t + \left(\frac{\partial \alpha}{\partial q}\right)_0 q E_0 cos 2\pi \upsilon_0 t\\ &= \alpha_0 E_0 cos 2\pi \upsilon_0 t + \left(\frac{\partial \alpha}{\partial q}\right)_0 E_0 cos 2\pi \upsilon_0 t cos 2\pi \upsilon_m t\\ &= \alpha_0 E_0 cos 2\pi \upsilon_0 t + \frac{1}{2}\left(\frac{\partial \alpha}{\partial q}\right)_0 q_0 E_0 cos\{2\pi(\upsilon_0 + \upsilon_m)t\} + \frac{1}{2}\left(\frac{\partial \alpha}{\partial q}\right)_0 q_0 E_0 cos\{2\pi(\upsilon_0 - \upsilon_m)t\}\end{aligned}$$

Equation 2.8

Upon examination, Equation 2.8 can be broken down into three distinct terms, the first of which is described by Equation 2.9. This term describes the elastic, or Rayleigh, scattering whereby there is no appreciable transfer of energy and therefore no change in frequency or change in polarisability tensor.

$$\alpha_0 E_0 cos 2\pi v_0 t$$

Equation 2.9

The second and third terms, as denoted by Equations 2.10 and 2.11, describe anti-Stokes and Stokes Raman scattering, respectively.

$$\frac{1}{2}\left(\frac{\partial\alpha}{\partial q}\right)_0 q_0 E_0 cos\{2\pi(v_0 + v_m)t\}$$

Equation 2.10

$$\frac{1}{2}\left(\frac{\partial\alpha}{\partial q}\right)_0 q_0 E_0 cos\{2\pi(v_0 - v_m)t\}$$

Equation 2.11

In the case of both Stokes and anti-Stokes Raman scattering, the change in frequency is proportional to the energy of the bond vibration in question. Upon closer examination, it is possible to discern further information from Equation 2.8. As the polarisability tensor varies with the bond vibration, the scattered field will change with respect to the input polarisation. Thus, examinations of the polarisation of the Raman scattered field can provide further information about a bond or molecule. Furthermore, it can be seen that if there is no induced nuclear movement, and therefore no change in polarisability, then there will be only elastic scattering. This second observation is the basis of one of the selection rules which underpin Raman scattering.

2.2.4 Molecular Vibrations

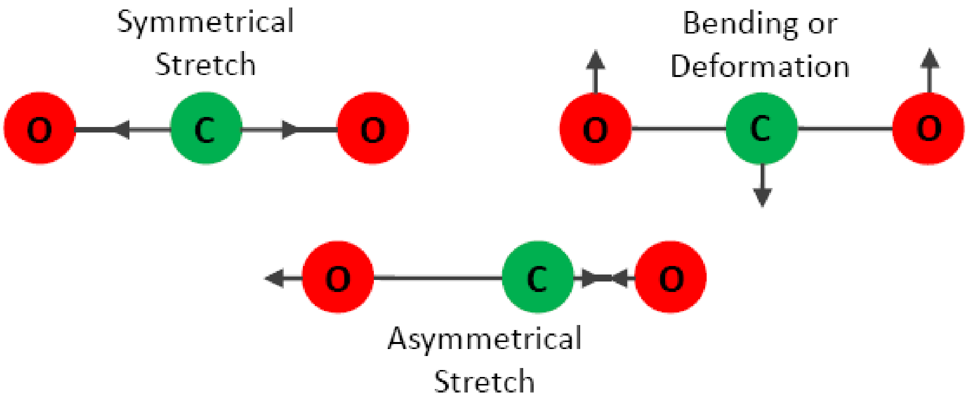

Figure 2.4 – Spring and ball representation of the possible bond vibrations in a carbon dioxide molecule. In each figure, the balls represent the atoms which comprise the molecule and the lines, or springs, the bond between the atoms.

The theory which has been presented up to now describes the process by which the interaction of a photon and molecule can result in Raman scattering. However, until now the process has been described in terms of a single type of vibration of a single bond within a molecule. The reality is somewhat more complicated; even the simplest of molecules can vibrate in a number of manners, although not all will be Raman active. As a simple example, a triatomic molecule such as carbon dioxide can undergo three distinct bond vibrations, as illustrated in Figure 2.4.

In the case of the carbon dioxide bond vibrations, only the symmetrical stretch is Raman active, as it is the only one which results in a change in polarisation. From this simple example of a three atom molecule, it is clear to see that the number of possible bond vibrations increases very quickly with increasing molecule size. For any non-linear molecule, the actual number of possible bond vibrations can be determined using Equation 2.12, where *N* is the number of atoms which comprise the molecule.

$$vibrational\ degrees\ of\ freedom = 3N - 6$$

Equation 2.12

It is also necessary to understand that the vibration of an individual bond may be affected by the close proximity and energy of one or more neighbouring bonds. In such cases, a group vibration is observed. This type of bond vibration is very common in biological samples due to the complex nature of the constituent molecules. Over the years, analysis of an extensive range of molecules has enabled the wavenumber ranges in which specific bond vibrations occur to be identified. Figure 2.5 details the wavenumber ranges of some common bond and group vibrations. The region 600 - 1800 cm^{-1} is named the fingerprint region, as this is the wavenumber range in which most of biological bond vibrations are contained.

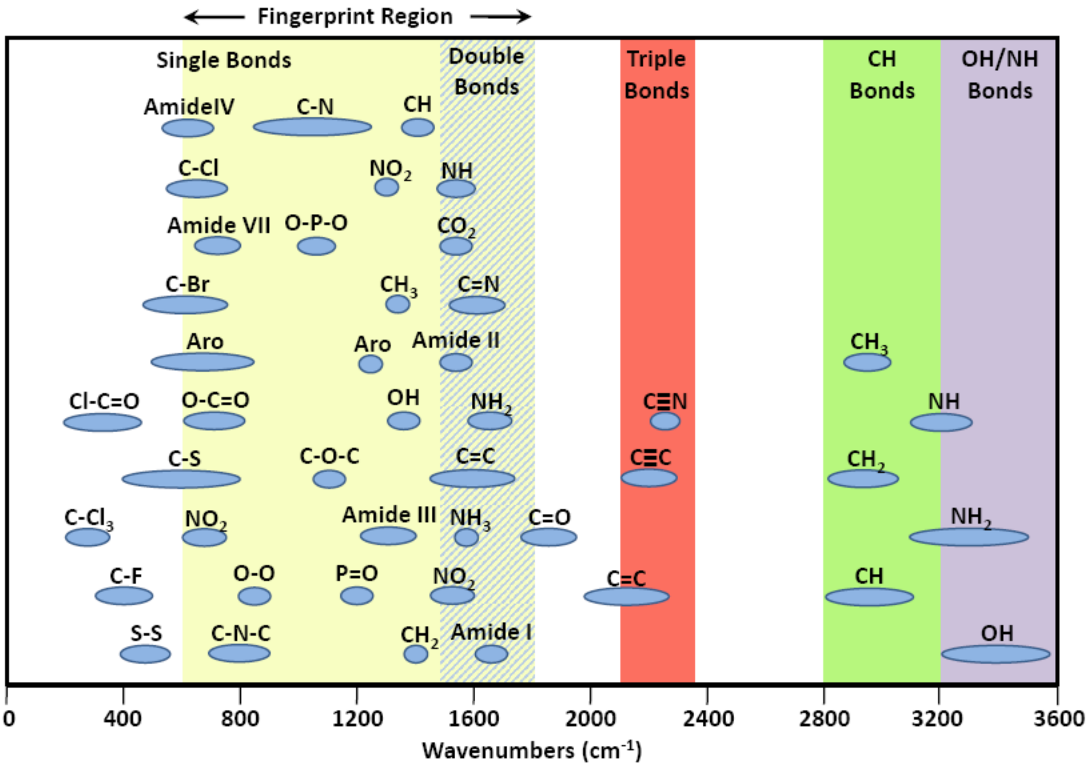

Figure 2.5 – The Raman shifts of common bond vibrations in the wavenumber range 0 – 3600 cm^{-1}. The fingerprint region, which denotes the range in which many of the bond vibrations associated with biological samples are observed, is generally accepted to fall in the range 600 - 1800 cm^{-1}. Figure inspired by tables presented in [117].

2.2.5 The Raman Spectrum

The power of Raman spectroscopy lies in the fact that it is possible to probe all constituent molecules in a sample simultaneously. As previously discussed, upon Raman scattering the incident photon is red shifted. That is, a portion of its energy has been transferred to molecule to induce the bond vibration. The resulting change in the inverse wavelength is known as the Raman shift, $\overline{\nu}$, as described by Equation 2.13.

$$\bar{\upsilon} = \frac{1}{\lambda_i} - \frac{1}{\lambda_s}$$

Equation 2.13

In Equation 2.13, the Raman shift has units of cm^{-1}, and λ_i and λ_s are the wavelengths of the incident and scattered light in cm.

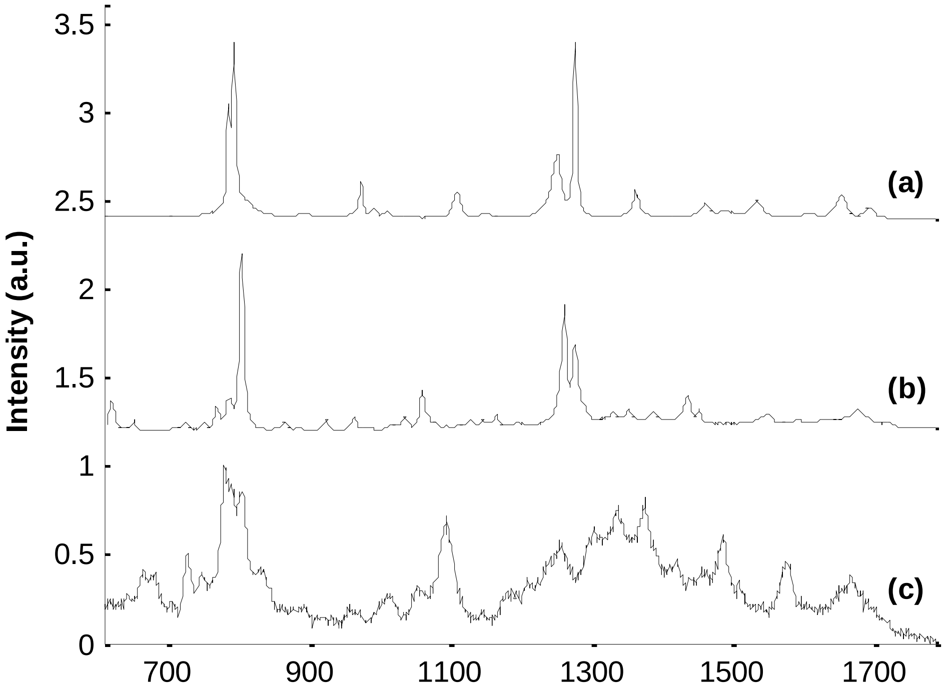

Figure 2.6 – Illustration of the relationship between the complexity of molecular structure and the corresponding Raman spectrum. (a) Cytosine, (b) deoxycytidine monophosphate and (c) DNA represent molecules of increasing complexity and accordingly, their corresponding Raman spectra are more complex.

As discussed previously, the larger the molecule, the greater the number of possible bond vibrations. In particular, large molecules which are comprised of many different types of atoms display a larger number of distinct bond vibrations, and thus a more complex Raman spectrum. In order to demonstrate the relationship between the complexity of the Raman spectrum and the studied molecule, Figure 2.6 shows Raman spectra taken from a range of molecules associated with DNA.

2.2.6 Raman Micro-Spectroscopy

Most often, the technique of Raman spectroscopy is combined with microscopy for the study of biological samples. This technique is termed Raman micro-spectroscopy or Raman microscopy. In this method, the sample is illuminated using a laser which is focused using a microscope objective. The scattered light is then collected using the same objective or another objective at some other orientation. The advantage of using such a technique is that small volumes can be probed within cells and tissues. Additionally, by employing automated microscope stages whole cells and tissue sections may be analysed, by sequentially moving and analysing the sample in a process known as Raman mapping. As the technique of Raman microscopy was used exclusively for the work which is presented in this thesis, a more in-depth coverage of this method is reported in Chapter 3.

2.2.7 Limitations of Raman Spectroscopy in Bioanalysis

Despite the power of Raman spectroscopy, as with any technique there are limitations. The most significant of which has already been mentioned; it is an inherently weak process with only 1 in 10 million photons being Raman scattered. This limitation coupled with the fact that biological samples are weak scatterers can lead to problems associated with the signal strength of the detected Raman signal.

Furthermore, many biological samples contain components which display autofluorescent properties. This autofluorescence is often several orders of magnitude greater than the

Raman signal and can often mask the Raman signal entirely. In such cases, switching from visible to near-infrared (NIR) lasers can help alleviate the problem to some extent. Similarly, NIR lasers are often employed in preference to visible lasers for the analysis of biological specimens, in an effort to prevent inducing photodamage. However, in many cases the choice of laser wavelength is a trade-off between minimising photodamage whilst maintaining reasonable signal strength, due to the fact that the Raman intensity, I, is proportional to the inverse fourth power of the laser wavelength, λ, as described by Equation 2.14. l, α and K in Equation 2.14 refer to the incident laser power, the polarisability of electrons in the molecule and a constant term, respectively.

$$I = Kl\alpha^2 \frac{1}{\lambda^4}$$

Equation 2.14

2.3 Raman Spectroscopy for Biomedical Applications

One of the early pioneers of biological analysis using Raman spectroscopy was John Edsall. This first work was involved with the investigation of selected amino acids and their ionisation in aqueous solution [118]. However, it was not until the development of photoelectric recording in the 1940s, and later lasers in the 1960s, that Raman spectroscopy began to be widely applied to bioanalysis.

In recent years, the use of Raman spectroscopy has extended into the field of medicine, with applications ranging from localisation of cellular components to identification of bacterial species and diagnosis of tissue pathology. As such, the following sections have been written to provide an introduction to the applications of Raman spectroscopy in the field of biology and biomedicine. For a more in depth analysis, there exist many comprehensive reviews detailing the extensive and varied application of Raman spectroscopy and its associated techniques in the field of biology and medicine [119-122].

2.3.1 Biomolecules

The complexity of Raman spectra increases with the size and complexity of the molecule being analysed. As such, it should be of no surprise that the first Raman spectroscopy endeavours in the field of biology were those which investigated the structure and interactions of isolated biomolecules and their derivatives.

Proteins

During the 1970s the investigation of proteins using Raman spectroscopy was extensively documented by Lord and co-workers in a series of publications which reported amongst others, the conformational studies of lysozyme, riobonuclease, α-chymotrypsin, bovine serum albumin, and β-lactoglobulin[123-127]. It was found that not only were the Raman spectra of poly amino acids useful in determining the structure-spectrum relationship, but also the secondary structure of the protein. Specifically, the amide I and amide III bands which occur as a result of C=O stretching and a mixture of C-N stretching and N-H in-plane bending in the polypeptide backbone, respectively. The frequency of the amide III band is especially sensitive to the secondary structure of the protein, displaying a frequency shift in α-helical, β-sheet and random coil proteins. The amide I band, although to a lesser extent, still exhibits some sensitivity to the backbone conformation[128]. More recently, Raman analysis of proteins and their subunits has been focused on a number of applications including enzyme-substrate interactions, protein-ligand interactions, viral assemblies and industrial biotechnology[129-131].

Lipids

Spectral characterisation of lipids using Raman spectroscopy has lead to a number of regions being identified as vibrations associated with lipid molecules. In the fingerprint region, significant bands are seen due to the in-plane CH_2 twisting mode, CH_2 scissoring mode, and carbonyl stretch in the region of 1300, 1440 - 1455, and 1735 cm^{-1} respectively. Furthermore, Raman bands arising due to the symmetric and asymmetric stretching of the methyl group are seen in the region of 2850 - 2895 cm^{-1}. This work has enabled the spectroscopic analysis of lipids in a variety of biological samples. The identification and localisation of cholesterol in cells and tissue has been reported in relation to atherosclerosis[132, 133]. The distribution of lipid bodies has also been mapped using Raman microscopy in fixed leukocytes[134]. Most recently, an advanced Raman technique known as coherent anti-Stokes Raman scattering (CARS) microscopy has been successfully applied to the study of single lipids bilayers[135] and the identification and distribution of lipid droplets[136, 137] and vesicles[138] in unfixed specimens. However, although CARS microscopy is capable of providing images of cellular component distribution in live cells, the cost of the equipment remains prohibitively high.

Nucleic Acids

The study of the bases, nucleosides and nucleotides of both DNA and RNA has been extensive, and has employed both standard and advanced Raman techniques [139-146]. As such, the Raman spectrum of nucleic acids are well characterised. Bands in the region of 1090 - 1100 cm^{-1} result from the symmetric stretching of the O-P-O linkage, whilst contributions resulting from a complex vibrational mode involving the deoxyribose-linked phosphodiester occur in the region of 830 - 840 cm^{-1}. In addition to the backbone, there are also bands in the Raman spectrum of nucleic acids which originate from the purine and pyrimidine bases. Ring breathing modes occur in the region 600 - 800 cm^{-1}and the in-plane vibrations of base residues in the region 1150 - 1600 cm^{-1}. Furthermore, analysis has shown that the position of certain Raman bands in the spectrum of DNA can be indicative of the conformation of the backbone[147]. In addition, the Raman spectra of nucleic acids are also capable of providing information regarding the effect of environmental conditions, such as temperature and pH[148-150]. This understanding of the Raman spectrum has enabled the localisation and analysis of nucleic acids in biological samples[151-153]. More recently, using a technique called tip-enhanced Raman scattering (TERS), which combines Raman spectroscopy and atomic force microscopy (AFM) to enhance the Raman signal, it has been demonstrated that it is possible to probe RNA homopolymers at a lateral resolution of a few nucleobases[154]. This advance is a significant step towards the development of nucleic acid sequencing using advanced Raman spectroscopic techniques.

2.3.2 Cells and Tissues

Since the early 1990s, the application of Raman spectroscopy to the study of biological systems has increased exponentially. The fields of study are too large in number to discuss fully in this thesis. This section however, is designed to provide an introduction to the type of analysis currently possible.

Bacteria

The study of bacteria by Raman spectroscopy has been extensive. The size of most bacterial species makes analysis with Raman microscopy very convenient. A single static spectrum can be used to characterise a single bacterium, making Raman a potentially rapid and efficient tool in this field. Much of the work to date has been involved in the differentiation of bacteria species based on their spectral signatures. Raman spectroscopy has been used in combination with a number of multivariate techniques, including principal component analysis[155], cluster analysis[155-158], and discriminant analysis[159, 160], amongst others. More recently, this has been extended to the discrimination of bacteria at the strain level[161, 162]. In particular, the application of the advanced Raman method of surface-enhanced Raman scattering (SERS) which uses roughened metal surfaces, or colloids, to enhance the Raman signal, has attracted attention in this field due to much of the variation between bacterial strains resulting from their surface proteins [163].

Eukaryotic Cells

Eukaryotic cells, however, are much larger in size; the average somatic cell measures approximately 10 μm in diameter. As such, the use of static Raman spectroscopy is less common. Yet, this methodology has still been used in certain applications including the identification and investigation of cellular inclusions[132] and structures[164, 165]. Static measurements have also been successfully applied in situations where the biochemical difference between sample groups is more significant than the heterogeneity of the cells measured, as in the discrimination of healthy and cancerous cells[166]. Alternatively, calculating the average of several spectra from different locations within the sample has been used to characterise heterogeneous samples such as cells[167]. Furthermore, laser beam shaping is a method which has been extensively utilised to circumvent the issues arising from static measurements in heterogeneous samples. The use of a cylindrical lens in combination with lasers, or diode lasers without circulising optics, results in a laser line as opposed to a spot. As such, when focused on the sample, a larger volume is analysed, overcoming many of the issues of heterogeneity. When applied to cellular analysis, a single static measurement can provide a representative spectrum for a single cell[151, 168-170].

A methodology for Raman spectroscopic measurements of cells which overcomes and characterises a cell’s heterogeneity is Raman mapping. This technique is implemented by moving either the sample using a motorised stage, or the laser over the sample by means of a scanning mirror. As such, consecutive measurements may be made over a wide region of the sample. Raman mapping combined with principal component analysis has been successfully used to locate cellular components in freeze dried cells without the need for labelling[171]. Furthermore, cellular structures and organelles have been distinguished using optimised cluster analysis of Raman mapping data in formalin fixed fibroblasts[172]. Cellular structure, including mitochondria, in fixed HeLa cells have also been distinguished using

Raman mapping data analysed using hierarchal cluster analysis[173]. The chemical and morphological changes which occur in cells as a result of chemically induced oxidative stress has been reported using Raman mapping and cluster analysis[174]. However, one of the major issues which surround Raman mapping as a technique for biological analysis is the prohibitively long sampling times. In order to map a cell with sufficient spatial resolution to provide a high resolution map can take hours. Improvements in instruments have enabled map acquisition times to be reduced significantly, but it still remains that Raman mapping is most suited to fixed samples.

Raman imaging, however, is an alternative technique which enables whole cell imaging without the need for labels and within a timescale which doesn't preclude live cell analysis. Uzunbajakava *et al.* measured the protein distribution in live lymphocytes and epithelial cells using direct Raman imaging[175]. Subsequently, the same researchers demonstrated Raman imaging of protein and DNA distribution in fixed healthy and apoptotic HeLa cells[152]. This technique has also been applied to the study of β-carotene in live bovine corpus luteum cells[176]. However, as this method investigates only selected regions of the Raman spectrum at any one time, it is most commonly used for the investigation of component distribution within cells. Furthermore, it requires *a priori* knowledge of the Raman bands of interest.

Live Cell Analysis

One of the distinct advantages of Raman as a technique for biological analysis is that there is no sample preparation required: It is possible to acquire Raman spectra without labelling or fixation. As such, this section will discuss the current applications of Raman spectroscopy in live cell analysis, whilst also mentioning current limitations. As previously discussed, Raman mapping is not suited to the study of live cells. Therefore, most live cell analysis has been performed using either direct imaging or averaged static measurements. Many of the most significant studies utilising direct imaging have been discussed previously, so the focus will be on static spectral measurement methodologies.

The application of using an expanded laser beam, either linear or elliptical in shape, has proven very effective in live cell analysis. Although the resulting spatial resolution of such a measurement is reduced, a large volume of the cell is probed at one time thus enabling rapid measurements. Typical acquisition times are of the order of minutes, depending upon the size and shape of the laser beam and cell, and the number of acquisitions per cell. This methodology has been used to examine a number of biological processes in live cells including the differentiation of murine embryonic stem cells[151, 169, 177], cell cycle dynamics[178] and cell death[170, 179]. It has also been used to investigate the distribution of haemoglobin in young and old erythrocytes[180]. Furthermore, the discrimination of healthy and cancerous cells[166, 181, 182] and different cancer types[183] has been well documented.

Tissues

The nature of disease causes fundamental changes to the biochemistry of the affected tissue. As such, Raman spectroscopy is ideally suited to the investigation of tissue pathology. Unsurprisingly, the field of oncology research has seen an exponential growth in the application of Raman spectroscopy for tissue diagnostics. Early spectroscopic measurement of normal and cancerous brain tissue has revealed lower lipid to protein ratio and higher levels of haemoglobin in tumours[184, 185]. More recently, the structural features and chemical composition of fresh frozen brain sections have been mapped using Raman fibre-optic probe technology[186-188]. Furthermore, successful discrimination between the Raman spectra of healthy, cancerous and necrotic brain tissue has been reported[189].

Similarly, the chemical composition of breast tissue is altered by disease. Spectroscopic analysis of benign, malignant and healthy breast tissue demonstrated that the collagen and fat content of the tissue are indicative of the pathology, with increased lipid and collagen content in malignant samples [190, 191]. Variation in the spectral signatures has enabled discrimination of different grades of ductal carcinomas[192]. As Raman spectroscopy has proven to be a non-destructive technique, the ultimate aim would be to develop a methodology to perform *in vivo* diagnoses. A recent study demonstrated analysis of calcifications through layers of skin and tissue up to 10mm using spatially offset Raman scattering (SORS) technology[193]. This technique works on the principle that the Raman scattering is collected from a location which is adjacent to the point of illumination. This advance indicates that it may be possible to perform *in vivo* diagnosis of breast cancer based on the presence of calcifications.

In addition to the field of oncology, Raman spectroscopy has been applied to the biochemical investigation of a range of other tissues. One of the most widely studied is bone. Both the organic matrix and mineral components of bone tissue have been well characterised using Raman spectroscopy, as has the ultrastructure and process of mineralisation[194-196]. However, the area which has generated most interest is that of the effect of disease on the chemistry and structure of bone[197, 198]. As osteoporosis is one of the most common diseases of the bone, it is unsurprising that its pathology has been extensively studied using Raman spectroscopy[199-202]. Raman has also been applied to the investigation of the effect of ageing on the biochemistry and ultrastructure of bone[203]. Furthermore, using knock-out models, the roles which specific genes play in the development and maintenance of bone tissue have also been studied[204]. Recently, focus has been turned to the transcutaneous analysis of bone using SORS, with a view to *in vivo* disease diagnosis[205-208].

The aforementioned applications are only those for which there has been extensive investigation. A number of other tissue types have been studied using Raman spectroscopy including lung[209-211], bladder[187, 212, 213], arterial[214-218] and colon[219-222]. However, the main issue which remains if Raman is to be successfully applied to clinical diagnostics is obtaining enough samples to ensure that results are statistical significant, and to ensure that algorithms display high sensitivity and specificity.

2.3.3 Raman and Female Reproductive Biology

Both Raman micro-spectroscopy and imaging have been used to monitor the presence and distribution of β-carotene in live luteal cells as a function of time [176]. Primary investigations of the efficacy of Raman spectroscopy for the differentiation of normal, benign, and malignant ovarian tissues have also been reported [223, 224]. However, cervical tissue is the most extensively studied in the field of female reproductive biology.

The use of Raman spectroscopy for the differentiation of cervical tissue pathologies has been pioneered by Anita Mahadevan-Jansen. *In vitro* identification of cervical precancer was first reported in 1998 [225]. Subsequently, the development of a dedicated fibre optic probe and measurement protocol enabled *in vivo* measurements [226]. Since then algorithms have been successfully developed to distinguish high-grade dysplasia, squamous metaplasia and normal ectocervical tissues [227, 228].

Recently, Raman spectroscopy has been applied to the analysis of human embryo developmental potential. This work reported the development of metabolomics assessment of day 3 embryo culture medium using Raman spectroscopy. The resulting algorithm which correlates the spectroscopic profile of culture medium with pregnancy outcome has been shown to have a sensitivity of 85.7 %, and a specificity of 76.5 % [103]. Furthermore, the first study investigating the application of Raman spectroscopy to the study of murine oocytes has recently been published. This work describes the discrimination of fixed GV and MII oocytes based upon their Raman spectral signatures in the high wavenumber region.

The authors attribute the spectral variation between groups to the change in the quantities and location of lipids that result from maturation[229].

Chapter 3

General Materials and Methods

This chapter provides an overview of the instrumentation which was used in the work that is reported in this thesis. Details regarding sample collection and preparation are presented. An in-depth discussion of the spectral preprocessing methods which have been implemented is also given. Specific details of the experimental setup are not provided, as these varied between experiments, and so are given in the appropriate chapters.

3.1 Sample Preparation

Unless otherwise stated, all work described in this section was performed in a laminar flow booth in order to preserve sample integrity and negate the need for antibiotic supplementation of media.

3.1.1 Collection of Pre-antral Follicles

Leibovitz medium (SigmaAldrich, UK) supplemented with 3 mg/ml of BSA (SigmaAldrich, UK) was used for the collection and dissection of ovarian tissue. Prior to use, the osmolarity of the Leibovitz medium was tested and adjusted to 285 ± 5 mOsm by the addition of sterile water. Upon dissolution of the BSA, the medium was syringe filtered, to remove any contaminants and undissolved proteins, using a cellulose-acetate syringe filter with 0.2 μm pore (Iwaki, Japan) into sterile flasks (Iwaki, Japan). The medium and glass embryo dishes were warmed to 37 °C and allowed to acclimatise overnight.

3 week old C57Bl6J x CBA females were sacrificed by cervical dislocation. The ovaries were explanted to embryo dishes containing 1ml of Leibovitz medium. All further work was performed under low magnification using a stereomicroscope fitted with a heated stage operating at 37 °C. Using 26G needles, the ovaries were “cleaned-up” by removing excess tissue and the basal membrane. Following this, the ovaries were bisected and transferred to new dishes and pre-antral follicles were dissected from the halved ovaries using 26 G and 30 G needles. Using the microscope graticule, follicles which measured approximately 180 μm in diameter, displayed even colour, contained a centrally located oocyte and which had attached thecal tissue were selected for subsequent experiments.

3.1.2 Culture of Pre-antral Follicles

α-MEM (GIBCO, UK) supplemented with 5 % foetal bovine serum, FBS, (Labtech, UK), 1 i.u/ml recombinant human FSH, r-FSH, (gifted from Edinburgh IVF unit) and 180 μM ascorbic acid (SigmaAldrich, UK) was used for follicle culture. Prior to use, the osmolarity of the α–MEM medium was tested and adjusted to 285 ± 5 mOsm by the addition of sterile water. After mixing, the medium was syringe filtered using a cellulose-acetate syringe filter with 0.2 μm pore (Iwaki, Japan) into sterile flasks (Iwaki, Japan). Round-bottomed 96-well culture plates (Iwaki, Japan) were prepared by adding 30 μl of the culture medium and overlaying with 75 μl of sterile filtered silicone fluid (DowCorning). Plates were warmed to 37 °C in a 5 % CO_2 environment and allowed to acclimatise overnight prior to use. Pre-antral follicles were transferred to the culture plates using BSA-coated Pasteur pipettes and were cultured individually for 6 days. During this time, follicles were moved to fresh media every day, with new media being prepared every second day.

3.1.3 *In Vitro* Maturation of Cumulus-Oocyte-Complexes

COCs, obtained from follicles which had been cultured for 6 days, were matured in α-MEM (GIBCO, UK) supplemented with 5 % FBS (Labtech, UK), 1 i.u/ml r- FSH (gifted from Edinburgh IVF unit) and 20 ng/ml epidermal growth factor, EGF, (Boehringer). Prior to use, the osmolarity of the α–MEM medium was tested and adjusted to 285 ± 5 mOsm by the addition of sterile water. After mixing, the medium was syringe filtered using a cellulose-acetate syringe filter with 0.2 μm pore (Iwaki, Japan) into sterile flasks (Iwaki, Japan). Flat-bottomed 6-well culture plates (Iwaki, Japan) were prepared by adding two 100 μl and one 200 μl drop of the culture medium and overlaying with 3.8 ml of sterile filtered silicone fluid (Dow Corning). Plates were warmed to 37 °C in a 5 % CO_2 environment and allowed to acclimatise overnight prior to use. Leibovitz medium was prepared and warmed as described in Section 3.1.1.

The cultured follicles were transferred to an embryo dish containing Leibovitz medium. COCs were recovered by rupturing the follicles using a 30 G needle. COCs were then transferred through the two 100 μl wash drops and into the 200 μl culture drop of the equilibrated maturation medium using a pulled BSA-coated Pasteur pipette. COCs were cultured for 24 hours at 37 °C under 5 % CO_2.

3.1.4 Superovulation of Mice

Stock solutions of pregnant mare serum gonadotrophin, PMSG, and human chorionic gonadotrophin, hCG, (Intervet, UK) were prepared by reconstituting the respective hormones in sterile physiological saline (SigmaAldrich, UK) to a concentration of 500 i.u./1000μl. Working solutions of PMSG and hCG were prepared to a concentration of 5 i.u./100μl. Both stock and working solutions were stored at -20 °C until required for use. C57Bl/6J female mice between 6 and 8 weeks of age received 5 i.u. of PMSG by intraperitoneal injection at 4pm on day 0. At 3pm on day 2, 47 hours after PMSG, the mice were injected with 5 i.u. of hCG. For the collection of fertilised oocytes for embryo culture, after hCG injection, females were left overnight with a proven male; the presence of a vaginal plug on the morning of sacrifice was used to identify if mating had occurred. Mice were sacrificed by cervical dislocation 18-20 hours after administration of hCG to enable the collection of oocytes

3.1.5 Assessment of Mice in Oestrous

Experienced personnel performed visual inspection of the vagina to assess for oestrous in mice, as the facilities required for vaginal smearing were not available.

3.1.6 Collection of *In Vivo* Matured Oocytes

M2 medium (SigmaAldrich UK) was used for the collection of oocytes from unstimulated and stimulated ovulation cycles. Prior to use, M2 was syringe filtered using a cellulose-acetate syringe filter with 0.2 μm pore (Iwaki, Japan). The medium and embryo dishes were warmed to 37 °C and allowed to acclimatise overnight. Oviducts were explanted to embryo dishes containing 1 ml of pre-warmed M2 medium within 5 minutes of sacrifice. Under low magnification, using a stereomicroscope fitted with a heated stage operating at 37 °C, COCs were released by puncturing the swollen ampullae with No5 dinmont forceps and were transferred to flat-bottomed 48-well plates containing 100 μl drops of warm M2 medium using pulled BSA-coated Pasteur pipettes.

3.1.7 Collection of Immature Oocytes

Pre-antral follicles, collected as described in Section 3.1.1, were transferred to an embryo dish containing Leibovitz medium and COCs were recovered by rupturing the follicles using a 30 G needle.

3.1.8 Oocyte Denudation

Hyaluronidase (SigmaAldrich, UK) was reconstituted to a working concentration of 3 mg/ml in Leibovitz medium (SigmaAldrich, UK) and was stored at -20 °C until required for use. Before use, hyaluronidase solution was warmed to 37 °C and vortexed to ensure it was properly suspended. The cumulus cells were removed from the oocytes by treating with hyaluronidase, at a final concentration of 0.3 mg/ml, for 1 - 2 minutes. Complete denudation of immature oocytes using hyaluronidase was found to be difficult. As such, mechanical removal using a super-fine bore Pasteur pipette was performed after hyaluronidase treatment. Following cumulus removal, oocytes were passed through three 5 minute washes of fresh medium before subsequent processing.

3.1.9 Embryo Culture

M16 medium (SigmaAldrich UK) was used for embryo culture. Prior to use, M16 was syringe filtered using a cellulose-acetate syringe filter with 0.2 μm pore (Iwaki, Japan). Flat-bottomed 6-well culture plates (Iwaki, Japan) were prepared by adding two 100 μl and eight 20 μl drops of the culture medium and overlaying with 3.8 ml of sterile filtered silicone fluid (Dow Corning). Plates were warmed to 37 °C in a 5 % CO_2 environment and allowed to acclimatise overnight prior to use. Fertilised oocytes were collected in the same way as *in vivo* matured oocytes, as described in Section 3.1.6. They were then transferred through the two 100 µl wash drops and distributed 10 to a culture drops using a pulled BSA-coated Pasteur pipette. The embryos were cultured for 24 and 48 hours at 37 °C under 5 % CO_2, so as to reach the 2 and 4-cell stage, respectively.

3.1.10 Oocyte and Embryo Fixation

Phosphate buffered saline (PBS) was prepared by diluting 100 ml of 10X PBS solution (SigmaAldrich, UK) in 900 ml of ultrapure water (SigmaAldrich, UK). The solution was aliquotted into 100 ml sterile reagent bottles before being autoclaved at 121 °C for 20 minutes.

4 % paraformaldehyde solution was prepared by adding 4 g of paraformaldehyde (Fisher Scientific, UK) to 90 ml of PBS in a conical flask and a couple drops of 1 M NaOH were added. The solution was heated gently to 50 °C on a heated stirrer plate. Once the paraformaldehyde had completely dissolved, the solution was cooled. The pH was tested to ensure it was in the range of 7.2 - 7.4 and the solution was made up to 100 ml by adding 10 ml of PBS. The solution was aliquotted and stored at -20 °C until required for use. 2.5 % glutaraldehyde solution was prepared by diluting 250 µl of 50 % glutaraldehyde solution (Fisher Scientific, UK) with 4.75 ml of PBS. 20, 30, 40 and 50 % ethanol solution were prepared by diluting 100 % ethanol in PBS, whilst a 70 % ethanol solution was prepared by diluting 100 % ethanol in ultrapure water to prevent precipitation of salts.

Before fixing, oocytes and embryos were passed through two 5 minute washes in pre-warmed PBS to remove residual proteins from the M2 medium. Following washing, oocytes were either fixed in 4 % paraformaldehyde for 30 minutes, 2.5 % glutaraldehyde for 30 minutes, or an ethanol series of 20, 30, 40, 50 and 70 % ethanol for 5 minutes each. All fixing was carried out at room temperature. After aldehyde fixation, the oocytes were passed through three 5 minutes washes in fresh PBS. Ethanol fixed oocyte were passed through the reverse ethanol series to rehydrate them. Oocytes were stored in PBS at 4 °C until analysis.

3.2 Raman Measurements

3.2.1 The Raman Microscope

All Raman measurements acquired throughout this work were collected using an InVia Raman microscope (Renishaw plc, UK). This instrument consists of a DM-IRB inverted microscope (Leica MicroSystems, Germany) coupled to a dispersive spectrometer (Renishaw plc, UK).

Figure 3.1 –Photograph of the Renishaw InVia Raman microscope used in this work.

The microscope was equipped with a 40x/0.65N.A. objective (Leica MicroSystems, Germany) and two digital webcams: One was integrated with the Raman software for sample visualisation and mapping; the second was independent of the system and was used for the acquisition of sample images. Figure 3.2 illustrates the main components of the InVia system. The excitation source used with the Renishaw system was a 400 mW 785 nm diode laser (Toptica, Germany). However, the maximum laser power available after the plasma filter was measured to be 110 mW as opposed to the expected 240 mW. With no attenuation, this resulted in a laser power of 70 mW before the objective. The laser power could be attenuated by a selection of neutral density filters (ND) which was software controlled. The available laser powers were 100, 50, 10, 5, 1, 0.5, 0.1, 0.05, 0.01, 0.005, 0.001, 0.0005, 0.0001, and 0.00005 % of the total source power. From here on in all quoted laser powers refer to the power measured before the microscope objective.

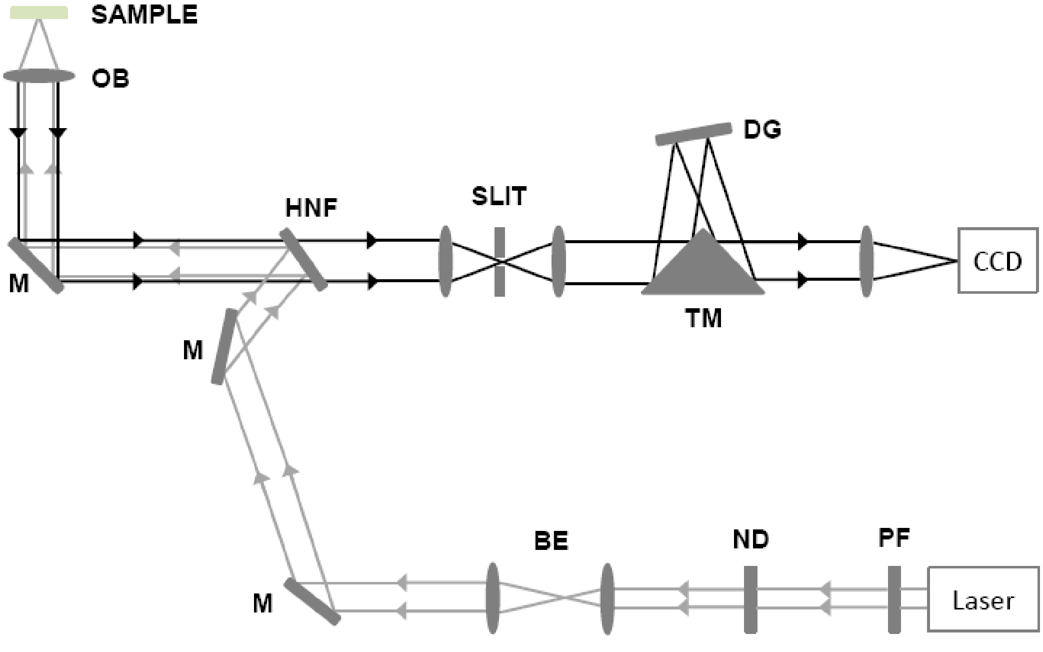

Figure 3.2 – Schematic of Renishaw InVia Raman microscope illustrating the key optical components and paths. The following components have been labelled: BE, beam expander; DG, diffraction grating; HNF, holographic notch filter; M, mirror; ND, neutral density filter OB, microscope objective; PF, plasma filter; and TM, triangular mirror. The incident laser and scattered light paths are depicted by the grey and black lines, respectively.

Light is collected in reflection mode, with a 180° back scattering configuration. The holographic notch filter reflects the Rayleigh scattering but transmits the Raman scattering, enabling Raman shifts as low as 100 cm^{-1} to be interrogated. Unlike many systems, the InVia does not use pinholes for confocal measurement. Instead, a two aperture system is implemented: Firstly, a confocal slit eliminates out-of-plane light on the y-axis, secondly, the binned CCD area is selected to eliminate out-of plane light on the x-axis.

The Raman scattered light is separated into its component wavelengths using a 1200 lines/mm grating. The light is detected using a Rencam thermoelectrically-cooled charge coupled device (CCD) with an array size of 578 by 385 and pixel size of 22 μm. Consequently, the spectral range which could be imaged in a single static acquisition was limited to approximately 570 cm^{-1}. However, using the SynchroScan mode in the WIRE 2.0 software, which moves the diffraction grating continuously throughout the measurement, the interrogated spectral range can be extended. Using the SynchroScan feature increases the spectral acquisition time; a static spectrum which was acquired in 10 s would take 37 s for the integration of the spectral range 450 - 1790 cm^{-1}.

The microscope is fitted with a precision motorised XYZ stage (Prior Scientific, UK). The precision controlled stage enables Raman mapping to be performed. In this technique, the stage, and thus sample, are progressively moved to allow the collection of individual spectra at various positions on a grid. This process of point-mapping enables a biochemical picture to be constructed for a sample which displays biochemical variation with location.

3.2.2 Raman Mapping Configurations

Two different mapping configurations are reported in the results; the rectangular raster map and the circular raster map as depicted in Figure 3.3. The former, involved the acquisition of spectra at 2 μm intervals on an orthogonal grid using a raster pattern. It can be seen from

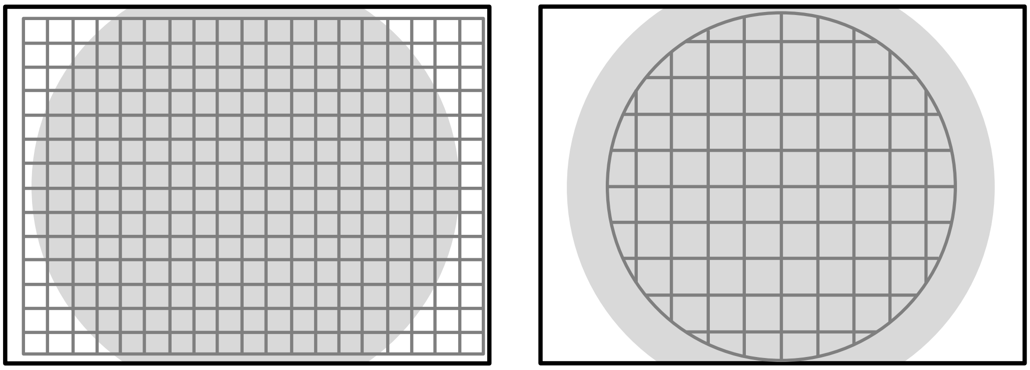

Figure 3.3 – Illustration of the two mapping configurations used for oocyte analysis. The first image depicts the rectangular mapping method which is reported in Chapter 5. The second image depicts the "reduced mapping" method, which is reported in Chapters 6 & 7.

Figure 3.3, this methodology results in some spectra being collected in regions with no oocyte present. The rectangular mapping protocol is very lengthy; it took approximately 18 hours to acquire the full rectangular maps, consisting of 1610 spectra, which are reported in this work. A second method, the reduced mapping protocol, as illustrated in the Figure 3.3, was developed to reduce the time required for oocyte analysis. This method involved the acquisition of spectra at regular intervals of 6 μm on a circular grid. As such, only positions in which the sample was present were interrogated.

3.2.3 Preparation of Raman Substrate and Sample Holders

Quartz coverslips (UQG Optics, UK) with a diameter of 25 mm and thickness of 200 μm were used as the substrate throughout this work. Furthermore, glass cloning rings with a diameter of 8 mm were used during the analysis of oocytes and liquids. Both the coverslips and cloning rings were reused in this work due to their prohibitive cost. As such, prior to use they were rinsed using acetone in order to remove residual silicone fluid and vacuum grease. They were then sonicated in a mild detergent soak for 10 minutes. Following this, in an ultrasonic bath they were twice washed in acetone for 10 minutes before being twice rinsed in ultrapure water for 10 minutes. All coverslips and cloning rings were stored in 70 %

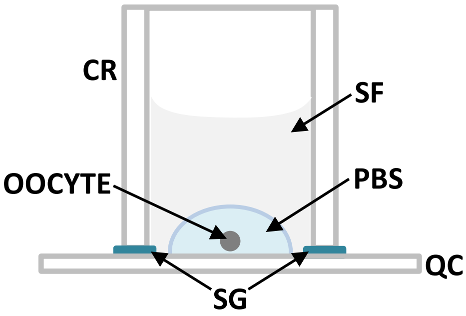

Figure 3.4 – Illustration depicting the sample holder construction for oocyte analysis, with the following components labelled: CR, cloning ring; QC, quartz coverslip; SF, silicone fluid; and SG, high vacuum silicone grease.

ethanol until required for use. Immediately before use the coverslips and cloning rings were removed from the alcohol soak and rinsed with ultrapure water before being dried under a stream of nitrogen.

Dry samples were prepared for Raman analysis by depositing an even layer of the substance on a clean quartz coverslip. For the analysis of liquids and oocytes, sample holders were made immediately prior to use, by fixing a glass cloning ring to a quartz coverslip using high vacuum silicone grease (Dow Corning, UK). In the case of liquid analysis, 150 μl of the substance of interest was added to sample holder using a micro-pipette. For oocyte analysis, a 10 μl drop of PBS was deposited on the quartz coverslip within the cloning cylinder, and the oocyte was transferred to the drop using a pulled Pasteur pipette. The PBS was then overlaid with 100 μl of silicone fluid to prevent evaporation, as illustrated in Figure 3.4.

3.3 Spectral Preprocessing

All spectral preprocessing was performed in MATLAB 7.0 using in-house written scripts.

3.3.1 Wavenumber Calibration

Instrument calibration is an important aspect of Raman spectroscopic analysis. This is especially true in applications involving the development of diagnostic algorithms and where data are obtained using different instruments. Diode lasers, unlike ion-based lasers such as Argon and Helium-Neon, are prone to wavelength instability. Therefore, it is important to ensure accurate calibration, as a shift of 0.1 nm in laser wavelength results in 1.6 cm^{-1} change in wavenumber. Consequently, a two stage wavenumber calibration was performed. The first stage of the calibration corrects for absolute wavelength shifts which result from changes in the optical path. The second corrects for shifts in laser emission wavelength.

Daily wavenumber calibration was performed prior to all experiments. A neon calibration lamp (Renishaw plc, Gloucestershire UK) was used for the absolute calibration of the wavelength abscissa. A neon spectrum (Figure 3.5) is obtained using a 37 s acquisition time over the wavelength range which is used in subsequent experiments, ensuring that none of the peaks are saturated. Selected neon emission bands are then used in the calibration. A third order polynomial is fitted to the experimental peak positions and the reported values.

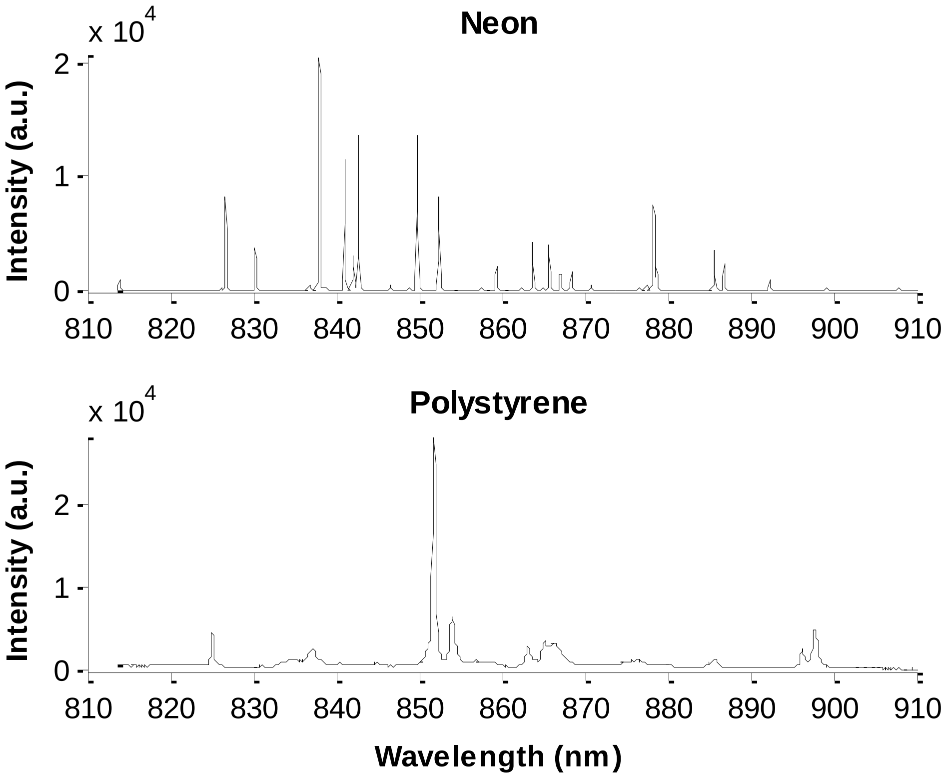

Figure 3.5 – Raman spectra acquired from the neon calibration lamp and the polystyrene standard.

The wavenumber scale is corrected for shifts in laser wavelength using a polystyrene secondary standard (Sigma Aldrich, UK). It was selected due to its stable and well defined Raman bands, and because it displays Raman peaks over the entire wavenumber range investigated in this work. A polystyrene spectrum (Figure 3.5) is obtained using a 37 s acquisition time and 7 mW laser power, over the wavelength range used in subsequent experiments.

The graphical user interface (GUI) which was produced in MATLAB 7.0 to perform the wavenumber calibration can be seen in Figure 3.6. The coefficients obtained from the neon calibration stage are used to adjust the wavelength abscissa to correct for optical path effects. Following this, the Raman wavenumber shift is calculated for the polystyrene spectrum by adjusting the laser wavelength until the Raman peaks agree, within accepted errors, with those published in the literature.

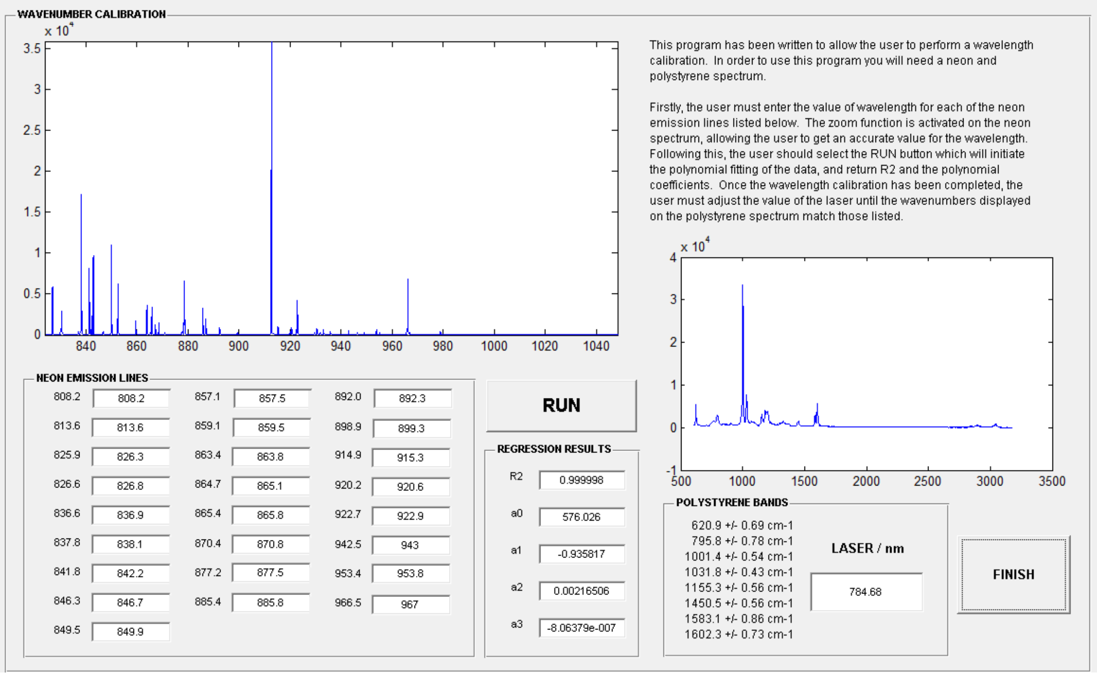

This program has been written to allow the user to perform a wavelength calibration. In order to use this program you will need a neon and polystyrene spectrum.

Firstly, the user must enter the value of wavelength for each of the neon emission lines listed below. The zoom function is activated on the neon spectrum, allowing the user to get an accurate value for the wavelength. Following this, the user should select the RUN button which will initiate the polynomial fitting of the data, and return R2 and the polynomial coefficients. Once the wavelength calibration has been completed, the user must adjust the value of the laser until the wavenumbers displayed on the polystyrene spectrum match those listed.

NEON EMISSION LINES

808.2	808.2	857.1	857.5	892.0	892.3
813.6	813.6	859.1	859.5	898.9	899.3
825.9	826.3	863.4	863.8	914.9	915.3
826.6	826.8	864.7	865.1	920.2	920.6
836.6	836.9	865.4	865.8	922.7	922.9
837.8	838.1	870.4	870.8	942.5	943
841.8	842.2	877.2	877.5	953.4	953.8
846.3	846.7	885.4	885.8	966.5	967
849.5	849.9				

REGRESSION RESULTS

R2	0.999998
a0	576.026
a1	-0.935817
a2	0.00216506
a3	-8.06379e-007

POLYSTYRENE BANDS

620.9 +/- 0.69 cm-1
795.8 +/- 0.78 cm-1
1001.4 +/- 0.54 cm-1
1031.8 +/- 0.43 cm-1
1155.3 +/- 0.56 cm-1
1450.5 +/- 0.56 cm-1
1583.1 +/- 0.86 cm-1
1602.3 +/- 0.73 cm-1

LASER / nm: 784.68

Figure 3.6 – Screenshot of the GUI produced in MATLAB for the wavenumber calibration.

3.3.2 Cosmic Ray Removal

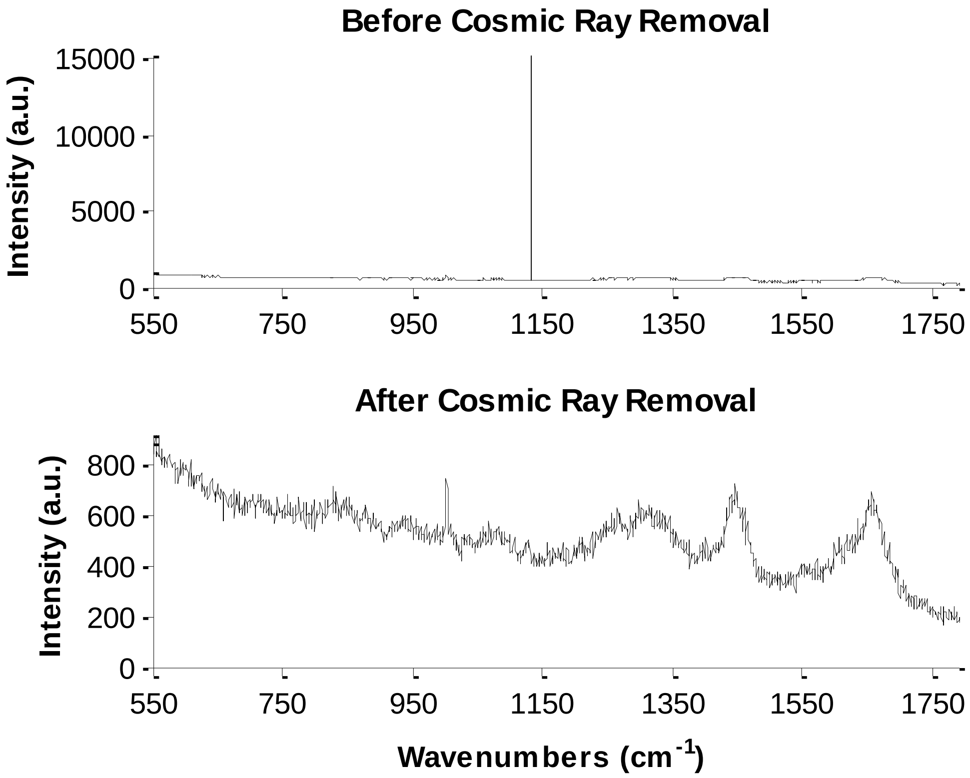

Figure 3.7 – Example illustrating the effect of cosmic rays on Raman spectra; the top spectrum shows a spectrum containing a cosmic ray and the bottom spectrum shows the same spectrum after application of the cosmic ray removal algorithm.

Cosmic spikes in the Raman spectrum result from high energy particles, known as cosmic rays, randomly hitting the CCD during spectral acquisition. The energy associated with these particles is far greater than energies associated with Raman scattering and as such, their presence can completely overwhelm the Raman spectrum, as illustrated in Figure 3.7. A GUI was produced in MATLAB which allowed cosmic spikes to be detected and removed by replacement with an average of the intensities of their neighbouring pixels.

3.3.3 Data Re-Sampling

So that spectra which had different wavenumber abscissa can be compared easily, the spectra underwent data re-sampling. This procedure used a cubic spline interpolation function to generate a new spectrum with a corresponding wavenumber axis sampling interval of 1 cm^{-1}.

3.3.4 Smoothing

Prior to background removal, the sample and PBS spectra were smoothed using a boxcar function. The sample spectra were smoothed using a 3-point boxcar function which returned the average of three adjacent points for each point. The PBS spectrum could be more heavily smoothed as it only had slowly changing gradients. As such, an 11-point boxcar function was used which returned the average of eleven adjacent points for each point. Using the boxcar functions resulted in tails at either end of the spectrum. These were removed by truncating the spectral region to 455 - 1780 $\mathrm{cm^{-1}}$.

3.3.5 Background Removal

In order to remove the spectral contributions arising from the quartz substrate, PBS buffer and system optics, background removal was performed. For each experiment, a spectrum of the PBS adjacent to the sample was acquired using the same experimental parameters. The algorithm used for the subtraction was that suggested by Maquelin *et al.*[230]. This method is not intended to subtract the exact amount of the non-oocyte signal, but instead subtract all contributions (sample and background) which cannot be distinguished from the background.

In order to implement this algorithm, the first derivative of the signal is calculated. The background corrected oocyte spectrum, O_{sub}, is then calculated according to Equation 3.1, where C and B are the uncorrected and background spectra, respectively. The background corrected oocyte spectrum was subsequently returned to its integrated form for further processing. The efficacy of this technique for the removal of background contributions from the oocyte spectrum is presented in Appendix 1.

$$O_{sub} = C - \frac{C \cdot B}{\|B\|^2} B$$

Equation 3.1

3.3.6 Baseline Removal

The varying fluorescence background which was present in the Raman spectra of oocytes was removed by subtracting a fourth order polynomial which was fitted through the points at 456, 478, 632, 800, 1142, 1512 and 1756 cm^{-1}.

3.3.7 Normalisation

To enable the comparison of spectra acquired from different samples on different days, it is necessary to perform some form of data normalisation. In this work two Raman measurement protocols were used; for each a different normalisation routine was used.

Total Intensity Normalisation

The average spectra obtained from the reduced mapping experiments described in Chapters 6 and 7 were subjected to an adjusted total intensity normalisation algorithm. This routine normalises a spectrum according to Equation 3.2.

$$x_{norm} = \frac{x}{\left\{\frac{\left(\sum_{i=1}^{n} x\right)}{n}\right\}}$$

Equation 3.2

In Equation 3.2, x and x_{norm} refer to the un-normalised and normalised spectra, respectively. The denominator is the integrated area of the non-normalised spectrum divided by the number of sampled wavenumbers, n. Problems can be encountered using this methodology if the denominator varies significantly between samples, as will be discussed in Chapter 6.

Multiplicative Signal Correction

The spectra collected in the mapping experiments described in Chapter 5 were corrected for variation in sample thickness, across the oocyte, using multiplicative signal correction (MSC). Before application of the MSC algorithm, the spectra which did not meet the threshold criterion of a total spectral intensity of 80,000 were excluded from the dataset. This process ensured that only spectra arising from the oocyte were included in the normalisation routine. MSC methodology was first described for the correction of variation in path length in IR spectra, but has since been used effectively to handle the effect of sample thickness variation in Raman spectra[209]. This technique is based upon the principle that an individual spectrum can be defined by an offset and a multiple of a reference spectrum, as described by Equation 3.3. In most cases, the reference spectrum is defined as the mean spectrum for the dataset being analysed.

$$x_i = a_i + b_i\bar{x} + e_i$$

Equation 3.3

In Equation 3.3, x_i and $\overline{x}$ refer to the individual and mean spectra, respectively, whilst a_i and b_i are constants which are found for each spectrum and e_i is a residual term. In this work the constants a_i and b_i were found by performing ordinary least squares (OLS) regression for each spectrum, using the robustfit function in MATLAB. Having found the value of the constants for each spectrum, the correction, as defined by Equation 3.4, can be performed.

$$x_{i,corrected} = \frac{x_i - a_i}{b_i}$$

Equation 3.4

3.4 Statistical Analysis

All univariate and multivariate statistical analysis was performed using MATLAB 7.0 and the Statistics Toolbox. Standard univariate statistical analysis, which included the calculation of arithmetic means, standard deviations and two-tailed unpaired t-tests, were used throughout this thesis. Specific details regarding the usage of univariate analysis is given in the appropriate Chapters. Conversely, full details of the multivariate statistical techniques which have been used in this work are reported in the following sections.

3.4.1 Unsupervised Multivariate Analysis of Spectroscopic Data

Unsupervised multivariate methodologies are used in applications where there is only an X-matrix and no other information available regarding the samples analysed. The underlying theory of unsupervised methods which have been utilised in this work will now be briefly introduced.

Singular Value Decomposition

In Chapter 4, singular value decomposition (SVD) was applied to the analysis of consecutive Raman spectra for the identification of induced photodamage, as was previously reported by Uzunbajakava *et al.*[152]. However, it also comprises the first stage of the principal component algorithm which was implemented in this work. The theory of SVD states that a data matrix A, consisting of (nxp) elements, can be decomposed into three constituent matrices U, Σ and V, according to Equation 3.5.

$$A = U\Sigma V^T$$

Equation 3.5

$$\Sigma_{ij} = \begin{cases} \sigma_i & 1 \leq i = j \leq n \\ 0 & i \neq j \end{cases}$$

Equation 3.6

In Equation 3.5, the data matrices U and V are orthonormal and span the column and row space of A, respectively. Σ is a diagonal matrix, as defined by Equation 3.6, which contains the singular values (SVs) that describe the relationship between the matrix U, V and A, as defined Equation 3.5. The SVs in Σ are non-negative, real values which appear in decreasing order. The underlying principle of applying SVD to the study of photodamage is that in a fixed sample, which has not undergone photo-induced degradation, consecutive spectra should not vary outside the range of accepted noise. Consequently, the first SV should adequately describe the entire dataset. Conversely, if sample degradation has occurred, changes in the Raman spectrum between consecutive measurements will lead to the requirement to include subsequent SVs.

Principal Component Analysis

Primarily, principal component analysis (PCA) is used to reduce the dimensionality of data sets, and as such, is the most widely used multivariate statistical method in spectroscopic data analysis. Considering spectroscopic data, a significant obstacle in performing statistical analysis is the large number of variables which are measured for a single observation, or spectrum; it is not uncommon to have upwards of 1000 variables, or wavenumber measurements, in a single Raman spectrum. In order to perform meaningful statistical analysis on such a data set, observations of the magnitude of 1 million would be required, which in most cases is unfeasible. If however, the number of dimensions, or variables, in the data set can be reduced then fewer observations are required.

For a (nxp) data matrix which consists of n observations in p variables, PCA generates new variables, known as principal components (PCs), that are a linear combinations of the original variables X_1, X_2,..., X_p, as described for PC1 by Equation 3.7. The resulting PCs are orthogonal, in p-dimensional space, to the original variables.

$$PC_1 = a_{11}X_1 + a_{12}X_2 + \dots + a_{1p}X_p$$

Equation 3.7

$$X_1 = x_{11} + x_{12} + \dots + x_{1n}$$

Equation 3.8

In Equation 3.7, the coefficients a_{11}, a_{12},...,a_{1p}, are known as PC loadings and a (pxp) matrix containing the loadings for each PC is generated during PCA. Analysis of these loadings enables the identification of the variables, in the original data set, which contribute to the observed variance.

PCA is performed such that the variance, that exists in the original data set, which is described by PC1 is maximised, whilst satisfying the condition outlined by Equation 3.9. Each successive PC is generated so that it describes the largest remaining variance in the original data.

$$\sum_{i=1}^{p} a_i^2 = 1$$

Equation 3.9

During the process of PCA, each observation is assigned a score for each generated PC, and as such, a (nxp) matrix of PC scores is generated. These scores describe the contribution which each PC makes to the original spectrum of each sample. As such, scatter plots of these scores can be used to visualise, in fewer dimensions, any variation and clustering which may exist in the sample data set. Furthermore, due to its capability in dimension reduction, PCA is often used as a data preprocessing method prior to other multivariate methods such as cluster analysis and linear discriminant analysis.

Cluster Analysis

Cluster analysis is a multivariate method concerned with the identification of groups within a data set which contains similar objects. In Chapter 5, cluster analysis has been applied to the investigation of intra-oocyte biochemical variation. There are a number of algorithms which have been proposed for cluster analysis, of which the partitioning and hierarchal methods are the two most common. In this work, the partitioning method has been used, therefore, only the theory underpinning this algorithm will be discussed.

The partitioning algorithm applied in this work is the k-means method. The algorithm is based upon the idea of optimising the criterion for subdivision of the data into a specified number of clusters, k. Considering a data set containing n observations (x_1, x_2, x_3, ...,x_n), such that each observation is a real vector containing d elements. The cluster analysis is achieved by minimising the total sum of the within-cluster sums of the point-to-cluster-centroid distances, as described by Equation 3.10. In this equation, the bracketed term refers to the chosen distance measure between the data point $x_i^{(j)}$ and the cluster centroid, c_j, which in this work was a Euclidean distance.

$$\min_{sumD} \sum_{j=1}^{k} \sum_{i=1}^{n} \left\| x_i^{(j)} - c_j \right\|^2$$

Equation 3.10

In order to begin the clustering process, both the number of clusters and the cluster centroids must be specified. Ordinarily, the initial centroids are selected at random from the data set. However, the choice of initial centroid can influence the partitioning result. As such, it is commonplace to repeat the clustering process using different starting centroids, otherwise known as performing a replicate, in order to achieve the optimum result. In this work, 20 replicates were performed for each cluster analysis. As previously discussed, cluster analysis is an unsupervised technique and therefore requires no *a priori* knowledge of the dataset. Therefore, the optimum number of clusters must be determined iteratively.

$$S_i = \frac{\left(\min_{j=1:k} b_{ij}\right) - \bar{a}_i}{\max_{j=1:k}\left(b_{ij}, \bar{a}_i\right)}$$

Equation 3.11

In this work, the number of clusters was determined by optimising the total sum of distances and the average silhouette value for each observation. The silhouette value is a measure of how similar a single observation is to the others in its cluster, and how dissimilar it is to those in other clusters[231]. Equation 3.11 defines the silhouette value, S, for a single observation i. The average distance between the ith point and the points in the each of the other clusters is defined by b_{ij}, whilst the average distance between the ith point and the other points in its cluster is given by $\overline{a_i}$. In each case, the number of clusters was chosen such that the total sum of distances was minimised whilst the average silhouette value was maximised.

Hotelling's T^2 Test

The Hotelling's T^2 test, as outlined in Equation 3.12, is a generalised form of the Student's t-test which is used in multivariate hypothesis testing[232]. The Hotelling's T^2 test was applied in Chapter 4 to test whether mean spectra obtained from sub-sampling protocols were indistinguishable from the mean spectrum obtained from a fully characterised sample.

$$T^2 = n(\bar{x} - \mu_0)' S^{-1} (\bar{x} - \mu_0)$$

Equation 3.12

In Equation 3.12, n and $\bar{x}$ are the number of spectra that comprise the data set and the mean spectrum of the sub-sampling protocol being tested, whilst μ_0 is the mean spectrum of the fully characterised sample. S is the sample covariance matrix which is calculated according to Equation 3.13.

$$S = \frac{1}{n-1} \sum_{i=1}^{n} (x_i - \bar{x})(x_i - \bar{x})'$$

Equation 3.13

In Equation 3.13 n, x_i and $\bar{x}$ are the number of spectra that comprise the data, the ith spectrum and the mean spectrum of the sub-sampling protocol being tested, respectively. Consequently, the result of Equation 3.12 has an F-distribution on p and n-p degrees of freedom in the case of the null-hypothesis, as described by Equation 3.14.

$$F_{test} = \frac{(n-p)}{p(n-1)} T^2$$

Equation 3.14

3.4.2 Supervised Multivariate Analysis of Spectroscopic Data

Supervised methods require some prior knowledge of the data set which is to be analysed. Ordinarily, these techniques are used for the classification of samples. Therefore, an understanding of the sample groupings or some other additional knowledge is required to utilise these algorithms.

Canonical Variate Analysis

The purpose of canonical variate analysis (CVA) is to investigate the separation of groups which are known to exist in a data set. The process is similar to that of PCA in that the new variables, known as canonical variates (CVs), are generated such that they are a linear combination of the real variables. However, in CVA the canonical variates are generated in order to maximise the between group variance.

Considering a (*nxp*) data matrix containing *n* observations in *p* variables for which the individuals can be classified into *g* groups. The total variation of this data set can be described as a combination of the between-group variation, *B*, and the within-group variation, *W*. The process of CVA finds a linear combination of the original variables such that the ratio of the between-group and within-group variation, *F*, is maximised as described by Equation 3.15[232].

$$F = \frac{\left\{\frac{1}{(g-1)} a'\boldsymbol{B_0}a\right\}}{\left\{\frac{1}{(n-g)} a'\boldsymbol{W_o}a\right\}}$$

Equation 3.15

In Equation 3.15, $\boldsymbol{B_0}$ and $\boldsymbol{W_0}$ refer to the between-groups sum-of-squares and cross-products matrix and the within-group sum-of-squares and cross-products matrix, as defined by Equations 3.16 and 3.17 respectively.

$$\boldsymbol{B_0} = \sum_{i=1}^{g} n_i(\overline{x_i} - \bar{x})(\overline{x_i} - \bar{x})'$$

Equation 3.16

$$\boldsymbol{W_0} = \sum_{i=1}^{g}\sum_{j=1}^{n_i}\left(x_{ij} - \overline{x_i}\right)\left(x_{ij} - \overline{x_i}\right)'$$

Equation 3.17

In Equation 3.16 and 3.17, x_{ij}, $\overline{x_i}$, and $\overline{x}$ denote the x value of the jth observation in the ith group, the sample mean vector of the ith group and the overall sample mean vector, respectively. The newly formed CVs, y_i, are related to the original variables, x_i, by the eigenvector, a, which contains the coefficients which optimise the criterion of maximising the ratio, F.

It should be noted that the maximum number of variables which may be used in CVA is equal to the difference between the number of observations, n, and the number of groups, g. However, if the number of variables is close to this limit, the separation of groups can appear far greater. As such, in this work PCA was performed prior to CVA in order to reduce the dimensionality of the data.

Chapter 4

Investigation of Experimental Parameters Affecting the Raman Spectrum of the Oocyte

In order to optimise the experimental protocol for oocyte spectral analysis a number of experimental parameters must first be considered. Consequently, this chapter addresses the effect which acquisition time and incident laser power have on signal to noise ratio and laser induced photodamage. Attention is also given to the subject of fixative selection and ooplasm sub-sampling. The work contained within this chapter forms the foundations of much of the later work contained within this thesis.

4.1 Introduction

As a technique, Raman spectroscopy offers many advantages, however it remains the case that the process of Raman scattering is inherently weak. Although there is currently much focus being given to advanced methodologies, such as SERS, TERS and CARS, advances in instrumentation has enabled Raman microscopy to remain a strong presence in the field of biophotonics. That being said, even for a given experimental setup, there are many experimental parameters which must be optimised to benefit from the full potential of this technique.

This chapter presents the results of a series of experiments which have been designed to optimise the collection of Raman spectra from oocytes, so as to ensure they are of sufficient quality to enable both univariate and multivariate analysis. Particular attention has been given to the selection of a fixative which minimises the impact on the ooplasm spectrum. Furthermore, an effort has been made to identify the number of spectra required to accurately characterise the ooplasm. This latter investigation is of great significance in the analysis of large heterogeneous samples, yet it appears that this is the first time that work of this type has been conducted for biological samples.

4.2 Materials and Methods

4.2.1 Preparation of Samples

For this work, COCs were collected from superovulated C57Bl/6J females 20 hours post hCG and were treated briefly with hyaluronidase to remove cumulus cells. Oocytes were washed twice in M2 followed by two washes in PBS, and were then pooled and any fragmented or degenerate oocytes discarded. In Experiments 1, 2 and 4, the selected oocytes were fixed for 30 minutes in 4 % paraformaldehyde solution. Following fixation, oocytes were thrice washed in PBS before being stored in PBS at 4 °C until required for use.

In Experiment 3, the effect of fixation on the oocyte spectrum was investigated for different fixatives protocols, as outlined in Table 4.1. Both the glutaraldehyde and paraformaldehyde fixation was carried out for 30 minutes at room temperature, whilst the ethanol fixation was performed by passing the oocytes through 20, 30, 40, 50 and 70 % ethanol solutions for 5 minutes each. After fixation, oocytes were rinsed and resuspended in PBS. Unfixed oocytes were washed in PBS and used immediately.

Group	Oocytes Analysed	Fixative	Fixation Time (min)
1	10	4% paraformaldehyde	30
2	10	2.5% glutaraldehyde	30
3	10	Ethanol series	5/pass
4	10	Unfixed	-

Table 4.1 – Protocols used for the investigation of suitable fixatives.

4.2.2 Raman Spectroscopy Measurements

Experiment 1: Photodamage Assessment

This series of experiments was necessary to establish if the incident laser, which is used during the Raman spectroscopic analysis, causes significant localised heating resulting in sample degradation. In order to assess if sample degradation had occurred spectra which were collected consecutively from the same location were compared: Non-noise spectral variation was taken to be indicative of induced photodamage.

In this work three laser powers were investigated, as outlined in Table 4.2. For each oocyte, 31 consecutive spectra were collected from the same location through its central focal plane. Each spectrum was integrated for 37 s over the spectral range 600 - 1790 cm^{-1}. Only two oocytes were analysed using a laser power of 7 mW as it was found that the signal to noise ratio (SNR) of the spectra at this power was insufficient for further analysis.

Group	Oocytes Analysed	Laser Power (mW)
1	2	7
2	5	35
3	5	70

Table 4.2 – Experimental parameters used for the investigation of induced photodamage.

Experiment 2: Optimisation of Signal to Noise Ratio

This series of experiments was necessary to establish the optimum acquisition time and incident laser power for subsequent work. In order to determine the optimum values for these parameters the SNR of the resulting spectra were determined: Higher values of SNR are indicative of a higher quality spectrum.

In this work, four acquisition times and three laser powers were investigated, as outlined in Table 4.3. A total of five oocytes were examined in each of the five experimental groups. For each oocyte, 31 individual spectra were collected at a constant interval of 10 μm through its central focal plane. The spectral range investigated was 600 - 1790 cm^{-1}.

Group	Oocytes Analysed	Acquisition Time (s)	Laser Power (mW)
1	5	37	7
2	5	37	35
3	5	37	70
4	5	74	35
5	5	111	35
6	5	222	35

Table 4.3 - Experimental parameters used for the investigation of SNR.

Experiment 3: Comparison of Fixatives

This series of experiments was necessary to establish the effect of chemical fixation on the Raman spectrum of the oocyte. In order to assess the presence of spectral artefacts resulting from fixation, the Raman spectra of oocytes which had been fixed using ethanol, glutaraldehyde or paraformaldehyde were compared with the spectra of unfixed oocytes. A total of ten oocytes were examined in each of the four fixative protocol groups. For each oocyte, 31 individual spectra were collected at a constant interval of 10 μm through the central focal plane of the oocyte. Each spectrum was integrated for 37 s over the spectral range 450 - 1790 cm^{-1} using a laser power of 35 mW. A spectrum of the PBS buffer which surrounded the oocyte was also acquired using the same experimental conditions. A spectrum of 100 % ethanol, 50 % glutaraldehyde solution and pure paraformaldehyde powder was also integrated for 37 s over the spectral range 450 - 1790 cm^{-1} using a laser power of 70 mW.

Experiment 4: Reduced Map Oocyte Characterisation

This series of experiments was necessary to establish the minimum number of spectra which were required to adequately characterise the cytoplasm of the oocyte, in an effort to minimise analysis time. In order to determine this, the average spectrum derived from different numbers of individual spectra was compared to the average spectrum of the fully characterised cytoplasm for each oocyte.

For this work, a total of four oocytes were examined. For each oocyte, the four collection protocols outlined in Table 4.4 were performed sequentially. Spectra were collected through the central focal plane of the oocyte and each spectrum was integrated for 37 s over the spectral range 600 - 1790 cm^{-1} using a laser power of 35 mW.

Protocol	Step Size (μm)	Number of Spectra	Mapping Time (min)
1	9	45	28
2	7	69	42.5
3	6	101	62
4	2	1610	993

Table 4.4 – Experimental parameters used for the investigation of the reduced map methodology.

4.2.3 Data Preprocessing and Extraction

All spectra were subjected to the cosmic ray removal protocol in order to remove the sharp intense peaks which can appear spuriously in Raman spectra. The wavelength scale of each spectrum was corrected using the neon and polystyrene spectra, such that spectra obtained at different times could be compared with confidence. No further preprocessing was performed for the spectra collected in Experiment 1.

In Experiments 3 and 4, initially the oocyte and PBS spectra were smoothed using a 3-point and 11-point boxcar function, respectively, truncated to the region 455 - 1780 cm^{-1}, and the PBS contributions were subtracted from the oocyte spectra using the first derivative orthogonal vector method suggested by Maquelin *et al.*[230].

Before subsequent processing the spectra were returned to their integrated form. Following this, for Experiments 2 - 4, the data was resampled such that the spectral sampling interval was set at 1cm^{-1}, and the autofluorescence was subtracted by fitting a fourth order polynomial through the points at 456, 478, 632, 800, 1142, 1512 and 1756 cm^{-1}. Next the data was truncated to the region 800 - 1790 cm^{-1} for experiment 2 and 800 - 1760 cm^{-1} for Experiments 3 and 4. Finally, each spectrum was offset corrected, such that the minimum intensity was set to zero and then normalised to its mean spectral intensity across all wavenumbers in order to account for fluctuations in laser intensity.

The spectra of the pure fixatives were truncated to the region 600 - 1780 cm^{-1}, offset corrected and normalised to their maximum spectral intensity. All data preprocessing was performed using MATLAB and in-house written scripts.

4.2.4 Data Examination and Statistical Analysis

All data visualisation and statistical analysis was performed using MATLAB 7.0 and the Statistics toolbox.

Experiment 1: Photodamage Assessment

For each data set, every second spectrum was selected to be included in the SVD calculation, as described in Chapter 3. The resulting SVs were examined using a log-linear plot.

Experiment 2: Optimisation of Signal to Noise Ratio

The level of noise was calculated to be the standard deviation of the intensities in the region 1765 - 1780 cm^{-1}, whilst the signal was assessed to be the intensity of the peak at 1659 cm^{-1}. An average SNR was found for each oocyte by calculating the arithmetic mean of the ratios from the 31 spectra. The mean and standard deviation of the SNR for each experimental setup was then calculated.

Experiment 3: Comparison of Fixatives

For each oocyte, an average spectrum was generated by taking the arithmetic mean, at each wavenumber, of the 31 processed spectra. The mean of the 10 average spectra from each of the four fixative protocol groups was then calculated. A difference spectrum was calculated by subtracting the mean spectrum of the unfixed group from the mean spectrum obtained for each of the three fixation protocols investigated. Subsequently, PCA was performed on the entire data set, comprising of the 40 mean spectra from the four treatment groups.

Experiment 4: Reduced Map Oocyte Characterisation

Firstly, so as to remove spectra which did not represent the ooplasm a threshold limit of 1.75 at 1002 cm^{-1} was imposed. For each oocyte, the mean spectrum for each of the four collection protocols was calculated. Following this, for each oocyte, PCA and CVA were performed on the data set consisting of all processed spectra from each of the treatment groups. Finally, using the scores of the first 18 PCs, the means resulting from each of the three reduced mapping protocols (protocols 1-3) were compared to the mean of the full mapping protocol (protocol 4) using a one sample Hotelling's T^2 test, as described in Chapter 3.

4.3 Results

The Raman spectrum of the murine oocyte, as illustrated by Figure 4.1, is complex and displays a significant number of overlapping bands in the fingerprint region. Upon closer examination, it can be seen that there are contributions resulting mainly from protein and lipid molecular vibrations.

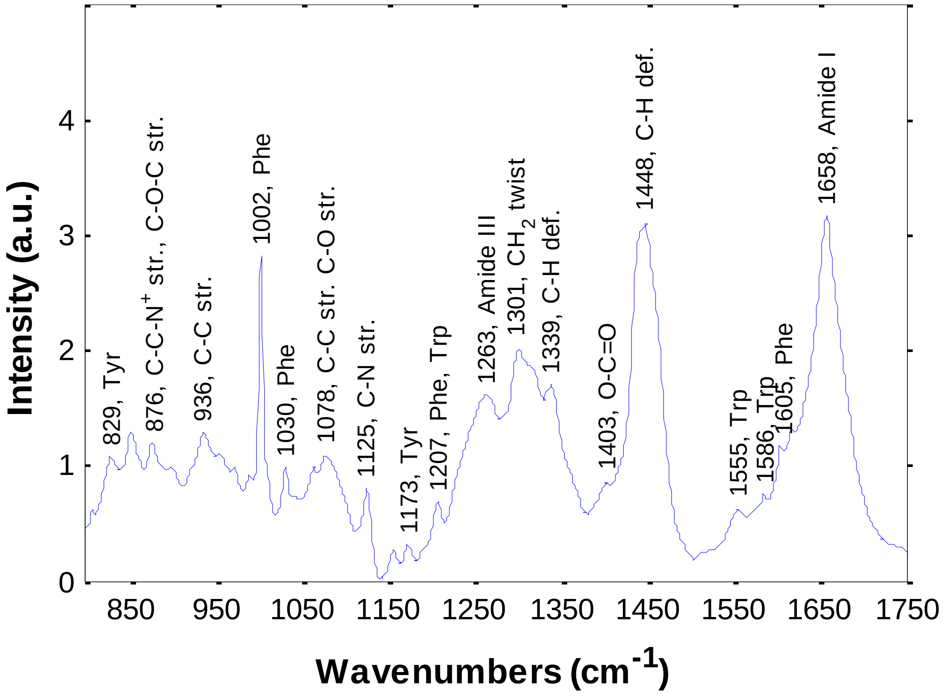

Figure 4.1 – Raman spectrum of a mature oocyte annotated to show the major peaks present in the wavenumber region 800-1760 cm^{-1}. The abbreviations str. and def. refer to vibrations arising from stretches and deformations, respectively.

Strong peaks are seen in the region of the amide I and amide III vibrations at 1658 cm^{-1} and 1255 cm^{-1}, respectively: Conversely, only a weak contribution seen in the region of the amide II band at 1550 cm^{-1}. The relatively small amide II band is not unexpected, as it is often only weakly Raman active, although it is often observed in the Raman spectra of proteins which have a β-sheet secondary structure. The phenomenon of Raman band broadening is often the result of overlapping bands. This is particularly true of the amide I region; the location of this band is particularly sensitive to the secondary structure of the proteins investigated. The precise location can occur anywhere in the region 1645 - 1675 cm^{-1}; the lower, intermediate and upper regions are indicative of a α-helical, random coil and β-sheet secondary structures, respectively. Furthermore, an overlap exists between the amide I band and the C=C stretch in unsaturated lipids and carbohydrates.

Non-overlapping contributions resulting from amino acids with aromatic side chains are seen at 829, 856, 1002, 1030, 1173, 1207, 1605 and 1621 cm^{-1}. The tyrosine doublet, which is observed at 829 and 856 cm^{-1}, is the result of in-plane ring breathing, while the sharp characteristic band at 1002 cm^{-1}, which is seen in the spectra of most biological samples, arises due to the symmetric ring breathing of phenylalanine. The peaks at 1030 and 1207 cm^{-1} occur due to the C-H in-plane stretch of phenylalanine and the aromatic-carbon stretch of both phenylalanine and tryptophan, respectively. Similarly, the peaks which form the shoulder of the amide I band at 1605 and 1621 cm^{-1} are attributed to phenylalanine and tyrosine. Furthermore, the non-overlapping contribution resulting from the CH_2 twist, which occurs in lipid molecules, is seen at 1301 cm^{-1}.

Additionally, due to the complexity of the biochemical composition of the ooplasm, it is expected that overlapping bands will exist in its spectrum. Such bands occur in the region of 1420 - 1480 cm^{-1} which corresponds to the C-H deformation in proteins, lipids and carbohydrates. Significant overlap also exists in the region below 1000 cm^{-1}, where contributions from proteins and carbohydrates, in particular, are observed. Furthermore, in some spectra, bands arising from the molecular vibrations of nucleic acids are observed. In particular, contributions from the nucleic acid ring breathing and CH_2 scissoring in the backbone are observed in the region 1350 - 1380 and 1410 - 1425 cm^{-1}, respectively. The Raman bands which are most commonly observed in the oocyte are outlined in Table 4.5.

Band (cm^{-1})	**Band Assignment**			
	Carbohydrates	**Lipids**	**Proteins**	**Nucleic Acids**
829			Tyr ring br.	
856			Tyr ring br.	
876	C-O-C ring br.		C-C-N sym str.	
936	C-O-C str.		C-C str. α-helix	
1002			Phe sym ring br.	
1030			Phe CH in-plane	
1078	C-O, C-C str.	C-C chain str.		
1090-1100				O-P-O str.
1125			C-N str.	
1157			C-C, C-N str.	
1173			Tyr C-H bend	
1200-1280			Amide III	
1207			Phe, Trp Ar-C	
1263		=C-H def.		
1301		CH_2 twist		
1339			C-H def.	
1350-1380				A, T ring br.
1403		O-C=O		
1410 -1425				CH_2 scissoring
1439		CH_2 def.		
1448			CH_2 def.	
1555			Trp	
1586			Trp	
1605			Phe	
1621			Tyr	
1650-1660	C=C, C=O	C=C, C=O		
1640-1680			Amide I	
1720-1760		C=O		

Table 4.5 – Tentative assignments for the bands observed in the Raman spectrum of the oocyte. Assignments were made on the basis of previously reported values for other biological samples[171, 179, 233].

There are a number of experimental parameters which can affect the efficacy of Raman spectroscopy in oocyte analysis. Consequently, consideration must be given to the design of the spectrum collection protocol, so as to ensure that the spectra obtained are of sufficient quality to enable subsequent statistical analysis. The results presented hereinafter describe the effect which four system parameters, including acquisition time, laser power, fixation and sub-sampling, have on the Raman spectrum of the oocyte. The findings reported here were used to design subsequent experiments, which are reported in Chapters 5 - 7.

4.3.1 Laser Threshold Testing

The analysis of the morphology of oocytes, by means of light microscopy, before and after 19 minutes of continuous laser irradiation revealed no obvious changes at a power of 7, 35 or 70 mW. However, the absence of detectable morphological changes did not preclude laser induced photodamage. As such, consecutive Raman spectra collected from the same location in fixed oocytes were analysed to identify the presence of spectral variation, and thus photodamage. SVD is a multivariate method which is capable of quantifying spectral variation and reporting it as a series of singular values.

Figure 4.2 presents the results obtained from the SVD analysis of consecutive spectra obtained from fixed oocytes using a laser power of 7, 35, and 70 mW, respectively. The appearance of Figure 4.2a and 4.2b, which represent the results using 7 and 35 mW respectively, are very similar. In both figures, the first SV is much larger than the other fifteen SVs. Furthermore, there exists very little difference between the latter fifteen SVs. These data indicate that, in both cases, the sixteen spectra analysed can be described accurately by one singular value. When considering the derivation of singular values, this indicates that no appreciable variation exists between the consecutive spectra. Upon closer examination of the data, it is observed that the latter fifteen SVs describe the noise which exists in the Raman spectra.

Conversely, the results presented for a laser power of 70 mW in Figure 4.2c show that whilst the first SV is much larger that the remaining fifteen, the second SV is significantly different from SVs 3 - 16. These data intimate that there exists variation between the sixteen spectra which cannot be attributed to noise. This was confirmed by the examination of the reconstructed spectra which showed significant variation between consecutive spectra at a number of wavenumbers. These findings were consistent with the results obtained from repeated experiments using different oocytes.

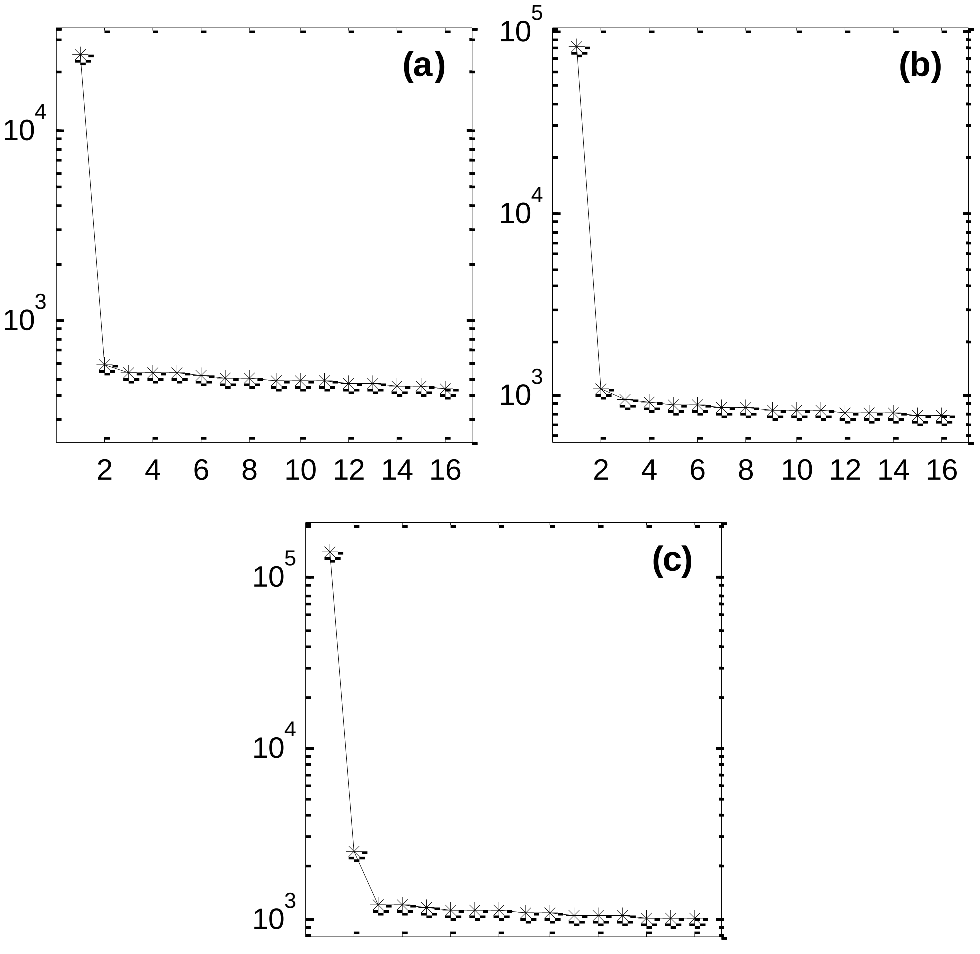

Figure 4.2 – Semi-logarithmic plots of singular values derived from consecutive spectra collected from a single central location within paraformaldehyde fixed oocytes. The plots display the results of the SVD analysis for three laser powers: (a) 7 mW; (b) 35 mW; and (c) 70 mW.

4.3.2 Optimisation of Signal to Noise

Firstly, the effect which the incident laser power has on SNR was examined. Due to the system design, it was not possible to investigate a continuous range of laser powers. Consequently, the laser powers interrogated correspond to 100, 50 and 10 % of the source power. The next available increment was 5 %, which resulted in a barely discernible signal and as such was not included in this study. Figure 4.3 depicts the average SNR, which represents the arithmetic mean of 5 oocytes, for each laser power, and their associated standard deviations. These results indicate that SNR increases with increasing laser power, and while it appears that this increase follows a linear relationship with respect to laser power, no accurate inference about the relationship can be gained due to the lack of available data. However, it is worth noting that the mean SNR for each of the laser powers tested was greater that the accepted limit of detection which is generally regarded as a SNR = 3[234].

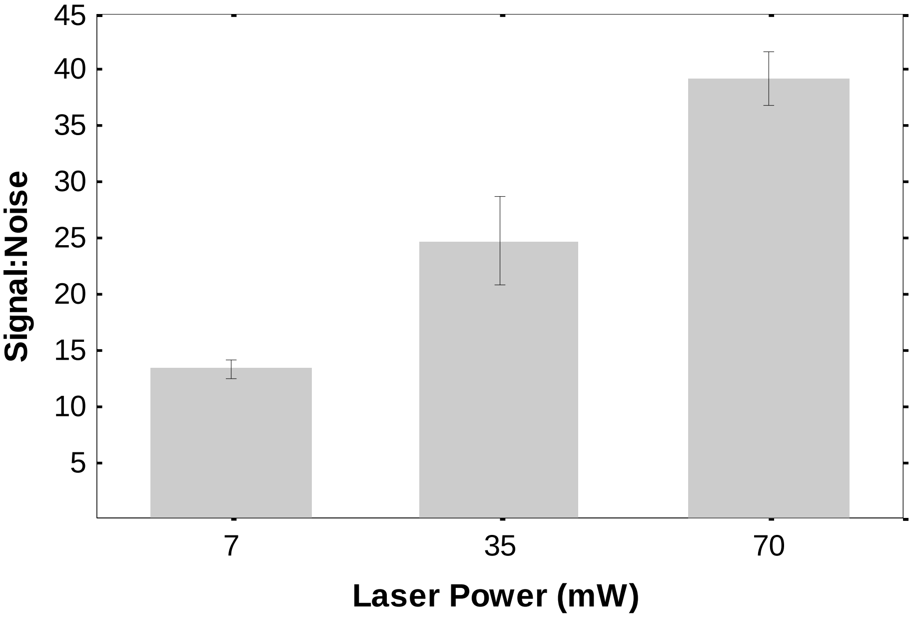

Figure 4.3 – Mean signal to noise ratios ± 1 standard deviation calculated from the 155 spectra (5 oocytes) for laser powers of 7, 35 and 70 mW and acquisition time of 37 seconds.

Subsequently, the effect which spectral acquisition time has on SNR was investigated. As a result of the software and system design the minimum acquisition time available for the spectral range 450 - 1790 cm^{-1} was 37 s, which was equivalent to 10 s per CCD fill. Consequently, integration times of 37, 74, 111 and 222 s, which corresponded to single pass acquisition times of 10, 20 30 and 60 s, were chosen for this study. Figure 4.4 depicts the average SNR, which represents the arithmetic mean of 5 oocytes, for each acquisition time, and their associated standard deviations. These results indicate that SNR increases with acquisition time according to 0.54 power relationship, which corresponds closely with the square root relationship described in literature for shot noise limited experiments[235]. As such, a 100 % increase in the acquisition time from 37 to 74 s only results in an increase in SNR of approximately 44 %.

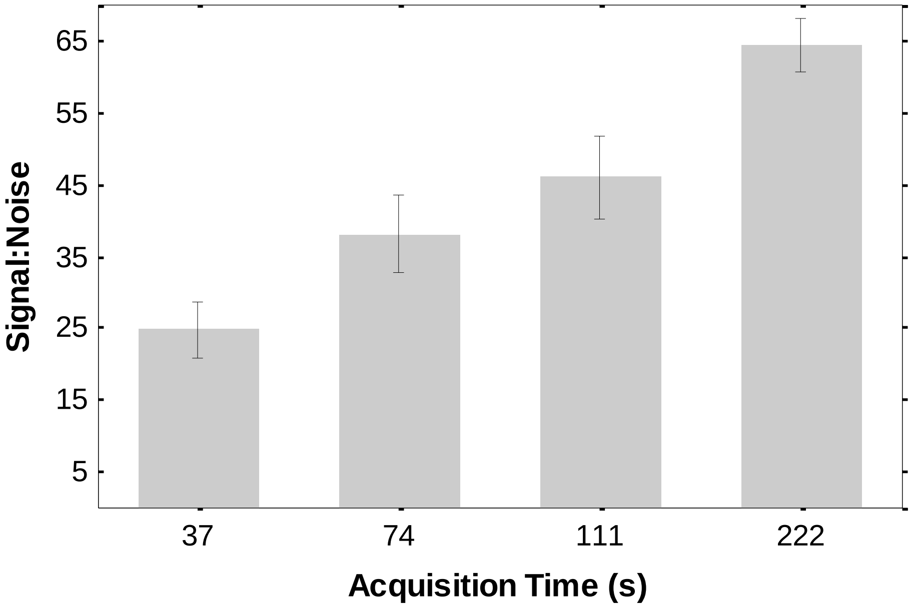

Figure 4.4 – Mean signal to noise ratios ± 1 standard deviation calculated from the 155 spectra (5 oocytes) for acquisition times of 37, 74 and 111 seconds and a laser power = 35 mW.

4.3.3 Identification of a Suitable Fixative

The work contained within this thesis is concerned with the analysis of fixed murine oocytes. However, the premise of the work is to develop Raman spectroscopy as a technique capable of the analysis of unfixed oocytes for developmental competence quantification. Consequently, the selection of the fixative used to preserve the oocyte in this work had to be carefully considered, such that it did not substantially affect the Raman spectrum and thus the transfer of the method from fixed to unfixed samples. To this end, three common fixative protocols were examined; ethanol, glutaraldehyde and paraformaldehyde fixation.

Initially, so as to identify any Raman bands arising from the presence of localised deposits of fixative within the oocytes, the Raman spectra of the pure substances were investigated. As such, Figure 4.5 depicts the Raman spectrum of each of the pure fixatives with the most significant band locations annotated. In the Raman spectrum of ethanol, the bands located at 884 and 1052 cm^{-1} correspond to the O-C-C symmetric and anti-symmetric stretch. Whilst the 1097, 1455, 1276 and 1483 cm^{-1} Raman bands have been assigned to the CH_3 in-plane rocking, CH_3 deformation, CH_2 twist and CH_2 scissor, respectively[236].

In aqueous solution, glutaraldehyde exists in various forms including its monomeric form, as the cyclic hemiacetal of its hydrate and a polymer of the latter[237], resulting in a more complicated Raman spectrum. Contributions resulting from C-H deformation are seen in the region of 803 - 965 cm^{-1}, whilst bands arising due to in-plane C-H rocking are observed between 1318 and 1444 cm^{-1}. The C=O band characteristic of aldehydes is located at 1715 cm^{-1}. Finally, contributions arising due to the C-O stretch in the cyclic hemiacetal hydrate are located in the region 1028 - 1195 cm^{-1}[117].

Finally, the examination of the paraformaldehyde spectrum shows strong contributions arising from the symmetric and anti-symmetric O-C-O stretch at 919 and 1092 cm^{-1}, respectively. Furthermore, peaks which have been tentatively assigned to CH_2 twisting, wagging and in-plane bending are observed at 1294, 1337 and 1491 cm^{-1}[238, 239].

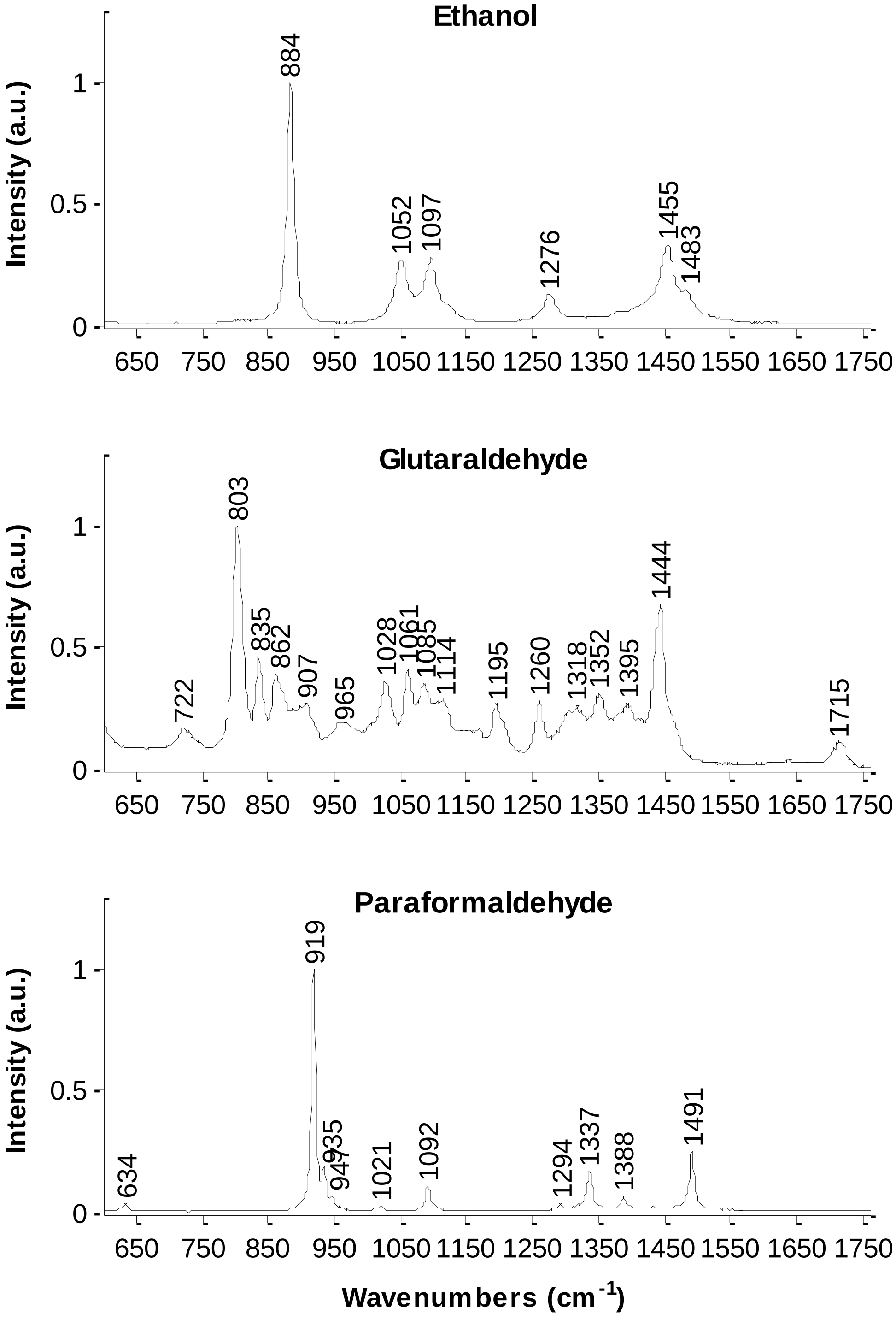

Figure 4.5 – Raman spectra of the three fixatives investigated, with major peak locations annotated.

Subsequently, the effect which each of the fixative protocols has on the Raman spectrum of the oocyte was examined. A total of 10 oocytes in each of the three groups, and a further 10 unfixed oocytes were analysed. So as to minimise the likelihood of induced photodamage in the unfixed oocyte, only 31 spectra, collected at a constant interval of 10 μm, were acquired from each oocyte. An average spectrum was generated for each of the 40 oocytes examined and subsequently a mean spectrum was calculated for each group.

Firstly, each of the average spectra derived from the three treatment protocols were compared with the mean spectrum of the unfixed group, the results of which are presented in Figure 4.6. In each of the three subplots, the average fixed and unfixed oocyte spectra are represented by the red and blue trace, respectively. The black trace shows the difference spectrum (= unfixed - fixed) for each fixative protocol. Initial observations indicate that significant spectral disruption results from ethanol and glutaraldehyde fixation, whilst less spectral variation is evident in paraformaldehyde fixed oocytes.

Closer examination of the difference spectrum derived from the ethanol fixed oocytes, reveals positive Raman bands in the region of known lipid vibrations. Specifically, strong positive intensities are seen in the region of the lipid C=C stretch at 1654 cm^{-1}, CH deformation at 1437 cm^{-1} and the CH_2 twist at1300 cm^{-1}. Other positive bands associated with lipid vibrations are observed at 713, 980, 1090, 1273 and 1739 cm^{-1}. These results indicate that the ethanol fixed oocytes have lower lipid content than their unfixed counterparts. Conversely, negative bands which are associated with protein molecular vibrations are observed in the difference spectrum. Significant negative contributions arising from the amide I, amide III and phenylalanine symmetric ring breathing are seen at 1674, 1238, and 1003 cm^{-1}, whilst other negative bands resulting from protein vibrations are observed at 620, 755, 828, 1031, 1605 cm^{-1}. These data would suggest that the ethanol fixed oocytes have greater protein content than unfixed oocytes. However, it is postulated that this observation is a result of the preprocessing routine which normalises the spectrum to its integrated area; the lower lipid contributions observed in the ethanol spectrum result in a lower integrated area which, in turn, could lead to more intense bands in non-lipid regions.

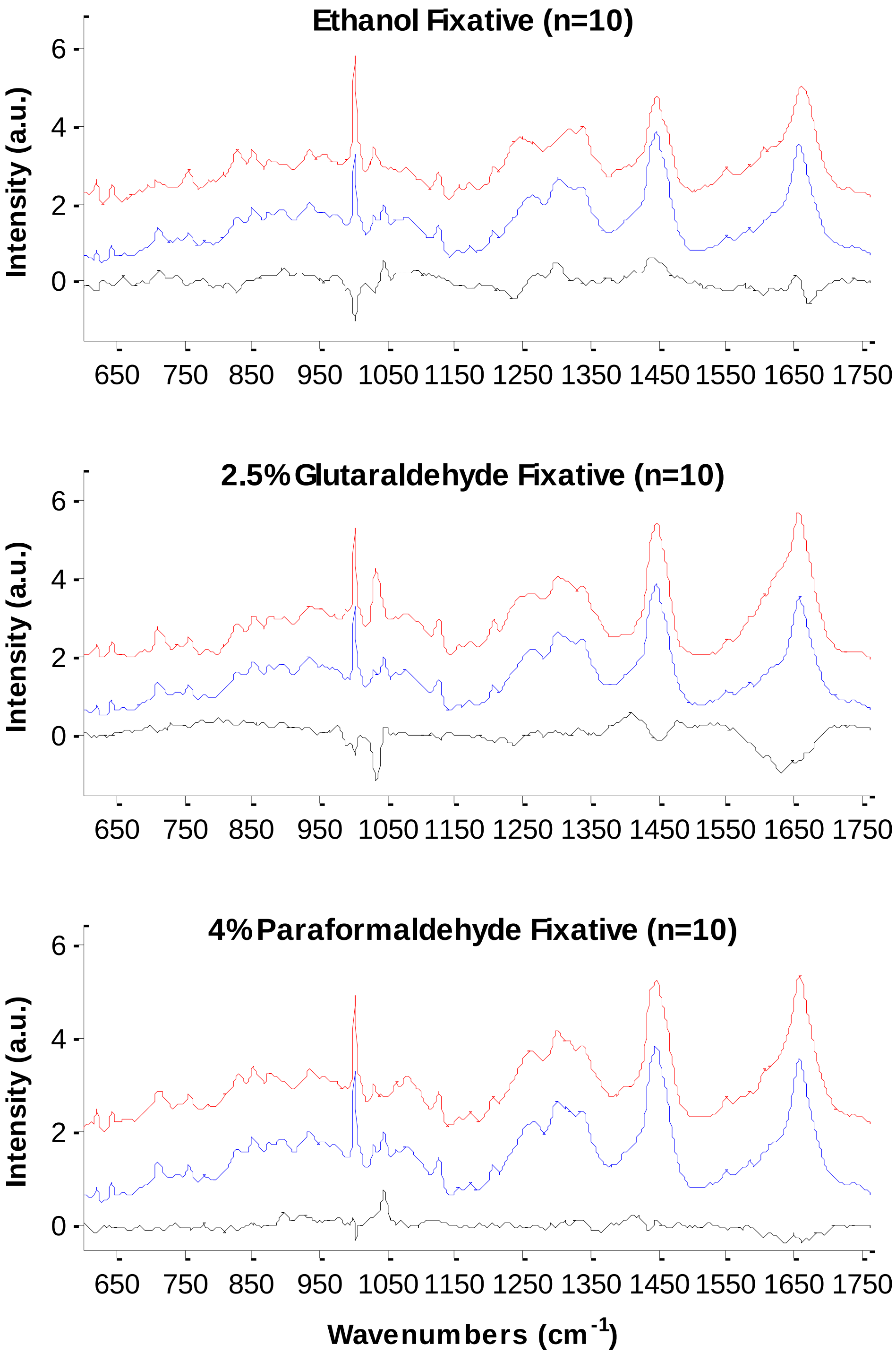

Figure 4.6 – Investigation of the effect of fixation on the Raman spectrum of the oocyte. In each plot, the fixed, unfixed and difference spectra are depicted by the red, blue and black plots, respectively.

Analysis of the difference spectrum, derived for the glutaraldehyde fixed oocytes, showed a strong negative band in the region of 1034 cm^{-1}. This observation has previously been reported in glutaraldehyde fixed samples and has been attributed to the formation of pyridinium-like compounds during the cross-linking of proteins[240]. Further strong negative bands are seen in the region of the phenylalanine symmetric ring breathing mode, amide III and amide I bands, where visual inspection reveals broadening of the envelope in the latter. Conversely, positive intensities are seen universally below 980 cm^{-1} and above 1700 cm^{-1}. Further positive contributions are observed in the region of 1370 - 1440 and 1460 - 1570 cm^{-1}, which are regions associated with nucleic acid base ring breathing modes.

Finally, from the difference spectrum calculated for the paraformaldehyde fixed oocytes it is apparent that the magnitude of the variance between the unfixed and fixed spectra is smaller than that of the other fixative protocols. Yet, negative contributions are observed in the region of the phenylalanine symmetric ring breathing at 1003 cm^{-1} and the amide I envelope at 1600 - 1680 cm^{-1}. Positive contributions are seen in the region of 890 - 980, 1100 - 1140 and 1400 - 1430 cm^{-1}.

Additionally, positive contributions, of varying magnitudes, are observed in all of the difference spectra in the regions of Raman shifts arising due to the molecular vibrations of nucleic acids, but in particular in the region of the purine ring breathing mode at 1480 cm^{-1}. Positive contributions are also seen below 1000 cm^{-1} in each of the difference spectra, although the true biochemical basis of these variations is difficult to discern due to the presence of overlapping bands in this region. Most significantly, in each difference spectra, a strong positive contribution is seen in the region of 1045 cm^{-1}, which has previously been attributed to the C-O and C-C stretches in furanose, a constituent of the RNA backbone[241].

Multivariate Analysis

PCA was performed to enable an unbiased statistical analysis of adjacent wavenumbers to be completed. The PCA was performed on a data matrix which contained the 40 average Raman spectra which had been collected from the three treatment, and one control, groups (n_{ETH}=10, n_{GLUT}=10, n_{PARA}=10, $n_{UNFIXED}$=10). Examination of the associated scree plot allows the variance in the original data space, which is described by each of the newly generated PCs, to be determined. It was found that approximately 80 % of the variance that existed in the 961 original variables is described by the first 2 PCs.

During the process of PCA, each spectrum is assigned a score for each generated PC. These scores describe the contribution which each PC makes to the original spectrum. As such, scatter plots of these scores can be used to visualise any variation and clustering which may exist in the sample data set. Figure 4.7 depicts the scores of the first and second PC for each oocyte sampled. Each individual oocyte from the ethanol, glutaraldehyde and paraformaldehyde fixed and unfixed groups is denoted by blue, red, magenta and green markers, respectively, with the group mean scores denoted as E, G P and L.

The scatter plot shows a distinction between the glutaraldehyde fixed oocytes and the other groups along the first PC. Additionally, a marked separation exists between the ethanol fixed oocytes and the other groups along the second PC. Furthermore, separation between the unfixed oocytes and the remaining fixed oocytes is also observed along the second PC, although to a lesser extent. It is apparent from Figure 4.7 that the paraformaldehyde fixative protocol provides the closest model to the unfixed oocyte, as evidenced by the comparison of the group means. Examination of the other PC scores revealed that all fixed oocytes are separated from the unfixed oocytes along the third PC, although the contribution of this PC to the overall variance was significantly lower.

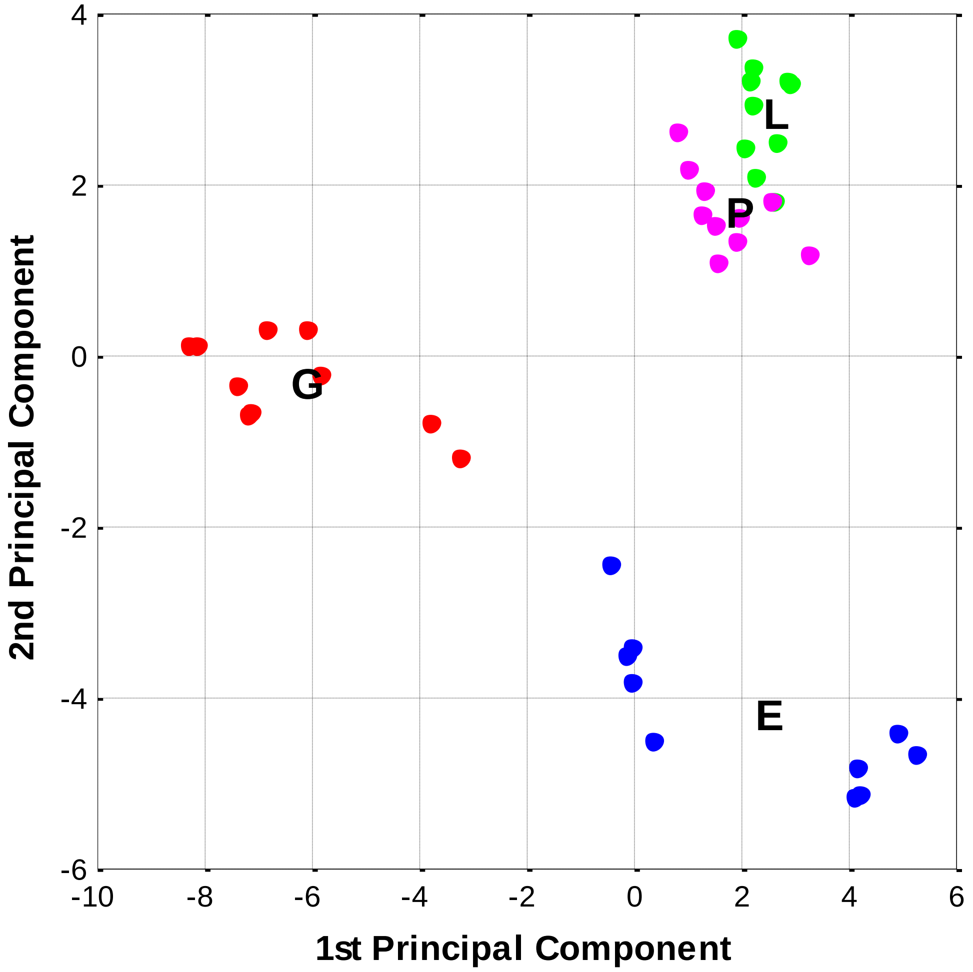

Figure 4.7 – Biplot showing the scores of each datum against the first and second component axes generated during the PCA. Ethanol, glutaraldehyde and paraformaldehyde fixed oocytes are depicted by the blue, red and magenta markers, respectively, whilst the green markers depict the unfixed oocytes. The mean score for the ethanol, glutaraldehyde and paraformaldehyde fixed groups and the unfixed group are denoted by E, G, P and L, respectively.

The tight clustering of the paraformaldehyde fixed and unfixed oocytes suggest that these treatments minimise the within-group variance. Whilst both the glutaraldehyde and ethanol fixed oocytes display greater within-group variance. However, the effect of outliers is more prominent in small data sets, and therefore the sample size would have to be extended in order to confirm these findings. Significantly, the results of the PCA further confirm that the paraformaldehyde fixative protocol provides the closest model to the unfixed oocyte.

So as to understand the biochemical variation that separates the three treatment groups, the PC loadings must be examined. As such, the loadings for the first three PCs against the original data space axis are presented in Figure 4.8. The first PC, which represents approximately 54 % of the overall variation, is remarkably similar to the difference spectrum generated for the glutaraldehyde fixed oocytes. Likewise, the second PC shows consistency with the ethanol derived difference spectrum. Finally, the third PC approximates the inverse of the paraformaldehyde derived difference spectrum. These data indicate that the difference spectra describe effectively the separation of the fixed and unfixed samples.

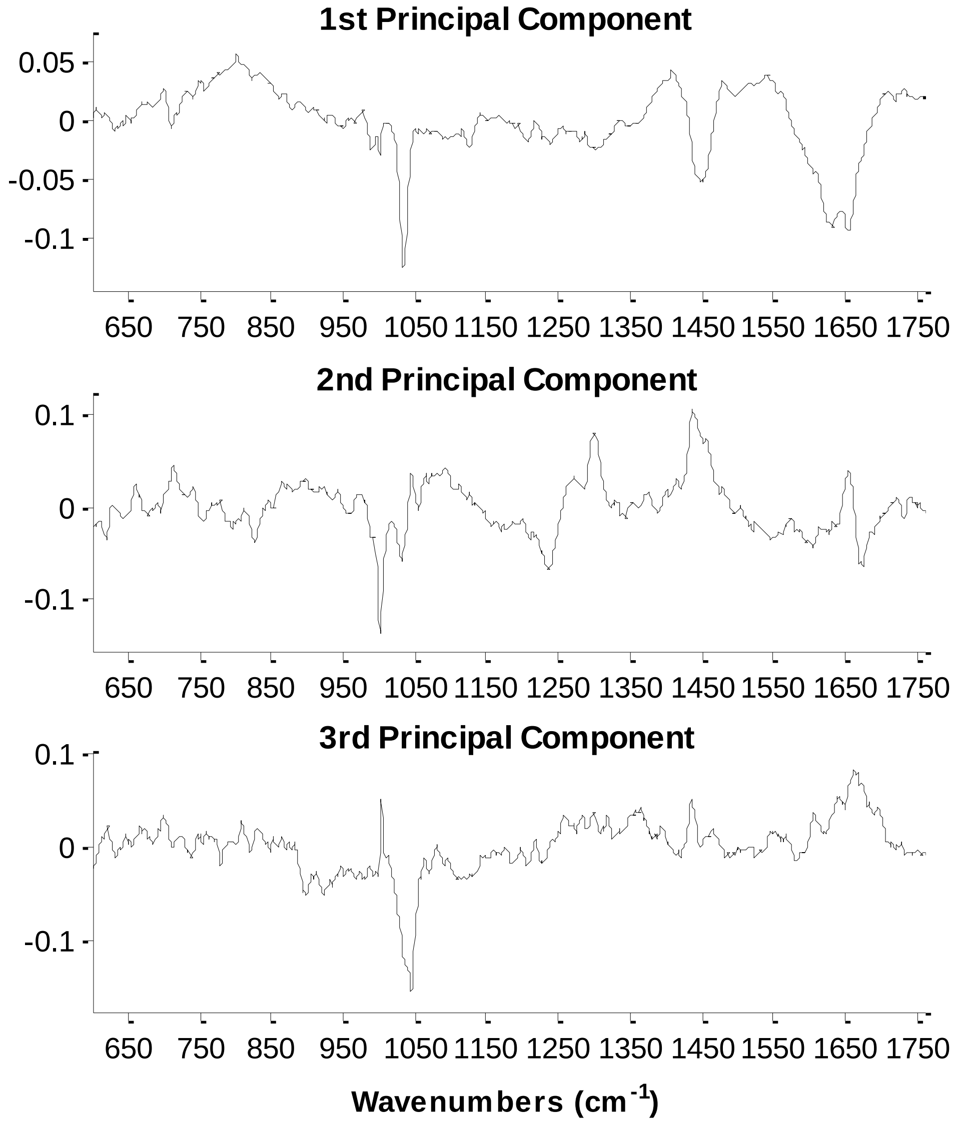

Figure 4.8 – Loadings of the first three components generated during the PCA.

4.3.4 Characterisation of Oocytes Using Sub-Sampling

Unlike the mammalian somatic cell, which has been routinely examined using Raman spectroscopy, the oocyte is of a size which presents challenges to rapid analysis. Raman mapping experiments enable spectroscopic analysis at regular intervals, and as such, provide a powerful method capable of producing detailed images revealing the biochemistry of heterogeneous samples. However, for a map with resolution of the order of several microns, thousands of spectra are required to characterise a murine oocyte, compared with only 50 for a somatic cell. As such, even with the most advanced instrumentation, the acquisition of a high resolution Raman map of a murine oocyte would take of the order of several hours, during which time significant biochemical modifications are likely to occur. Consequently, the application of high resolution mapping experiments is constrained to the study of fixed oocytes. Therefore, in order to design a method which enabled the rapid analysis of murine oocytes, a study was conducted to investigate the number of spectra which could accurately describe the ooplasm.

A total of 4 oocytes were examined for this work: For each, Raman maps consisting of 45, 69, 101 and 1610 individual spectra collected at regular intervals of 9, 7, 6 and 2 μm, respectively, were acquired. An average spectrum was generated for each of the mapping experiments for each of the four oocytes. Figure 4.9 presents the results for the first oocyte.

Initial examination of the average spectra calculated from each of the mapping protocols for the first oocyte indicates little variation. The most significant difference between these spectra is the SNR. As would be expected, the SNR is smallest for the 45-point map and gradually improves as the number of spectra averaged increases. Furthermore, the standard deviation observed for each protocol was relatively consistent across all wavenumbers and between protocols. These findings were consistent with those observed for the other oocytes which were analysed during this study.

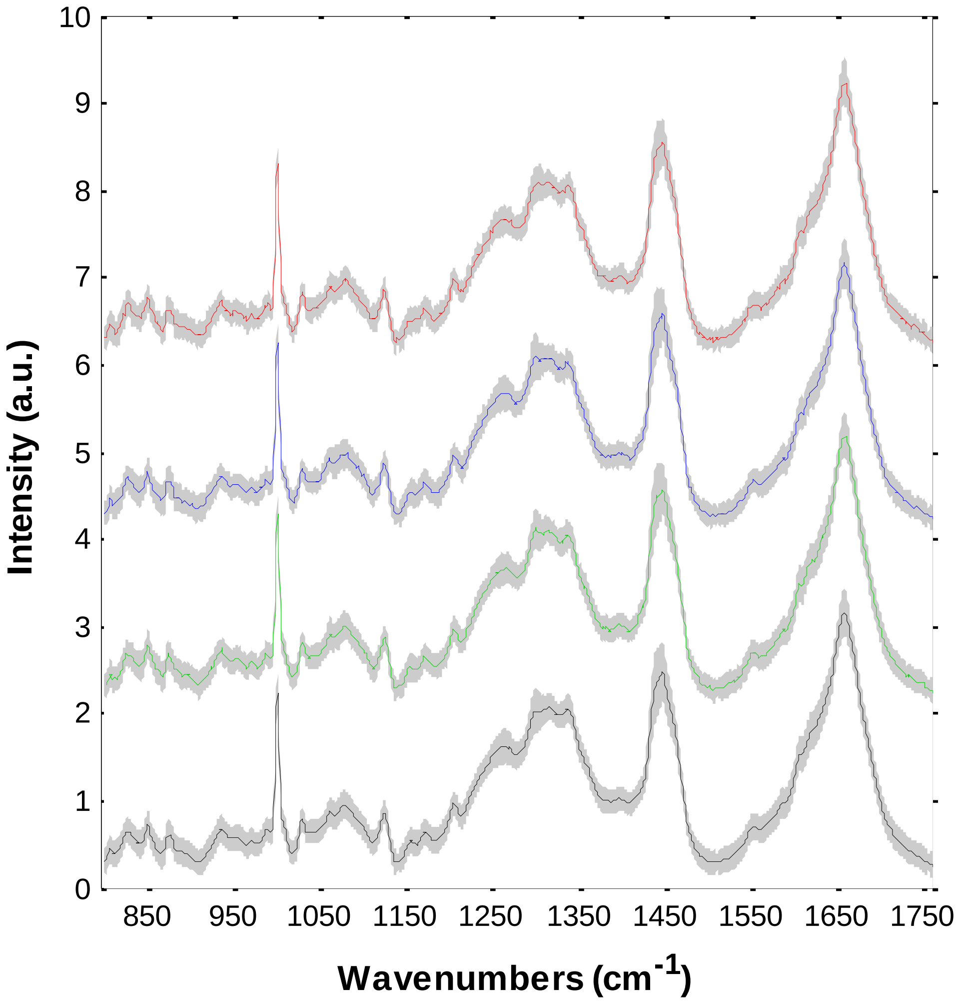

Figure 4.9 – Comparison of the average spectra obtained from one oocyte using different mapping protocols. The average spectra calculated from 1610, 101, 69 and 45 points which were collected at constant intervals of 2, 6, 7 and 9 μm are depicted by the black, green, blue and red spectra, respectively. The grey shaded area represents the region corresponding to ± one standard deviation for each spectrum. The spectra have been offset for clarity.

Given the similarity of the average spectra obtained for each protocol, it was necessary to perform more detailed quantitative analysis using multivariate methodologies. Therefore, for each oocyte, PCA was performed simultaneously on the individual spectra acquired from each of the reduced maps and the average spectrum calculated for the full-map. Analysis of the resulting PC loadings indicated that the first 18 PCs, which accounted for approximately 62 % of the total variance, described the majority of the non-noise spectral variance: No PC beyond this point accounted for more than 50 % of the variance described by a single original variable, or wavenumber. As such, so as to compare the data, and visualise it in fewer dimensions CVA was performed using the scores of the first eighteen PCs. The results of the CVA revealed that the hypothesis which stated that all of the groups means lie in zero-dimensional space cannot be rejected; accordingly, the multivariate analysis of variance indicated that the null hypothesis which states that the means are equal cannot be rejected. This is confirmed in Figure 4.10 which shows the scores on the first and second CV for each of the spectra derived from each of the reduced mapping experiments and their corresponding group means. However, this biplot also demonstrates that the mean of the map containing 101 points is closest to the mean derived from the full map.

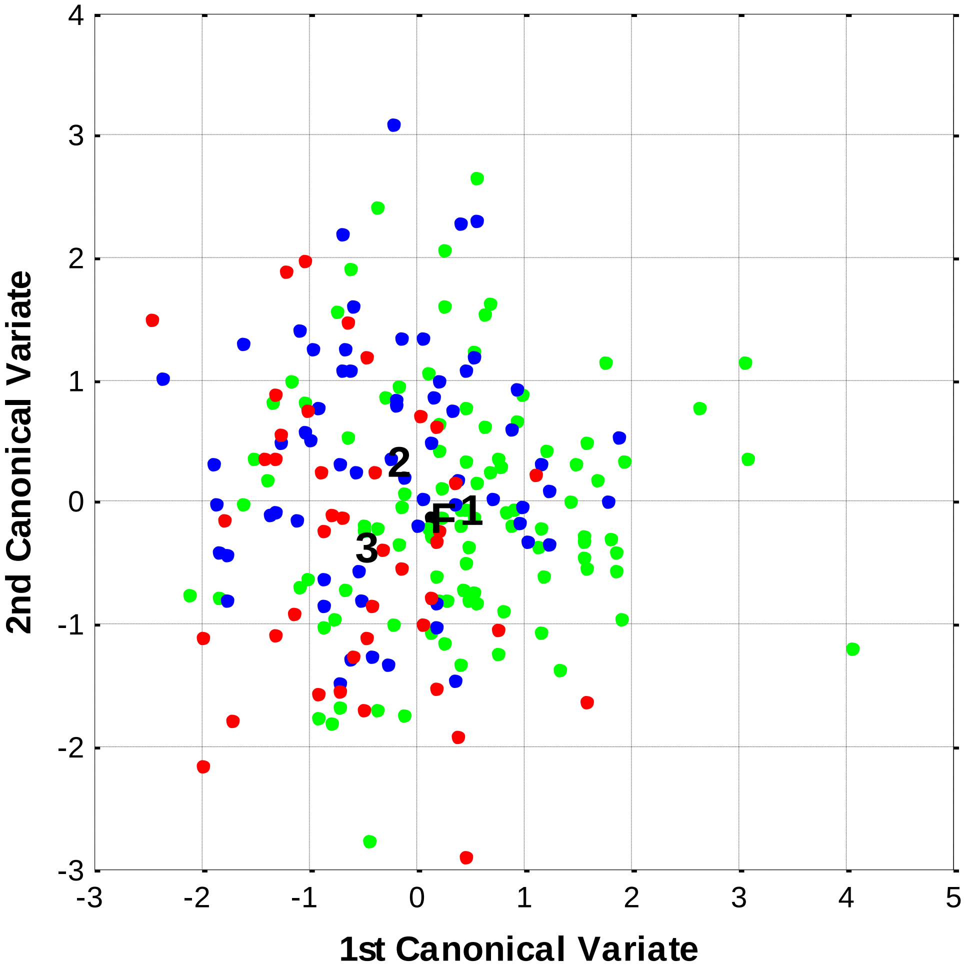

Figure 4.10 – Biplot showing the scores of the first and second CVs obtained from the first 18 PCs. Each marker depicts an individual spectrum obtained from a reduced mapping experiment. Green, blue and red markers depict spectra obtained from the 101, 69 and 45 point reduced maps. The mean scores for the full map, 101, 69 and 45-point reduced maps are depicted by F, 1, 2 and 3, respectively.

Number of Spectra	Step Size (μm)	Map Acquisition Time (min)	Average Spectrum SNR	Hotelling's T^2 Test	
				$F_{critical}$	F_{test}
45	9	28	232 ± 52	3.96	2.59
69	7	42.5	300 ± 87	3.12	1.89
101	6	62	344 ± 89	2.76	2.04
1610	2	993	727 ± 116	-	-

Table 4.6 – Results obtained from each mapping protocol for the oocyte presented in Figure 4.10. In each case, the Hotelling's T^2 test compared the mean spectrum obtained from the protocol with the mean spectrum obtained from the fourth protocol; the F distribution was evaluated at $\alpha=0.001$.

Further analysis was conducted in the form of the Hotelling's T^2 test, which can be regarded as the multivariate analogue of the Student's t-test, and is closely related to the square of the Mahalanobis distance. In this instance, Hotelling's T^2 is a statistical measure of the pooled multivariate distance of the spectra derived for each reduced map, from the mean spectrum calculated for the full mapping experiment. In the case of the null-hypothesis – such that the means are equal – T^2 can be described by an F-distribution. Table 4.6 presents the results of the Hotelling's T^2 test, from which it can be seen that the null hypothesis cannot be rejected for any of the reduced mapping experiments, which further confirms the results of the CVA. The mean and standard deviation of the SNR for the average spectrum derived in each case is also presented in Table 4.6. As predicted by SNR theory, an increase in SNR is observed with an increase in the number of spectra acquired.

4.4 Discussion

Laser Threshold Testing

An important consideration in the design of any analytical experiment is that of the maintenance of sample integrity during the period of analysis. This is of particular significance in the laser-based spectroscopic analysis of biological samples. It has been discussed previously that the energy of an incident photon is proportional to its wavelength;

higher photon energies are observed with decreasing wavelength. Consequently, near infrared (NIR) lasers are often selected in preference to visible lasers for the Raman investigation of biological samples[242]. In accordance with this theory, a 785 nm laser was selected for this work to minimise the effect of photodamage. A further advantage of working in the NIR region is the reduction in the observed sample autofluorescence which often overwhelms the Raman signal of biological materials.

There exists a precedent for the use of lasers in the field of ARTs; the use of laser-assisted hatching, ICSI, zona-drilling and blastomere ablation have all been reported. Although a number of lasers have been suggested, it is generally agreed that those which operate in the UV region, or close to the absorption of key molecules, should be avoided. The indium-gallium-arsenic-phosphorus (InGaAsP) diode laser, which operates at 1.48 μm, has been routinely reported for use in various ART-associated procedures[243]. In many cases, no deleterious effects have been reported, although it is recognised that the absence of morphological changes does not preclude damage.

Hollis *et al.* attempted to model localised heating induced during focused laser zona drilling using the InGaAsP laser[244]. However, the reported results suggested excessively high temperature gradients which are not supported by experiment. The authors accept that the model is limited as it considers neither laser scattering nor axial heating. In another study, which included axial heating, peak temperatures exceeding 100 °C were predicted for laser exposures of 15 ms and source power of 40 mW[245]. This study approximates the thermal constants of the oocyte to be equal to water. On this basis, as the absorption coefficient of water at 785 nm is of the order of three magnitudes smaller than at 1480 nm it is predicted that the heating effect of the laser used in this work will be much less.

The method of comparing successive spectra using SVD in order to detect spectral variation arising from laser induced photodamage has been applied successfully elsewhere[152]. The results presented here support the theory that morphological assessment alone is not sufficient to detect photodamage, as no morphological variation was observed in any of the oocytes despite the presence of spectral change. As no photodamage was detected after 19 minutes in either the 7 or 35 mW irradiated oocytes both of these laser powers appear to be below the damage threshold. However, due to concerns regarding SNR and so as to minimise acquisition times, it was decided that subsequent experiments would be performed using a laser power of 35 mW.

The design of the work included in this thesis is such that it may be transferred to unfixed samples. However, for that to happen, further assessment of induced photodamage in live oocytes would be required. In such cases, the method applied here would not be appropriate, as it is not unreasonable to assume that in a dynamic cell spectral changes would occur during the testing period. Consequently, a suitable alternative would be to monitor development to blastocyst following IVF in irradiated oocytes. This however, is likely to require large sample sizes. As such, preliminary work investigating the expression of induced heat shock proteins (HSPs) following laser irradiation may provide an insight into localised heating and heat shock.

Optimisation of SNR

Classically, SNR is defined as the mean of a given intensity divided by its standard deviation. This definition, however, is not suitable for the investigation of heterogeneous biological samples, as it would require a high number of repeated measurements at exactly the same location within the sample. In situations where the classical method is not appropriate, as in this work, an alternative method of defining the noise as the standard deviation of a region containing no signal has proven effective. Furthermore, in order to overcome the issues resulting from the heterogeneous nature of the ooplasm, spectra were collected from 31 locations within each oocyte for the SNR analysis. Calculating the average of the SNR determined at each of these locations enabled a more accurate SNR value to be determined for each set of investigated experimental parameters.

There are many types of noise which can affect the quality of the Raman spectrum, such as dark current and read noise, both of which are instrument specific. In this work, however, the spectra are shot noise limited. This type of noise arises as a result of the random nature of the photons arriving at the CCD detector. However, as with many biological samples, a large sloping fluorescence background is observed in the unprocessed spectrum of the oocyte and this background too has an associated shot noise. As a consequence of the random nature of the background shot noise, it cannot be subtracted during the removal of the fluorescence background. Consequently, in this instance the calculated noise is a summation of the noise arising from both the background and sample.

Over the spectral region of interest, the ratio of the intensities arising from the oocyte signal and the fluorescence background ranges from approximately 0.25 to 0.65 in the unprocessed spectra. Consequently, it is likely that at the lower end of the spectral range the SNR is limited by the background shot noise. From theory, in such cases it is known that increasing acquisition time results in the deterioration of SNR[235]. Although this is not observed in the SNR results presented in Figure 4.4, it should be noted that the SNR is calculated from the higher end of the spectral region where the contribution of the fluorescence background to the overall intensity is smaller.

In selecting the optimum acquisition time, not only was the resulting SNRs considered, but also the total analysis time. Although low SNR spectra can prove problematic for subsequent data analysis, the recorded SNRs for all acquisition times investigated were sufficiently high that they would not prevent multivariate or univariate interpretation. As a result, minimising the total measurement time was pivotal to the selection of the spectral acquisition time. Furthermore, consideration was given to the heterogeneous nature of the sample: It was recognised that it would be more informative to acquire two 37 s spectra from different locations than a single 74 s spectrum. Therefore, an acquisition time of 37 s, corresponding to the minimum single fill time of 10 s, was selected for all subsequent analysis.

Identification of a Suitable Fixative

The choice of fixative and its effect on the sample must be considered when designing any experiment; not only must it preserve the biochemistry of interest, but it must also not adversely affect the method of analysis. Consequently, this subject has attracted great attention in the field of Raman bioanalysis. Published studies appear to indicate that there is no universally applicable fixative which minimises spectral effects[246]. Instead, the type and magnitude of induced spectral changes appear to be sample specific for any given fixative protocol.

In this work, the three fixative protocols investigated were selected due to their common application in the study of oocytes. They belong to two categories of fixative; ethanol belongs to the group of precipitating fixatives, whilst glutaraldehyde and paraformaldehyde belong to the group of cross-linking agents.

Unlike the cross-linking fixatives, it was found that oocyte morphology was detrimentally affected by ethanol fixation. A significant reduction in the volume of the oocyte was observed, although this was remedied to a large extent upon rehydration. It was found that the zona pellucida either dissolved or was damaged to such an extent that it was shed. Furthermore, a marked darkening of the ooplasm was observed, which possibly results from the accumulation of partially dissolved lipids. The latter was a concern regarding photodamage resulting from absorption mechanisms. The reduction of intensities in the Raman spectrum associated with lipid vibrations is in accordance with the mechanism of the dissolution of many of the oocyte's lipid deposits by ethanol. However, although ethanol is often chosen as a fixative for preservation of nucleic acids, some changes are observed in the spectrum in regions associated with the vibrations of RNA and DNA. Changes in the hydration of these molecules may have affected their vibration intensities or else some material may have been lost through the permeabilised membrane.

The fixation mechanism by which glutaraldehyde preserves samples involves the formation of cross-links, known as Schiff bases, between amino groups. Most often the cross-links are formed between lysine residues present on the exterior of proteins, although other amino acids are known to react with glutaraldehyde. Although good morphological preservation was observed in glutaraldehyde specimens, a significant increase in the intensity of the region 1600 - 1680 cm^{-1} is observed in the spectrum of these oocytes. It is thought that this increase is the result of the strong Raman signal attributed to the C=N stretch of the Schiff base[117]. It is postulated that the use of a low concentration glutaraldehyde fixative is responsible for the absence of the widely reported autofluorescence which results from the precipitation of the free aldehyde. However, it remains that the spectrum of the glutaraldehyde fixed oocytes are dominated by the presence of the pyridinium vibration at 1034 cm^{-1}. Furthermore, it has been postulated that although glutaraldehyde does not cross-link nucleic acids, they are maintained in the tight network of the cross-linked proteins. This would explain the observed reduction in the intensities arising from nucleic acid vibrations in the spectra of glutaraldehyde fixed specimens.

As with glutaraldehyde, good preservation of oocyte morphology was observed in the paraformaldehyde fixed samples. Although paraformaldehyde is a cross-linking aldehyde fixative like glutaraldehyde, the mechanism by which the sample is preserved is different. Paraformaldehyde fixes samples through the formation of covalent bonds known as methylene bridges and, as with glutaraldehyde, these cross-links are often formed between lysine residues. One of the reported advantages of paraformaldehyde is its ability to cross-link, and thus preserve, nucleic acids[247]. This explains the reduction in observed intensities associated with nucleic acid ring breathing modes and the RNA sugar vibration. However, the mechanism responsible for the increased intensity observed in the amide I region of the paraformaldehyde fixed oocytes remains unclear. It is postulated that this is a sampling artefact which occurs as a result of the sub-sampling of a highly heterogeneous sample. This could be confirmed by extending the study to include more samples.

Upon comparison of the three fixative protocols investigated, it was found that paraformaldehyde performed the best. It showed good performance in maintaining sample morphology and only minimal impact on the Raman spectrum of the oocyte. As such, the use of 4 % paraformaldehyde was chosen as the fixative for all subsequent work.

Characterisation of the Oocyte by Sub-Sampling

One of the main obstacles in the spectroscopic analysis of the oocyte is its size. Using the instrumentation available for this work, complete characterisation of the oocyte would require the collection of over a thousand spectra. Given that the minimum acquisition time is approximately 37 s, this results in prohibitively long experiments. Consequently, focus was turned to the determination of the optimum number of spectra which can accurately characterise an individual oocyte.

This issue of sub-sampling is not often encountered in the analysis of cells, as published works almost exclusively deal with the analysis of somatic cells which are significantly smaller. It is however, an issue for the investigation of tissue samples which are often of the order of millimetres in size. Yet, in the analysis of tissue, researchers are commonly interested in specific regions, or morphological features of the tissue. As such, spectra are either acquired in large numbers from a localised region of the sample, or at a constant interval which enable the identification of the smallest morphological feature of interest. In any case, the sampling interval is often arbitrarily chosen.

In this work however, we are less interested in the identification of specific features, but instead the biochemical characterisation of the oocyte. A recently published paper which describes infrared spectroscopic analysis for the discrimination of immature and mature oocytes used only a single line scan, consisting of 16 spectra collected at 4μm intervals, to characterise each oocyte[229]. This method enabled the discrimination of the two groups; however, the biochemical variation between those groups is likely to be greater than that which exists between some of the samples which are to be investigated in this work. Consequently, the approach of acquiring spectra at constant intervals throughout the ooplasm was adopted in this work.

In an effort to quantify the effect of sub-sampling on the proper characterisation of the oocyte, three sub-sampling protocols were tested. The average spectrum calculated for each was then compared to the average spectrum calculated for the fully characterised oocyte. Results of the CVA and Hotelling's T^2 test indicated that the average spectrum calculated for each sampling protocol provided a good approximation. However, analysis of the CV biplot presented in Figure 4.10 suggested that upon increasing the number of spectra, a closer approximation of the oocyte's average spectrum was achieved.

Additionally, the SNR of the average spectrum obtained from each of the sampling protocols was analysed. It was found that the SNR improvement obtained by increasing the number of spectra collected approximates a 0.35 power relationship. This is less than the improvement suggested by theory, whereby SNR should increase according to $\sqrt{n}$ [234]. However, this correlation is based upon the repeated measurement of a homogeneous sample, a criteria that the oocyte does not meet. Accordingly, it is not unexpected that a different relationship is observed; the intensity of the signal collected at each location is likely to vary significantly in relation to the local biochemical composition. In particular, the presence of cytoplasmic granularity is likely to significantly affect the measured SNR. Therefore, the decision regarding the selection of the number of spectra for oocyte characterisation was not based upon the measured SNR improvement alone.

The results obtained from the sub-sampling experiments indicated that any of the three protocols would provide an adequate approximation of the oocyte spectrum. However, it was also noted that upon increasing the number of average spectra, the approximation improved. Considering these results and the heterogeneous nature of the ooplasm, for subsequent analysis where high resolution mapping was not suitable, reduced mapping was performed such that 101 spectra were collected at a constant interval of 6 μm.

4.5 Conclusions

The work presented here has highlighted the need for careful consideration of experimental design when planning Raman spectroscopic analysis of biological samples. The results obtained in this study lead to the selection of 4 % paraformaldehyde as the fixative for subsequent work. Furthermore, a spectral acquisition time of 37 s and laser power of 35 mW were found to provide good SNR and not induce sample photo-degradation. Finally, it was established that an oocyte could be accurately characterised by 101 spectra collected by sub-sampling at an interval of 6 μm.

Chapter 5

Investigation of Intra-Oocyte Biochemical Variation Using Raman Mapping Methodology

Temporal changes in the organisation and biochemical profile of the cytoplasm of oocytes and embryos is well established. However, the visualisation of these alterations often requires complicated staining protocols. This work aims to investigate the application of Raman micro-spectroscopic mapping for the investigation of intra-oocyte and intra-embryo biochemical variation, with a view to providing an alternative method for monitoring the complex processes of oocyte cytoplasmic maturation and embryo cleavage.

5.1 Introduction

The oocyte is a complex cell which changes significantly during its development and maturation. During the period of growth and development, the ooplasm increases markedly in volume. However, more significant are the biochemical modifications which occur at this time. There is a marked increase in RNA expression and protein production, organelle copy numbers increase, and cytoskeletal organisation is constantly changing. For example, cortical granules appear and migrate to the periphery of the oocyte in preparation for recruitment in the polyspermy block reaction. These modifications indicate that there exists significant temporal biochemical variation within the oocyte.

Raman micro-spectroscopic mapping has previously been reported for the visualisation of biochemical variation within cells[172] and tissues[210]. In addition to simple univariate techniques, several multivariate methodologies have been described for the elucidation of biochemical variation. In particular, both hierarchical[173] and k-means optimised[171, 174] cluster analysis have been used for identifying regions of similarity in Raman maps. A recent paper has described Raman mapping of GV and MII oocytes[248]; however, hierarchical cluster maps were described for the high wavenumber region (2800 - 3100 cm^{-1}) only and consequently, mainly describe variation in lipid structure and distribution.

In this work, the use of Raman mapping for the visualisation of biochemical variation within GV and MII oocytes and early-stage embryos is reported. The spectral mapping described was performed in the fingerprint region, and thus enables the investigation of all major macromolecule groups. The presentation of univariate maps enables the visualisation of protein and lipid distributions. Furthermore, multivariate maps generated using k-means cluster analysis enable the change in location and relative concentrations of specific macromolecule groups during development to be investigated.

5.2 Materials and Methods

5.2.1 Sample Selection and Preparation

Pre-antral follicles displaying good morphology were dissected from the ovaries of 3-week old mice; GV oocytes were collected by rupturing pre-antral follicles and IVM oocytes were collected after the 24 hour maturation of COCs which had been obtained from pre-antral follicles cultured for 6 days. Fertilised oocytes, which had been collected from superovulated mice displaying a vaginal plug after being placed overnight with a proven male, were cultured for 24 and 48 hours to obtain 2-cell and 4-cell embryos, respectively. All oocytes and embryos were washed thrice in PBS before being fixed for 30 minutes in 4 % paraformaldehyde. After fixing, samples were washed thrice in PBS and were stored in PBS at 4 °C until Raman analysis. Bovine serum albumin (BSA), immunoglobulin G from human serum, 1,2-Dioleoyl-sn-Glycero-3-phosphocholine (DOPC), 1,2-Dipalmitoyl-sn-Glycero-3-phosphocholine (DPPC) and calf thymus DNA (SigmaAldrich, UK) were analysed without any further processing.

5.2.2 Raman Spectroscopy Measurements

Measurements were taken from each sample using the rectangular mapping acquisition protocol outlined in the Chapter 3. Briefly, 1610 individual spectra were collected at a constant interval of 2 μm through the central focal plane of the oocyte or embryo. Each spectrum was integrated for 37 s over the spectral range 450 - 1790 cm^{-1} using a laser power of 35 mW. A spectrum of the PBS buffer which surrounded the oocyte was also acquired using the same experimental conditions. Spectra of a polystyrene standard and a neon light source were also taken in order to calibrate the wavenumber scale. Individual Raman spectra were acquired for the chemical standards using the same experimental conditions.

5.2.3 Data Preprocessing and Extraction

The 1610 spectra which were collected for each sample were treated as a group and subjected to a preprocessing routine, which is described in more detail in Chapter 3. Firstly, the data underwent cosmic ray removal in order to remove the sharp intense peaks which spuriously appear in Raman spectra. The wavelength scale was corrected using the neon and polystyrene spectra, such that spectra obtained at different times could be compared with confidence. Subsequently, the oocyte spectra and PBS spectrum were smoothed using a 3-point and 11-point boxcar function, respectively. In order to remove the tails which result from this type of smoothing, the data was truncated to the region 455 - 1780 cm^{-1}. However, prior to this, the data was resampled such that the spectral sampling interval was set at $1cm^{-1}$. The spectral contribution of the PBS was then subtracted using the first derivative orthogonal vector method suggested by Maquelin *et al.*[230]. Following the correction for PBS contributions, the spectra were returned to their integrated form. The remaining fluorescence background was subtracted by fitting a fourth order polynomial through the points at 456, 478, 632, 800, 1142, 1512 and 1756 cm^{-1}. The spectra were further truncated to the region 800 - 1760 cm^{-1} and then each spectrum was offset corrected, such that the minimum intensity was set to zero. The dataset was passed through a threshold filter, based upon the integrated spectral area, to eliminate spectra which didn't arise from the sample. Finally, the remaining spectra were corrected for variations in sample thickness and fluctuations in laser intensity, using multiplicative signal correction (MSC). The spectra acquired for the chemical standards were smoothed using a 3-point boxcar function and then re-sampled such that the spectral sampling interval was set at 1 cm^{-1}. The spectral region was truncated to the region 800 - 1780 cm^{-1} and the fluorescence background removed by fitting a second order polynomial. The spectra were offset corrected before finally being normalised using the total intensity normalisation routine. All data preprocessing was performed using MATLAB and in-house written scripts.

5.2.4 Data Analysis and Statistics

Two univariate chemical maps were generated for each sample; the first displayed the intensity of the phenylalanine band at 1002 cm^{-1}, and the second the intensity of the C-H deformation at 1437 cm^{-1}. Multivariate analysis of the sample maps was performed using k-means cluster analysis. In the case of each sample, the optimum number of clusters was determined by considering the average silhouette value and sum of distances. Pseudo-colour images were produced to show the distribution of the determined clusters. Finally, the relative composition of the average spectrum for each cluster was approximated by fitting a selection of scaled biochemical standard spectra using an ordinary least squares routine with non-negative coefficient constraint: The fit residuals are presented in Appendix 2.

5.3 Results

The biochemical standards used for the OLS fitting of the spectra obtained from the cluster analysis included substances belonging to all the major macromolecule groups. The two protein standards, BSA and immunoglobulin, were chosen to provide spectra of proteins displaying α-helical and β-sheet secondary structure and the Raman spectra of DOPC, DPPC and calf thymus DNA provided reference spectra for unsaturated and saturated phospholipids and nucleic acids, respectively. Three further standards, including mannose, glycogen and baker’s yeast RNA, were included in the OLS model but zero coefficients were returned for all spectra. The zero coefficients for RNA and non-zero coefficients for DNA was unexpected. However, the spectrum obtained from the RNA was dominated by an autofluorescence which was not observed in the DNA spectrum. Consequently, the processed RNA spectrum was very noisy and lacked the spectral definition observed for the DNA. It is postulated that the non-zero coefficients obtained for DNA is more likely to reflect the presence of RNA, which is known to be abundantly in the oocyte. This theory is supported by the similarity in the functional groups present in both RNA and DNA.

Figure 5.1 presents the normalised spectra of the macromolecule standards which were used in the spectral fitting. Contributions arising from the amide III and amide II vibrations, at 1230 - 1260 and 1550 - 1565 cm^{-1}, which are observed in the immunoglobulin spectrum are absent from the BSA spectrum. The strong band, at 1090 - 1100 cm^{-1}, which is observed in the DNA spectrum results from the O-P-O stretch in the backbone, while further Raman bands arising from the pyrimidine and purine bases are seen in the region 1250 - 1580 cm^{-1}. Raman bands arising from the =C-H bending and C=C stretching vibrations are observed in the spectrum of the unsaturated DOPC but are absent from the saturated DPPC. A broad band is present at 1650 cm^{-1} in the PBS spectrum which arises from H_2O bending vibrations.

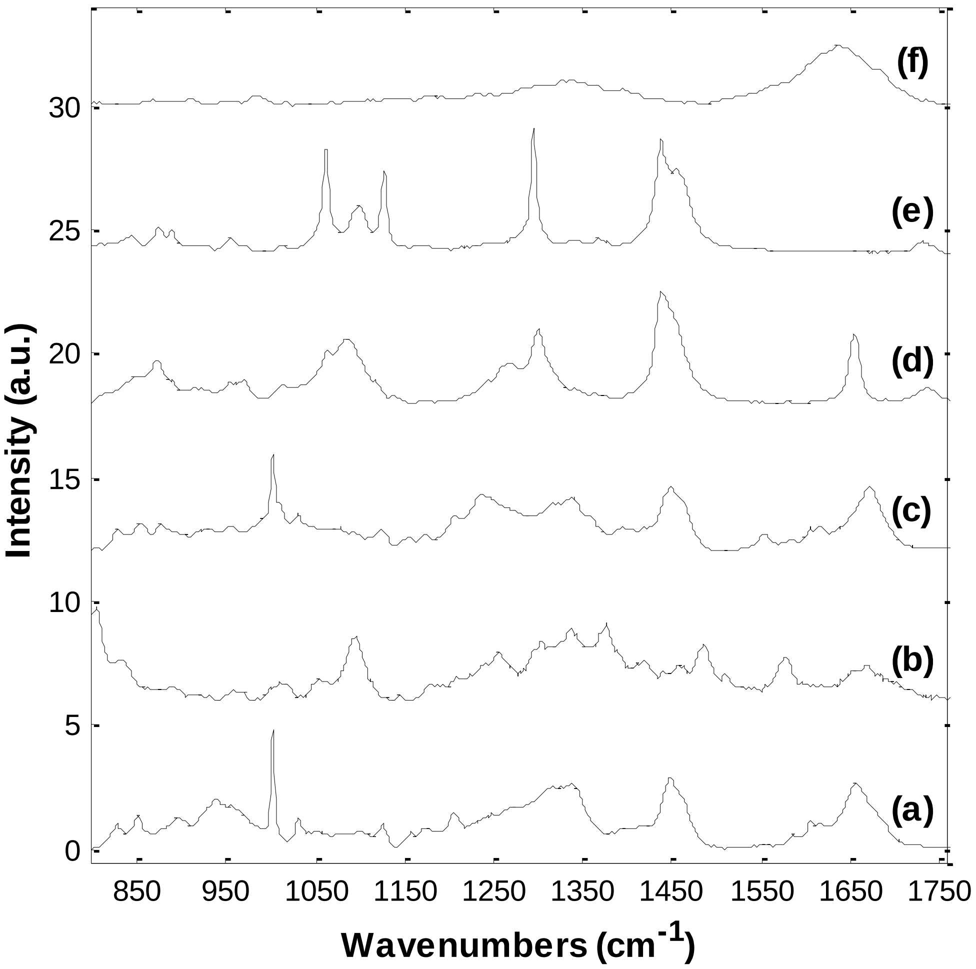

Figure 5.1 – Raman spectra of standards used for least-squares fitting of average cluster spectra: (a) BSA; (b) DNA; (c) immunoglobulin; (d) DOPC; (e) DPPC; (f) PBS.

5.3.1 The Germinal Vesicle Oocyte

It can be seen from Figure 5.2c, which shows the intensity of the phenylalanine band at 1002 cm^{-1}, that proteins are distributed throughout the ooplasm. However, higher intensities are observed in the peripheral regions of the ooplasm. This high protein concentration is not attributed to the glycoprotein zona pellucida, as the intensity threshold filter removed contributions arising from this structure. Conversely, the intensity plot of the C-H deformation, arising from lipids, at 1437 cm^{-1} (Figure 5.2d) indicates a distinct perinuclear lipids distribution. A marginally darker region is seen to surround the germinal vesicle in the white light image (Figure 5.2a), indicating that the darker regions of the ooplasm are associated with high lipid concentrations.

Analysis of the sum of distances and average cluster silhouette values which were generated during the k-means cluster analysis revealed the optimum number of clusters to be three. The distribution of the three clusters within the oocyte can be seen from the pseudo-colour image in Figure 5.2b. Comparison of Figures 5.2b and 5.2d shows good correlation between regions of high lipid intensity and the distribution of the red cluster. Furthermore, the distribution of the blue cluster appears to match the regions of the intense phenylalanine stretches which are observed in Figure 5.2c, indicating that the blue cluster may describe protein rich regions of the cytoplasm. It is unclear from the univariate images to what the green cluster, which is present on the periphery of the ooplasm, can be attributed.

Analysis of the mean spectra from each of the clusters, which are presented in Figure 5.2e, enables greater elucidation as to the biochemical variation which exists within the GV oocyte. The mean spectrum for the red cluster (red trace) displays higher contributions in the region of the C-C stretch and the CH_2 and CH deformations at 1060 - 1090, 1300 and 1437 cm^{-1}, which are associated with lipids. The mean spectra derived from the blue (blue trace) and green (green trace) clusters both show increased contribution around 1340 cm^{-1},

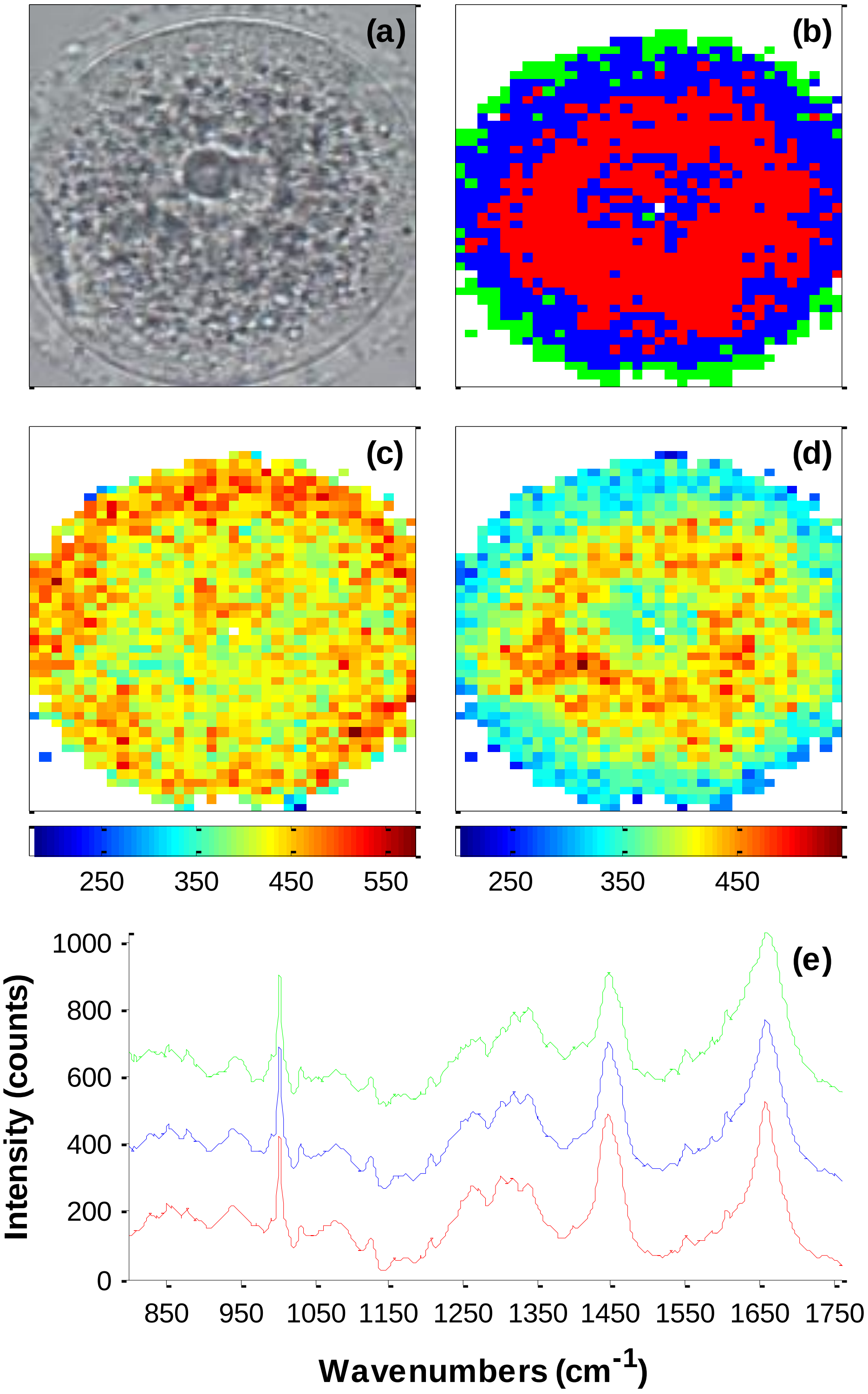

Figure 5.2 – Image panel displaying Raman mapping results for a GV oocyte; (a) white light image of the oocyte; (b) pseudo-colour image created from k-means cluster analysis; (c) univariate intensity plot for phenylalanine band at 1002 cm^{-1} (d) univariate intensity plot for CH_2 stretch at 1437 cm^{-1} and (e) average spectra for each cluster shown in panel (b).

which is a region associated with the C-H deformation in proteins. However, the green trace also displays more prominent bands around 1370 and 1410 cm^{-1}, that are known to arise in RNA from pyrimidine ring breathing and CH_2 scissoring in the backbone, respectively[249].

These observations are consistent with the results obtained from the OLS fitting of the mean cluster spectra (Table 5.1). It can be seen from these results that 24 % of the mean spectrum from the red cluster can be attributed to lipids, whilst only 17.1 and 13 % can be attributed to lipid vibrations in the blue and green clusters, respectively. Although the contribution of β-sheet proteins is relatively constant across the clusters, higher α-helical protein contributions are observed in both the blue and red clusters. Significantly, the relative contribution of nucleic acids is highest in the green cluster, which is observed exclusively at the periphery of the ooplasm, indicating a higher concentration of RNA in this region. The contribution of PBS in the mean cluster spectra increases from the red to blue to green clusters. In the lipid-rich regions, described by the red cluster, it is likely that localised hydration would be lower. However, almost 40 % of the green cluster spectrum is attributed to PBS. It is postulated that this results from the reduced sampling volume present at the edge of the oocyte.

Component	Red Cluster		Blue Cluster		Green Cluster	
α-helix protein	52.5	(35.2)	45.1	(29.5)	27.4	(17.5)
Nucleic acids	3.1	(2.1)	7.0	(4.6)	14.5	(9.3)
β-sheet protein	28.6	(19.2)	33.4	(21.9)	33.1	(21.2)
DOPC	35.7	(24.0)	26.1	(17.1)	20.3	(13.0)
DPPC	0.0	(0.0)	0.0	(0.0)	0.3	(0.2)
PBS	29.2	(19.6)	41.1	(26.9)	60.8	(38.9)
	149.2		152.7		156.4	
Pearson R^2	0.86		0.88		0.81	

Table 5.1 – Results of the standard spectra least squares fit of the mean cluster spectra derived from the k-means cluster analysis of the GV oocyte presented in Figure 5.2. The values in the brackets indicate the percentage contribution of each standard to the average cluster spectrum. The Pearson's R^2 value indicates the goodness of fit achieved.

5.3.2 The Metaphase II Oocyte

It can be seen from Figure 5.3c, which shows the intensity of the phenylalanine band at 1002 cm^{-1}, that there exists protein aggregations within the ooplasm, with particular high concentrations located in the peripheral regions of the oocyte. Significantly, an asymmetric distribution of phenylalanine Raman intensities is observed across the animal-vegetal axis, which could indicate the existence of oocyte polarisation. Similarly, the intensity plot of the CH deformation, arising from lipids, at 1437 cm^{-1} (Figure 5.3d) displays regions of lipid aggregation throughout the ooplasm. As with the GV oocyte, the location of the lipid aggregates appear to correspond to dark regions present in the white light image of the MII oocyte (Figure 5.3a).

Analysis of the sum of distances and average cluster silhouette values which were generated during the k-means cluster analysis revealed the optimum number of clusters to be three. The distribution of the three clusters within the oocyte can be seen from the pseudo-colour image in Figure 5.3b. Comparison of Figures 5.3b and 5.3d shows good correlation between regions of high lipid intensity and the distribution of the red cluster. Furthermore, the distribution of the green cluster appears to match the regions of the intense phenylalanine stretches which are observed in Figure 5.3c, indicating that this cluster may describe protein rich regions of the cytoplasm. The blue cluster, which is distributed throughout the ooplasm, appears to correspond to a biochemical profile which lies between the lipid-rich red cluster and the protein-rich green cluster.

Analysis of the mean spectra from each of the clusters, which are presented in Figure 5.3e, enables greater elucidation as to the biochemical variation which exists within the MII oocyte. The mean spectrum for the red cluster (red trace) displays significantly higher contributions in the region of the C-C stretch and the CH_2 and CH deformations and carboxyl stretch at 1060 - 1090, 1300, 1437 and 1745 cm^{-1}, which are associated with lipids.

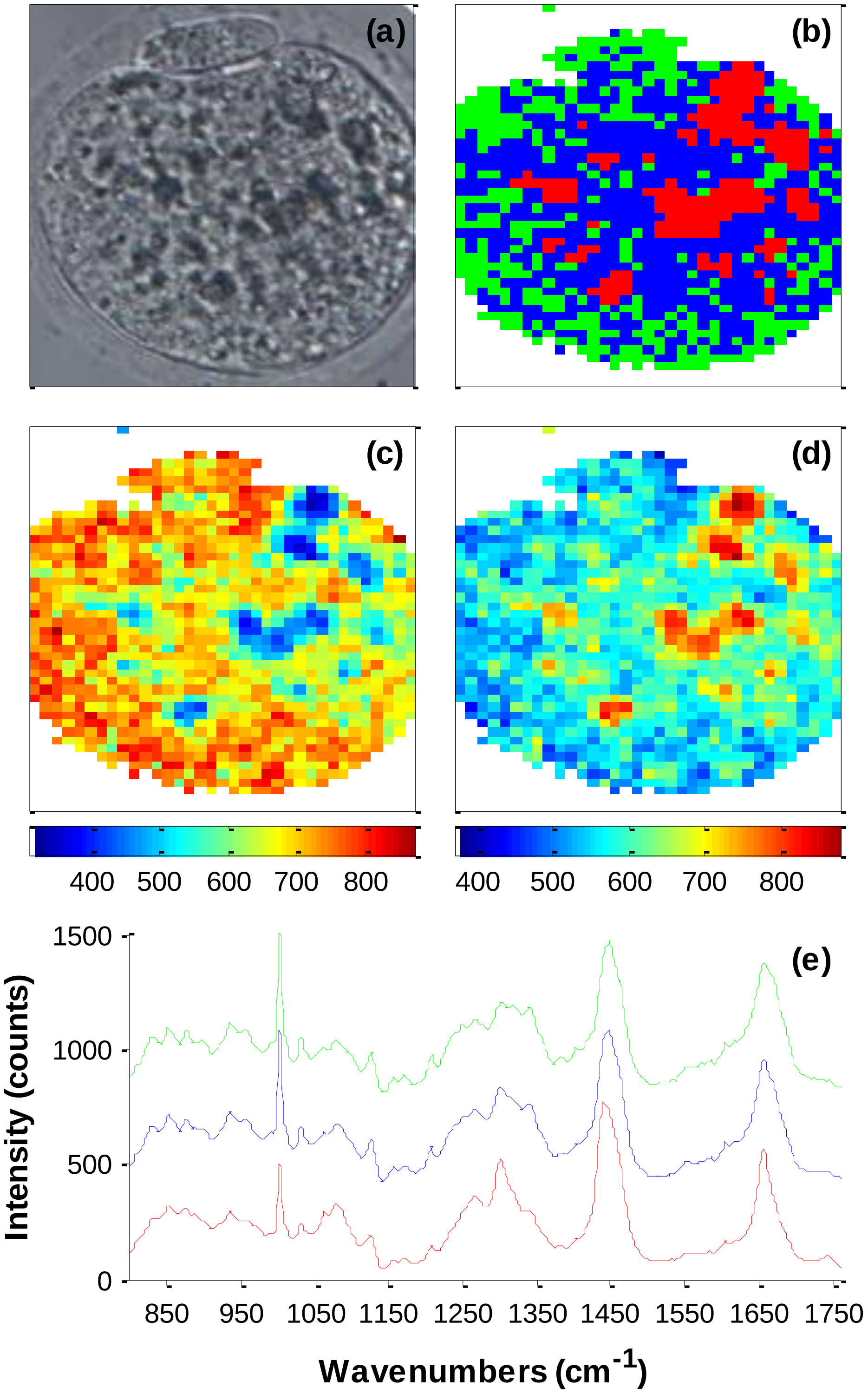

Figure 5.3 – Image panel displaying Raman mapping results for an IVM oocyte; (a) white light image of the oocyte; (b) pseudo-colour image created from k-means cluster analysis; (c) univariate intensity plot for phenylalanine band at 1002 cm^{-1} (d) univariate intensity plot for CH_2 stretch at 1437 cm^{-1} and (e) average spectra for each cluster shown in panel (b).

The mean spectra derived from the blue (blue trace) and green (green trace) clusters both show significantly increased contributions around 930 - 970 and 1340 cm^{-1}, which is a region associated with the C-C stretch and C-H deformation in proteins. Furthermore, the green trace also displays a prominent shoulder at 1670 cm^{-1}which is indicative of an amide I shift resulting from an increase in β-sheet protein concentration.

Examination of the results obtained from the OLS fitting of the mean cluster spectra (Table 5.2) shows that the sum of coefficients for each cluster is greater for the MII oocyte when compared to the GV oocyte. This result indicates an accumulation of macromolecules during the progression from GV to MII. In particular, there are marked increases in lipids and both α-helical and β-sheet proteins during the period of cytoplasmic maturation, which is concomitant with a decrease in PBS contribution during the same period. Furthermore, only the red cluster spectrum for the MII oocyte had contributions arising from nucleic acids, amounting to 1.1 %; this was significantly lower than the 2.1 - 9.3 % observed in the GV oocyte cluster spectra, suggesting a decrease in the concentration of RNA present in the mature oocyte.

Component	Red Cluster		Blue Cluster		Green Cluster	
α-helix protein	68.6	(36.1)	85.2	(42.9)	81.4	(39.7)
Nucleic acids	2.1	(1.1)	0.0	(0.0)	0.0	(0.0)
β-sheet protein	33.9	(17.8)	54.5	(27.5)	59.6	(29.1)
DOPC	76.6	(40.3)	50.0	(25.2)	42.1	(20.6)
DPPC	2.0	(1.0)	0.0	(0.0)	0.0	(0.0)
PBS	6.9	(3.6)	8.8	(4.4)	21.8	(10.6)
	190.0		198.4		204.9	
Pearson R^2	0.93		0.92		0.91	

Table 5.2 – Results of the standard spectra least squares fit of the mean cluster spectra derived from the k-means cluster analysis of the IVM oocyte presented in Figure 5.3. The values in the brackets indicate the percentage contribution of each standard to the average cluster spectrum. The Pearson's R^2 value indicates the goodness of fit achieved.

5.3.3 The 2-cell Embryo

It can be seen from Figure 5.4c, which shows the intensity of the phenylalanine band at 1002 cm^{-1}, that particularly high concentrations of protein are present in the peripheral regions of the blastomeres, or constituent cells, of the 2-cell embryo. Conversely, the intensity plot of the CH deformation, arising from lipids, at 1437 cm^{-1} (Figure 5.4d) displays centrally located regions of lipid-rich material within each blastomere. However, it is worth noting that in each blastomere a small region within the lipid-rich area is lipid deficient. Furthermore, unlike the GV and MII oocytes the white light image (Figure 5.4a) does not reveal any morphological associations with the observed lipid-rich regions.

Analysis of the sum of distances and average cluster silhouette values which were generated during the k-means cluster analysis revealed the optimum number of clusters to be three. The distribution of the three clusters within the oocyte can be seen from the pseudo-colour image in Figure 5.4b. Comparison of Figures 5.4b and 5.4d shows good correlation between regions of high lipid intensity and the distribution of the red cluster. Furthermore, the distribution of the blue cluster appears to match the regions of the intense phenylalanine stretches which are observed in Figure 5.4c, indicating that this cluster may describe protein rich regions of the cytoplasm. The green cluster, which is distributed throughout the cytoplasm, appears to correspond to a biochemical profile which lies between the lipid-rich red cluster and the protein-rich blue cluster.

Analysis of the mean spectra from each of the clusters, which are presented in Figure 5.4e, enables greater elucidation as to the biochemical variation which exists within the 2-cell embryo. The mean spectrum for the red cluster (red trace) displays significantly higher contributions in the region of the C-C stretch and the CH_2 and CH deformations at 1060 - 1090, 1300, 1437 cm^{-1}, which are associated with lipids. The mean spectrum derived for the blue cluster shows greater contributions in the region of 930 - 970, 1030, 1125, 1157,

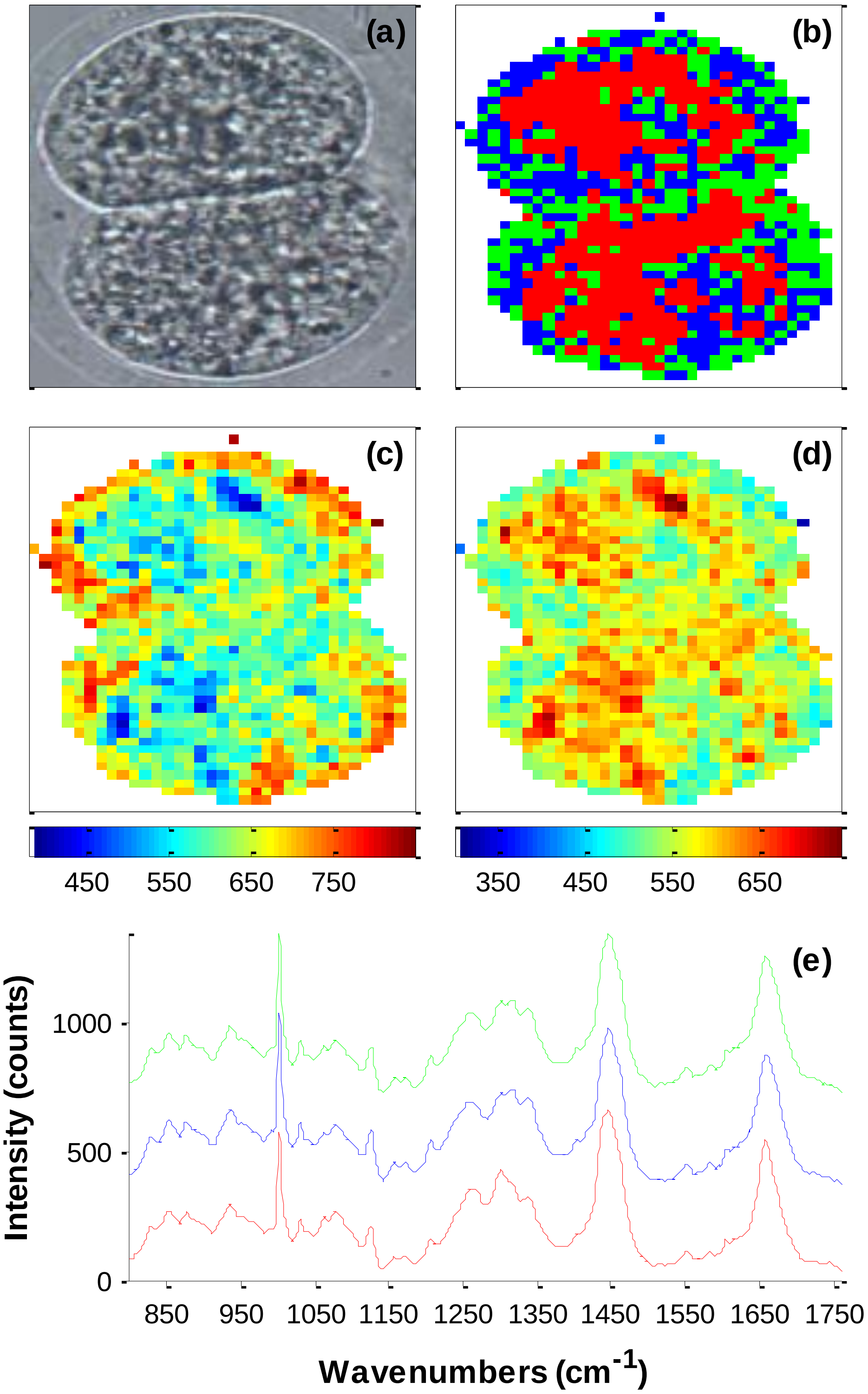

Figure 5.4 – Image panel displaying Raman mapping results for a 2-cell embryo; (a) white light image of the oocyte; (b) pseudo-colour image created from k-means cluster analysis; (c) univariate intensity plot for phenylalanine band at 1002 cm^{-1} (d) univariate intensity plot for CH_2 stretch at 1437 cm^{-1} and (e) average spectra for each cluster shown in panel (b).

1163, 1207 and 1310 - 1340 cm^{-1}, which are all regions associated with the protein molecular vibrations. Finally, the mean spectrum derived from the green cluster displayed slightly elevated contributions in the regions of the lipid C-H deformation at 1437 cm^{-1} , a reduction in the intensity of the amide III band around 1250 cm^{-1} and broadening of the amide I envelope consistent with a elevated concentrations of water.

Examination of the results obtained from the OLS fitting of the mean cluster spectra (Table 5.3) shows that the sum of coefficients for each cluster is slightly lower for the 2-cell embryo when compared to the mature oocyte, but still higher than those observed for the immature oocyte. This result suggests a decrease in cytoplasmic macromolecular concentration during the fertilisation and cleavage process; in particular, a slight drop in α-helical protein and unsaturated lipid content is observed. Conversely, each of the clusters shows contributions arising from saturated lipids which were not present in the oocytes. Furthermore, it can be seen from the OLS results that no contributions arising from nucleic acids are present in the 2-cell cluster spectra; this is consistent with the fall in nucleic acid content which was observed during cytoplasmic maturation.

Component	Red Cluster		Blue Cluster		Green Cluster	
α-helix protein	70.2	(39.3)	74.6	(39.5)	66.8	(36.1)
Nucleic acids	0.0	(0.0)	0.0	(0.0)	0.0	(0.0)
β-sheet protein	49.3	(27.6)	72.2	(38.3)	59.3	(32.0)
DOPC	53.9	(30.1)	38.5	(20.4)	41.0	(22.1)
DPPC	0.8	(0.5)	0.5	(0.2)	2.1	(1.1)
PBS	4.5	(2.5)	2.9	(1.5)	16.0	(8.6)
	178.8		188.7		185.2	
Pearson R^2	0.95		0.95		0.93	

Table 5.3 – Results of the standard spectra least squares fit of the mean cluster spectra derived from the k-means cluster analysis of the 2-cell embryo presented in Figure 5.4. The values in the brackets indicate the percentage contribution of each standard to the average cluster spectrum. The Pearson's R^2 value indicates the goodness of fit achieved.

5.3.4 The 4-cell Embryo

It can be seen from Figure 5.5c, which shows the intensity of the phenylalanine band at 1002 cm^{-1}, that particularly high concentrations of protein are present in the peripheral regions of the blastomeres of the 4-cell embryo. Additional protein-rich regions are seen to bisect some of the blastomeres. Conversely, the intensity plot of the CH deformation, arising from lipids, at 1437 cm^{-1} (Figure 5.5d) displays lipid aggregates distributed throughout the blastomeres. Comparison with the white light image (Figure 5.5a) reveals that some of the lipid-rich regions are associated with darker regions of the cytoplasm. Furthermore, it is suggested that the lower intensities which are observed for the bottom right blastomere result due to the blastomere being situated outwith the imaging focal plane (Figure 5.5a).

Analysis of the sum of distances and average cluster silhouette values which were generated during the k-means cluster analysis revealed the optimum number of clusters to be three. The distribution of the three clusters within the oocyte can be seen from the pseudo-colour image in Figure 5.5b. Comparison of Figures 5.5b and 5.5d shows good correlation between regions of high lipid intensity and the distribution of the red cluster. Furthermore, the distribution of the blue cluster appears to match the regions of the intense phenylalanine stretches which are observed in Figure 5.5c, indicating that this cluster may describe protein rich regions of the cytoplasm. It is unclear from the univariate images to what the green cluster, which is located on the periphery of the blastomeres, can be attributed.

Analysis of the mean spectra from each of the clusters, which are presented in Figure 5.5e, enables greater elucidation as to the biochemical variation which exists within the 4-cell embryo. The mean spectrum for the red cluster (red trace) displays significantly higher contributions in the region of the C-C stretch and the CH_2 and CH deformations at 1060 - 1090, 1300, 1437 cm^{-1}, which are associated with lipids. The mean spectrum derived for both the blue and green clusters show greater contributions in the region of 1310 - 1340 cm^{-1},

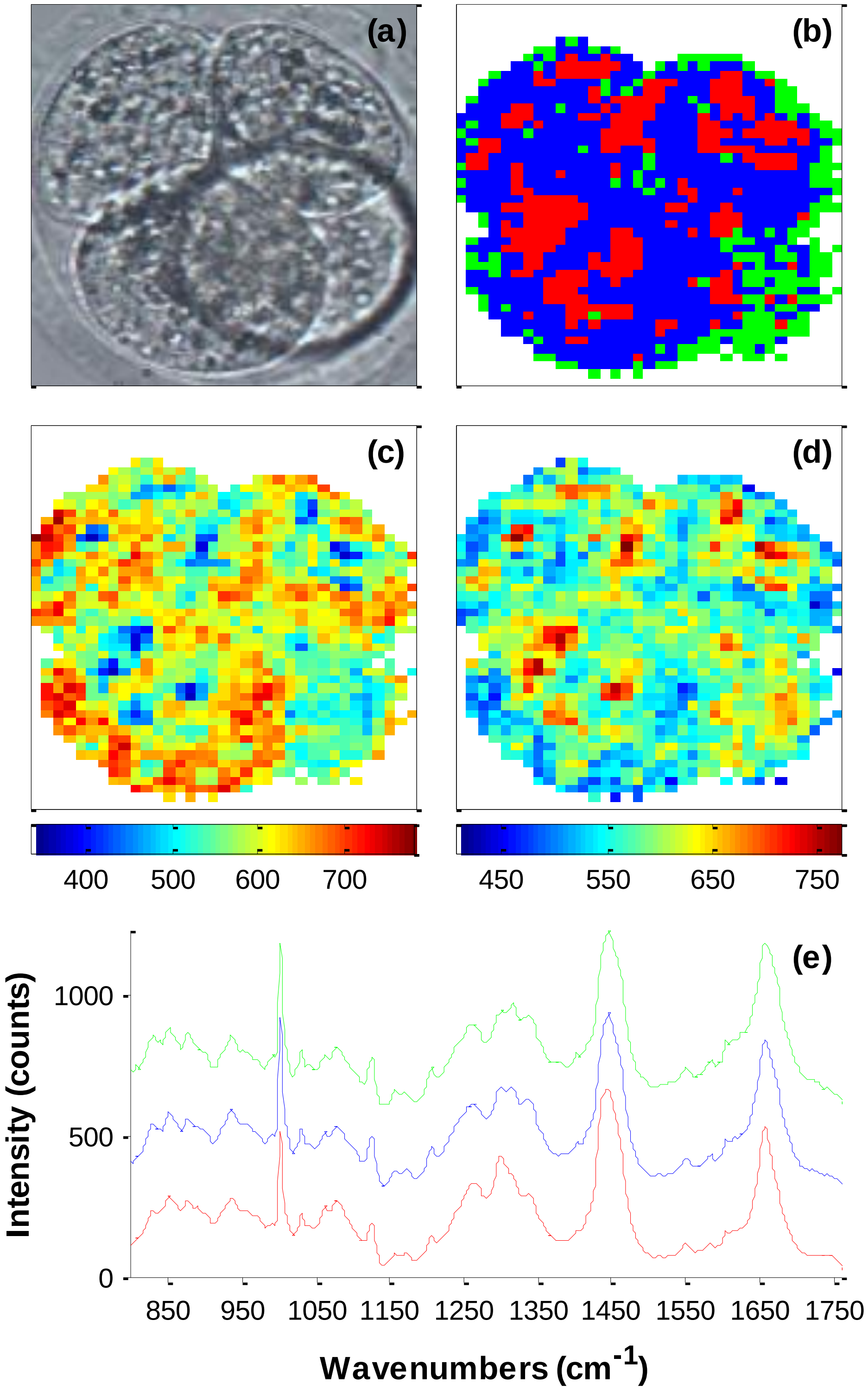

Figure 5.5 – Image panel displaying Raman mapping results for a 4-cell embryo; (a) white light image of the oocyte; (b) pseudo-colour image created from k-means cluster analysis; (c) univariate intensity plot for phenylalanine band at 1002 cm^{-1} (d) univariate intensity plot for CH$_2$ stretch at 1437 cm^{-1} and (e) average spectra for each cluster shown in panel (b).

which is associated with the C-H deformation in proteins. Furthermore, the spectrum of the blue cluster displays strong contributions around 930 - 970, 1030 and 1173 cm^{-1}, which are regions indicative of β-sheet protein vibrations. Conversely, the mean spectrum derived from the green cluster displayed slightly elevated contributions in the regions of 1370 - 1410 cm^{-1}, which is suggestive of the presence of nucleic acids. There is also broadening of the amide I envelope which is consistent with elevated concentrations of water in this cluster.

Examination of the results obtained from the OLS fitting of the mean cluster spectra (Table 5.4) shows that the sum of coefficients for each cluster are similar to those obtained for the 2-cell embryo. This result suggests that no net change in the total macromolecular concentration occurs during the further cleavage of the early-stage embryo. However, changes in the relative concentration of macromolecules are observed; a small drop in protein content and an increase in unsaturated lipid content are observed. A further increase in the contributions arising from saturated lipids is also seen in the spectra derived from the 4-cell embryo. It is suggested that the increase of PBS contributions in the green cluster spectrum are the result of the blastomeres not completely filling the imaging focal plane.

Component	Red Cluster		Blue Cluster		Green Cluster	
α-helix protein	66.8	(38.5)	73.7	(40.9)	57.2	(29.8)
Nucleic acids	0.0	(0.0)	0.0	(0.0)	5.0	(2.6)
β-sheet protein	35.9	(20.7)	47.6	(26.4)	49.3	(25.7)
DOPC	60.3	(34.8)	45.2	(25.1)	44.2	(23.0)
DPPC	2.4	(1.4)	0.9	(0.5)	3.2	(1.7)
PBS	8.1	(4.6)	12.7	(7.1)	33.1	(17.2)
	173.4		180.1		191.9	
Pearson R^2	0.92		0.91		0.84	

Table 5.4 – Results of the standard spectra least squares fit of the mean cluster spectra derived from the k-means cluster analysis of the 4-cell embryo presented in Figure 5.5. The values in the brackets indicate the percentage contribution of each standard to the average cluster spectrum. The Pearson's R^2 value indicates the goodness of fit achieved.

5.4 Discussion

The Raman maps which are presented in this chapter were acquired using a point-mapping protocol and, as such, the total acquisition time was approximately 18 hours. It is recognised that this acquisition time is excessive and unsuitable for the analysis of unfixed samples. However, it is not intended that this methodology would serve as a diagnostic protocol in a clinical setting. Instead, this work was performed to investigate the potential of Raman spectroscopy for the analysis and monitoring on biochemical variation in the oocyte and early embryo, for application in ovarian research. As such, the analysis of fixed samples and longer acquisition times are more acceptable. That being said, some instrumental modifications would enable the mapping time to be reduced: Using a larger CCD array would reduce the map time to approximately 5 hours and the implementation of line mapping, whereby a column of map pixels are integrated simultaneously, could further reduce mapping times. The implementation of these modifications, coupled with the use of the automated preprocessing and data analysis program which has been written, could thus provide an adjunct technique for oocyte visualisation in the research setting.

The selection of GV and MII oocytes for this work was intended to provide an opportunity to investigate the biochemical alterations and cytoskeletal reorganisation which are associated with cytoplasmic maturation, and the potential of Raman spectroscopy for visualising this process. Furthermore, the inclusion of Raman maps acquired from early-stage embryos provided an insight into the biochemical alterations which occur after fertilisation and during early cleavage.

One of the main issues which had to be addressed in the preprocessing stage was the variation in sample thickness, which exists across the oocyte. At the edge of the oocyte, the volume from which Raman scattering is collected is not fully occupied by the oocyte, as demonstrated in Figure 5.6. The application of multiplicative signal correction has

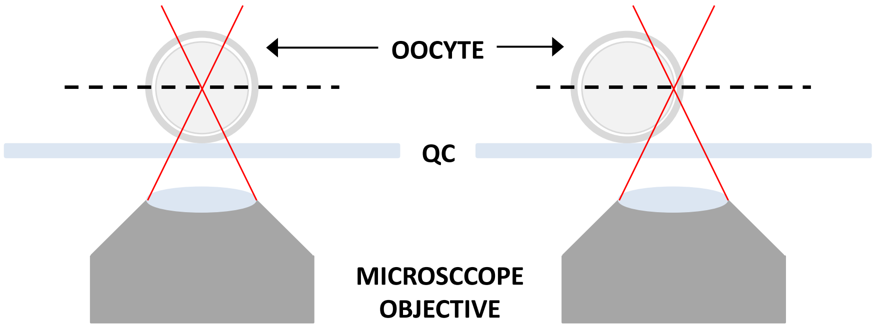

Figure 5.6 – Illustration of the effect of variation in sample thickness on illumination and scattering volume; the image on the left shows that the oocyte completely fills the scattering volume, whereas, the image rights shows that the oocyte only partially fills the scattering volume. QC denotes the quartz coverslip upon which the oocyte was mounted.

previously been reported for sample thickness correction[209]. Minimal variation was observed in the integrated spectral intensity across the oocyte after implementation of MSC, indicating that this technique successfully addresses the variation in sample thickness.

Comparison of the univariate images, which were generated from the intensity of the C-H deformation at 1437 cm^{-1}, and the pseudo-colour images generated during the cluster analysis provided an insight into the redistribution of lipids during the process of cytoplasmic maturation and cleavage. In each case, it appeared that the lipid-rich regions of the sample were associated with the red cluster. In the immature oocyte, a perinuclear distribution of lipids is observed (Figure 5.2d). At the GV stage, oocytes have not accumulated large lipid deposits, such as those observed in the mature oocyte (Figure 5.3d). As such, it is postulated that many of the lipid vibrations observed in the GV oocyte arise from the lipid-rich mitochondrion. This theory is supported by the correlation between the lipid-rich regions, which were identified by the univariate and cluster maps, and the widely reported perinuclear distribution of mitochondria in the GV oocyte[36, 250].

The results obtained for the MII oocyte, indicate that the mature oocyte contains significantly higher concentrations of lipids when compared to the immature oocyte. This result is consistent with the accumulation of lipid deposits and increase in mitochondrial copy number which is known to occur during cytoplasmic maturation. Examination of the corresponding images indicates several regions of intense lipid aggregation, as identified by the red cluster in the pseudo-colour image. These regions are identified in the white light image by dense dark regions in the cytoplasm. It is unclear whether these regions are the result of mitochondrial aggregates, which have been reported in MII oocytes[250, 251], or accumulated lipid deposits which are thought to be energy stores equivalent to yolk. Intermediate lipid vibration intensities are observed throughout the cytoplasm, as depicted by the blue cluster in Figure 5.3, which are characteristic of the mitochondrial distribution reported for MII oocytes.

The sum of the OLS coefficients for both the 2-cell and 4-cell embryos was lower than those observed for the MII oocyte, indicating that there is a loss of macromolecules from the cytoplasm during the process of fertilisation and cleavage. This finding is consistent with the reported change in dry mass of oocytes and embryos during development[252]. In particular, a significant reduction in lipid content is observed between the MII and 2-cell stage. This is most likely a result of the recruitment of lipid droplets for membrane production during cleavage. Contributions arising from saturated lipids are observed in both the 2-cell and 4-cell embryo, yet they are absent from the oocytes, however it is unclear why this change occurs. It is suggested that as the highest concentrations are observed predominantly in the green cluster, which is close to the cell membrane, that these saturated lipids are associated with the membrane structure whose surface area increases upon cleavage.

Comparison of the univariate images, which were generated from the intensity of the phenylalanine symmetric stretch at 1002 cm^{-1}, and the pseudo-colour images generated during the cluster analysis provided an insight into the redistribution of proteins during the process of cytoplasmic maturation and cleavage. In the GV oocyte, high protein intensities are observed in the cortical region of the ooplasm, which are identified by the blue cluster. This distribution is consistent with the cortical location of the Golgi apparatus, whose primary role is the production of glycoproteins for the zona pellucida, and the migration of the cortical granules to the periphery of the ooplasm, in preparation for recruitment during the sperm block reaction[33].

The results obtained for the MII oocyte, indicate that the mature oocyte contains significantly higher concentrations of proteins when compared to the immature oocyte. This result is in accordance with the increase in cellular protein production and the number of sub-cellular structures, including the fibrous lattices, which occurs during cytoplasmic maturation. Examination of the corresponding images, show that proteins are distributed throughout the ooplasm of the MII oocyte, although some asymmetry is observed to exist across the animal-vegetal axis. In the mouse, the role of oocyte polarity in subsequent embryonic cleavage is still not fully resolved[253]. However, if this asymmetry represents polarisation it suggests that the use of Raman spectroscopy could provide further insight in this matter. In particular, the application of Raman imaging could enable temporal investigations of polarity and embryo cleavage.

The univariate images for both the 2-cell and 4-cell embryos display particularly high contributions from proteins at the periphery of the blastomeres. This observation suggests peripheral localisation of ribosomes, which is consistent with the uptake of amino acids that has been reported to be essential for successful embryo development. Additionally, the 4-cell univariate image shows some protein-rich regions bisecting the blastomeres which could be indicative of imminent cleavage. It is noteworthy that the coefficients derived during the OLS fit of the 4-cell embryo show a decrease in the contribution of proteins when compared to the MII and 2-cell embryo. This is in accordance with the reported decrease in total protein content during the first few days of murine embryo development[254].

The results of the OLS fitting also revealed that the RNA contributions, which were sizeable in the GV oocyte, reduced significantly in the MII oocyte, and were completely absent in the 2-cell embryo. However, small contributions were observed in the 4-cell embryo. The reduction between the GV and MII stage is supported by evidence of RNA degradation upon resumption of meiosis. Furthermore, it is widely acknowledged that by the 2-cell stage the maternal RNA has almost entirely degraded[30]. At this point the embryonic genes are "switched on" and embryonic RNA production increases, which would account for the increase in RNA contributions observed in the 4-cell embryo[255].

The absence of contributions from carbohydrates in the OLS fitting of the sample spectra is unexpected, as oocytes are known to contain glycogen granules which are thought to form part of the "mammalian yolk". However, it is suggested that due to their small size, these membrane bound vesicles do not contribute significantly to spectrum of the interrogated volume. The region from which Raman scattering is collected is determined by a number of parameters; the numerical aperture of the microscope objective, spectrometer confocal slit width and refractive index mismatches can all affect the actual volume sampled[256, 257]. The use of an immersion microscope objective with higher numerical aperture would enable Raman maps, corresponding to thinner optical sections, to be acquired. This experimental modification could reveal more detailed macromolecule localisation than is presented in this work. However, the Raman spectrum of the immersion medium and optical coatings and the transmission efficiency must all be considered when selecting a suitable microscope objective.

5.5 Conclusions

The work presented in this chapter has demonstrated that Raman microscopic mapping can be used to investigate the biochemical variation which exists within the oocyte and embryo at different stages of development. Specifically, marked changes in protein and lipid distributions are observed in samples derived from different developmental stages. Much of the observed macromolecule localisation is consistent with previously documented temporal changes in cytoplasm organisation. OLS fitting of the mean spectra derived from the k-means cluster analysis revealed significant changes in the relative concentrations of macromolecules between the studied developmental stages. Of particular interest was the asymmetric distribution of macromolecules in the MII oocyte, a phenomenon which could be the result of oocyte polarisation. This observation indicates that Raman spectroscopy could be used for the investigation of oocyte polarity and subsequent embryo cleavage.

Chapter 6

A Raman Spectroscopic Analysis of the Biochemistry of Oocyte Development

A quantitative technique for the assessment of oocyte maturity would undoubtedly improve the efficiency of ART methodologies. As such, this work presents the use of Raman spectroscopy for the discrimination of GV and IVM oocytes, reporting the biochemical basis of their distinction. Furthermore, a logistic regression model for the classification of oocyte maturity is described.

6.1 Introduction

The determination of the progression of oocyte maturation has been recognised as being one of the main obstacles to improving the efficiency of IVF treatments[33]. Whilst some advances in the assessment of nuclear maturation have been made with the development of techniques such as birefringence imaging[68, 70, 72], issues remain with the quantification of ooplasmic maturation.

The cytoplasm of the oocyte undergoes extensive alteration during the progression from the GV to MII stage of meiosis, as demonstrated in Chapter 5. The accumulation of organelles, macromolecules and the cytoskeletal reorganisation, all contribute to the changing biochemical profile of the ooplasm during this period of maturation. In particular, an upregulation in protein expression, an increase in mitochondrial copy number and an increase in lipid deposits are all observed during oocyte cytoplasmic maturation. These marked changes in the biochemical profile of the ooplasm during development and maturation should make the oocyte an ideal candidate for spectroscopic investigation. Indeed, a recent paper describes the use of IR spectroscopy for the discrimination of GV and MII oocytes collected from stimulated cycles[248].

The effect of exogenous hormonal stimulation on oocyte biochemistry has not yet been fully described. Therefore, it is of interest to compare immature and mature oocytes collected from follicles which have not been subjected to the elevated hormonal levels used during stimulation. Furthermore, the analysis of immature and mature oocytes, which originate from the same follicular cohort, enables a more objective examination of the biochemical modifications which occur during the maturation process. In this work, the use of Raman spectroscopy combined with PCA-CVA is described for the discrimination of immature and mature oocytes. Furthermore, the development of a logistic regression algorithm, using Raman intensity ratios, for the classification of oocyte maturity is described for the first time.

6.2 Materials and Methods

A total of 7,777 Raman spectra which were acquired from 77 oocytes formed the basis of this study: These data were then analysed in combination with spectra acquired during the work reported in Chapter 7. This particular study was concerned with the examination of the biochemical variations which exist between immature and mature oocytes and the ability of Raman spectroscopy to detect these differences. Initially, the biochemical variation between immature and mature oocytes was examined using oocytes collected from the same follicular cohort; GV oocytes were collected from pre-antral follicles (n=39, 4 replicates) and *in vitro* matured oocytes were collected from cultured pre-antral follicles(n=38, 4 replicates). Later, further comparisons were investigated using oocytes collected after stimulated (n=59, 4 replicates) and unstimulated (n=38, 4 replicates) ovulation cycles.

6.2.1 Sample Selection and Preparation

The treatment protocols for each oocyte group are discussed in detail in Chapter 3, but a brief overview of the collection and treatment will be presented here. Pre-antral follicles displaying good morphology were dissected from the ovaries of 3-week old mice and pooled for subsequent treatment. Half of the follicles were immediately ruptured and the enclosed GV oocytes were collected (GV oocytes: **GV**). The remaining pre-antral follicles were cultured for 6 days before maturing the COCs for a final 24 hours (*in vitro* matured oocytes: **IVM**). Mice were superovulated by administering PMSG, followed 47 hours later by hCG, with superovulated oocytes being collected 18 hours after hCG injection (superovulated oocytes: **SO**). Oocytes from unstimulated cycles were collected from mice which were judged to be in oestrous by vaginal examination (unstimulated mature oocytes: **USO**). All oocytes were washed thrice in PBS before being fixed for 30 minutes in 4 % paraformaldehyde solution. After fixing, oocytes were washed thrice in PBS and were stored in PBS at 4 °C until Raman analysis.

6.2.2 Raman Spectroscopy Measurements

Measurements were taken from each oocyte using the reduced map acquisition protocol outlined in Chapter 3. Briefly, 101 individual spectra were collected at a constant interval of 6 μm through the central focal plane of the oocyte. Each spectrum was integrated for 37 s over the spectral range 450 - 1790 cm^{-1} using a laser power of 35 mW. A spectrum of the PBS buffer which surrounded the oocyte was also acquired using the same experimental conditions. Spectra of a polystyrene standard and a neon light source were also taken in order to calibrate the wavenumber scale.

6.2.3 Data Preprocessing and Extraction

The 101 spectra which were collected for each oocyte were treated as a group and subjected to a preprocessing routine, which is described in more detail in Chapter 3. Firstly, the data underwent cosmic ray removal in order to remove the sharp intense peaks which spuriously appear in Raman spectra. The wavelength scale was corrected using the neon and polystyrene spectra, such that spectra obtained at different times could be compared with confidence. Subsequently, the oocyte spectra and PBS spectrum were smoothed using a 3-point and 11-point boxcar function, respectively. In order to remove the tails which result from this type of smoothing, the data was truncated to the region 455 - 1780 cm^{-1}. However, prior to this, the data was resampled so that the spectral sampling interval was set at 1 cm^{-1}. The spectral contribution of the PBS was then subtracted using the first derivative orthogonal vector method suggested by Maquelin *et al.*[230]. Following the correction for PBS contributions, the spectra were returned to their integrated form. The remaining fluorescence background was subtracted by fitting a fourth order polynomial through the points at 456, 478, 632, 800, 1142, 1512 and 1756 cm^{-1}. Next, an average spectrum was generated by taking the arithmetic mean of the 101 processed spectra. The average spectra were truncated to the region 800 - 1760 cm^{-1} for the data analysis. Following this, each spectrum was offset corrected, such that the minimum intensity was set to zero. Finally, each spectrum was normalised to its mean spectral intensity across all wavenumbers in order to account for fluctuations in laser intensity. All data preprocessing was performed using MATLAB and in-house written scripts.

6.2.4 Data Analysis and Statistics

Initially, the processed average spectra were grouped according to their treatment. The mean spectrum, and its standard deviation, was then calculated for each oocyte group. Using a two-tailed, unpaired t-test (α=0.0001), the GV and *in vitro* matured groups were compared in order to locate spectral regions which are significantly different. PCA and CVA were also performed on the entire data set, consisting of all mean spectra, to investigate the discrimination of the two groups.

Subsequently, logistic regression was performed on the intensity ratios of three Raman peaks which were found to be significantly different by t-test. Logistic regression is a common method implemented in biomedical research, as it is capable of relating a number of continuous independent variables to a binary dependant variable. Unlike linear regression which fits the measured data using a linear relationship, logistic regression uses the non-linear logit link function, which ensures that the outcome is constrained to values between 0 and 1.

The development of the algorithm was performed in MATLAB using built-in functions for generalised linear regression. The algorithm was trained to classify oocyte maturity (mature = 1 and immature = 0) and was created using independent training and validation sets. Spectra from GV and IVM oocytes were randomly allocated to either the training (3/5 of oocytes from each group) or validation (2/5 of oocytes from each group) sets. Based upon the results of the t-test and the PCA, three peaks were identified as inputs for the algorithm.

The intensity of these peaks with respect to the phenylalanine stretch at 1003 cm^{-1}, which showed no significant variation between groups, was used to build the model, as described by Equation 6.1.

$$ln\left(\frac{p}{p-1}\right) = \beta_0 + \beta_1\left(\frac{I_{1303}}{I_{1003}}\right) + \beta_2\left(\frac{I_{1447}}{I_{1003}}\right) + \beta_3\left(\frac{I_{1606}}{I_{1003}}\right)$$

Equation 6.1

In Equation 6.1, p represents the probability that a particular oocyte belongs to the mature group (i.e. y = 1). As such, the left hand side of the equation is equivalent to the log odds of the oocyte belonging to the mature group. β_0, β_1, β_2 and β_3 represent the derived coefficients determined for the independent variables, which in this case are the intensity ratios.

Using leave-one-out cross validation methodology combined with sequential forward feature selection, the model coefficients were optimised such that the deviance, as defined by -2 log likelihood ratio, of the model fit was minimised. The predictive ability of the algorithm was then tested using the validation data set. Furthermore, in order to test the robustness of the model, its predictive ability was tested using data obtained from unstimulated and stimulated ovulation cycles.

6.3 Results

Upon examination of the average spectra obtained from the GV and IVM oocytes prior to normalisation, it can be seen that a greater overall intensity is observed for the IVM oocytes, when compared to the GV oocytes, as illustrated in Figure 6.1. This marked difference is not unexpected when considering the samples being investigated; GV oocytes are known to contain fewer proteins, lipids and organelles than their mature counterparts. The significance of this overall difference in intensity during the normalisation process can be seen from Figure 6.1. After normalisation, it appears that GV oocytes contain more protein than *in vitro* matured oocytes. This, however, is known not to be true; instead this is an artefact resulting from the total intensity normalisation procedure. It is essential that the spectra are normalised prior to analysis, to account for fluctuations in laser intensity, especially as these experiments were conducted over an extended period of time. However, these artefacts mean that particular care must be taken when interpreting the results obtained from these analyses, so as to prevent incorrect conclusions regarding macromolecular concentrations. It should be noted however, that the total intensity normalisation procedure preserves intensity ratios, and thus ratios will provide a more robust comparison method.

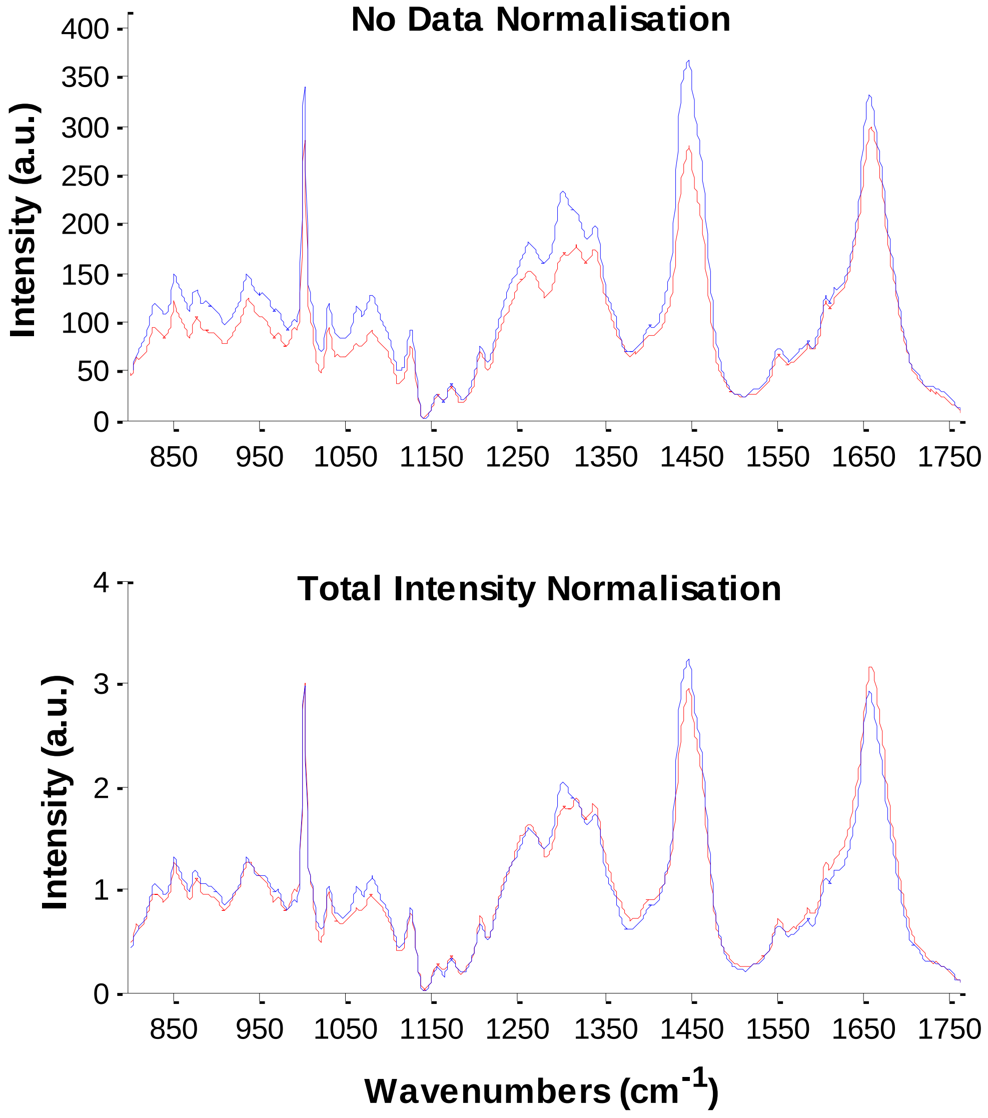

Figure 6.1 – Illustration of the effect of normalisation on the average spectra with significantly different overall intensities. In each plot, the blue and red traces represent the average spectra for the IVM and GV oocyte groups, respectively.

The GV and IVM oocytes examined in this work were collected by selecting follicles, which met strict criteria regarding size and morphology, from the same follicular cohort. The selected follicles were divided into two groups, with one set being cultured to provide IVM oocytes, and the others immediately ruptured to provide GV oocytes. To examine the synchronicity of the oocyte and follicular development, the mean spectra and their associated standard deviations were calculated for the two groups, as depicted by Figure 6.2. Greater spectral variation can be seen within the GV group when compared to the IVM group.

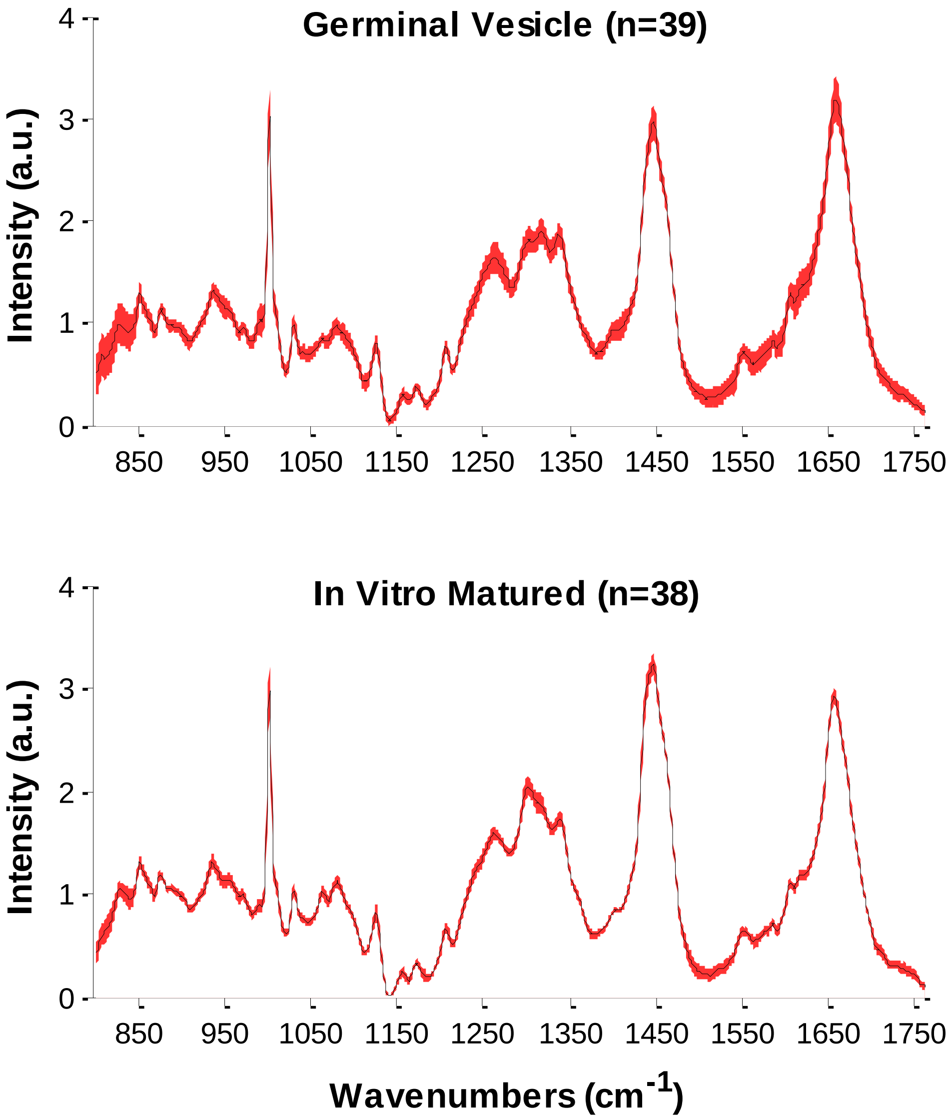

Figure 6.2 – Mean Raman spectrum +/- 1 standard deviation for the GV and IVM groups. In each plot, the black trace depicts the mean spectrum and the red region the standard deviation. Greater spectral variation can be seen within the GV group, as evidenced by the larger standard deviations.

In order to further investigate this variation, and any deviation which exists between the two sample groups, a difference spectrum was calculated. Furthermore, an unpaired two-tailed t-test was performed to identify regions of statistical significance. Figure 6.3 details the results of this comparison. Large variations are observed in the difference spectrum in the region of 1040 - 1090, 1290 - 1310, 1430 - 1490 and 1600 - 1700 cm^{-1}, which correspond to the C-C stretch and CH_2 twist in lipids, the CH_2 deformation and the amide I envelope, respectively. Furthermore, examination of the t-test results shows 18 peak locations to be significantly different between the two groups, as annotated in Figure 6.3. Lower intensities were observed in IVM oocytes at 990, 1207, 1338, 1385, 1551, 1586, 1606, 1620 and 1658 cm^{-1}, which with the exception of 1385 cm^{-1}, all arise due to protein bond vibrations. Conversely, higher intensities were observed in IVM oocytes at 876,890, 896, 972, 1042, 1063, 1080, 1303 and 1447 cm^{-1}, which predominately arise due to lipid bond vibrations.

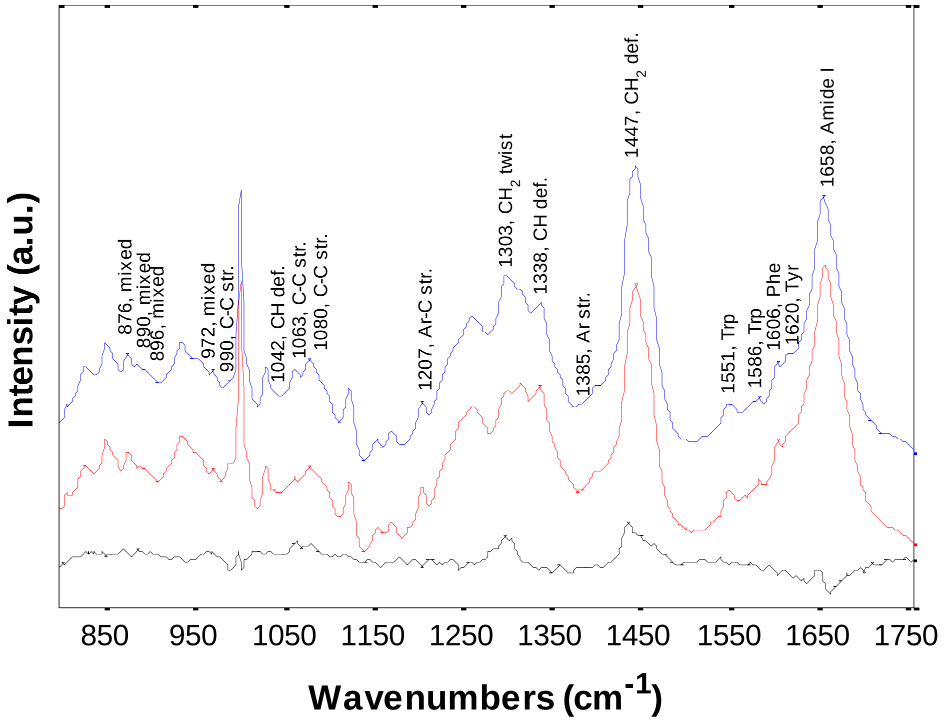

Figure 6.3 – Mean spectra for GV and IVM oocytes and the associated difference spectrum (IVM-GV) depicted by the red, blue and black plots, respectively. Raman bands which were judged to be significantly different (p=0.0001) by an unpaired t-test are annotated.

Multivariate Analysis of Sample Groups

Although the univariate statistics, which have been presented thus far, are useful for gaining an understanding of the variation which exists between the sample groups, they do not provide a true representation of data, such as that collected by Raman spectroscopy. A more effective method for simultaneous analysis of spectroscopic data is multivariate statistical analysis. High dimensionality is one of the major obstacles to statistical analysis of spectroscopic data. So as to avoid the requirement of analysing excessively large numbers of samples, the data is subjected to dimension reduction, by means of PCA. In this work, the PCA was performed on a data matrix which contained the 77 average Raman spectra which had been collected from the two sample groups (n_{GV} = 39, n_{IVM} = 38). The variance in the original data space which is described by each PC is depicted by the scree plot in Figure 6.4. Over 95 % of the variance that existed in the original data is described by the first 10 PCs, although it can be seen that little additional variance is described by each PC after the sixth.

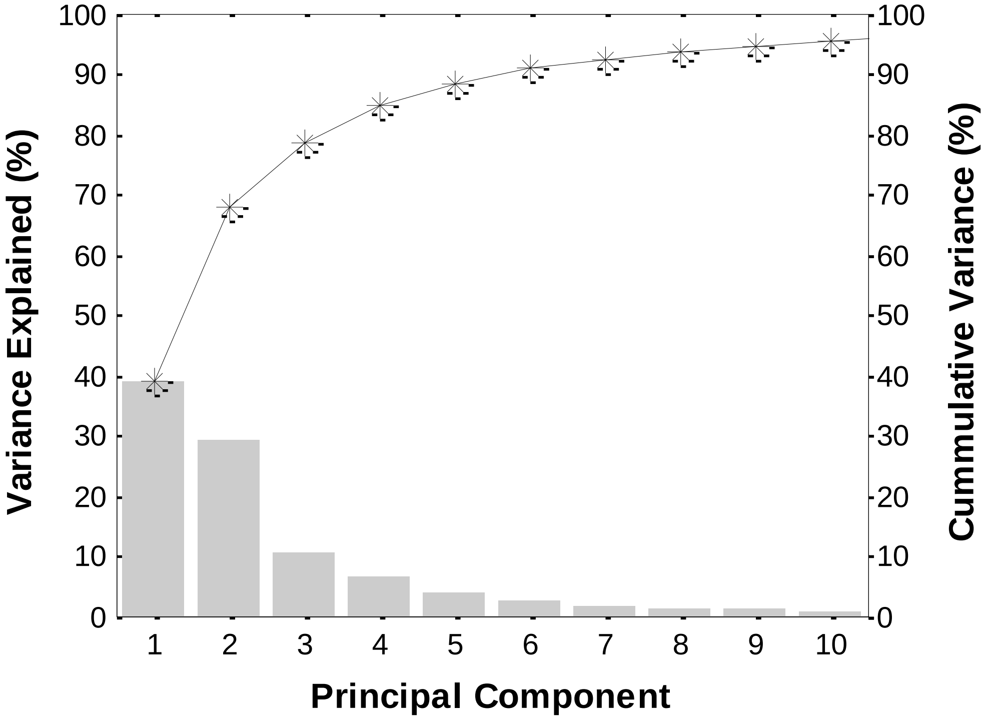

Figure 6.4 – Variance explained by each new variable generated during the principal component analysis of the 77 average spectra collected for the two sample groups.

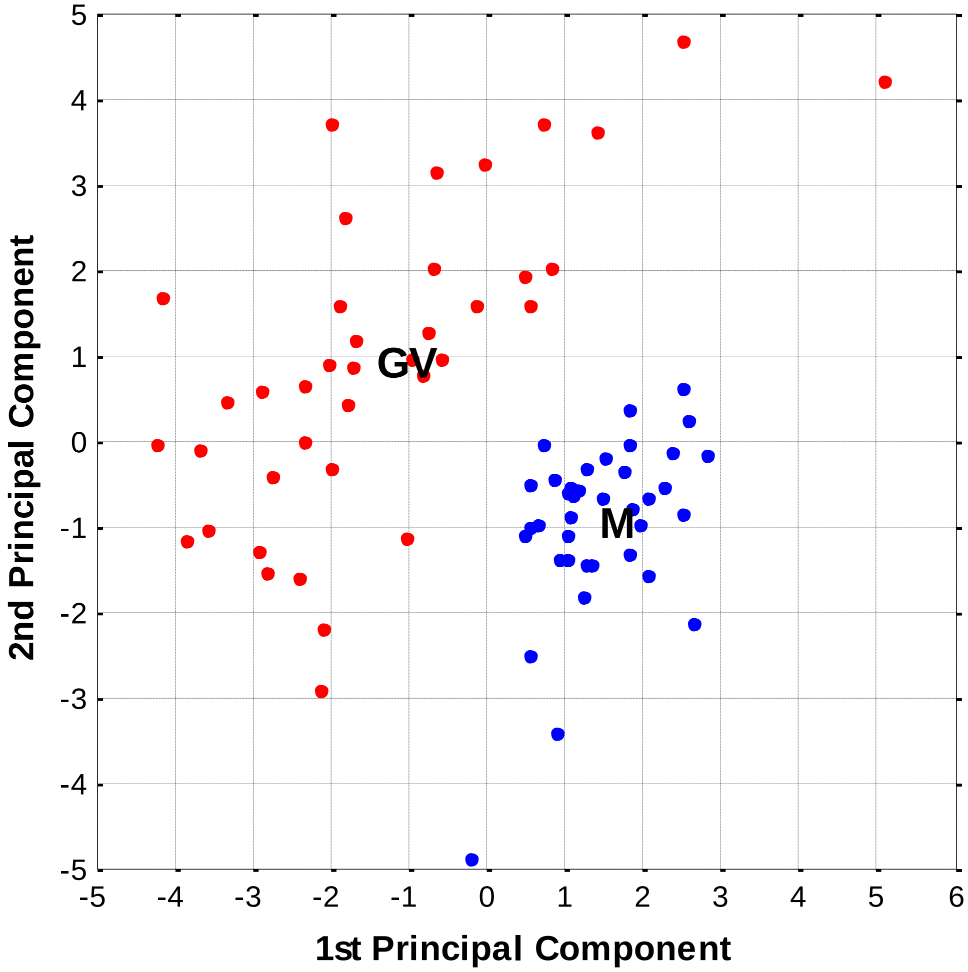

Figure 6.5 – Biplot showing the scores of each datum against the first and second component axes generated during the principal component analysis. The individual GV and IVM oocytes are depicted by the red and blue markers, while their mean scores are denoted by GV and M, respectively.

During PCA, each spectrum is assigned a score for each of the newly generated PCs which describe the contribution which each PC makes to the original spectrum. Figure 6.5 depicts the scores of the first and second PC for each oocyte sampled. It can be seen that there is a clear distinction between the immature and mature oocytes, with separation of the two groups along both the first and second PC. Although a spread of scores along the other significant PCs is observed, there exists no distinction between the groups in these dimensions. The large inter-oocyte variance within the GV group which was observed during the univariate analysis is further confirmed by the comparatively large variance in PC scores when compared to the tightly clustered IVM oocyte group scores. Furthermore, it should be noted that upon examination, no obvious within groups clusters were observed for the different experimental replicates.

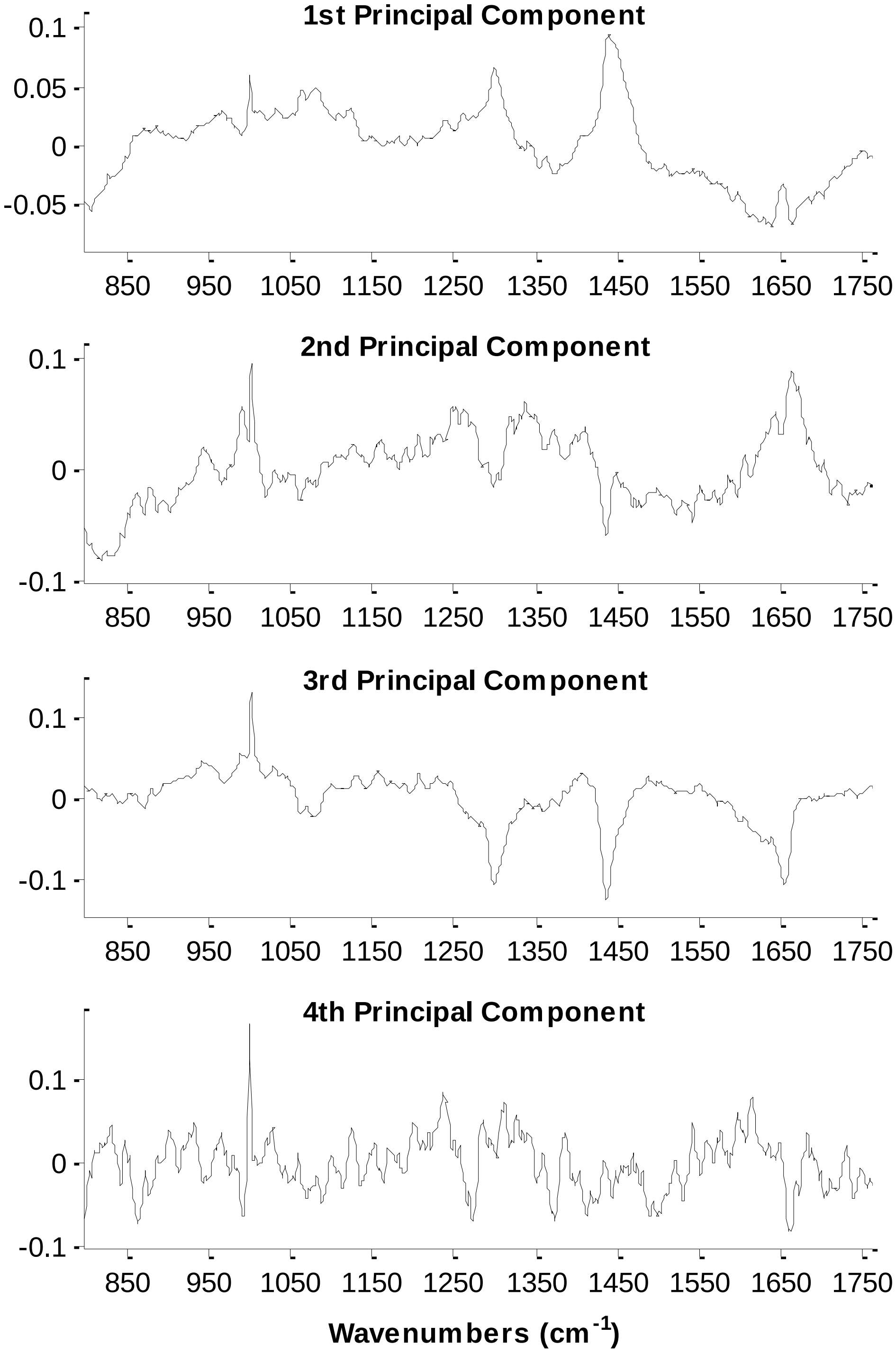

Figure 6.6 – PC loadings for the first four components calculated during PCA.

So as to understand the biochemical variation which separates the two groups, the PC loadings must be examined. As the first four PCs describe the majority of the variation which existed between the samples, the plots of these PCs against the original data space axis are present in Figure 6.6. The first PC is very similar in appearance to the difference spectrum presented in Figure 6.3; positive loadings are observed in the region 1050 - 1140, 1290 - 1310 and 1430 - 1465 cm^{-1} which are regions predominately associated with lipid bond vibrations, whilst negative loadings are observed in the region of protein aromatic residue vibrations and the amide I envelope at 1550 - 1700 cm^{-1}. Conversely, the second PC, which also described separation of the two sample groups, shows positive loadings associated with protein bond vibrations. Specifically, positive contributions are observed in the region of the C-C stretch at 990 cm^{-1}, the amide III band at 1240 - 1280 cm^{-1}, the C-H deformation at 1340 cm^{-1} and the amide I envelope at 1600 - 1670 cm^{-1}. The third and fourth PCs did not describe any separation of the two sample groups, but instead described inter-oocyte biochemical variance.

Although from the results of the PCA it appears that the majority of the variance which is present in the dataset exists as a result of the biochemical variation between immature and mature oocytes, the variance described by PCs 3 - 6 is non-trivial. As such, it is sensible to combine these data to examine if the groups can still be well separated using CVA. This analysis revealed that the group means could be successfully separated in one dimension by a single canonical variate, CV_1, as defined by Equation 6.2, where PC_1, PC_2, PC_3, PC_4, PC_5 and PC_6 are the corresponding PC scores for a given oocyte.

$$CV_1 = 1.04PC_1 - 0.92PC_2 - 0.71PC_3 + 0.40PC_4 + 0.2PC_5 + 0.54PC_6$$

Equation 6.2

Equation 6.2 confirms the results obtained from the PCA, such that the first and second PCs contribute most to the differentiation of the two groups. It is worth noting that analysis

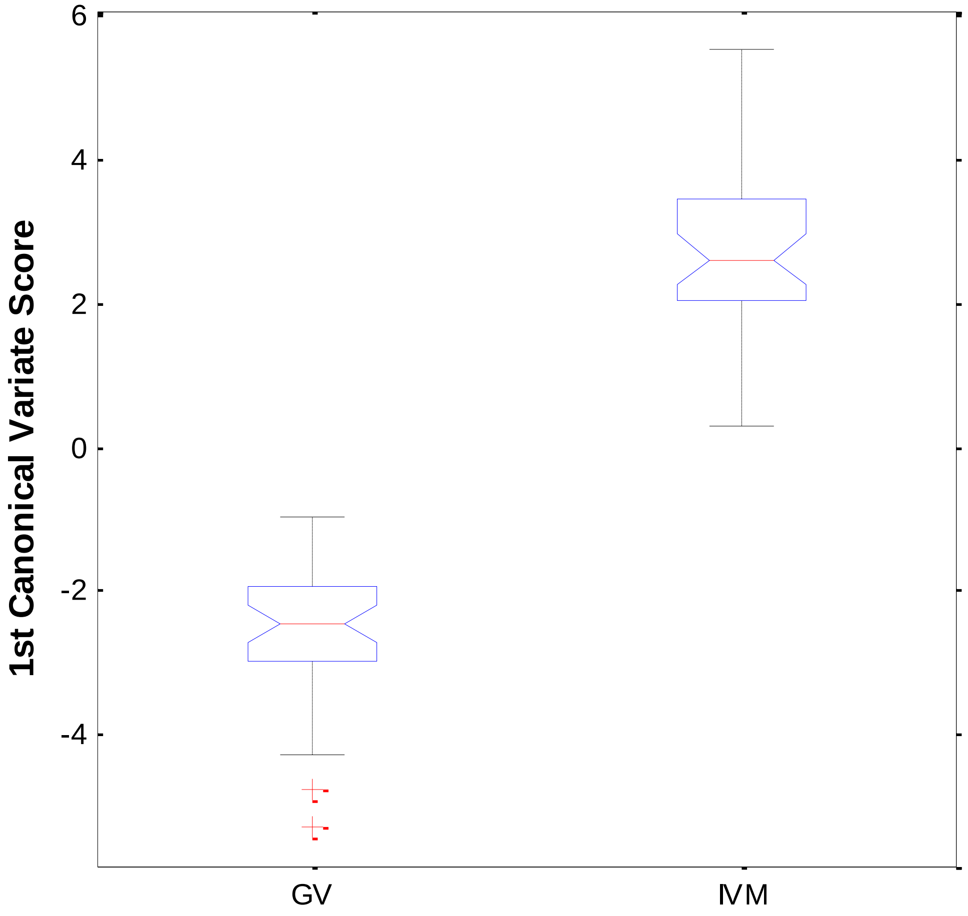

Figure 6.7 – Boxplot showing 1^{st} canonical variate scores for the two sample groups. For each group, the red line indicates the median and the box displays the line of the first and third quartiles. The black whiskers extend 1.5 times the inter-quartile rand in both directions. Data outwith this range is considered to be an outlier and is annotated with a red cross.

showed that increasing the number of PCs did not further improve the results of the CVA. Figure 6.7 depicts a boxplot generated using the results of the CVA. It can be seen that there exists a clear distinction of the two groups with no overlap evident.

Algorithm Development and Testing

Although the multivariate statistical analysis presented in the previous section illustrates the significant biochemical variation which exists between the sample groups, its use in the classification of additional samples is limited by its methodology. An alternative approach, given the marked spectral differences observed between the immature and mature oocyte, would be to develop a classification algorithm based upon specific spectral intensities which could be easily extracted from new samples.

The intensities of the peaks located at 1303, 1447 and 1606 cm^{-1} were selected as model inputs. These peaks were identified as being significantly different by the two-tailed t-test and demonstrated significant loadings in both PC1 and PC2 which had successfully separated the two oocyte groups. As no significant difference was observed in the phenylalanine peak at 1003 cm^{-1}, it was selected for standardising the selected intensities. Optimisation of the model was performed using leave-one-out cross validation sequential feature selection methodology. This process found the intensity ratio of 1447 cm^{-1} redundant, which led to the final model as described by Equation 6.3.

$$ln\left(\frac{p}{1-p}\right) = -14.12 + 47.27\frac{I_{1303}}{I_{1003}} - 43.25\frac{I_{1606}}{I_{1003}}$$

Equation 6.3

Using the model defined above, a blinded analysis of the model's predictive ability was performed using the independent validation set which consisted of 2/5 of the original data. Furthermore, the capability of the model in predicting oocyte maturity irrespective of the method of maturation was also tested using oocytes collected after unstimulated and stimulated ovulation cycles. The scores which were calculated by the model for each of the oocytes are depicted in Figure 6.8. These data show that only 1 of 15 GV oocytes were misclassified as being mature, whilst only 1 of 15 IVM oocytes were misclassified as being immature, equating to a sensitivity of 93.3 % and specificity of 93.3 %. Significantly, although the model was not constructed using oocytes which had been matured *in vivo*, the classification of ovulated oocytes was successful. Only 2 of 38 oocytes collected after unstimulated ovulation and 6 of 59 collected after stimulated ovulation were misclassified, which only results in a minor reduction in sensitivity to 92.0 %.

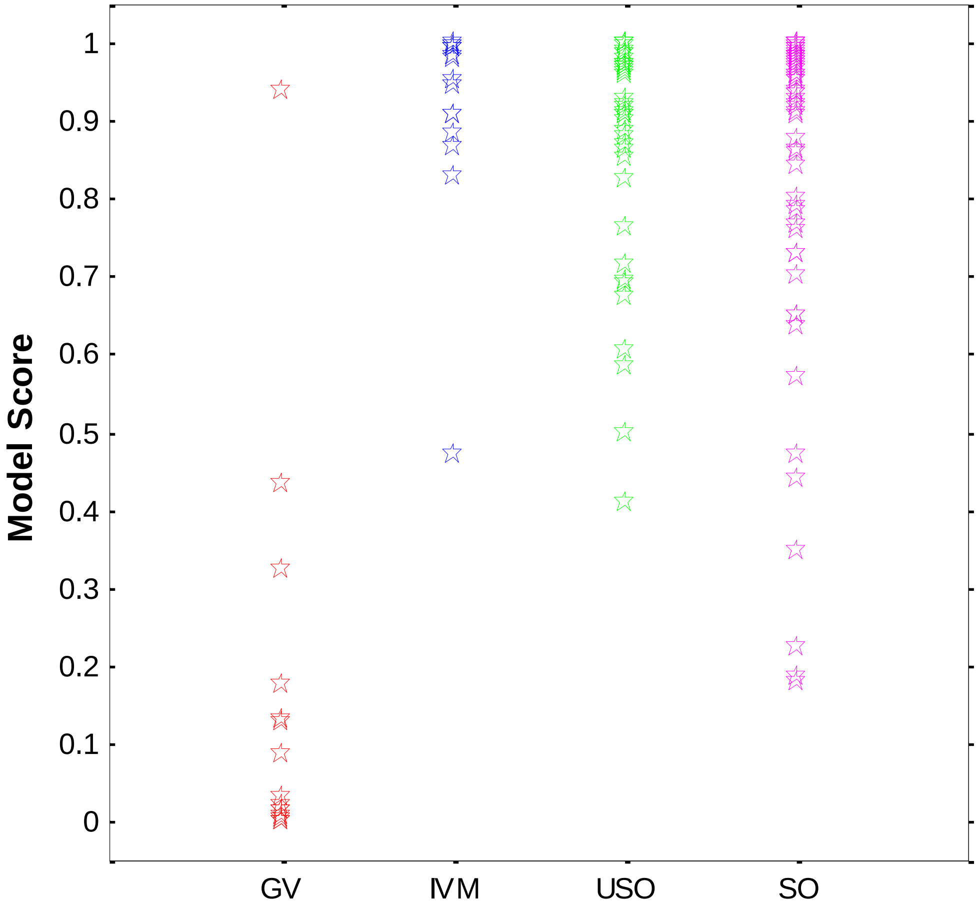

Figure 6.8 – Scatter plot depicting the results of the logistic regression for validation group. The red, blue, green and magenta markers denote GV (n=15), IVM (n=15), unstimulated (n=38) and superovulated (n=59) oocytes, respectively.

6.4 Discussion

As it is intended that this work could be transferred to the analysis of unfixed samples, the use of the reduced mapping methodology was employed, so as to minimise integration times and laser exposure. It is, however, recognised that the 1 hour integration times used in this work are still too lengthy for the real-time assessment of oocyte maturity. However, some simple instrumental modifications would enable the reduction of analysis times. In particular, the use of Raman imaging, as will be discussed shortly, could potentially reduce acquisition times to several minutes per oocyte. Such alterations would certainly facilitate real-time assessment.

In the field of ARTs, the assessment of oocyte maturity has attracted much attention, yet many of the techniques currently available lack the independent quantification required to significantly improve the efficiency of these treatments. That being said, significant progress has been made in the assessment of nuclear maturation through the development of techniques such as birefringence imaging of the meiotic spindle. This methodology has been reported to quantify developmental competence based upon the retardance of polarised light by the highly-structured spindle[69, 70, 72]. However, there have been conflicting results reported using this technique[258], which are indicative of the presence of factors other than meiotic maturity affecting subsequent developmental competence. In particular, cytoplasmic maturity has been identified as being pivotal to not only successful nuclear maturation, but also developmental competence. Currently, there is no quantitative method for assessing the extent of cytoplasmic maturation in the oocyte. As such, the focus of the work presented in this chapter has been to investigate the biochemical changes which occur during the period of cytoplasmic reorganisation and maturation using Raman spectroscopy, with a view to the development of a quantitative measure of oocyte maturation.

It is recognised that GV oocytes are readily identifiable by the presence of the centrally located germinal vesicle, and therefore, a quantitative technique is not required for their discrimination from mature oocytes. However, their selection for this work was intended to provide an opportunity to investigate the ooplasmic alterations which occur during the late oocyte growth phase and cytoplasmic maturation, and to identify the potential of Raman spectroscopy for monitoring this process. In order to benefit oocyte assessment in a clinical setting, further insight into the final modifications which take place during ooplasmic maturation would be required. It is suggested that the analysis of oocytes recovered from cultured pre-antral follicles prior to COC maturation would provide a good model for this future work.

Comparison of the mean spectra derived from the GV and IVM oocytes prior to normalisation show a marked difference in overall spectral intensity. This result demonstrates the sensitivity of Raman spectroscopy to the changing concentrations of macromolecules. During the latter stages of oocyte growth, which continues until the early antral follicle stage, there is an increase in protein synthesis, and accumulation of cytoplasmic inclusions and an increase in organelle copy number[17, 30], with further modifications taking place during cytoplasmic maturation. Consequently, it is unsurprising that the Raman spectroscopic profile of the mature oocyte indicates the presence of a larger number of bond vibrations across the entire spectral range.

The intensity difference presents an issue in the analysis of biochemical variation between the two oocyte groups. Specific spectral markers are of interest in this work, because non-normalised intensity fluctuations are not a robust method for diagnostic classification, as a number of experimental factors, including laser fluctuations, can affect absolute spectral intensity. As a result, the spectra in this work were subjected to spectral area normalisation. This methodology is, however, not ideal as the spectral interpretation must account for the variation in denominator; although it should be noted that this method of normalisation preserves the spectral ratios which existed in the original data. It is proposed that the use of an external intensity calibration source would provide an alternate normalisation routine, enabling correction for experimental factors but retaining the original spectral intensity differences.

It is apparent from the analysis of the standard deviation of the normalised spectra and the results of the PCA that much greater spectral variation exists in the GV oocytes when compared to the mature oocytes. The source of the oocytes from each group should be considered when interpreting this observation. Late pre-antral follicles, approximately 180µm in diameter which showed good morphology and contained a centrally located oocyte were the originating source of oocytes in both cases. However, unlike the IVM group which underwent 6 days of culture, during which some follicles became atretic and were discarded, the GV group were collected immediately from follicles which were at the same stage as those used for culture. These observations coupled with the fact that many pre-antral follicles are lost to atresia indicate that the method used for the selection of GV oocytes may not preclude follicles, and therefore oocytes, which have intrinsic abnormalities. Furthermore, late pre-antral follicles contain oocytes which are still undergoing growth, and as such are subject to significant biochemical change and cytoplasmic reorganisation, a process which is known to be non-linearly related to follicle diameter[259].

Analysis of the difference spectrum obtained for the GV and IVM normalised group means indicate that there are several spectral regions which distinguish these samples, many of which are specific to lipid molecular vibrations. These findings were further confirmed by the results of the t-test and PCA, whereby GV oocytes were found to have significantly lower contributions arising from lipid vibrations when compared with IVM oocytes. These data are concomitant with the processes known to be involved in the latter stages of oocyte growth, and subsequently, cytoplasmic maturation. One of the important aspects of oocyte growth is the increase in cytoplasmic organelles, and in particular the increase in mitochondria. It is possible that these double-membrane bound organelles contribute the increase lipid bond vibrations. However, more likely are contributions arising from the lipid droplets that accumulate throughout ooplasmic maturation[260, 261] and which are thought to be energy reserves for subsequent embryonic development and membrane production[33]. Depending upon the source of the marked increase in lipid contributions, the transfer of this methodology for quantification of maturity in human oocytes may prove problematic, as the lipid droplet content of human oocytes is lower than that of murine oocytes[262].

The significant biochemical variation which exists between the two groups made these samples ideal candidates for the construction of a classification algorithm based upon specific spectral markers for the discrimination of immature and mature oocytes. Logistic regression was selected in preference to ordinary linear regression as it is more suited to modelling binary outcomes, such that the outcomes can only take one of two values; in this work, the two outcomes were chosen to be mature and immature. However, that being said, logistic regression is most often applied in the field of biomedical research where the predictor variables represent the measurement of entirely independent characteristics, which is not true of the intensity ratios applied in this study.

Two issues had to be overcome in the construction of the classification algorithm: multicollinearity of independent variables and complete separation of data. It was found that there was a high degree of correlation, or multicollinearity, between many of Raman shifts which were identified by the t-test. As such, including all of these intensities in the model was not possible. Doing so would have resulted in poor estimates of the model coefficients[263]. Consequently, the intensities which were included in the model were selected by analysing the correlation matrix for the independent and dependant variables. However, selection of independent variables for the model had to be further refined in order to overcome the problem of complete separation. Logistic regressions are computed by maximising the log-likelihood function of the model. Complete separation occurs where a given vector, or set of model coefficients, can correctly classify all the samples, which in turn leads to a non-finite solution to log-likelihood function[264] and inflated coefficient standard errors. This is an issue which often occurs in the construction of logistic regression models using small to medium sized data sets.

Further logistic regression was performed using the integrated spectral areas of the statistically significantly regions in an effort to overcome the problem of multicollinearity.

However, problems of complete separation were still encountered, and work was focused on the original model. Increasing the sample size for future work is likely to overcome the problem of complete separation and provide the opportunity to extend the model to include further independent variables. Furthermore, statisticians have proposed the use of ridge regression or penalised likelihood estimators to help overcome the issue of multicollinearity, although there is no firm solution[232].

The final model demonstrated good performance in the classification of GV and IVM oocytes leading to a sensitivity of 93.3 % and specificity of 93.3 %. Moreover, it performed well on the classification of mature oocytes obtained using different protocols. It is noteworthy that the highest number of misclassifications occurred for the superovulated oocyte group. This is unsurprising, as it is probable that some follicles were recruited prematurely in response to the exogenous hormonal stimulation. Although very high sensitivities and specificities were obtained for these samples, it is anticipated that the discrimination of oocytes collected shortly before ovulation would be less distinct when compared to the mature oocytes. Consequently, it is likely that a larger number of independent variables would be required for the construction of a classification algorithm and problems of complete separation are less likely.

The development of the regression model identified two spectral intensities for the discrimination of immature and mature oocytes. As one of the main goals of this work is to create a diagnostic method which would enable the rapid real-time quantification of oocyte maturity, the Raman protocol would require modification. One possible solution for reducing acquisition times would be to implement Raman imaging as opposed to Raman micro-spectroscopy. Raman imaging is analogous to fluorescence imaging in the sense that selected Raman bands are interrogated using a combination of an expanded laser beam and bandpass filters. Using this technique would enable the analysis of the entire oocyte as opposed to selected locations, and thus vastly reduce analysis times.

6.5 Conclusions

The work presented here demonstrates that immature and mature oocytes have distinct cytoplasmic spectral profiles. Furthermore, the results show that a logistic regression model constructed using Raman intensity ratios can be used to successfully classify oocyte maturity. Further studies which include oocytes collected prior to the final stages of maturation are required in order to extend the algorithm to a multinomial model for classification of GV, MI and MII oocytes. The development of a Raman imaging protocol would also benefit future work by enabling live-cell analysis.

Chapter 7

A Raman Spectroscopic Analysis of the Biochemistry of Oocyte Maturation and Quality

A quantitative technique is required for the effective development and testing of new ART methodologies in the lab. As such, this study presents for the first time the use of Raman spectroscopy for the direct analysis of oocytes matured and ovulated using different protocols. Furthermore, the potential of Raman spectroscopy of the assessment of oocyte quality will be presented.

7.1 Introduction

In recent years there has been an exponential growth in the application of ARTs in the field of fertility treatment. New technologies are constantly being developed so as to overcome the obstacles faced by both female and male infertility. However, the lack of quantitative methodologies which enable the assessment of the developmental implications of these new techniques remains an issue.

Raman spectroscopy enables the analysis of both fixed and unfixed biological samples and is capable of acquiring information regarding the biochemical constituents of a sample without labelling. As such, this technique is capable of providing biochemical information which is complementary to that obtained using fluorescence microscopy. However, Raman is also capable of providing information for diagnostic algorithms, as evidenced by previous work in cancer identification[181, 182, 189, 190], and more relevantly, pregnancy outcome[102, 103]. Although not designed to provide information about the presence of specific macromolecules, Raman can provide an overview of the presence of functional groups which can then be interpreted. This technique is particularly powerful when used in combination with multivariate statistical methods.

In this work, Raman spectroscopy was used for the first time to investigate the biochemistry which underpins the *in vitro* maturation and superovulation of oocytes, enabling a comparison to be made with oocytes collected after unstimulated ovulation. Although instrumental limitations precluded live cell analysis in this study, similar protocols could be performed on unfixed samples. Furthermore, the first report of direct quality assessment using Raman spectroscopy is discussed.

7.2 Materials and Methods

A total of 13,635 Raman spectra were acquired from 135 oocytes for this study. These spectra were used in two distinct examinations of the biochemistry of oocyte maturation and quality. The first study was concerned with the examination of the extent to which external factors affect the biochemistry of maturation mechanisms and the ability of Raman spectroscopy to detect these differences. In this study, a total of 135 oocytes, from three treatment groups, were examined. The treatments investigated were superovulation (**SO**: n=59, 4 replicates) and *in vitro* maturation (**IVM**: n=38, 4 replicates); the third treatment group, unstimulated ovulation (**USO**: n=38, 4 replicates), was used as the control group. Subsequently, the superovulation group (n=59, 4 replicates) was used for the second study. This was designed to investigate whether Raman spectroscopy could be used to identify oocyte quality based upon direct analysis of oocyte biochemistry.

7.2.1 Sample Selection and Preparation

Mice were superovulated by administering PMSG, followed 47 hours later by hCG, with superovulated oocytes being collected 18 hours after hCG injection. The IVM group were obtained from pre-antral follicles which had been cultured for 6 days before the final 24 hours COC maturation period. The control group consisted of USO oocytes collected from mice in oestrous, as judged by vaginal examination. All oocytes were washed thrice in PBS before being fixed for 30 minutes in 4 % paraformaldehyde solution. After fixing, oocytes were washed thrice in PBS and were stored at 4 °C until Raman analysis.

7.2.2 Raman Spectroscopy Measurements

Measurements were taken from each oocyte using the reduced map acquisition protocol outlined in the Chapter 3. Briefly, 101 individual spectra were collected at a constant interval of 6 μm through the central focal plane of the oocyte. Each spectrum was integrated for 37 s over the spectral range 450 - 1790 cm^{-1} using a laser power of 35 mW. A spectrum of the PBS buffer which surrounded the oocyte was also acquired using the same experimental conditions. Spectra of a polystyrene standard and a neon light source were also taken in order to calibrate the wavenumber scale. Prior to Raman measurement, a white light microscopy image was acquired for each oocyte, which was subsequently used for morphological assessment.

7.2.3 Data Preprocessing and Extraction

The 101 spectra which were collected for each oocyte were treated as a group and subjected to a preprocessing routine, which is described in more detail in Chapter 3. Firstly, the data underwent cosmic ray removal and the wavelength scale was calibrated using the neon and polystyrene spectra. Subsequently, the oocyte spectra and PBS spectrum were smoothed using a 3-point and 11-point boxcar function, respectively. To remove the tails which result from this type of smoothing, the data was truncated to the region 455 - 1780 cm^{-1}. However, prior to this, the data was resampled so that the spectral sampling interval was set at 1 cm^{-1}. The spectral contribution of the PBS was then subtracted using the first derivative orthogonal vector method suggested by Maquelin *et al.*[230]. Following the correction for PBS contributions, the spectra were returned to their integrated form. The remaining fluorescence background was subtracted by fitting a fourth order polynomial through the points at 456, 478, 632, 800, 1142, 1512 and 1756 cm^{-1}. Next, an average spectrum was generated by taking the arithmetic mean of the 101 processed spectra. The spectra were truncated to the region 800 - 1760 cm^{-1} for the data analysis. Following this, each spectrum was offset corrected, such that the minimum intensity was set to zero. Finally, each spectrum was normalised to its mean spectral intensity across all wavenumbers in order to account for fluctuations in laser intensity. All data preprocessing was performed using MATLAB and in-house written scripts.

7.2.4 Data Analysis and Statistics

For the first study, the processed average spectra were grouped according to their treatment. The mean spectrum, and its standard deviation, was then calculated for each treatment group. Using a two-tailed unpaired t-test (α=0.05), the IVM and SO groups were both compared to the USO control group in order to locate spectral regions which are significantly different. Subsequently PCA and CVA were performed on the entire data set, consisting of all mean spectra from the three treatment groups.

For the second study, the processed average spectra were grouped according to their quality, as assessed by morphological appearance. Cytoplasmic granularity and the size of the perivitelline space were the criteria chosen for oocyte grading. Table 7.1 details the morphological features that define each grade.

Grade	Morphological Appearance
1	No cytoplasmic granularity and small perivitelline space
2	Presence of cytoplasm granularity
3	Large perivitelline space
4	Presence of cytoplasmic granularity and large perivitelline space
5	Fragmented oocyte

Table 7.1 – Description of morphological features used to grade oocytes.

Initially, grades 2 - 5 were combined to create a group classed as poor quality. Using a two-tailed unpaired t-test (α = 0.05), the grade 1 oocytes were compared to the poor quality oocytes. PCA and CVA were performed on the entire data set, consisting of all mean spectra from the five grades. Finally, all ratio combinations of the peaks which were judged to be significant from the t-test were calculated for each oocyte.

7.3 Results

7.3.1 Maturation Method

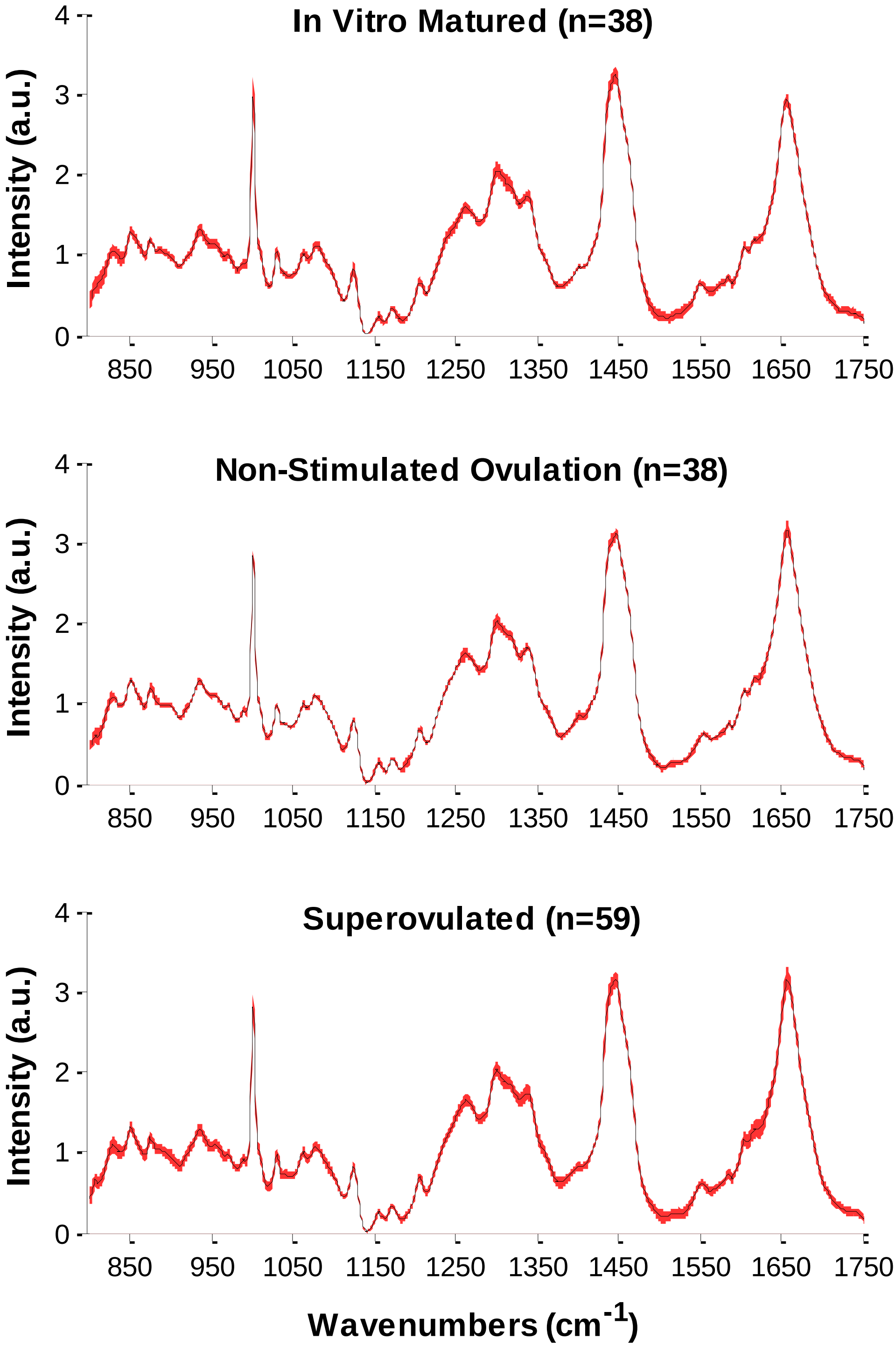

Figure 7.1 – Mean Raman spectrum +/- 1 standard deviation for each maturation group.

The first study was concerned with the biochemical variation which results from the method of selection and maturation of the ovarian follicle and resulting oocyte. As such, the mean and associated standard deviation was calculated for each of the three treatment groups; oocytes matured *in vitro* and those collected after unstimulated and stimulated ovulation. It was observed that, unlike in Chapter 6, there was no significant difference in the total integrated spectral intensity between groups. Consequently, the mean spectra of each of the treatment groups can be compared without consideration of artefacts introduced during the normalisation procedure. Figure 7.1 displays the arithmetic mean ± one standard deviation, signified by the red region, at each wavenumber for each treatment group; initial examination reveals that there is very little spectral variation between the three groups. However, upon closer inspection, it can be seen that larger standard deviations exist for the *in vitro* matured and superovulated groups when compared to the unstimulated control group, demonstrating a greater inter-oocyte variation within these groups.

Univariate Comparison of Treatment Group Means

In order to investigate further this variation and any deviations which exist between the sample groups, spectral differences were calculated for the two treatment groups relative to the control group. Furthermore, unpaired two-tailed t-tests were performed to identify regions of statistical significance. Figure 7.2 details the results of the comparison between the IVM and unstimulated ovulation groups. Only subtle differences are apparent in the difference spectrum, which is depicted by the black plot, although intensity variations are present in the region of the 1002 cm^{-1} phenylalanine band, amide III, amide I and C-H deformation. Upon examination of the results of the t-test, it can be seen that 14 peak locations show a statistically significant difference between the two groups. Many of the variations which tested as being statistically significant, as annotated on Figure 7.2, are Raman shifts corresponding to vibrations in protein molecules. However, some are in

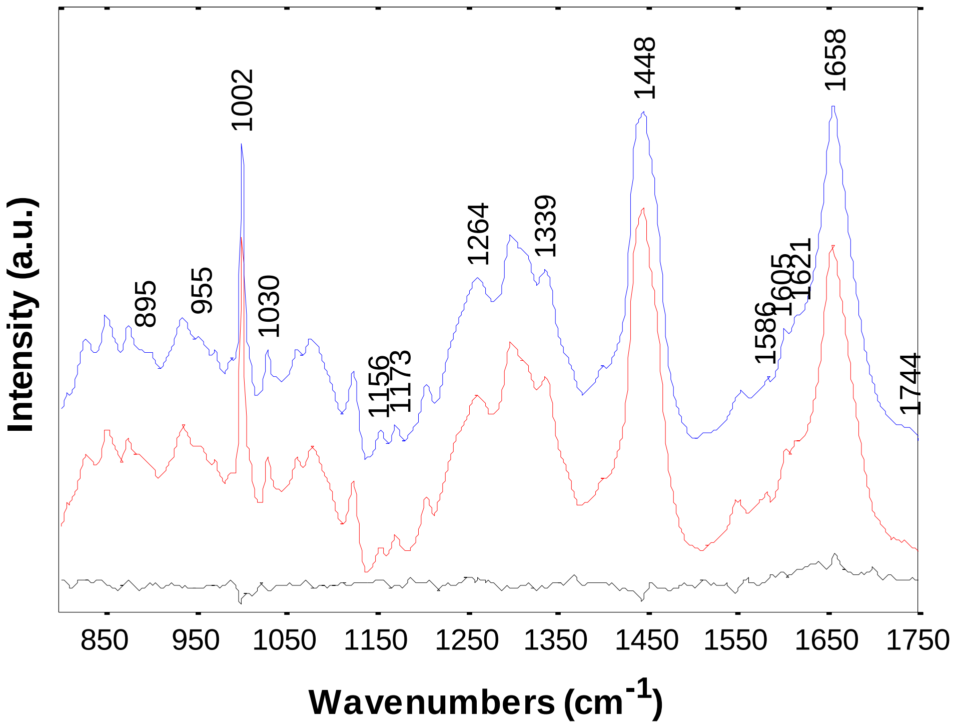

Figure 7.2 – Mean spectra for IVM and unstimulated ovulated oocytes and the associated difference spectrum (unstimulated – IVM) depicted by the red, blue and black plots, respectively. Raman bands which were judged to be significantly different (p=0.005) by an unpaired t-test are annotated.

regions of overlapping bands, whilst the peak at 955 cm^{-1} results from the phosphodiester linkage present in nucleic acids and lipids and the peak at 1744 cm^{-1} represents the C=O ester vibration present in lipids.

Direct comparison of the oocytes collected after super- and unstimulated ovulation shows very little variation between the two group means, as illustrated by the difference spectrum which is depicted as the black plot in Figure 7.3. This observation is confirmed when the results of the t-test are examined. Only 5 peak locations are judged to be significantly different, as opposed to 14 in the comparison between the IVM and unstimulated oocyte groups. Differences associated with aromatic acid residues and the C-H deformation in proteins are seen at 1040, 1173 and 1339 cm^{-1}, whilst variations arising from the C-H rocking and C=O ester linkage in lipids are seen at 891 and 1744 cm^{-1}.

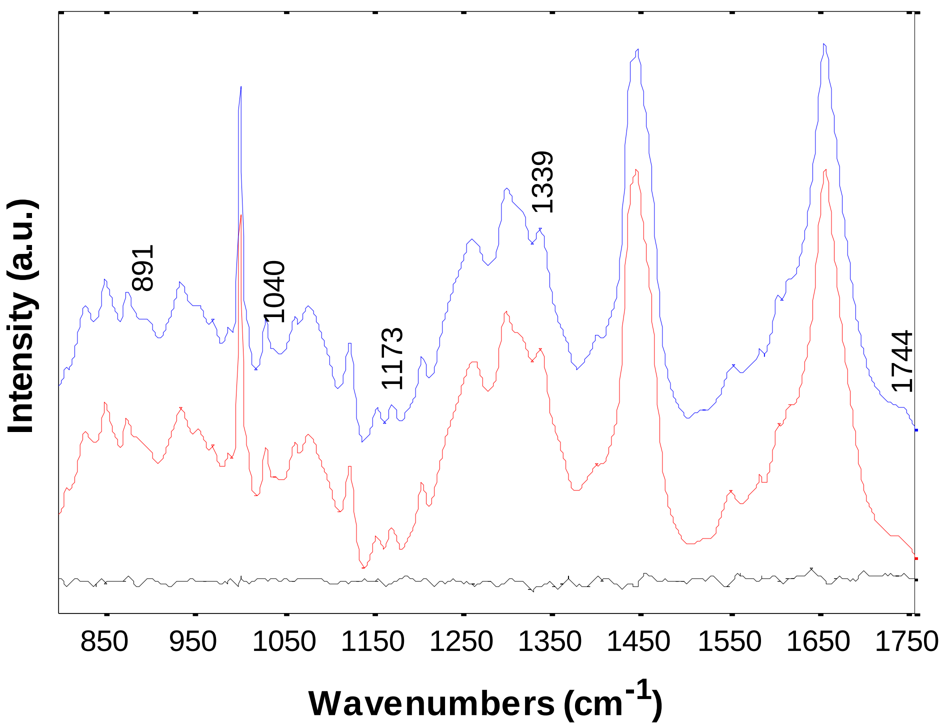

Figure 7.3 – Mean spectra for super- and unstimulated ovulated oocytes and the associated difference spectrum (unstimulated – superovulated) depicted by the red, blue and black plots, respectively. Bands which were judged to be significantly different (p=0.005) by an unpaired t-test are annotated.

Multivariate Analysis of Treatment Groups

Whilst univariate statistical analysis, such as that presented in the previous section, is useful for gaining an insight into the relationship between treatment groups, it does not provide a true representation of data such as that collected by Raman spectroscopy. As with most statistical methods, the t-test used in the previous section has constraints which must be met in order to benefit from the true power of the test. One of these constraints is that the independent variables measured should be mutually exclusive. This does not hold for any type of spectrum, as all intensities are a function of their neighbouring intensities. However, so that this test could be used for this work, an additional constraint was imposed such that only local maxima were included in the test. Conversely, multivariate analysis enables the spectral data to be assessed in an unbiased simultaneous fashion.

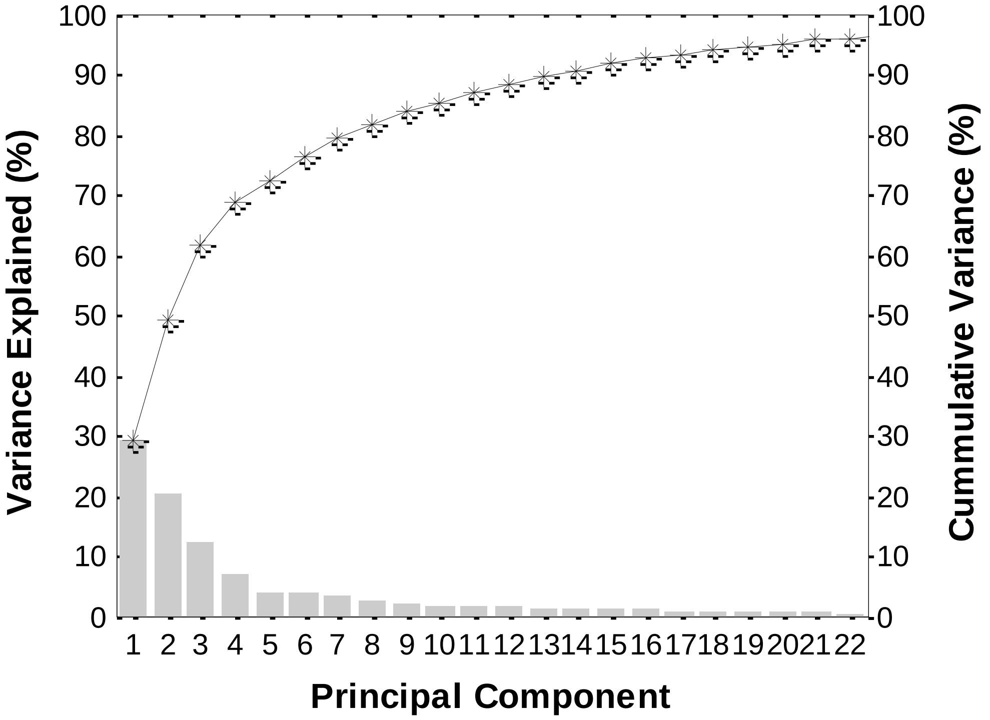

Figure 7.4 – Variance explained by each new variable generated during the principal component analysis of the 135 average spectra collected for the three maturation categories.

Firstly, PCA was performed on a data matrix which contained the 135 average Raman spectra that had been collected from the three treatment groups (n_{IVM}=38, n_{NSO}=38, n_{SO}=59). The scree plot (Figure 7.4) depicts the variance in the original data space which is described by each of the newly generated PCs; over 95 % of the variance that existed in the 961 original variables is described by the first 22 PCs. However, the plot begins to plateau after the fourteenth PC, which indicates that the PCs beyond this contribute little more to the description of the original variance. Indeed, after the fourteenth PC, each PC describes less variance than was contained within a single original variable.

The scatter plot shown in Figure 7.5 depicts the scores of the first and fourth PC for each oocyte sampled from the IVM, USO and SO groups. The scatter plot shows a distinction between the IVM and unstimulated group along the first PC. Furthermore, a marked separation exist between the IVM group and the other groups along the forth PC. Although a

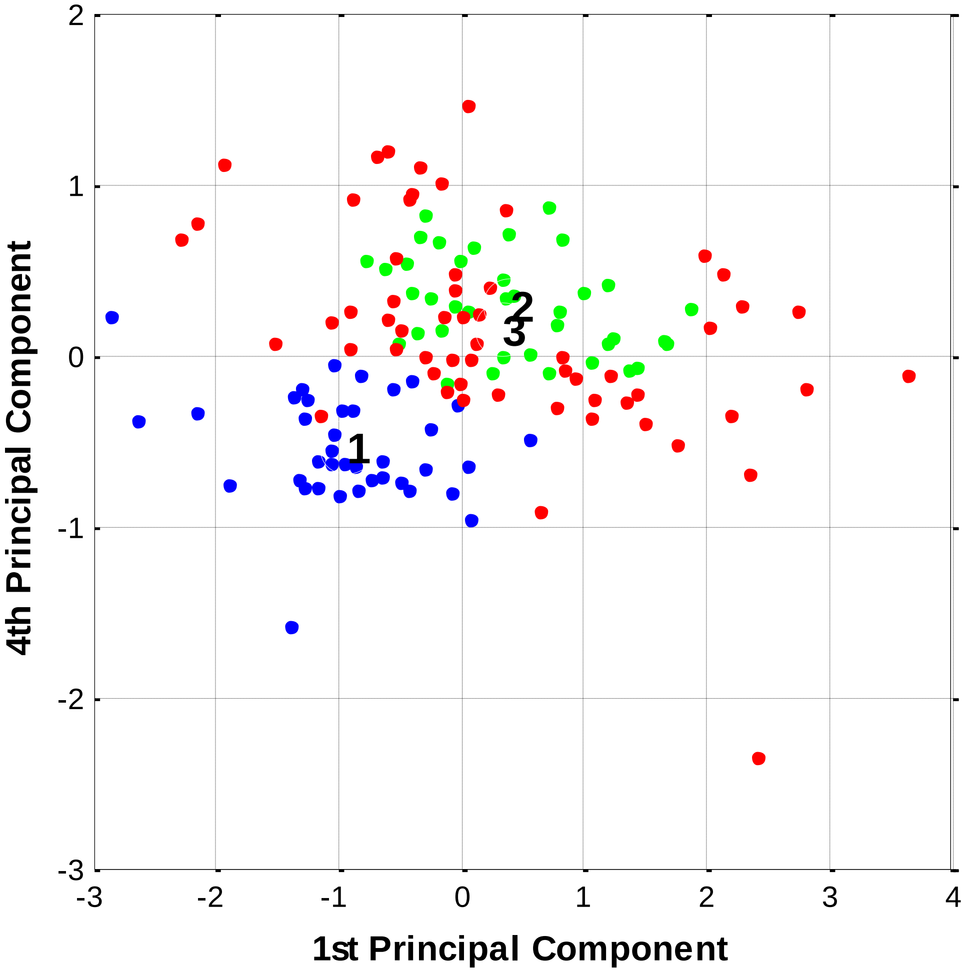

Figure 7.5 – Biplot showing the scores of each datum against the first and fourth component axes generated during the principal component analysis. The IVM, unstimulated and superovulated oocytes are depicted by the blue, green and red markers, respectively. The mean score for the IVM, unstimulated and superovulated groups are denoted by 1,2 and 3, respectively.

spread of scores along the other significant PCs is observed, there exists no distinction between the groups in these dimensions. The group means for the unstimulated and superovulated groups are very close to one another, whilst the IVM group mean appears distinct. Furthermore, the variance of the scores for the superovulated group is greater than that of the unstimulated or IVM groups, as demonstrated by the tight clustering of the latter groups. Although the means of the unstimulated and superovulated groups are close and distinct from the IVM group, Figure 7.5 shows that the scores of the superovulated group overlap with both the unstimulated and IVM groups. It should be noted that upon examination no within group clusters were observed for the different experimental replicates.

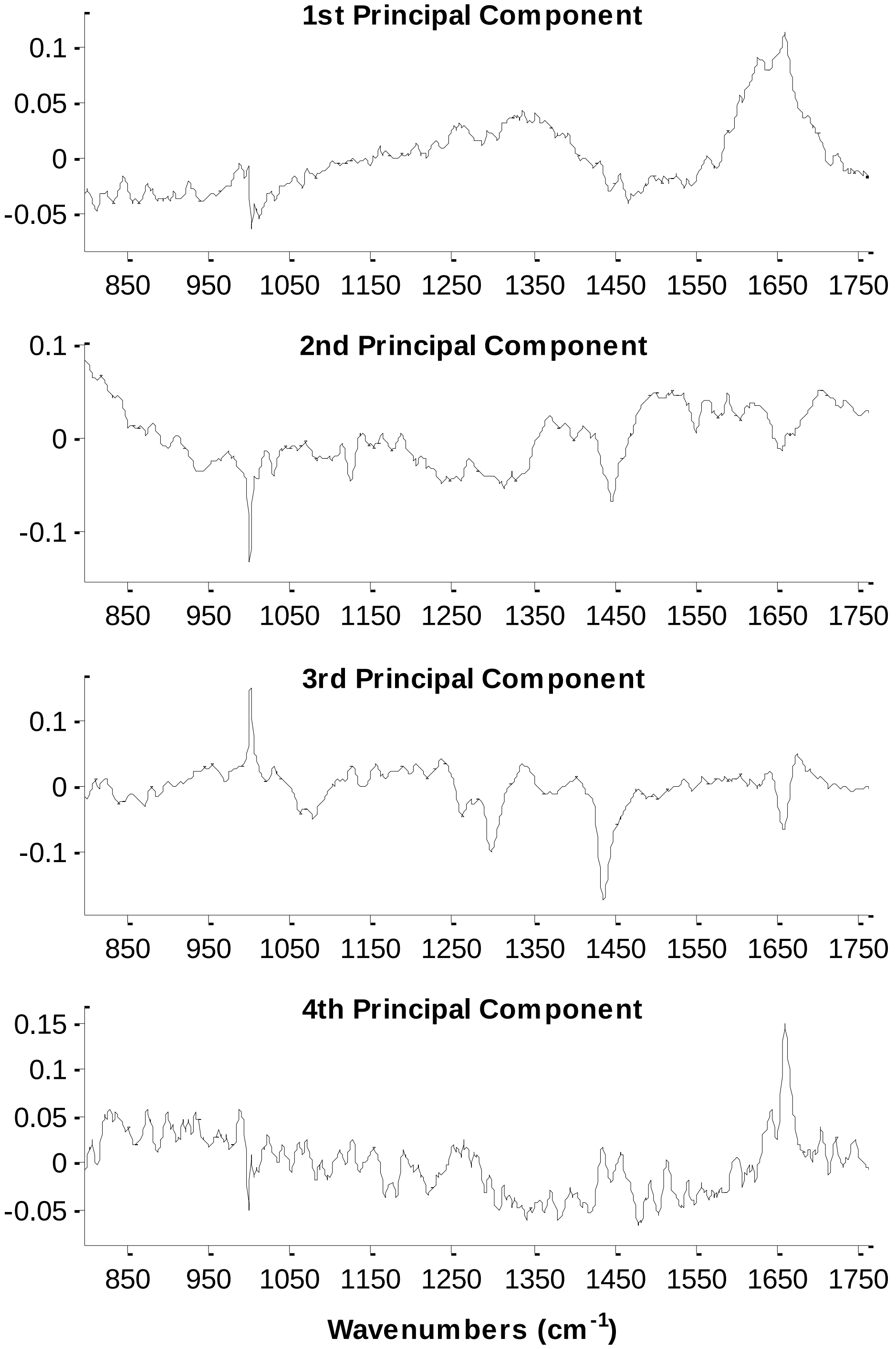

Figure 7.6 – PC loadings for the first four components calculated during PCA.

So as to understand the biochemical variation that separates the three treatment groups, the PCs must be examined. As the first four PCs described the majority of the non-noise variation which existed between the samples, the plots of these PCs against the original data space axis are presented in Figure 7.6. The loadings for the first and fourth PC show that positive scores are associated with greater contributions from lipid molecular vibrations located in the region of 990, 1301, 1441 and 1710 - 1745 cm^{-1}, whilst larger peaks in the region of 1263 and 1658 cm^{-1} are also associated with positive scores. However, it is difficult to attribute these peaks to a molecule group due to the overlapping of lipid and protein contributions in both of these regions.

As PC1 and PC4 only describe around 40 % of the total variance in the original data, it is sensible to investigate the separation of the treatment groups using the data in the first 14 PCs combined. As such, CVA was performed using the scores from the first fourteen PCs.

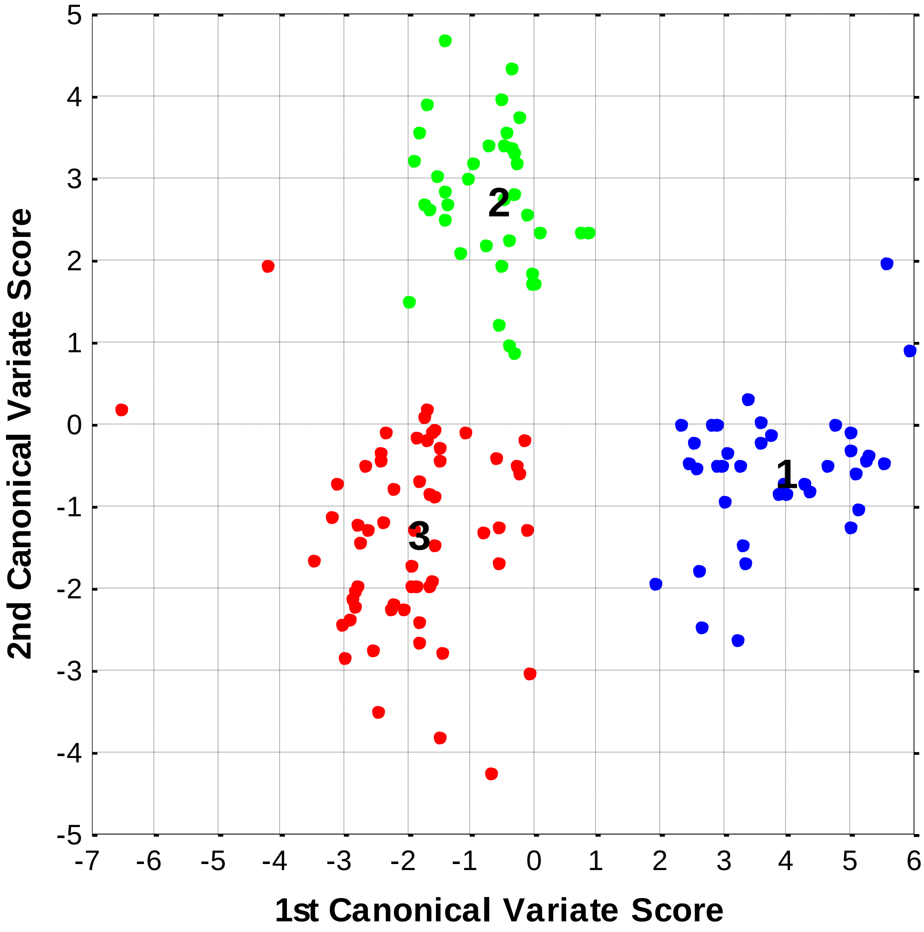

Figure 7.7 - Biplot showing the scores of each datum against the first and second component axes generated during the canonical variate analysis. The IVM, unstimulated and superovulated oocytes are depicted by the blue, green and red markers, respectively. The mean score for the IVM, unstimulated and superovulated groups are denoted by 1,2 and 3, respectively.

The results of the CVA revealed that the three treatment groups could be separated in two dimensions, as illustrated in Figure 7.7. Separation of the IVM group from the *in vivo* ovulated groups is observed along the axis of the first CV, whilst separation of the USO control oocytes from the SO and IVM oocytes is observed along the axis of the second CV. Examination of the CV loadings revealed that first PC contributes most significantly to the separation of the three groups along both the first and second CV axes.

These results confirm those obtained from the PCA analysis which revealed that the IVM group mean is distinct from those of the *in vivo* matured groups. However, the CVA also revealed that there exists a difference in the spectral profile of oocytes collected after stimulated and unstimulated ovulation cycles. It is also worth noting that the variation in the CV scores for the superovulated group is larger than both the IVM and unstimulated groups suggesting greater intra-group variation, which is consistent with the results presented in Figure 7.5.

7.3.2 Quality Assessment

Upon examination of the three methods of follicle recruitment and oocyte maturation, it was observed that a greater inter-oocyte spectral variance existed in the superovulated group. Furthermore, the morphological appearance of oocytes from this group was also more varied than the other treatment groups, with a number of oocytes appearing to have significant morphological defects. As such, an attempt was made to reconcile the presence of spectral variation within this group with oocyte morphological presentation. The superovulated oocytes (n = 59) were graded, blind, based upon their morphological appearance. Due to the small sample size, the oocytes were grouped as being of good or poor quality, as judged by the morphology, for some of the subsequent analysis. The poor group contained all oocytes belonging to grades 2 - 5 (n = 35), whilst grade one oocytes were assigned as being of good quality (n = 24).

Univariate Analysis of Oocyte Grades

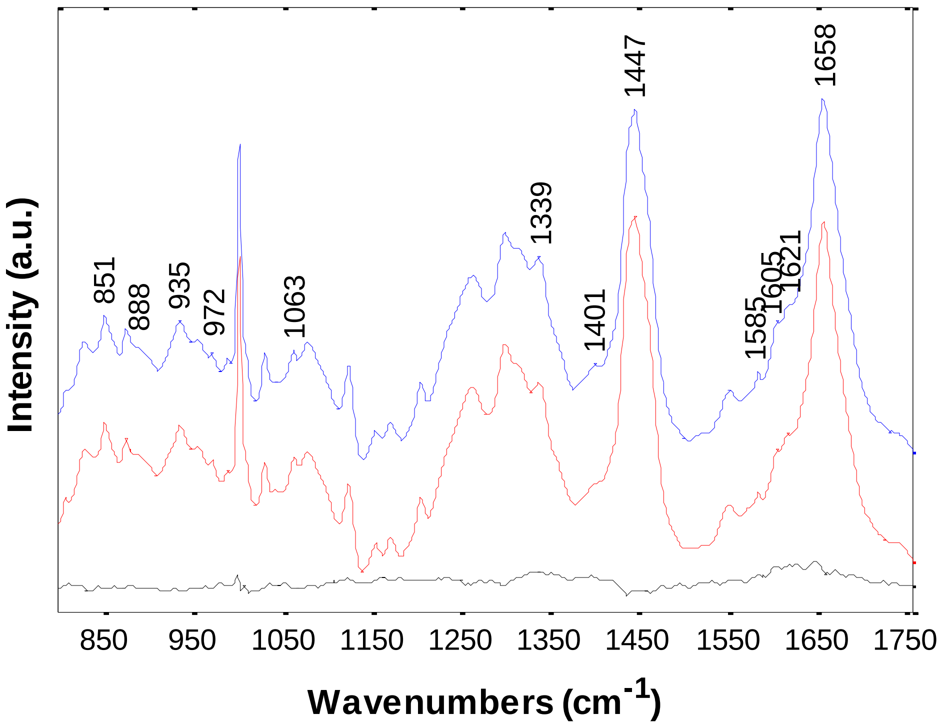

Figure 7.8 – Mean spectra for poor quality and grade 1 superovulated oocytes and the associated difference spectrum (grade 1 – poor) depicted by the red, blue and black plots, respectively. Raman bands which were judged to be significantly different (p=0.01) by an unpaired t-test are annotated.

A simple univariate analysis was performed to determine if spectral variations exist between the good and poor quality groups. A difference spectrum, depicted by the black plot in Figure 7.8, was calculated and a two-tailed unpaired t-test was performed at each wavenumber for the two groups to identify spectral locations where significant ($p = 0.01$) difference occur. Figure 7.8 details the results with significant peaks annotated.

Some subtle, yet marked, differences are observed in the difference spectrum, particularly in the region of the amide I and CH twist vibrations. Upon examination of the results of the t-test, it can be seen that 12 peak locations show a statistically significant difference between the two groups. In particular, greater intensities were observed in the grade 1 oocytes at 1339, 1401, 1585, 1605, 1621 and 1658 cm^{-1}, which with the exception of 1401 cm^{-1} correspond to protein vibrations. The peak at 1401 cm^{-1} arises due to the presence of the symmetric carboxylate stretch in fatty acids. Conversely, a reduction in intensity of the peaks occurring at 851, 888, 905, 972, 1063 and 1447 cm^{-1} were observed in grade 1 oocytes when compared to those of poor quality. Some of the lower peaks are difficult to assign due to overlapping bands in this region, but possible sources could be fatty acids, saccharides or amino acid residues, whilst the 1063 cm^{-1} peak is associated with the C-C chain stretch in lipids. The increase in the 1447 cm^{-1} band, which occurs as a result of C-H deformation, is attributed to lipids due to the presence of the shoulder below it and the lack of a discernable shoulder at 1460 cm^{-1} which occurs in proteins.

The ultimate aim of the spectroscopic analysis of oocytes would be to generate an algorithm based upon selected spectral intensities that could be used to classify oocytes based upon quality. However, due to the small sample size, generating and testing an algorithm with 12 variables proved unsuccessful. As an alternative, the use of intensity ratios is often used for classification purposes. Therefore, all ratio combinations of the 12 significant peak locations were calculated for each oocyte. One ratio in particular, 1605:1447, demonstrated good separation between the oocyte grades. Figure 7.9 presents the results of this ratio for each of the five grades.

Analysis of the ROC curve for these data indicated that with the ratio cut-off set at 0.3752 the oocytes could be separated with a high degree of certainty, as outlined in Table 7.2.

Comparison	**Sensitivity**	**Specificity**
Grade 1 vs. Grade 2	87.5	83.3
Grade 1 vs. Poor	87.5	88.6

Table 7.2 – Sensitivities and specificities calculated using a ratio cut-off of 0.3752 for superovulated grade1 vs. grade2 and good vs. poor oocytes.

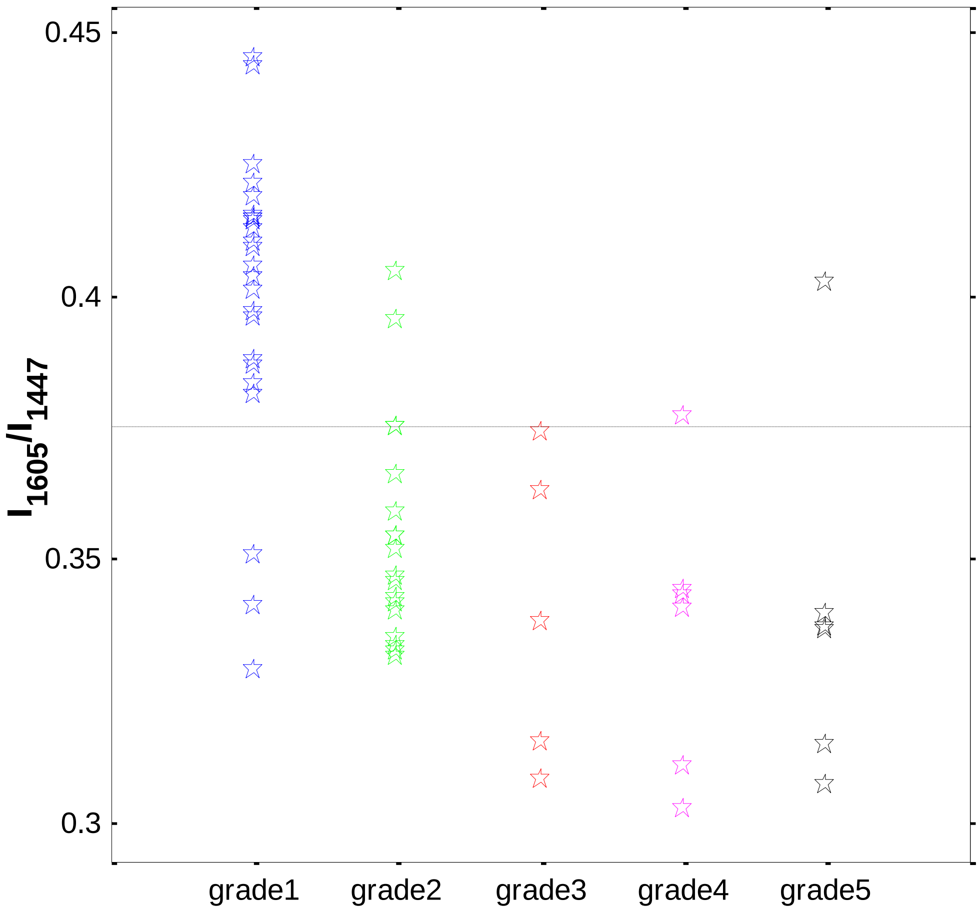

Figure 7.9 – Scatter plot depicting the ratios of intensity at 1605 and 1447 for each mean spectra from the superovulated oocyte group. The blue, green, red, yellow and magenta markers denote the grade of oocyte from one through to five, as judged by morphological appearance. The dashed line indicates the cut-off (0.3752) which was determined by analysis of the ROC curve.

Only three grade 1 oocytes were misclassified when a cut-off of 0.3752 was used, equating to a sensitivity of 87.5 %. All oocytes originating from grades 3 were correctly classified at this level, whilst only one grade 4 and one fragmented oocyte were misclassified. The specificity of the comparison between grade 1 and grade 2 was slightly lower than that comparing grade 1 and poor quality oocytes. This result is not unusual, since that oocytes belonging to grades 3 - 5 are more severely compromised than those belonging to grade 2.

So as to investigate whether there exists any similarities in the spectral profile of the graded superovulated oocytes and the other treatment groups, the ratio of the 1605 to 1447 cm^{-1}

intensities were calculated for the USO, IVM and grade 1 and poor quality superovulated oocytes. The results are presented in a boxplot in Figure 7.10. It can be seen that the median of the ungraded oocytes, which were collected after unstimulated ovulation, sits above the cut-off which was determined from the ROC curve. This result indicates that the spectral profile of the USO group is more closely related to the grade 1 profile. Conversely, the IVM group sits entirely below the cut-off, indicating that the profile in more similar to that of the poor quality SO oocytes.

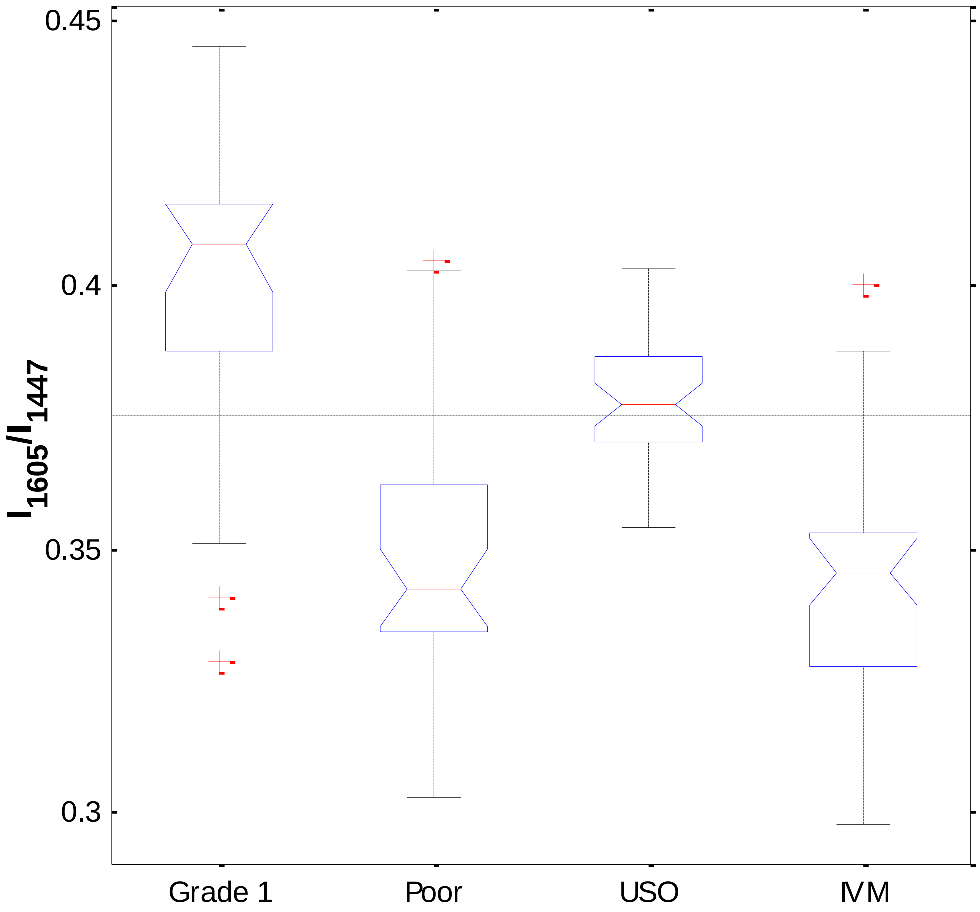

Figure 7.10 - Boxplot depicting the ratio of intensities at 1605 and 1447 for the grade 1, poor quality, unstimulated ovulation and in vitro matured groups. For each group, the red line indicates the median and the box displays the line of the first and third quartiles. The black whiskers extend 1.5 times the inter-quartile range in both directions. Data outwith this range is considered to be an outlier and is annotated with a red cross. The dashed line indicates the cut-off (0.3752) which was determined by analysis of the ROC curve.

Multivariate Analysis of Oocyte Grades

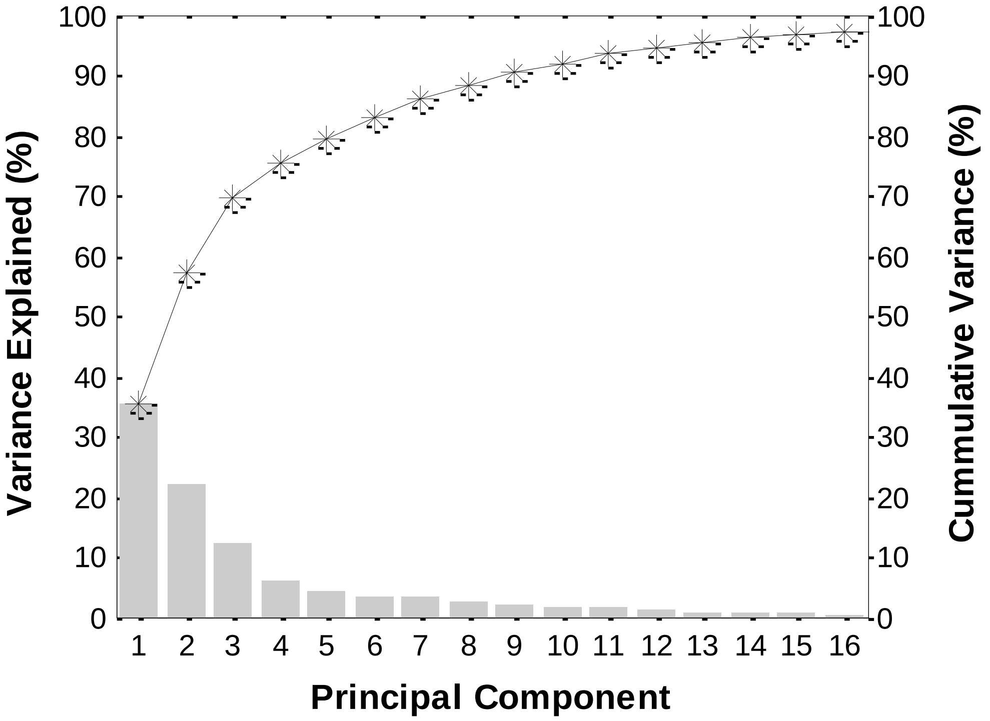

Figure 7.11 – Variance explained by each new variable generated during the principal component analysis of the 59 average spectra collected for superovulated oocytes.

So as to reduce the dimensionality and investigate any apparent clustering of the quality data, PCA was performed. From this the scree plot (Figure 7.11), it can be seen that the first PC accounts for approximately 35 % of the total spectral variance, whilst the first 16 PCs describe approximately 97 % of the variance. A plateau occurs in the scree plot around the twelfth PC, indicating that the first twelve PCs, which account for approximately 95 % of the total variance, can adequately describe the data.

A scatter plot of the scores of the first and second PC for each superovulated oocyte is shown in Figure 7.12. There exists an approximate separation of the good and poor quality oocytes along the first PC. Furthermore, upon examination of the means of the two groups there is a small separation along the axis of the second PC. However, Figure 7.12 also illustrates the large variation which exists between the samples. Due to the small sample size, it is possible

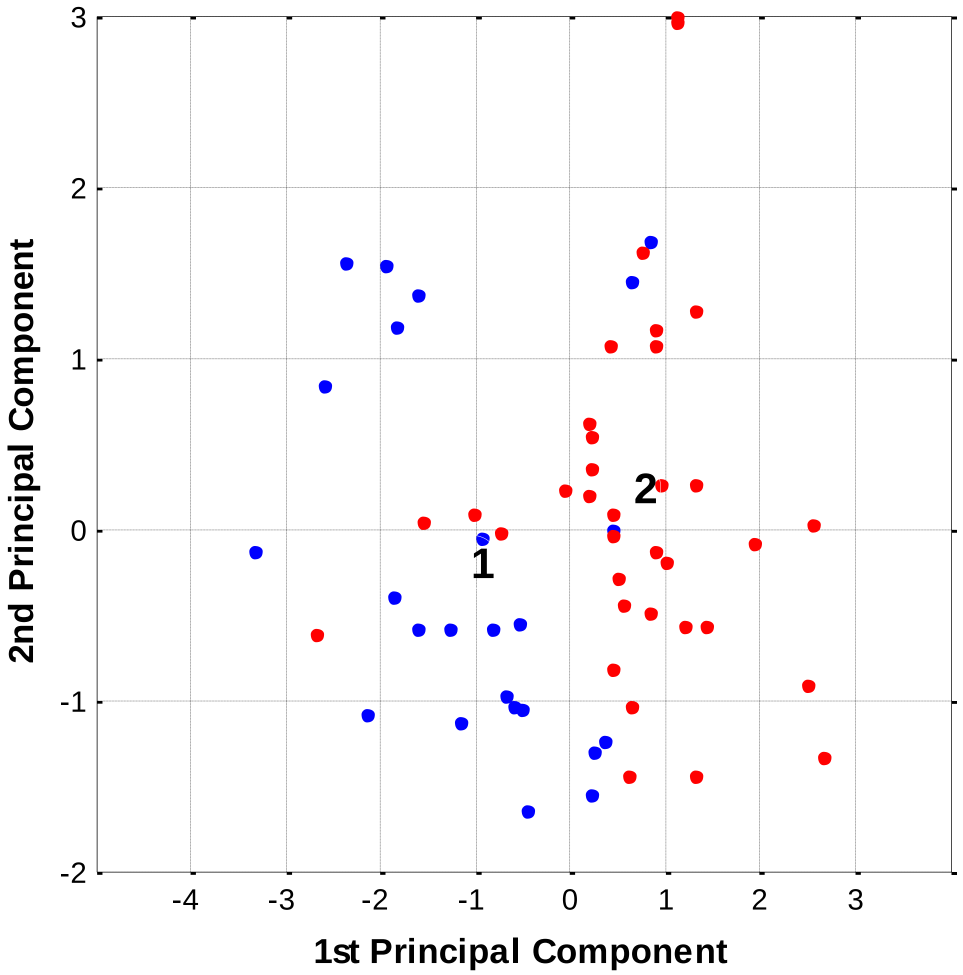

Figure 7.12 – Biplot showing the scores of each datum against the first and second component axes generated during PCA. The oocyte are grouped as either good quality (blue) or poor quality (red). The mean score of the high quality and poor groups are denoted by the numbers 1 and 2, respectively.

that this variation represents outliers, as opposed to the true separation of the data, although the spread of the poor quality oocytes may be intrinsic to the samples rather than an artefact of the sample size.

The PC loadings for the first three PCs are presented in Figure 7.13. The first PC, which represents approximately 35 % of the overall variation, shows some contributions from background fluorescence. However, there are also negative loadings associated with proteins at 1002, 1228, 1340, 1605 and 1622 cm^{-1} and positive loadings associated with lipids at 1065, 1440, 1466, 1716 and 1744 cm^{-1}. These loadings indicate that the separation which is present in Figure 7.12 occurs as a result of variation in the proportions of proteins and lipids in the oocytes. The second PC loadings are predominately positive and are very similar in appearance to the spectrum of an oocyte, indicating that this PC describes general intensity variations which exist between samples. In contrast, the third PC shows positive and negative loadings resulting from biochemical variation; positive loadings at 1002, 1032, 1238, 1334 and 1674 cm^{-1} are associated with proteins and negative loadings at 1065, 1263, 1299 and 1436 cm^{-1} arise from lipid molecular vibrations. A negative loading also exists around 1654 cm^{-1}, which may results from the amide I vibration or C=O lipid stretch.

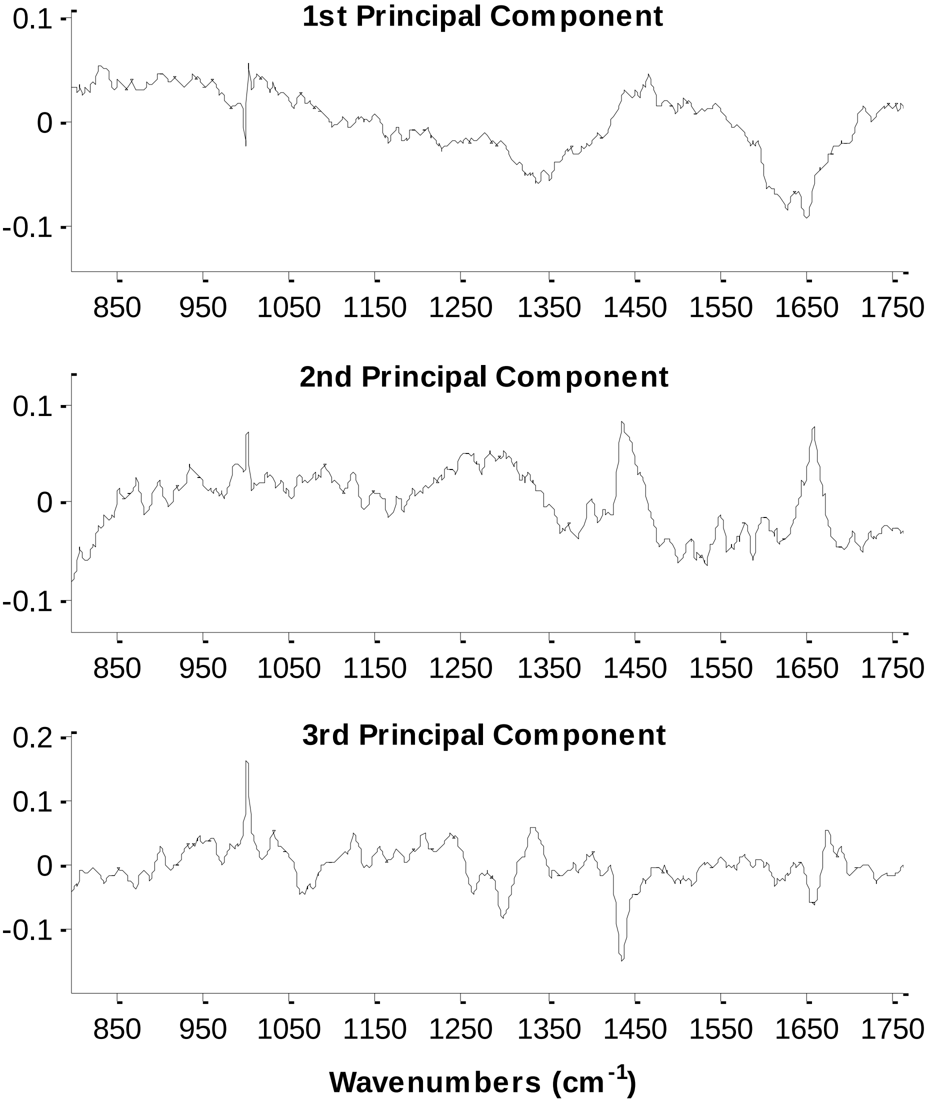

Figure 7.13 – PC loadings for the first three components calculated during PCA.

CVA was performed on the scores of the first twelve PCs so as to further investigate the relationship between these loadings and oocyte quality. Examination of the CV loadings demonstrates that both the scores of the first and second PCs contribute most to the separation of the two oocyte grades. A scatter plot of the first CV score as a function of oocyte quality (Figure 7.14) demonstrates that positive CV scores are associated with good quality oocytes whilst negative scores are indicative of poor quality oocytes.

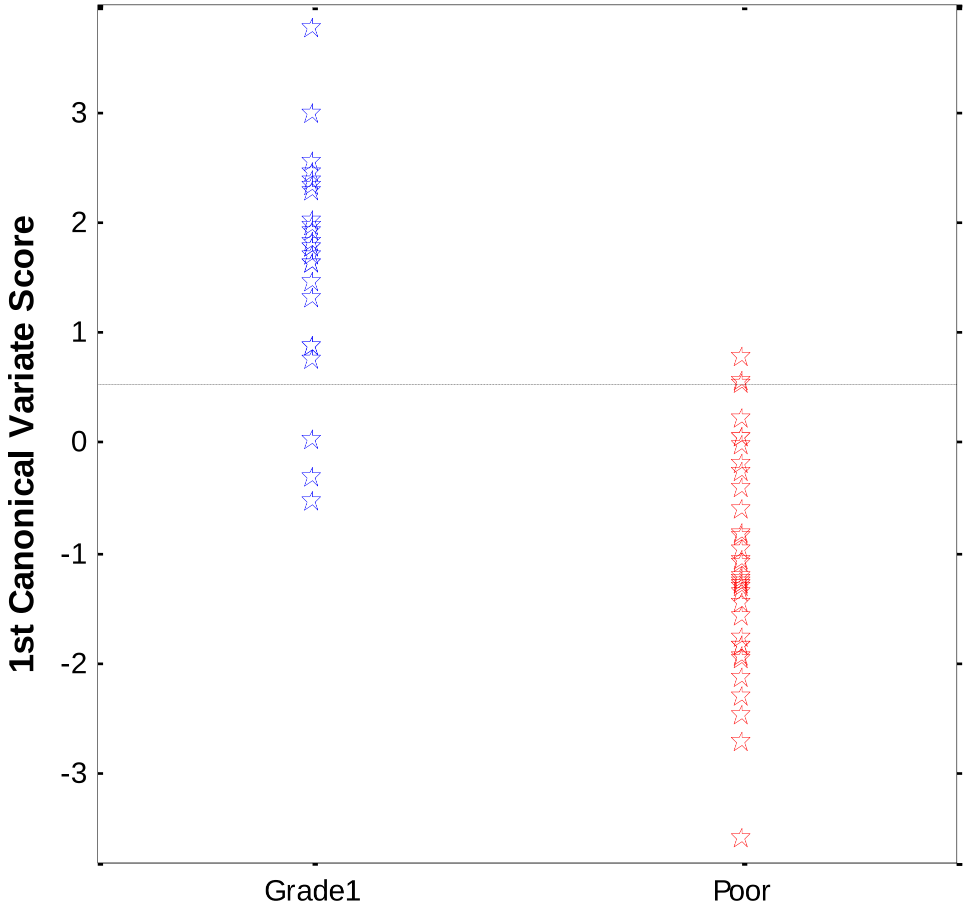

Figure 7.14 – Scatter plot showing the scores of the first canonical variate derived from the mean spectrum of each oocyte for the superovulated group. The blue and red markers denote the grade of oocyte as good or poor respectively. The dashed line at 0.5133 depicts the optimum cut-off as judged by analysis of the ROC curve.

	Sensitivity	**Specificity**
Grade 1 vs. Poor	87.5	94.3

Table 7.3 – Sensitivities and specificities calculated using a ratio cut-off of 0.5133 for superovulated grade1 vs. grade2 and good vs. poor oocytes.

Analysis of the ROC curve for these data indicated that with the ratio cut-off set at 0.5133 the oocytes could be separated with a high degree of certainty, as outlined in Table 7.3. Using 0.5133 as the cut-off resulted in only three grade 1 oocytes being misclassified, equating to a sensitivity of 87.5 %, whilst 2 poor quality oocytes were wrongly classified, equating to a specificity of 94.3 %. This result is similar to that obtained using the single intensity ratio outlined in the previous section.

7.4 Discussion

In the first instance, this work had been designed to investigate the effect of external stimuli and environmental factors on the maturation of oocytes. The use of oocytes collected from females in oestrous provided a control against which other treatments could be compared, as no intervention had been used in their selection. Conversely, the analysis of superovulated oocytes obtained from mice which had been stimulated using exogenous hormones enabled observations regarding follicle recruitment and external stimuli to be investigated. Finally, the use of *in vitro* maturated oocytes provided an opportunity to determine the reliability of culture methods for oocyte growth, maturation and competence. Upon initial morphological examination, the oocytes originating from the IVM and oestrous groups showed consistently good quality oocytes, with few classical abnormalities. In contrast, the oocytes collected after superovulation showed greater variation in morphological characteristics. Oocytes from this group were not graded prior to analysis, in order to ensure that a representative sample of the pathologies that make up this group were analysed.

As this work is a precursor to the development of a technique which could be used for the analysis of live oocytes with subsequent monitoring of development, integration times and laser exposure were of particular importance. Whilst high resolution spectral maps, such as those which are described in Chapter 5, are useful for investigating biochemical variation for further understanding the samples, they are of limited value for diagnostics due to the long acquisition times required. The use of reduced mapping methodology in this work enabled sampling of the entire oocyte in a much reduced time of approximately 1 hour as opposed to the 18 hours required for full map integration. It is recognised that this integration time is still too lengthy for real-time diagnostics of oocytes. However, some simple instrumental modifications would enable this to be significantly reduced. For example, the use of a larger CCD array which allows the collection of the entire spectral range in a single integration would reduce the acquisition time to approximately 17 minutes. Furthermore, the use of an expanded laser beam, as described in other works[178, 179, 265], could reduce the number of spectra required to characterise the oocyte, enabling rapid live cell analysis.

Although IVM has attracted much attention, the variation in protocols has led to different opinions of its efficacy. The process of follicular growth and oocyte maturation *in vivo* is a highly orchestrated process which is regulated by a number of environmental factors. Consequently, the replication of this process *in vitro* has proved difficult. Significant attention has been given to the optimisation of the *in vitro* growth of pre-antral follicles/ovarian tissue and subsequent maturation of oocytes in the mouse model. Despite this, whilst results suggest that IVM can support normal nuclear maturation, it fails to produce oocytes with cytoplasmic competency resulting in poorer fertilisation efficiencies. It has been postulated that the reduced developmental competence following IVM may result from one or more of three mechanisms: The culture environment does not support cytoplasmic maturation; the protocol induces an asynchrony between nuclear and cytoplasmic maturation; or the oocytes possess an intrinsically reduced developmental potential[266].

Comparison of the mean spectra from the IVM and the oestrous groups show a number of subtle yet significant differences, many of which are specific to protein molecular vibrations. This result was further confirmed by the PCA-CVA analysis, whereby IVM oocytes were found to have lower spectral contributions arising from protein vibrations than either unstimulated or superovulated oocytes. These data are consistent with the findings of several authors who have reported lower protein expression in IVM murine[267], bovine[268] and human[269] oocytes, when compared to their *in vivo* matured counterparts. In certain instances, some proteins were found to be absent in the IVM oocytes, whilst Kim *et al.* identified significantly reduced β-actin and insulin-like growth factor II expression[267].

The process of releasing the COC from its follicle is known to stimulate spontaneous resumption of meiosis, whilst the use of EGF in the maturation media aids this process. It has been suggested that the lower protein content of IVM oocytes results from the early resumption of meiosis, which is associated with the termination of the cumulus-oocyte gap junctions [270] and is known to be associated with a decrease in the absolute rate of protein synthesis[271]. During the third replicate of the culture process, several of the follicles ruptured, despite the addition of ascorbic acid which is known to significantly increase the maintenance of basal lamina integrity[272]. In these instances it would be expected that resumption of meiosis would occur spontaneously, and at an earlier time than the oocytes derived from intact follicles. Consequently, it would be fair to assume that these oocytes would show lower protein content than their counterparts. This, however, was not observed, suggesting that either meiosis did not resume early for these samples or that the early resumption of meiosis did not adversely affect the acquisition of ooplasmic proteins.

The source of the oocytes in the IVM group must also be considered. Unlike the unstimulated *in vivo* group, in which follicles are recruited in large numbers and only a small cohort are ultimately chosen for ovulation, the IVM oocytes originate from pre-antral follicles which were selected on the basis of their size and morphology. It has been postulated that the process of follicular atresia is a method by which sub-optimal follicles and oocytes are disposed, with the pre-antral to antral transition accounting for the greatest loss. Consequently, the method of selection of pre-antral follicles for culture may not preclude follicles and/or oocytes which contain intrinsic abnormalities. However, unlike many protocols in other species, the mice were not primed using hormones prior to follicle collection. As such, the follicle cohort should have represented a more uniform distribution, intimating that the origin source does not adversely affect the outcome. Similarly, the lack of a discernable overlap between the unstimulated and IVM groups and the relatively small within group variation seen for the IVM oocytes, as judged by the results of PCA-CVA, would suggest that the follicular origin plays an insignificant role in the separation of these groups.

Other extrinsic properties could account for the difference between the groups. It has previously been reported that the size of *in vitro* grown oocytes is less than *in vivo* controls[267, 273]. Although no precise measurements were taken in the work presented here, such variation could result in concentration, and thus spectral, discrepancies between the two groups. However, it would follow that the smaller IVM oocytes would have greater spectral intensities representative of higher substrate concentrations, which was not observed. Additionally, the effect of genetic strain must be considered; the IVM oocytes were derived from F1 (C57/Bl6J x CBA) hybrid females whilst the unstimulated and superovulated oocytes were derived from C57/Bl6J inbred females. Previous investigations have reported strain specific variations in oocyte maturation, specifically related to nuclear maturation, microtubule organisation[274] and response to hormone stimulation[275]. It was found that *in vivo* matured hybrid oocytes had more microtubule organising centres (MTOCs) than inbred oocytes, although fewer MTOCs were observed in IVM oocytes when compared to their *in vivo* matured counterparts[274]. Furthermore, under certain culture conditions the number of MTOCs was found to be strain independent yet still lower than *in vivo* matured oocytes. These findings indicate that it is unlikely that the variation between the *in vitro* and *in vivo* matured oocytes arises as a result of strain specific phenotypes. However, further work incorporating hybrid unstimulated and superovulated oocytes would be beneficial.

The results and observations presented in this work suggest that some mechanism is responsible for reduced accumulation of macromolecules, and in particular proteins, during the *in vitro* follicular growth phase and oocyte maturation. This is concomitant with the observation of cytoplasmic immaturity and reduced developmental competence reported by several researchers. Whilst the origins of this variation are difficult to isolate, several experimental factors have been excluded. However, it is still unclear whether sub-optimal culture conditions are responsible for reduced cytoplasmic maturation and formation of gap junctions or if it is the result of early onset of meiosis resumption. The data presented indicates that the spectral profile of the cytoplasm of oocytes could be used to investigate the biochemistry underpinning IVM in more detail.

Ordinarily *in vivo*, follicles are continuously recruited from the primordial pool, via a gonadotrophin independent process, to enter into the growth phase which for most follicles will extend to the late pre-antral or early antral phase of follicular growth. The follicles' fate at this point is decided by the concentration of circulating FSH; if it is below a certain threshold the follicles will undergo atresia, whilst if it is high enough growth will proceed for a small cohort of the available follicles. This is the first point at which follicles are thought to be actively selected, although the mechanism by which this is achieved is still unclear.

Similarly, it is also the stage at which the majority of follicles will undergo atresia. Of the selected follicles only a species-specific number will reach the pre-ovulatory stage with the remaining subordinate follicles ultimately reverting to atresia. This selection stage is determined by the establishment of dominant follicles, a process which is regulated by indirect endocrine and direct follicle-follicle interactions[276]. Experiments involving the co-culture of follicles have shown that when in contact, one follicle will establish itself as dominant although this is not an irreversible process[277]. This suggests *in vivo*, that only a small number of follicles in a cluster will become dominant.

Conversely, during superovulation high levels of exogenous hormones are administered in order to recruit a higher than normal number of follicles to progress to the second selection stage. As discussed previously, the mechanism of the first selection process is unclear. Specifically, it is unknown if this is a method of removing intrinsically abnormal or poor quality follicles/oocytes. Furthermore, the high levels of circulating gonadotrophin have been reported to have a detrimental effect on follicles which are highly vascularised in the later stages of maturation[266, 278]. Consequently, the effect of ovarian hyper-stimulation on the oocyte, when compared to natural ovulation, was investigated by the spectral analysis of superovulated oocytes.

Comparison of the mean spectra of the superovulated and unstimulated groups indicates that they are more similar to one another than the IVM group mean. However, several significant deviations were noted from the t-test namely at 891, 1040, 1173, 1339 and 1744 cm^{-1}, corresponding to slight variations in protein, lipid and possibly carbohydrate molecular vibrations. Further analysis using PCA reveals that the mean of the superovulated and unstimulated groups are indeed very similar, as depicted by Figure 7.5. However, the results of the CVA indicated that there does exist spectral variation between these groups, although it is less marked than the difference observed between the USO and IVM groups.

Furthermore, the results presented in Figure 7.10 suggest that much of the variance which is observed between the USO and SO groups could be accounted for the greater incidence of poor quality oocytes in the latter group. The similarity of the superovulated and control oocytes, when compared to the IVM oocytes (Figure 7.5), indicates that the *in vivo* environment plays a significant role in the maintenance of oocyte maturation, specifically cytoplasmic maturation. The closeness of the means should, perhaps, not be unforeseen as many of the superovulated oocytes could have been expected to be ovulated under an unstimulated protocol.

Upon closer inspection of the results it is apparent that more significant variation exists within the superovulated group than either the IVM or unstimulated groups, as evidenced by Figure 7.1 and 7.5. This is of greater significance given that the superovulated group contains 1.5 times the number of samples of the other groups (n = 59 vs. n = 38), which should reduce the impact of outliers. However, given the significant range of morphology in this category, a large within-group spectral variation is not unusual. Figure 7.5 which shows the scores of the first and fourth PC for each oocyte demonstrates that an overlap exists between the IVM and superovulated oocytes along the first PC. The wavenumber loadings indicate that this PC predominately describes variation in protein vibrations. The overlap region occurs in the low negative score range intimating that some of the superovulated oocytes have lower protein content than the unstimulated controls, as is seen with IVM oocytes. It is proposed that this may arise due to the asynchrony of folliculogenesis and oogenesis which results in the resumption of meiosis prior to complete cytoplasmic maturation. Additionally, there are oocytes which have greater positive scores along the first PC axis, indicating oocytes with greater protein content than the control group. It is postulated that these may represent post-mature oocytes which are characterised by a number of factors including a large perivitelline space[279]. As the superovulation protocol recruits greater numbers, it is likely that the follicles vary slightly in their developmental stage.

Similarly, the extent of vascularisation and the local environment of each follicle will be likely to differ, meaning that the stimuli for maturation will vary between follicles. These factors combined, could describe the presence of post-mature oocytes in the superovulated cohort. This supposition could be investigated further with the inclusion of *in vivo* aged oocytes.

The large variation in the number and morphology of the oocytes collected after superovulation, as seen in this work, is well documented and has been reported to be strain dependent in mice[275, 280, 281]. It is difficult to elucidate whether this variation in morphology is the result of the recruitment of sub-optimal follicles/oocytes for ovulation, the gonadotrophin stimulation itself or indeed a combination of these factors. However, further work was performed to investigate whether the variation in oocyte quality could be predicted by Raman spectroscopy. The comparison of the mean spectra for grade 1 and poor quality oocytes displayed numerous regions of significant difference. Specifically, grade 1 oocytes displayed increased intensities associated with protein vibrations and lower intensities resulting from lipids and saccharides, when compared to oocytes judged as being of poor quality.

The examination of various ratios of the significantly different peaks yielded a ratio which provided a good separation of the oocyte qualities: The ratio of the peak arising due to phenylalanine at 1605 cm^{-1} and the peak at 1447 cm^{-1} which was assigned to C-H deformation of lipids. It was found that the higher this ratio, which represented the proportion of protein to lipids in the oocyte, the better the quality. Analysis of ROC curves provided a cut-off of 0.3752 which corresponded to a sensitivity of 87.5 % and specificity of 88.6 %. These findings concur with previous results which indicate that good quality oocytes have high protein content. This result also indicates that poor quality oocytes have a higher lipid content which would result in a lower protein to lipid ratio. As most of the poor quality oocytes had cytoplasmic granularity to some extent, it is suggested that this is the source of the increased lipid content, which has been confirmed by other researchers[248]. Similar results were obtained using PCA-CVA analysis, whereby the quality of oocytes was separated successfully on the basis of their protein and lipid contents.

These results suggest that it is possible to discern oocyte quality by analysing the ratio of its ooplasm protein to lipid ratio. Prior to drawing further conclusions, the sample size should be increased so as to ensure that the effect of outliers is minimised. However, should the results of future work be found to be consistent, Raman imaging could be employed to enable rapid quality testing of unfixed oocytes.

7.5 Conclusions

The work presented here demonstrates that unstimulated and superovulated oocytes have ooplasm with similar biochemical composition, whilst IVM oocytes have lower protein content which is consistent with incomplete cytoplasmic maturation. Furthermore, the quality of superovulated oocytes can be distinguished by the ratio of protein to lipid in their ooplasm. These results suggest that Raman spectroscopy is a powerful technique for the analysis of oocyte maturation, ovulation mechanism and quality.

Chapter 8

General Discussion and Conclusions

8.1 Discussion

As discussed in Chapter 1, throughout its development, the oocyte undergoes extensive modification to prepare it for successful fertilisation and embryonic development. It is well recognised that oocyte development and maturation are highly intricate processes which are temporally regulated, in part, by the oocyte's surrounding environment. Consequently, in order to fully appreciate the implications of manipulating these processes, as is done during ARTs, it is necessary to further the understanding of the underlying biochemistry of oocyte development and maturation.

Currently, there are numerous techniques which are used routinely for the investigation of oocyte biology in a research setting. However, few are suitable for application in a clinical setting due to the destructive nature of the sample preparation and lengthy protocols, as with histology and electrophoresis. Therefore, as discussed in Chapter 1, there has been a significant research effort to develop a quantitative technique for the assessment of oocyte maturation and quality. This has lead to methods such as birefringence spindle imaging and metabolomic assessment of culture media, both of which have shown significant promise. However, as yet, there has been no advancement in the development of a technique for the direct assessment of ooplasm maturity and quality.

The technique of Raman spectroscopy, as introduced in Chapter 2, is now widely applied to the study of biological samples. Furthermore, it has been shown to be effective in the discrimination of a number of pathologies in both cellular and tissue systems. In contrast to many other available techniques, it is capable of probing multiple biochemical constituents simultaneously, thus revealing a "biochemical fingerprint" for any given sample. As such, it was hypothesised that Raman spectroscopy could prove to be a powerful technique in the field of oocyte biology. Consequently, the principal aim of this thesis was to determine the potential of Raman spectroscopy when applied to the field of oocyte biology. In an effort to identify this potential, this thesis addressed three main areas of investigation: **I. intra-oocyte biochemical variation**; **II. the biochemistry of oocyte maturation**; and finally, **III. the effect of environment on the mature oocyte *in vivo* and *in vitro*.**

Initially, to investigate the presence of intra-ooplasm biochemical variation, oocytes from various stages of development and early-stage embryos were analysed using high resolution Raman mapping, in combination with univariate and multivariate analysis. This work, described in Chapter 5, revealed temporal changes in the distribution of biochemical constituents, and in particular lipids and proteins, during oocyte maturation and early embryonic development.

OLS fitting of the mean spectra obtained from the k-means cluster analysis, for each sample, provided greater insight into the changes in the relative composition of the cytoplasm at these key developmental milestones. The observed changes in protein, lipid and RNA concentrations were consistent with those previously reported. Although the spectral fitting described in this work returned small residuals, it is suggested that the OLS fitting could be further improved by isolating some of the reference compounds from oocytes.

The results presented in Chapter 5 not only confirmed many of the previously reported modifications associated with oocyte maturation and early embryonic development, but also demonstrated the power of Raman spectroscopic mapping for the study of spatial distributions of biochemical constituents within this unique cell. However, in order for Raman spectroscopy to be routinely applied in this field, the issues associated with sampling time must be addressed: It is recognised that even in a research setting the 18 hour integration time reported in this work is too lengthy. In particular, if this technique is to be applied to unfixed cells the sampling time would need to be reduced by around 200 fold.

As was discussed in Chapter 5, some simple instrument modifications would enable to sampling time to be significantly reduced; increasing the CCD array size would reduce integration times to less than 5 hours and implementing line-mapping, as opposed to point mapping, could further reduce sampling times to the order of minutes. Alternatively, Raman imaging could be implemented to provide a biochemical map at a specific Raman band, such as the phenylalanine stretch. Although this method only enables the investigation of a specific Raman band at any one time, an image at that band could be acquired in several minutes. As such, with an optimised instrumental set-up, Raman mapping or imaging could be used to great effect in the visualisation of unfixed oocytes and early stage embryos. Most significantly, using these techniques would enable temporal analysis without fixation, permeabilisation or labelling.

An interesting feature which was identified in the Raman maps of the mature oocyte was the apparent asymmetric distribution of the proteins and lipids about the animal-vegetal axis. The underlying mechanism regulating this asymmetry is unclear, but it is postulated that it may be a manifestation of cytoplasm polarisation. As yet, the presence of this phenomenon in mammalian oocytes is still under debate. Consequently, performing sequential Raman analysis of zygotes during the early cleavage stages may reveal any association between the asymmetrical organisation of the cytoplasm and the resulting cleavage planes.

So as to investigate the biochemical modifications which are associated with oocyte cytoplasmic maturation, and identify the ability of Raman spectroscopy in monitoring these changes, in Chapter 6 the spectral signatures of GV and IVM oocytes were compared. Due to the prohibitively long acquisition times of the sampling protocol reported in Chapter 5, a faster mapping protocol which comprised of sub-sampling the ooplasm at 6 μm intervals was adopted in this work.

It was found that the Raman signatures of oocytes derived from pre-antral and *in vitro* cultured follicles revealed significant variation. In particular, a marked increase in lipid contributions was observed in the mature oocytes. It is postulated that the lipid increase is a result of the accumulation of lipid droplets, which are thought to form part of the “mammalian yolk”, and mitochondria. These findings are consistent with the modifications which are known to take place during cytoplasmic maturation and with the results presented in Chapter 5.

A logistic regression algorithm, which was built using the ratios of Raman bands that were significantly different between the immature and mature oocyte groups, was found to successfully discriminate between immature oocytes and oocytes matured under different conditions. In building the algorithm, problems were encountered with complete separation whereby there exists no unique solution to the maximum-likelihood problem. This is a problem which is commonly reported for small to medium-sized data sets, and in this work, was overcome by reducing the number of input variables in the algorithm. As such, in future work, if the sample size were increased it is likely that additional input variables would be required to adequately discriminate between the treatment groups.

Both ovarian stimulation and *in vitro* maturation of oocytes are routinely used in clinical ART protocols. Yet, the effect of superovulation on oocyte quality is little understood and it has long been recognised that oocytes undergo incomplete cytoplasmic maturation *in vitro*. As such, in Chapter 7 the spectral signatures of oocytes derived from unstimulated and stimulated cycles and those which had been matured *in vitro* were compared, in an effort to understand the biochemistry which underpins the effect of environmental stimuli on oocyte maturation. It was found that although biochemically similar, *in vitro* matured oocytes demonstrated reduced protein content when compared to their *in vivo* matured counterparts. This finding was consistent with the early termination of gap-junctions which is routinely reported for IVM oocytes in the literature. As such, it is suggested that culture protocols could be optimised by comparing the spectral signatures of oocytes collected after unstimulated ovulation cycles and IVM.

Unsurprisingly, greater spectral variation was observed in the superovulated group, which was consistent with the greater variation in morphological quality which is reported for oocytes collected from stimulated cycles. As such, an effort was made to reconcile the spectral signature with morphological quality for the superovulated group. It was found that the ratio of protein-to-lipid was indicative of quality; oocytes displaying a lower protein-to-lipid content were found to be of lower morphological quality. Furthermore, upon comparison, it was found that oocytes collected from unstimulated cycles displayed protein-to-lipid ratios which more closely resembled good quality superovulated oocytes. Conversely, IVM oocytes displayed protein-to-lipid ratios closer to those of poor quality superovulated oocytes. However, unlike the poor quality superovulated oocytes which displayed higher lipid content, the IVM oocytes displayed lower protein content.

It is noteworthy that in much of the previous work which has reported the application of Raman spectroscopy, used in combination with PCA, that only a few PCs are required to describe the variance which exists in the original data. In contrast, in the work which is reported in Chapter 7, upwards of 20 PCs were required to describe around 95 % of the variance that existed between the oocytes collected using different maturation protocols. This result is not unexpected as the most commonly reported application of Raman-PCA is in the field of cancer diagnostics. In such cases, significant biochemical variation, in specific wavenumber regions, is seen between the normal and malignant samples and thus, few PCs are required to describe the variance. Conversely, in cases, such as those reported in Chapter 7, where the biochemical variation is less marked and contained within more wavenumbers, more PCs are required to adequately characterise the variance which exists between samples.

Due to the complexity of the process of oocyte development and maturation, it is unlikely that any single method would be able to provide an accurate assessment of oocyte quality. Instead, as discussed in Chapter 1, it is probable that a combination of techniques would provide a more accurate measure of quality and competence. The work described in this thesis has been concerned with the direct analysis of cytoplasmic maturation in the oocyte. Consequently, it is suggested that the implementation of a second complementary technique, which is capable of assessing nuclear maturation, would provide a more complete quantisation of oocyte quality. In particular, it is proposed that birefringence spindle imaging would provide a useful adjunct to cytoplasmic Raman assessment. However, as most Raman substrates are highly birefringent, and therefore unsuitable for use in birefringence imaging, the experimental setup would have to include two separate sampling windows.

8.2 Concluding Remarks

It has been shown that the significant biochemical variation which exists within the cytoplasm of oocytes and embryos can be visualised using high resolution Raman maps. In addition, using the faster sub-sampling collection protocols, it has been shown that the spectral signatures of immature and mature oocytes are distinct and that the biochemical profile of the cytoplasm is dependent upon the conditions under which the oocyte is matured. As such, the work presented in this thesis has demonstrated the vast potential of Raman spectroscopy when applied in the field of oocyte biology research. However, in a wider sense, this research could be considered to form the foundations for further studies in which Raman is used for the investigation of unfixed oocytes and embryos. Such work would enable a more complete assessment of what constitutes a good quality oocyte, and may help optimise clinical protocols used in ARTs.

Appendix 1

Examination of Background Removal

A1.1 Introduction

The spectra presented in this thesis have been subjected to background removal using the orthogonal vector method suggested by Maquelin *et al.*[230]. This method removes signal which cannot be differentiated from that of the background. As such, a spectrum which is representative of the background arising from the optics, quartz coverslip and PBS buffer is required. In this work, the background spectrum was collected from a location adjacent to the sample. Figure A1.1 shows a spectrum derived from a single static measurement before and after the implementation of the background removal algorithm. The background spectrum which was collected for the same sample is also presented.

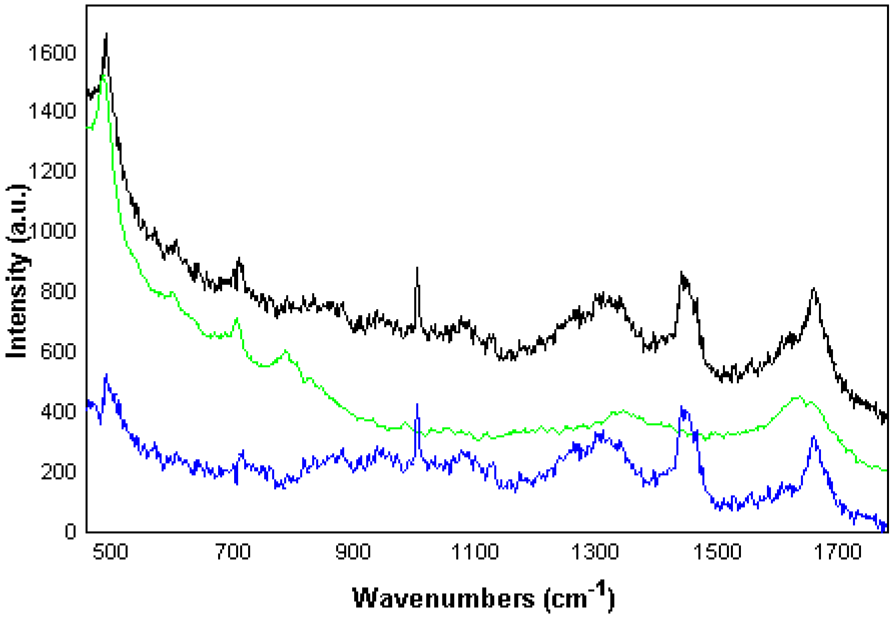

Figure A1.1 – Demonstration of the background removal method described in Chapter 3. In the plot the unprocessed spectrum originating from the sample and the spectrum collected from the surrounding buffer are represented by the black and green traces, respectively. The blue spectrum represents the zero-offset spectrum derived from the sample after the implementation of the orthogonal vector method described in Chapter 3.

A1.2 Comparison of Subtraction Methods

To enable the investigation of the efficacy of the orthogonal vector method for background subtraction, the resulting background subtracted spectrum was compared to a spectrum which has undergone a simple, direct background subtraction. In Figure A1.2, the red trace represents the result of the direct method, whilst the blue trace represents the result of the orthogonal vector method. Furthermore, the zero-offset uncorrected spectrum is included to enable a more objective assessment of the two methods.

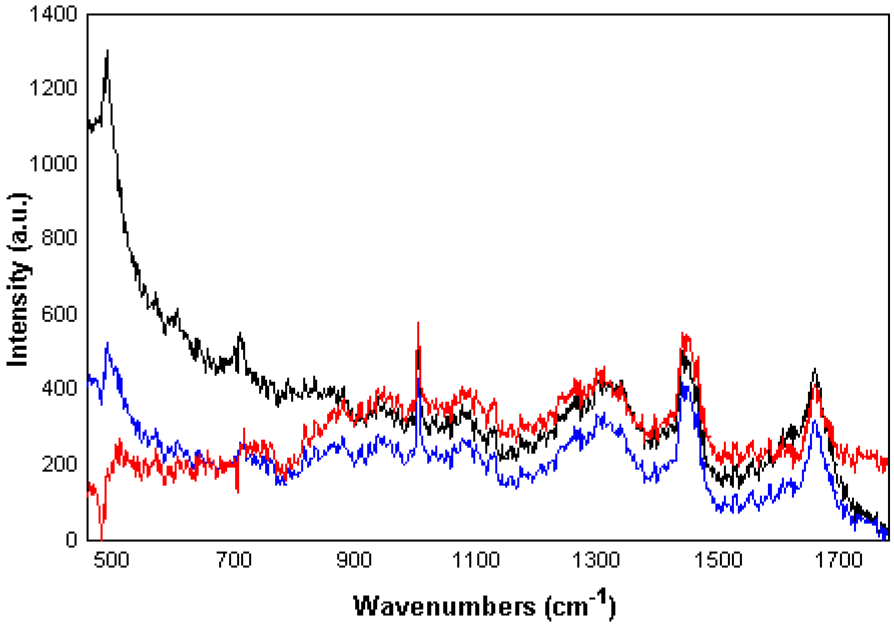

Figure A1.2 – Investigation of the background removal method described in Chapter 3. In the plot the zero-offset spectrum originating from the sample prior to subtraction is depicted by the black trace. The blue spectrum represents the zero-offset spectrum derived from the sample after the implementation of the orthogonal vector method described in Chapter 3. As a comparison, the red trace represents the corrected spectrum after the implementation of a simple background subtraction (sample-background).

In both cases, a narrowing of the amide I envelope, when compared to the uncorrected spectrum, indicates that the signal arising from the background in this region has been successfully subtracted. Furthermore, the peak which is seen in the region of 700 cm^{-1} in the uncorrected spectrum is absent in both corrected spectra. One difference which is evident between the two corrected spectra is the shape of the resulting baseline. The direct method results in a rapidly changing baseline, whilst the orthogonal method reveals a more slowly changing baseline which is more representative of the fluorescence which arises from the sample. This is most likely because the vector method is implemented using the first derivative. This difference in shape is significant, as it is more straightforward to correct for a slowly changing baseline.

Appendix 2

Examination of Spectral Fitting

A2.1 Introduction

OLS fitting of the mean spectra derived from the k-means cluster analysis in Chapter 5 was performed using a selection of reference spectra. In each case, the goodness of fit was represented by an R^2 value. However, these values provide no information about which regions of the spectrum are poorly fit. As such, the residual at each wavenumber was calculated for each spectrum, the results of which are presented in Figures A2.1 – A2.12.

In each case, analysis of the residuals reveals that the fit is poorer in the region of 990 - 1010, 1245 - 1270 and 1660 - 1670 cm^{-1} which correspond to the phenylalanine symmetric stretch, amide III and amide I vibrations, respectively. As many of the poorly fitted regions correspond to Raman shifts associated with proteins, future OLS models could benefit from the inclusion of a protein standard which has been isolated from oocytes, or indeed, follicular fluid.

A2.2 The GV Oocyte

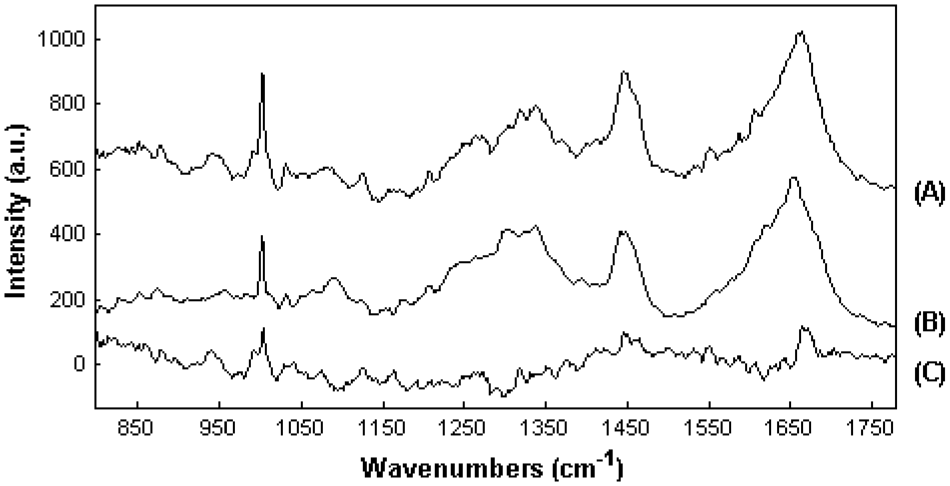

Figure A2.1 – Results of the OLS fitting of the mean spectrum derived for the green cluster in the GV oocyte. The plot shows (A) the mean spectrum derived from the original data (B) the fitted spectrum obtained from the OLS fitting and (C) the residual spectrum which is calculated by subtracting B from A. The spectra have been offset for clarity.

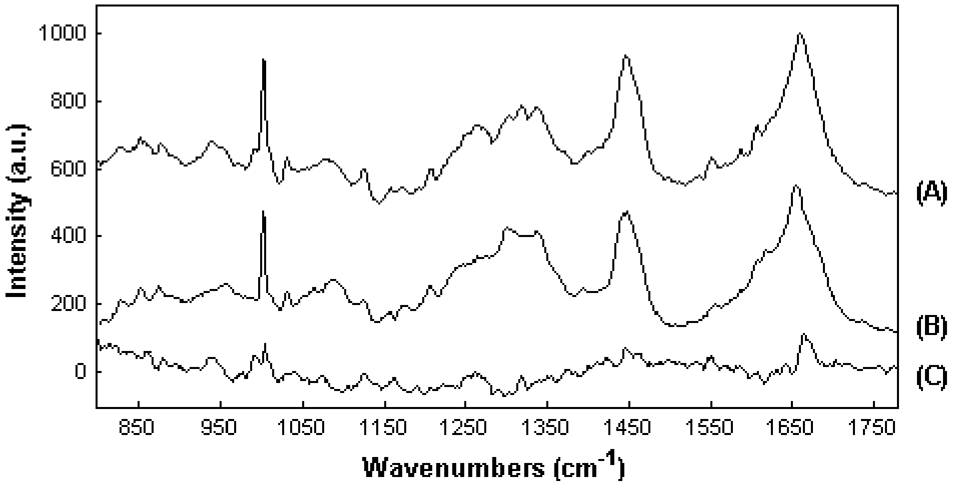

Figure A2.2 – Results of the OLS fitting of the mean spectrum derived for the blue cluster in the GV oocyte. The plot shows (A) the mean spectrum derived from the original data (B) the fitted spectrum obtained from the OLS fitting and (C) the residual spectrum which is calculated by subtracting B from A. The spectra have been offset for clarity.

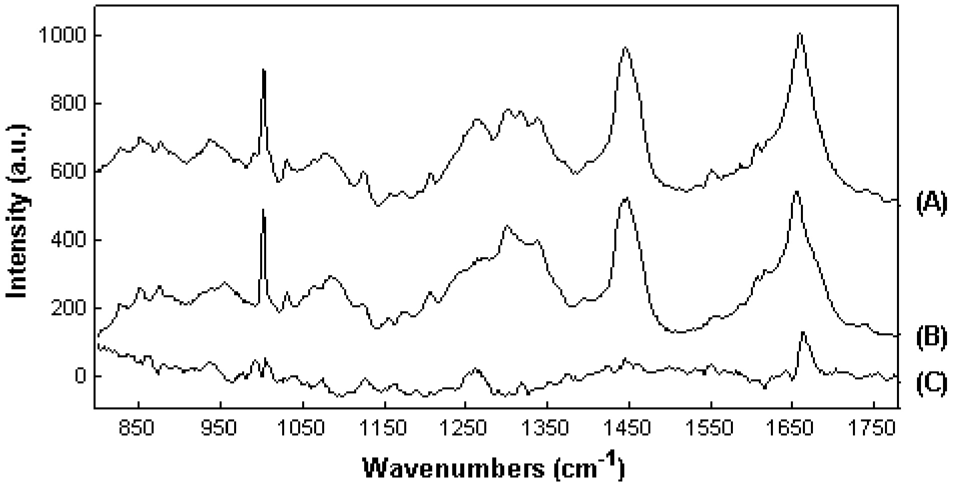

Figure A2.3 – Results of the OLS fitting of the mean spectrum derived for the red cluster in the GV oocyte. The plot shows (A) the mean spectrum derived from the original data (B) the fitted spectrum obtained from the OLS fitting and (C) the residual spectrum which is calculated by subtracting B from A. The spectra have been offset for clarity.

A2.3 The Metaphase II Oocyte

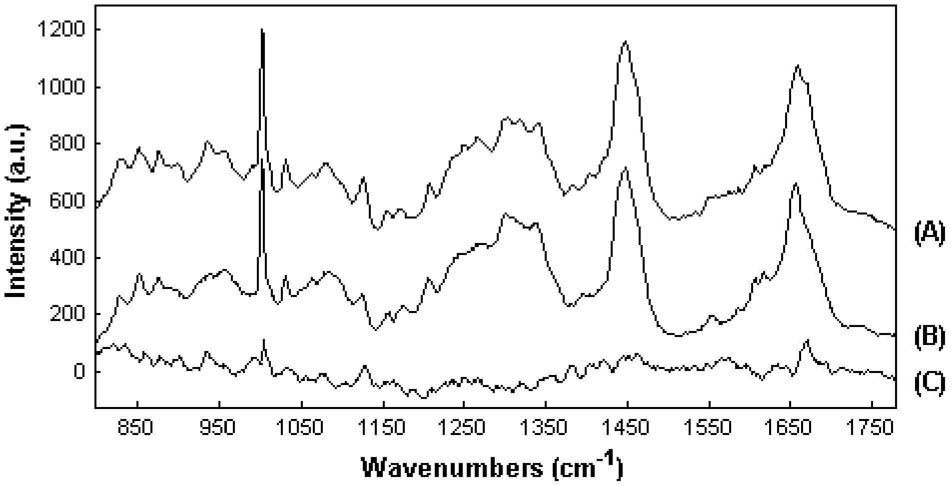

Figure A2.4 – Results of the OLS fitting of the mean spectrum derived for the green cluster in the MII oocyte. The plot shows (A) the mean spectrum derived from the original data (B) the fitted spectrum obtained from the OLS fitting and (C) the residual spectrum which is calculated by subtracting B from A. The spectra have been offset for clarity.

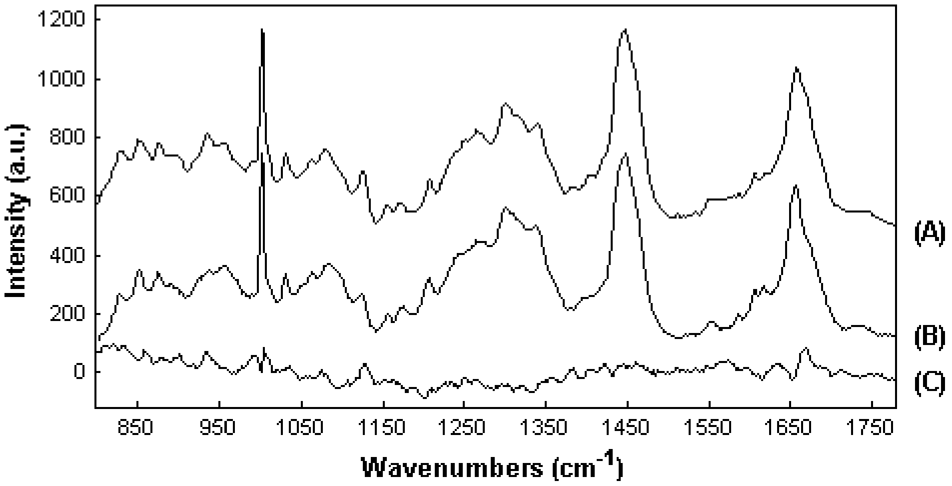

Figure A2.5 – Results of the OLS fitting of the mean spectrum derived for the blue cluster in the MII oocyte. The plot shows (A) the mean spectrum derived from the original data (B) the fitted spectrum obtained from the OLS fitting and (C) the residual spectrum which is calculated by subtracting B from A. The spectra have been offset for clarity.

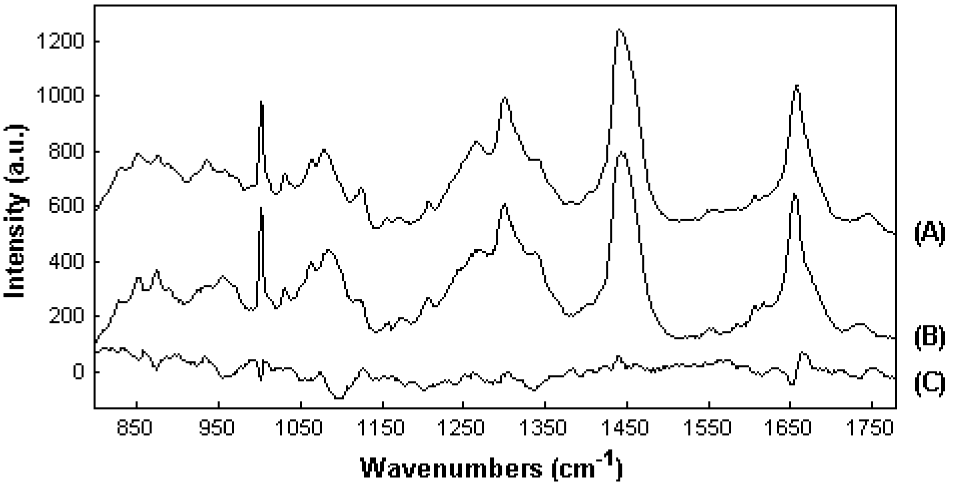

Figure A2.6 – Results of the OLS fitting of the mean spectrum derived for the red cluster in the MII oocyte. The plot shows (A) the mean spectrum derived from the original data (B) the fitted spectrum obtained from the OLS fitting and (C) the residual spectrum which is calculated by subtracting B from A. The spectra have been offset for clarity.

A2.4 The 2-cell Embryo

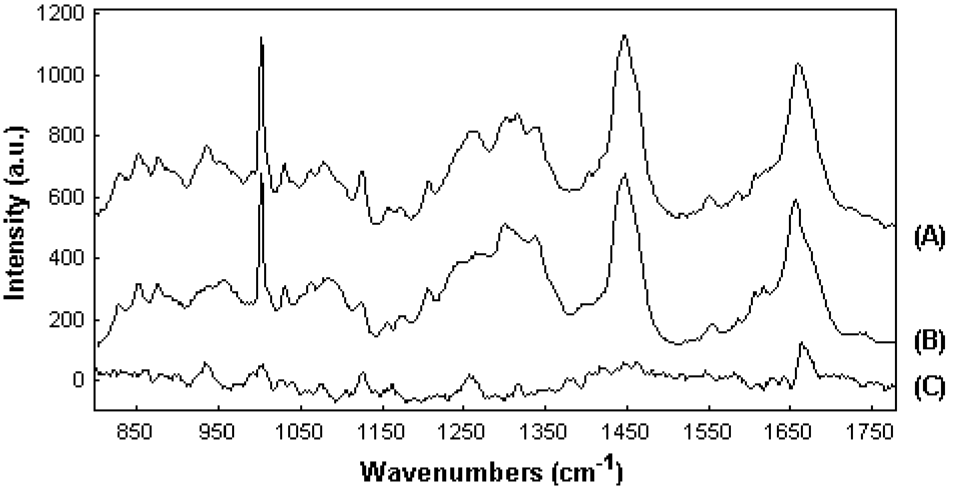

Figure A2.7 – Results of the OLS fitting of the mean spectrum derived for the green cluster in the 2-cell embryo. The plot shows (A) the mean spectrum derived from the original data (B) the fitted spectrum obtained from the OLS fitting and (C) the residual spectrum which is calculated by subtracting B from A. The spectra have been offset for clarity.

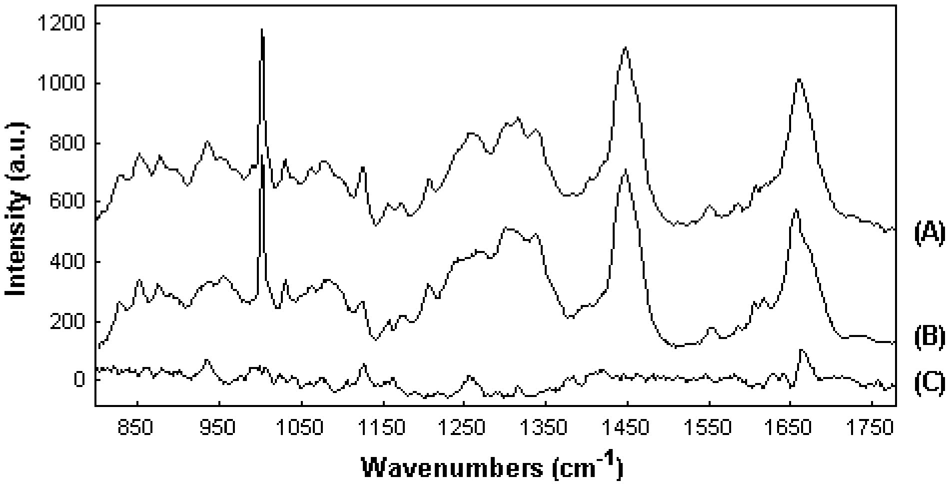

Figure A2.8 – Results of the OLS fitting of the mean spectrum derived for the blue cluster in the 2-cell embryo. The plot shows (A) the mean spectrum derived from the original data (B) the fitted spectrum obtained from the OLS fitting and (C) the residual spectrum which is calculated by subtracting B from A. The spectra have been offset for clarity.

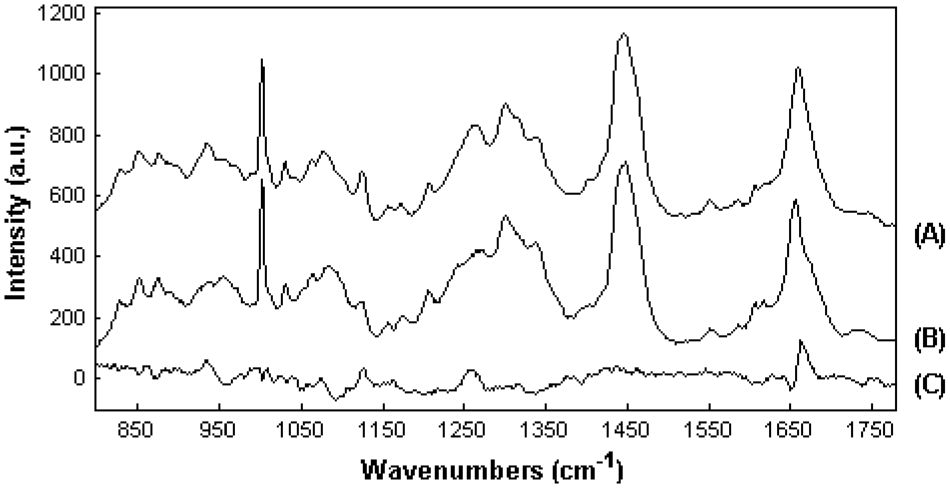

Figure A2.9 – Results of the OLS fitting of the mean spectrum derived for the red cluster in the 2-cell embryo. The plot shows (A) the mean spectrum derived from the original data (B) the fitted spectrum obtained from the OLS fitting and (C) the residual spectrum which is calculated by subtracting B from A. The spectra have been offset for clarity.

A2.5 The 4-cell Embryo

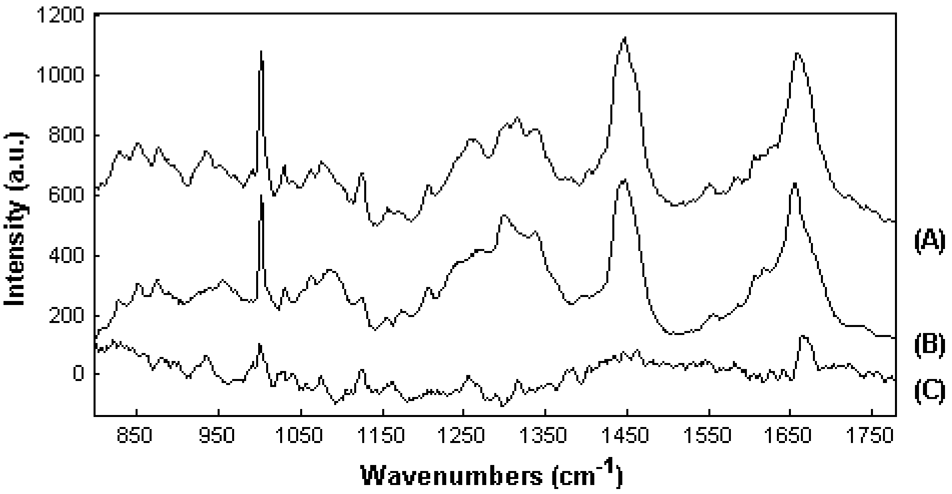

Figure A2.10 – Results of the OLS fitting of the mean spectrum derived for the green cluster in the 4-cell embryo. The plot shows (A) the mean spectrum derived from the original data (B) the fitted spectrum obtained from the OLS fitting and (C) the residual spectrum which is calculated by subtracting B from A. The spectra have been offset for clarity.

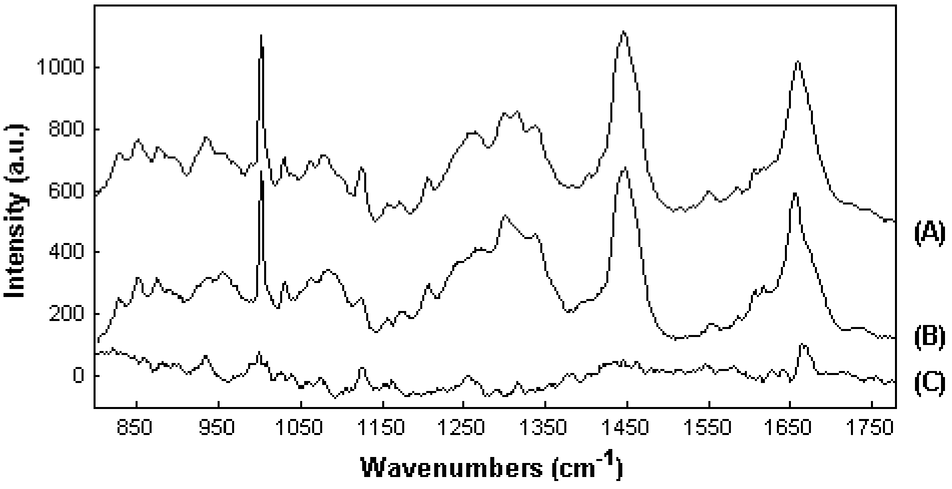

Figure A2.11 – Results of the OLS fitting of the mean spectrum derived for the blue cluster in the 4-cell embryo. The plot shows (A) the mean spectrum derived from the original data (B) the fitted spectrum obtained from the OLS fitting and (C) the residual spectrum which is calculated by subtracting B from A. The spectra have been offset for clarity.

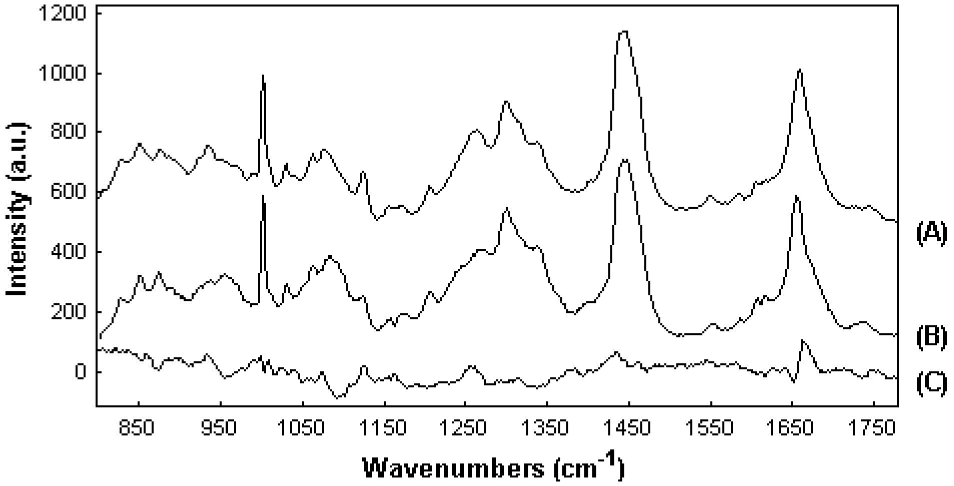

Figure A2.12 – Results of the OLS fitting of the mean spectrum derived for the red cluster in the 4-cell embryo. The plot shows (A) the mean spectrum derived from the original data (B) the fitted spectrum obtained from the OLS fitting and (C) the residual spectrum which is calculated by subtracting B from A. The spectra have been offset for clarity.

References

1. HFEA, *Fertility Facts and Figures 2007*. 2009, Human Fertility and Embryology Authority. p. 14.

2. HFEA, *A long term analysis of the HFEA Register data 1991 - 2006*. 2007, Human Fertility and Embryology Authority. p. 100.

3. Wang, J. and M.V. Sauer, *In vitro fertilization (IVF): a review of 3 decades of clinical innovation and technological advancement.* Ther Clin Risk Manag, 2006. **2**(4): p. 355-64.

4. DeBaun, M.R., E.L. Niemitz, and A.P. Feinberg, *Association of in vitro fertilization with Beckwith-Wiedemann syndrome and epigenetic alterations of LIT1 and H19.* Am J Hum Genet, 2003. **72**(1): p. 156-60.

5. Hansen, M., et al., *Assisted reproductive technologies and the risk of birth defects--a systematic review.* Hum Reprod, 2005. **20**(2): p. 328-38.

6. Hansen, M., et al., *The risk of major birth defects after intracytoplasmic sperm injection and in vitro fertilization.* N Engl J Med, 2002. **346**(10): p. 725-30.

7. Capel, B., et al., *Migration of mesonephric cells into the mammalian gonad depends on Sry.* Mech Dev, 1999. **84**(1-2): p. 127-31.

8. Yoshida, H., et al., *Stepwise requirement of c-kit tyrosine kinase in mouse ovarian follicle development.* Dev Biol, 1997. **184**(1): p. 122-37.

9. Johnson, J., et al., *Germline stem cells and follicular renewal in the postnatal mammalian ovary.* Nature, 2004. **428**(6979): p. 145-50.

10. Johnson, J., et al., *Oocyte generation in adult mammalian ovaries by putative germ cells in bone marrow and peripheral blood.* Cell, 2005. **122**(2): p. 303-15.

11. Zou, K., et al., *Production of offspring from a germline stem cell line derived from neonatal ovaries.* Nat Cell Biol, 2009. **11**(5): p. 631-6.

12. Canning, J., Y. Takai, and J.L. Tilly, *Evidence for genetic modifiers of ovarian follicular endowment and development from studies of five inbred mouse strains.* Endocrinology, 2003. **144**(1): p. 9-12.

13. Peters, H., *The development of the mouse ovary from birth to maturity.* Acta Endocrinol (Copenh), 1969. **62**(1): p. 98-116.

14. Gosden, R.G., *Ovulation 1: Oocyte development through life*, in *Gametes - The Oocyte*, J.G. Grudzinskas and J.L. Yovich, Editors. 1995, Cambridge University Press: Cambridge. p. 119-149.

15. Pepling, M.E. and A.C. Spradling, *Mouse ovarian germ cell cysts undergo programmed breakdown to form primordial follicles.* Dev Biol, 2001. **234**(2): p. 339-51.

16. Lintern-Moore, S. and G.P. Moore, *The initiation of follicle and oocyte growth in the mouse ovary.* Biol Reprod, 1979. **20**(4): p. 773-8.

17. van den Hurk, R. and J. Zhao, *Formation of mammalian oocytes and their growth, differentiation and maturation within ovarian follicles.* Theriogenology, 2005. **63**(6): p. 1717-51.

18. Myers, M., et al., *Methods for quantifying follicular numbers within the mouse ovary.* Reproduction, 2004. **127**(5): p. 569-80.

19. Murray, A.A. and N. Spears, *What makes a good egg?*, in *Implantation and early development*, H.O.D. Critchley, I.T. Cameron, and S.K. Smith, Editors. 2005, RCOG Press: London. p. xiv, 304 p.

20. Durlinger, A.L., et al., *Anti-Mullerian hormone inhibits initiation of primordial follicle growth in the mouse ovary.* Endocrinology, 2002. **143**(3): p. 1076-84.

21. Parrott, J.A. and M.K. Skinner, *Kit-ligand/stem cell factor induces primordial follicle development and initiates folliculogenesis.* Endocrinology, 1999. **140**(9): p. 4262-71.

22. Hutt, K.J., E.A. McLaughlin, and M.K. Holland, *KIT/KIT ligand in mammalian oogenesis and folliculogenesis: roles in rabbit and murine ovarian follicle activation and oocyte growth.* Biol Reprod, 2006. **75**(3): p. 421-33.

23. Jagarlamudi, K., et al., *Oocyte-specific deletion of Pten in mice reveals a stage-specific function of PTEN/PI3K signaling in oocytes in controlling follicular activation.* PLoS One, 2009. **4**(7): p. e6186.

24. Murray, A. and N. Spears, *Follicular development in vitro.* Semin Reprod Med, 2000. **18**(2): p. 109-22.

25. Matzuk, M.M., et al., *Intercellular communication in the mammalian ovary: oocytes carry the conversation.* Science, 2002. **296**(5576): p. 2178-80.

26. Dong, J., et al., *Growth differentiation factor-9 is required during early ovarian folliculogenesis.* Nature, 1996. **383**(6600): p. 531-5.

27. Ginsburg, M., M.H. Snow, and A. McLaren, *Primordial germ cells in the mouse embryo during gastrulation.* Development, 1990. **110**(2): p. 521-8.

28. Chiquoine, A.D., *The identification, origin, and migration of the primordial germ cells in the mouse embryo.* Anat Rec, 1954. **118**(2): p. 135-46.

29. Mintz, B. and E.S. Russell, *Gene-induced embryological modifications of primordial germ cells in the mouse.* J Exp Zool, 1957. **134**(2): p. 207-37.

30. Picton, H., D. Briggs, and R. Gosden, *The molecular basis of oocyte growth and development.* Mol Cell Endocrinol, 1998. **145**(1-2): p. 27-37.

31. Richards, A.J., G.C. Enders, and J.L. Resnick, *Differentiation of murine premigratory primordial germ cells in culture.* Biol Reprod, 1999. **61**(4): p. 1146-51.

32. Schultz, R.M. and P.M. Wassarman, *Biochemical studies of mammalian oogenesis: Protein synthesis during oocyte growth and meiotic maturation in the mouse.* J Cell Sci, 1977. **24**: p. 167-94.

33. Gosden, R.G. and M. Bownes, *Molecular and cellular aspects of oocyte development*, in *Gametes - The Oocyte*, J.G. Grudzinskas and J.L. Yovich, Editors. 1995, Cambridge University Press: Cambridge. p. 23-53.

34. Wassarman, P.M., C. Liu, and E.S. Litscher, *Constructing the mammalian egg zona pellucida: some new pieces of an old puzzle.* J Cell Sci, 1996. **109 (Pt 8)**: p. 2001-4.

35. Ferreira, E.M., et al., *Cytoplasmic maturation of bovine oocytes: structural and biochemical modifications and acquisition of developmental competence.* Theriogenology, 2009. **71**(5): p. 836-48.

36. Tokura, T., et al., *Sequential observation of mitochondrial distribution in mouse oocytes and embryos.* J Assist Reprod Genet, 1993. **10**(6): p. 417-26.

37. Wassarman, P.M. and W.J. Josefowicz, *Oocyte development in the mouse: an ultrastructural comparison of oocytes isolated at various stages of growth and meiotic competence.* J Morphol, 1978. **156**(2): p. 209-35.

38. Wischnitzer, S., *An electron microscope study of cytoplasmic organelle transformations in developing mouse oocytes.* Development Genes and Evolution, 1970. **166**(2): p. 150-172.

39. Van Blerkom, J. and M.N. Runner, *Mitochondrial reorganization during resumption of arrested meiosis in the mouse oocyte.* Am J Anat, 1984. **171**(3): p. 335-55.

40. Zamboni, L., *Ultrastructure of mammalian oocytes and ova.* Biol Reprod Suppl, 1970. **2**: p. 44-63.

41. Ducibella, T., et al., *Quantitative studies of changes in cortical granule number and distribution in the mouse oocyte during meiotic maturation.* Dev Biol, 1988. **130**(1): p. 184-97.

42. Gosden, R.G., *Oogenesis as a foundation for embryogenesis.* Mol Cell Endocrinol, 2002. **186**(2): p. 149-53.

43. Bachvarova, R., et al., *Changes in total RNA, polyadenylated RNA, and actin mRNA during meiotic maturation of mouse oocytes.* Dev Biol, 1985. **108**(2): p. 325-31.

44. Downs, S.M., *Ovulation 2: Control of the resumption of meiotic maturation in mammalian oocytes*, in *Gametes - The Oocyte*, J.G. Grudzinskas and J.L. Yovich, Editors. 1995, Cambridge University Press: Cambridge. p. 150-192.

45. Talbot, P., B.D. Shur, and D.G. Myles, *Cell adhesion and fertilization: steps in oocyte transport, sperm-zona pellucida interactions, and sperm-egg fusion.* Biol Reprod, 2003. **68**(1): p. 1-9.

46. Hammitt, D.G., et al., *Prediction of nuclear maturity from cumulus-coronal morphology: influence of embryologist experience.* J Assist Reprod Genet, 1992. **9**(5): p. 439-46.

47. Testart, J., et al., *A study of factors affecting the success of human fertilization in vitro. I. Influence of ovarian stimulation upon the number and condition of oocytes collected.* Biol Reprod, 1983. **28**(2): p. 415-24.

48. Rattanachaiyanont, M., A. Leader, and M.C. Leveille, *Lack of correlation between oocyte-corona-cumulus complex morphology and nuclear maturity of oocytes collected in stimulated cycles for intracytoplasmic sperm injection.* Fertil Steril, 1999. **71**(5): p. 937-40.

49. Ebner, T., et al., *Blood clots in the cumulus-oocyte complex predict poor oocyte quality and post-fertilization development.* Reprod Biomed Online, 2008. **16**(6): p. 801-7.

50. Ng, S.T., T.H. Chang, and T.C. Wu, *Prediction of the rates of fertilization, cleavage, and pregnancy success by cumulus-coronal morphology in an in vitro fertilization program.* Fertil Steril, 1999. **72**(3): p. 412-7.

51. Bar-Ami, S., H. Gitay-Goren, and J.M. Brandes, *Different morphological and steroidogenic patterns in oocyte/cumulus-corona cell complexes aspirated at in vitro fertilization.* Biol Reprod, 1989. **41**(4): p. 761-70.

52. Lin, Y.C., et al., *Human oocyte maturity in vivo determines the outcome of blastocyst development in vitro.* J Assist Reprod Genet, 2003. **20**(12): p. 506-12.

53. Gregory, L., et al., *A study of the cumulus-corona cell complex in in-vitro fertilization and embryo transfer; a prognostic indicator of the failure of implantation.* Hum Reprod, 1994. **9**(7): p. 1308-17.

54. Xia, P., *Intracytoplasmic sperm injection: correlation of oocyte grade based on polar body, perivitelline space and cytoplasmic inclusions with fertilization rate and embryo quality.* Hum Reprod, 1997. **12**(8): p. 1750-5.

55. Balaban, B., et al., *Oocyte morphology does not affect fertilization rate, embryo quality and implantation rate after intracytoplasmic sperm injection.* Hum Reprod, 1998. **13**(12): p. 3431-3.

56. De Sutter, P., et al., *Oocyte morphology does not correlate with fertilization rate and embryo quality after intracytoplasmic sperm injection.* Hum Reprod, 1996. **11**(3): p. 595-7.

57. Serhal, P.F., et al., *Oocyte morphology predicts outcome of intracytoplasmic sperm injection.* Hum Reprod, 1997. **12**(6): p. 1267-70.

58. Ebner, T., et al., *Occurrence and developmental consequences of vacuoles throughout preimplantation development.* Fertil Steril, 2005. **83**(6): p. 1635-40.

59. Ebner, T., et al., *Prognosis of oocytes showing aggregation of smooth endoplasmic reticulum.* Reprod Biomed Online, 2008. **16**(1): p. 113-8.

60. Loutradis, D., et al., *Oocyte morphology correlates with embryo quality and pregnancy rate after intracytoplasmic sperm injection.* Fertil Steril, 1999. **72**(2): p. 240-4.

61. Ebner, T., et al., *First polar body morphology and blastocyst formation rate in ICSI patients.* Hum Reprod, 2002. **17**(9): p. 2415-8.

62. Ebner, T., et al., *Elective transfer of embryos selected on the basis of first polar body morphology is associated with increased rates of implantation and pregnancy.* Fertil Steril, 1999. **72**(4): p. 599-603.

63. Ebner, T., et al., *Prognostic value of first polar body morphology on fertilization rate and embryo quality in intracytoplasmic sperm injection.* Hum Reprod, 2000. **15**(2): p. 427-30.

64. Ciotti, P.M., et al., *First polar body morphology before ICSI is not related to embryo quality or pregnancy rate.* Hum Reprod, 2004. **19**(10): p. 2334-9.

65. De Santis, L., et al., *Polar body morphology and spindle imaging as predictors of oocyte quality.* Reprod Biomed Online, 2005. **11**(1): p. 36-42.

66. Verlinsky, Y., et al., *Is there any predictive value of first polar body morphology for embryo genotype or developmental potential?* Reprod Biomed Online, 2003. **7**(3): p. 336-41.

67. Liu, L., et al., *A reliable, noninvasive technique for spindle imaging and enucleation of mammalian oocytes.* Nat Biotechnol, 2000. **18**(2): p. 223-5.

68. Cohen, Y., et al., *Spindle imaging: a new marker for optimal timing of ICSI?* Hum Reprod, 2004. **19**(3): p. 649-54.

69. Madaschi, C., et al., *Spindle imaging: a marker for embryo development and implantation.* Fertil Steril, 2007.

70. Wang, W.H., et al., *Developmental ability of human oocytes with or without birefringent spindles imaged by Polscope before insemination.* Hum Reprod, 2001. **16**(7): p. 1464-8.

71. Rama Raju, G.A., et al., *Meiotic spindle and zona pellucida characteristics as predictors of embryonic development: a preliminary study using PolScope imaging.* Reprod Biomed Online, 2007. **14**(2): p. 166-74.

72. Braga, D.P., et al., *Prognostic value of meiotic spindle imaging on fertilization rate and embryo development in in vitro matured human oocytes.* Fertil Steril, 2007.

73. Bianchi, V., et al., *Meiotic spindle imaging in human oocytes frozen with a slow freezing procedure involving high sucrose concentration.* Hum Reprod, 2005. **20**(4): p. 1078-83.

74. Chen, C.K., et al., *Evaluation of meiotic spindles in thawed oocytes after vitrification using polarized light microscopy.* Fertil Steril, 2004. **82**(3): p. 666-72.

75. Rienzi, L., et al., *Polscope analysis of meiotic spindle changes in living metaphase II human oocytes during the freezing and thawing procedures.* Hum Reprod, 2004. **19**(3): p. 655-9.

76. Wang, W.H., et al., *Limited recovery of meiotic spindles in living human oocytes after cooling-rewarming observed using polarized light microscopy.* Hum Reprod, 2001. **16**(11): p. 2374-8.

77. Liu, L., et al., *Increased birefringence in the meiotic spindle provides a new marker for the onset of activation in living oocytes.* Biol Reprod, 2000. **63**(1): p. 251-8.

78. Thomas, N., et al., *Fourier transform infrared spectroscopy of follicular fluids from large and small antral follicles.* Hum Reprod, 2000. **15**(8): p. 1667-71.

79. Tarlatzis, B.C., et al., *Growth hormone, oestradiol, progesterone and testosterone concentrations in follicular fluid after ovarian stimulation with various regimes for assisted reproduction.* Hum Reprod, 1993. **8**(10): p. 1612-6.

80. Wunder, D.M., et al., *Steroids and protein markers in the follicular fluid as indicators of oocyte quality in patients with and without endometriosis.* J Assist Reprod Genet, 2005. **22**(6): p. 257-64.

81. Mendoza, C., et al., *Relationship between fertilization results after intracytoplasmic sperm injection, and intrafollicular steroid, pituitary hormone and cytokine concentrations.* Hum Reprod, 1999. **14**(3): p. 628-35.

82. Mendoza, C., et al., *Follicular fluid markers of oocyte developmental potential.* Hum Reprod, 2002. **17**(4): p. 1017-22.

83. Verpoest, W.M., et al., *Relationship between midcycle luteinizing hormone surge quality and oocyte fertilization.* Fertil Steril, 2000. **73**(1): p. 75-7.

84. Artini, P.G., et al., *Relationship between human oocyte maturity, fertilization and follicular fluid growth factors.* Hum Reprod, 1994. **9**(5): p. 902-6.

85. Jimena, P., et al., *Insulin and insulin-like growth factor I in follicular fluid after induction of ovulation in women undergoing in vitro fertilization.* J Reprod Fertil, 1992. **96**(2): p. 641-7.

86. Wang, T.H., et al., *Insulin-like growth factor-II (IGF-II), IGF-binding protein-3 (IGFBP-3), and IGFBP-4 in follicular fluid are associated with oocyte maturation and embryo development.* Fertil Steril, 2006. **86**(5): p. 1392-401.

87. Wu, Y.T., et al., *High bone morphogenetic protein-15 level in follicular fluid is associated with high quality oocyte and subsequent embryonic development.* Hum Reprod, 2007. **22**(6): p. 1526-31.

88. Takahashi, C., et al., *Anti-Mullerian hormone substance from follicular fluid is positively associated with success in oocyte fertilization during in vitro fertilization.* Fertil Steril, 2008. **89**(3): p. 586-91.

89. Yanaihara, A., et al., *High concentrations of lactoferrin in the follicular fluid correlate with embryo quality during in vitro fertilization cycles.* Fertil Steril, 2007. **87**(2): p. 279-82.

90. Anifandis, G., et al., *Serum and follicular fluid leptin levels are correlated with human embryo quality.* Reproduction, 2005. **130**(6): p. 917-21.

91. Georgios, A., et al., *Serum and follicular fluid leptin levels are correlated with human embryo quality.* Reproduction, 2005. **130**: p. 917-921.

92. Mantzoros, C.S., et al., *Predictive value of serum and follicular fluid leptin concentrations during assisted reproductive cycles in normal women and in women with the polycystic ovarian syndrome.* Hum Reprod, 2000. **15**(3): p. 539-44.

93. Sinclair, K.D., et al., *Amino acid and fatty acid composition of follicular fluid as predictors of in-vitro embryo development.* Reprod Biomed Online, 2008. **16**(6): p. 859-68.

94. Gerard, N., et al., *Analysis of the variations of follicular fluid composition during follicular growth and maturation in the mare using proton nuclear magnetic resonance (1H NMR).* Reproduction, 2002. **124**(2): p. 241-8.

95. Huyser, C., F.L. Fourie, and P. Levay, *Spectrophotometric analysis of human follicular fluid with regard to in vitro fertilization (IVF) parameters, follicular protein, and hormone content.* J Assist Reprod Genet, 1993. **10**(5): p. 371-8.

96. Smitz, J., et al., *Endocrine profile in serum and follicular fluid differs after ovarian stimulation with HP-hMG or recombinant FSH in IVF patients.* Hum Reprod, 2007. **22**(3): p. 676-87.

97. Stadtmauer, L., et al., *Follicular fluid insulin-like growth factor-I and insulin-like growth factor-binding protein-1 and -3 vary as a function of ovarian reserve and ovarian stimulation.* J Assist Reprod Genet, 1998. **15**(10): p. 587-93.

98. O'Callaghan, D., et al., *Effect of nutrition and superovulation on oocyte morphology, follicular fluid composition and systemic hormone concentrations in ewes.* J Reprod Fertil, 2000. **118**(2): p. 303-13.

99. Brison, D.R., et al., *Identification of viable embryos in IVF by non-invasive measurement of amino acid turnover.* Hum Reprod, 2004. **19**(10): p. 2319-24.

100. Houghton, F.D., et al., *Non-invasive amino acid turnover predicts human embryo developmental capacity.* Hum Reprod, 2002. **17**(4): p. 999-1005.

101. Seli, E., et al., *Noninvasive metabolomic profiling of embryo culture media using proton nuclear magnetic resonance correlates with reproductive potential of embryos in women undergoing in vitro fertilization.* Fertil Steril, 2008. **90**(6): p. 2183-9.

102. Scott, R., et al., *Noninvasive metabolomic profiling of human embryo culture media using Raman spectroscopy predicts embryonic reproductive potential: a prospective blinded pilot study.* Fertil Steril, 2008. **90**(1): p. 77-83.

103. Seli, E., et al., *Noninvasive metabolomic profiling of embryo culture media using Raman and near-infrared spectroscopy correlates with reproductive potential of embryos in women undergoing in vitro fertilization.* Fertil Steril, 2007. **88**(5): p. 1350-7.

104. Vergouw, C.G., et al., *Metabolomic profiling by near-infrared spectroscopy as a tool to assess embryo viability: a novel, non-invasive method for embryo selection.* Hum Reprod, 2008. **23**(7): p. 1499-504.

105. Nagy, Z.P., et al., *Metabolomic assessment of oocyte viability.* Reprod Biomed Online, 2009. **18**(2): p. 219-25.

106. Cillo, F., et al., *Association between human oocyte developmental competence and expression levels of some cumulus genes.* Reproduction, 2007. **134**(5): p. 645-50.

107. McKenzie, L.J., et al., *Human cumulus granulosa cell gene expression: a predictor of fertilization and embryo selection in women undergoing IVF.* Hum Reprod, 2004. **19**(12): p. 2869-74.

108. Zhang, X., et al., *Studies of gene expression in human cumulus cells indicate pentraxin 3 as a possible marker for oocyte quality.* Fertil Steril, 2005. **83 Suppl 1**: p. 1169-79.

109. Bettegowda, A., et al., *Identification of novel bovine cumulus cell molecular markers predictive of oocyte competence: functional and diagnostic implications.* Biol Reprod, 2008. **79**(2): p. 301-9.

110. Hasegawa, J., et al., *Reduction of progesterone receptor expression in human cumulus cells at the time of oocyte collection during IVF is associated with good embryo quality.* Hum Reprod, 2005. **20**(8): p. 2194-200.

111. Altarescu, G., et al., *Successful polar body-based preimplantation genetic diagnosis for achondroplasia.* Reprod Biomed Online, 2008. **16**(2): p. 276-82.

112. Verlinsky, Y., et al., *Polar body-based preimplantation diagnosis for X-linked disorders.* Reprod Biomed Online, 2002. **4**(1): p. 38-42.

113. Braude, P., et al., *Preimplantation genetic diagnosis.* Nat Rev Genet, 2002. **3**(12): p. 941-53.

114. Smith, E. and G. Dent, *Modern Raman spectroscopy : a practical approach*. 2005, Chichester: John Wiley. x, 210 p.

115. Chalmers, J.M. and P.R. Griffiths, *Handbook of vibrational spectroscopy*. 2002, Chichester: Wiley. 5 v. (xviii, 3862 p.).

116. Ferraro, J.R. and K. Nakamoto, *Introductory Raman spectroscopy*. 1994, Boston ; London: Academic Press.

117. Socrates, G. and G.I.c.g.f. Socrates, *Infrared and Raman characteristic group frequencies : tables and charts*. 3rd ed. ed. 2001, Chichester: Wiley. xv, 347 p.

118. Edsall, J., T. , *Raman Spectra of Amino Acids and Related Compounds I. The Ionization of the Carboxyl Group.* The Journal of Chemical Physics, 1936. **4**(1): p. 1-8.

119. Carey, P.R., *Raman spectroscopy, the sleeping giant in structural biology, awakes.* J Biol Chem, 1999. **274**(38): p. 26625-8.

120. Diem, M., et al., *A decade of vibrational micro-spectroscopy of human cells and tissue (1994-2004).* Analyst, 2004. **129**(10): p. 880-5.

121. Owen, C.A., et al., *Progress in Raman spectroscopy in the fields of tissue engineering, diagnostics and toxicological testing.* J Mater Sci Mater Med, 2006. **17**(11): p. 1019-23.

122. Swain, R.J. and M.M. Stevens, *Raman microspectroscopy for non-invasive biochemical analysis of single cells.* Biochem Soc Trans, 2007. **35**(Pt 3): p. 544-9.

123. Bellocq, A.M., R.C. Lord, and R. Mendelsohn, *Laser-excited Raman spectroscopy of biomolecules. 3. Native bovine serum albumin and beta-lactoglobulin.* Biochim Biophys Acta, 1972. **257**(2): p. 280-7.

124. Chen, M.C. and R.C. Lord, *Laser-excited Raman spectroscopy of biomolecules. VIII. Conformational study of bovine serum albumin.* J Am Chem Soc, 1976. **98**(4): p. 990-2.

125. Chen, M.C., R.C. Lord, and R. Mendelsohn, *Laser-excited raman spectroscopy of biomolecules. IV. Thermal denaturation of aqueous lysozyme.* Biochim Biophys Acta, 1973. **328**(2): p. 252-60.

126. Lord, R.C. and N.T. Yu, *Laser-excited Raman spectroscopy of biomolecules. II. Native ribonuclease and alpha-chymotrypsin.* J Mol Biol, 1970. **51**(2): p. 203-13.

127. Lord, R.C. and N.T. Yu, *Laser-excited Raman spectroscopy of biomolecules. I. Native lysozyme and its constituent amino acids.* J Mol Biol, 1970. **50**(2): p. 509-24.

128. Chen, M.C. and R.C. Lord, *Laser-excited Raman spectroscopy of biomolecules. VI. Some polypeptides as conformational models.* J Am Chem Soc, 1974. **96**(15): p. 4750-2.

129. Overman, S.A., et al., *Effects of virion and salt concentrations on the Raman signatures of filamentous phages fd, Pf1, Pf3, and PH75.* Biochemistry, 2004. **43**(41): p. 13129-13136.

130. Tuma, R. and G.J. Thomas Jr, *Mechanisms of virus assembly probed by Raman spectroscopy: the icosahedral bacteriophage P22.* Biophysical Chemistry, 1997. **68**: p. 17-31.

131. Rodriguez-Casado, A., et al., *Structure of bacteriophage P22 portal protein in relation to assembly: investigation by Raman spectroscopy.* Biochemistry, 2001. **40**: p. 13583-13591.

132. Hawi, S.R., et al., *Raman microspectroscopy of intracellular cholesterol crystals in cultured bovine coronary artery endothelial cells.* J Lipid Res, 1997. **38**(8): p. 1591-7.

133. Romer, T.J., et al., *Raman spectroscopy for quantifying cholesterol in intact coronary artery wall.* Atherosclerosis, 1998. **141**: p. 117-124.

134. van Manen, H., et al., *Single-cell Raman and fluorescence microscopy reveal the association of lipid bodies with phagosomes in leukocytes.* Proceedings of the National Academy of Science of the United States of America, 2005. **102**(29): p. 10159-10164.

135. Potma, E.O. and X.S. Xie, *Detection of single lipid bilayers with coherent anti-Stokes Raman scattering (CARS) microscopy.* Journal of Raman Spectroscopy, 2003. **34**: p. 642-650.

136. Hellerer, T., et al., *Monitoring of lipid storage in Caenorhabditis elegans using coherent anti-Stokes Raman scattering (CARS) microscopy.* Proceedings of the

National Academy of Science of the United States of America, 2007. **104**(37): p. 14658-14663.

137. Nan, X., J. Cheng, and X.S. Xie, *Vibrational imaging of lipid droplets in live fibroblast cells with coherent anti-Stokes Raman scattering microscopy.* Journal of Lipid Research, 2003. **44**: p. 2202-2208.

138. Cheng, J., et al., *Multiplex coherent anti-Stokes Raman scattering microspectroscopy and study of lipid vesicles.* Journal of Physical Chemistry B, 2002. **106**: p. 8493-8498.

139. Mathlouthi, M., A. Seuvre, and J.L. Koenig, *FT-IR and laser-raman spectra of adenine and adenosine.* Carbohydrate Research, 1984. **131**: p. 1-15.

140. Mathlouthi, M., A. Seuvre, and J.L. Koenig, *FT-IR and laser-Raman spectra of thymine and thymidine.* Carbohydrate Research, 1984. **134**: p. 23-38.

141. Mathlouthi, M., A. Seuvre, and J.L. Koenig, *FT-IR and laser-Raman spectra of cytosine and cytidine.* Carbohydrate Research, 1986. **146**: p. 1-13.

142. Mathlouthi, M., A. Seuvre, and J.L. Koenig, *FT-IR and laser-Raman spectra of guanine and guanosine.* Carbohydrate Research, 1986. **146**: p. 15-27.

143. Rimai, L., et al., *Studies of Raman spectra of water solutions of adenosine tri-, di-, and monophosphate and some related compounds.* Biophysical Journal, 1969. **9**: p. 320-329.

144. Fodor, S.P.A., et al., *Ultraviolet resonance Raman spectroscopy of the nucleotides with 266-, 240-, 218, and 200-nm pulsed laser excitation.* Journal of the American Chemical Society, 1985. **107**: p. 1520-1529.

145. Rasmussen, A. and V. Deckert, *Surface- and tip-enhanced Raman scattering of DNA components.* Journal of Raman Spectroscopy, 2006. **37**: p. 311-317.

146. Kneipp, K., et al., *Detection and identification of a single DNA base molecule using surface-enhanced Raman scattering (SERS).* Physical Reviews E, 1998. **57**(6): p. 6281-6284.

147. Erfurth, S.C., E.J. Kiser, and W.L. Peticolas, *Determination of the backbone structure of nucleic acids and nucleic acid oligomers by laser Raman scattering.* Proceedings of the National Academy of Science of the United States of America, 1972. **69**(4): p. 938-941.

148. Ke, W., D. Yu, and J. Wu, *Raman spectroscopic study of the influence on herring sperm DNA of heat treatment and ultraviolet radiation.* Spectrochimia Acta Part A, 1999. **55**: p. 1081-1090.

149. Muntean, C.M. and G.M.J. Segers-Nolten, *Raman microspectroscopic study of effects of Na(I) and Mg(II) ions on low pH induced DNA structural changes.* Biopolymers, 2003. **72**: p. 225-229.

150. O'Connor, T., et al., *The pH-dependant structure of calf thymus DNA studied by Raman spectroscopy.* Biophysical Chemistry, 1982. **15**(1): p. 53-64.

151. Notingher, I., et al., *In situ spectroscopic study of nucleic acids in differentiating embryonic stem cells.* Vibrational Spectroscopy, 2004. **35**: p. 199-203.

152. Uzunbajakava, N., et al., *Nonresonant confocal Raman imaging of DNA and protein distribution in apoptotic cells.* Biophys J, 2003. **84**(6): p. 3968-81.

153. Peticolas, W.L., et al., *Laser Raman microscopy of chromosomes in living eukaryotic cells: DNA polymorphism in vivo.* Journal of Raman Spectroscopy, 1996. **27**: p. 571-578.

154. Bailo, E. and V. Deckert, *Tip-enhanced Raman spectroscopy of single RNA strands: Towards a novel direct-sequencing method.* Angewandte Chemie - International Edition, 2008. **47**(9): p. 1658-1661.

155. Xie, C., et al., *Identification of single bacterial cells in aqueous solution using confocal laser tweezers Raman spectroscopy.* Anal Chem, 2005. **77**(14): p. 4390-7.

156. Harz, M., et al., *Micro-Raman spectroscopic identification of bacterial cells of the genus Staphylococcus and dependence on their cultivation conditions.* Analyst, 2005. **130**(11): p. 1543-50.

157. Kirschner, C., et al., *Classification and identification of enterococci: a comparative phenotypic, genotypic, and vibrational spectroscopic study.* J Clin Microbiol, 2001. **39**(5): p. 1763-70.

158. Berger, A.J. and Q.Y. Zhu, *Identification of oral bacteria by Raman microspectroscopy.* Journal of Modern Optics, 2003. **50**(15-17): p. 2375-2380.

159. Mello, C., et al., *Rapid differentiation among bacteria that cause gastroenteritis by use of low-resolution Raman spectroscopy and PLS discriminant analysis.* Analytical and Bioanalytical Chemistry, 2005. **383**(4): p. 701-706.

160. Mello, C., et al., *Fast differentiation of bacteria causing pharyngitis by low resolution Raman spectroscopy and PLS-discriminant analysis.* Journal of the Brazilian Chemical Society, 2008. **19**(1): p. 29-34.

161. Maquelin, K., et al., *Rapid epidemiological analysis of Acinetobacter strains by Raman spectroscopy.* J Microbiol Methods, 2006. **64**(1): p. 126-31.

162. Rosch, P., et al., *Chemotaxonomic identification of single bacteria by micro-Raman spectroscopy: application to clean-room-relevant biological contaminations.* Appl Environ Microbiol, 2005. **71**(3): p. 1626-37.

163. Jarvis, R.M. and R. Goodacre, *Discrimination of bacteria using surface-enhanced Raman spectroscopy.* Anal Chem, 2004. **76**(1): p. 40-7.

164. Puppels, G.J., et al., *Raman microspectroscopic approach to the study of human granulocytes.* Biophys J, 1991. **60**(5): p. 1046-56.

165. Ramanauskaite, R.B., et al., *Carotenoid levels in human lymphocytes measured by Raman microspectroscopy.* Pure and Applied Chemistry, 1997. **69**(10): p. 2131-2134.

166. Chan, J.W., et al., *Nondestructive identification of individual leukemia cells by laser trapping Raman spectroscopy.* Anal Chem, 2008. **80**(6): p. 2180-7.

167. Notingher, I., et al., *In situ non-invasive spectral discrimination between bone cell phenotypes used in tissue engineering.* J Cell Biochem, 2004. **92**(6): p. 1180-92.

168. Verrier, S., et al., *In situ monitoring of cell death using Raman microspectroscopy.* Biopolymers, 2004. **74**(1-2): p. 157-62.

169. Notingher, I., et al., *In situ spectral monitoring of mRNA translation in embryonic stem cells during differentiation in vitro.* Anal Chem, 2004. **76**(11): p. 3185-93.

170. Notingher, I., et al., *Spectroscopic study of human lung epithelial cells (A549) in culture: living cells versus dead cells.* Biopolymers, 2003. **72**(4): p. 230-40.

171. Krafft, C., et al., *Mapping of single cells by near infrared Raman microspectroscopy.* Vibrational Spectroscopy, 2003. **32**: p. 75-83.

172. Krafft, C., et al., *Identification of organelles and vesicles in single cells by Raman microspectroscopic mapping.* Vibrational Spectroscopy, 2005. **38**: p. 85-93.

173. Matthaus, C., et al., *Label-free detection of mitochondrial distribution in cells by nonresonant Raman microspectroscopy.* Biophys J, 2007. **93**(2): p. 668-73.

174. Krafft, C., et al., *Studies on stress-induced changes at the subcellular level by Raman microspectroscopic mapping.* Anal Chem, 2006. **78**(13): p. 4424-9.

175. Uzunbajakava, N., et al., *Nonresonant Raman imaging of protein distribution in single human cells.* Biopolymers, 2003. **72**(1): p. 1-9.

176. Arikan, S., et al., *Raman spectroscopy and imaging of beta-carotene in live corpus luteum cells.* Anim Reprod Sci, 2002. **71**(3-4): p. 249-66.

177. Notingher, I., et al., *Multivariate analysis of Raman spectra for in vitro non-invasive studies of living cells.* Journal of Molecular Structure, 2005. **744-747**: p. 179-185.

178. Swain, R.J., G. Jell, and M.M. Stevens, *Non-invasive analysis of cell cycle dynamics in single living cells with Raman micro-spectroscopy.* J Cell Biochem, 2008. **104**(4): p. 1427-38.

179. Notingher, I., J. Selvakumaran, and L.L. Hench, *New detection system for toxic agents based on continuous spectroscopic monitoring of living cells.* Biosens Bioelectron, 2004. **20**(4): p. 780-9.

180. Kang, L.L., et al., *Confocal Raman microscopy on single living young and old erythrocytes.* Biopolymers, 2008. **89**(11): p. 951-9.

181. Jess, P.R., et al., *Early detection of cervical neoplasia by Raman spectroscopy.* Int J Cancer, 2007. **121**(12): p. 2723-8.

182. Chan, J.W., et al., *Micro-Raman spectroscopy detects individual neoplastic and normal hematopoietic cells.* Biophys J, 2006. **90**(2): p. 648-56.

183. Harvey, T.J., et al., *Spectral discrimination of live prostate and bladder cancer cell lines using Raman optical tweezers.* J Biomed Opt, 2008. **13**(6): p. 064004.

184. Krafft, C., et al., *Near infrared Raman spectroscopy to study the composition of human brain tissue and tumors*, in *Diagnostic Optical Spectroscopy in Biomedicine II*. 2003, Proceedings of SPIE-OSA Biomedical Optics: Munich, Germany.

185. Krafft, C., et al., *Near infrared Raman spectroscopic mapping of native brain tissue and intracranial tumors.* Analyst, 2005. **130**(7): p. 1070-7.

186. Krafft, C., et al., *Raman and infrared spectroscopic mapping of human primary intracranial tumors: a comparative study.* Journal of Raman Spectroscopy, 2006. **37**: p. 367-375.

187. Koljenovic, S., et al., *Tissue characterization using high wave number Raman spectroscopy.* J Biomed Opt, 2005. **10**(3): p. 031116.

188. Koljenovic, S., et al., *Discriminating vital tumor from necrotic tissue in human glioblastoma tissue samples by Raman spectroscopy.* Lab Invest, 2002. **82**(10): p. 1265-77.

189. Amharref, N., et al., *Discriminating healthy from tumor and necrosis tissue in rat brain tissue samples by Raman spectral imaging.* Biochim Biophys Acta, 2007. **1768**(10): p. 2605-15.

190. Haka, A.S., et al., *Diagnosing breast cancer by using Raman spectroscopy.* Proc Natl Acad Sci U S A, 2005. **102**(35): p. 12371-6.

191. Chowdary, M.V., et al., *Discrimination of normal, benign, and malignant breast tissues by Raman spectroscopy.* Biopolymers, 2006. **83**(5): p. 556-69.

192. Rehman, S., et al., *Raman spectroscopic analysis of breast cancer tissues: identifying differences between normal, invasive ductal cacinoma and ductal carcinoma in situ of the breast tissue.* Journal of Raman Spectroscopy, 2007. **38**: p. 1345-1351.

193. Stone, N., et al., *Subsurface probing of calcifications with spatially offset Raman spectroscopy (SORS): future possibilities for the diagnosis of breast cancer.* Analyst, 2007. **132**(9): p. 899-905.

194. Kazanci, M., et al., *Bone osteonal tissues by Raman spectral mapping: orientation-composition.* J Struct Biol, 2006. **156**(3): p. 489-96.

195. Timlin, J.A., et al., *Spatial distribution of phosphate species in mature and newly generated mammalian bone by hyperspectral Raman imaging.* Journal of Biomedical Optics, 1999. **4**(1): p. 28-34.

196. Morris, M.D., et al., *Bone tissue ultrastructural response to elastic deformation probed by Raman spectroscopy.* Faraday Discuss, 2004. **126**: p. 159-68; discussion 169-83.

197. Lakshmi, R.J., et al., *Osteoradionecrosis (ORN) of the mandible: A laser Raman spectroscopic study.* Applied Spectroscopy, 2003. **57**: p. 1100-1116.

198. Timlin, J.A., et al., *Raman spectroscopic imaging markers for fatigue-related microdamage in bovine bone.* Anal Chem, 2000. **72**(10): p. 2229-36.

199. McCreadie, B.R., et al., *Bone tissue compositional differences in women with and without osteoporotic fracture.* Bone, 2006. **39**(6): p. 1190-5.

200. Kavukcuoglu, N.B., et al., *Osteopontin deficiency and aging on nanomechanics of mouse bone.* J Biomed Mater Res A, 2007. **83**(1): p. 136-44.

201. Silva, M.J., et al., *Decreased collagen organization and content are associated with reduced strength of demineralized and intact bone in the SAMP6 mouse.* J Bone Miner Res, 2006. **21**(1): p. 78-88.

202. Yerramshetty, J.S. and O. Akkus, *The associations between mineral crystallinity and the mechanical properties of human cortical bone.* Bone, 2008. **42**(3): p. 476-82.

203. Akkus, O., F. Adar, and M.B. Schaffler, *Age-related changes in physicochemical properties of mineral crystals are related to impaired mechanical function of cortical bone.* Bone, 2004. **34**(3): p. 443-53.

204. Balooch, G., et al., *TGF-beta regulates the mechanical properties and composition of bone matrix.* Proc Natl Acad Sci U S A, 2005. **102**(52): p. 18813-8.

205. Matousek, P., et al., *Noninvasive Raman spectroscopy of human tissue in vivo.* Appl Spectrosc, 2006. **60**(7): p. 758-63.

206. Schulmerich, M.V., et al., *Transcutaneous Raman spectroscopy of murine bone in vivo.* Appl Spectrosc, 2009. **63**(3): p. 286-95.

207. Schulmerich, M.V., et al., *Transcutaneous fiber optic Raman spectroscopy of bone using annular illumination and a circular array of collection fibers.* J Biomed Opt, 2006. **11**(6): p. 060502.

208. Schulmerich, M.V., et al., *Subsurface and transcutaneous Raman spectroscopy and mapping using concentric illumination rings and collection with a circular fiber-optic array.* Appl Spectrosc, 2007. **61**(7): p. 671-8.

209. Krafft, C., et al., *Raman and FTIR imaging of lung tissue: Methodology for control samples.* Vibrational Spectroscopy, 2008. **46**: p. 141-149.

210. Koljenovic, S., et al., *Raman microspectroscopic mapping studies of human bronchial tissue.* J Biomed Opt, 2004. **9**(6): p. 1187-97.

211. Huang, Z., et al., *Near-infrared Raman spectroscopy for optical diagnosis of lung cancer.* Int J Cancer, 2003. **107**(6): p. 1047-52.

212. de Jong, B., et al., *Raman spectroscopic detection of changes in molecular composition of bladder muscle tissue caused by outlet obstruction.* Vibrational Spectroscopy, 2003. **32**: p. 57-65.

213. de Jong, B.W., et al., *Discrimination between nontumor bladder tissue and tumor by Raman spectroscopy.* Anal Chem, 2006. **78**(22): p. 7761-9.

214. van de Poll, S.W.E., et al., *In situ investigation of the chemical composition of ceroid in human atherosclerosis by Raman spectroscopy.* Journal of Raman Spectroscopy, 2002. **33**: p. 544-551.

215. Buschman, H.P., et al., *Raman microspectroscopy of human coronary atherosclerosis: biochemical assessment of cellular and extracellular morphologic structures in situ.* Cardiovasc Pathol, 2001. **10**(2): p. 69-82.

216. van de Poll, S.W.E., et al., *On-line detection of cholesterol and calcification by catheter based Raman spectroscopy in human atherosclerotic plaque ex vivo.* Heart, 2003. **89**(9): p. 1078-1082.

217. Buschman, H.P., et al., *Diagnosis of human coronary atherosclerosis by morphology-based Raman spectroscopy.* Cardiovasc Pathol, 2001. **10**(2): p. 59-68.

218. Buschman, H.P., et al., *In vivo determination of the molecular composition of artery wall by intravascular Raman spectroscopy.* Anal Chem, 2000. **72**(16): p. 3771-5.

219. Shim, M.G., et al., *In vivo near-infrared Raman spectroscopy: demonstration of feasibility during clinical gastrointestinal endoscopy.* Photochem Photobiol, 2000. **72**(1): p. 146-50.

220. Molckovsky, A., et al., *Diagnostic potential of near-infrared Raman spectroscopy in the colon: differentiating adenomatous from hyperplastic polyps.* Gastrointest Endosc, 2003. **57**(3): p. 396-402.

221. Chowdary, M.V., et al., *Discrimination of normal and malignant mucosal tissues of the colon by Raman spectroscopy.* Photomed Laser Surg, 2007. **25**(4): p. 269-74.

222. Widjaja, E., W. Zheng, and Z. Huang, *Classification of colonic tissues using near-infrared Raman spectroscopy and support vector machines.* Int J Oncol, 2008. **32**(3): p. 653-62.

223. Krishna, C.M., et al., *FTIR and Raman microspectroscopy of normal, benign, and malignant formalin-fixed ovarian tissues.* Anal Bioanal Chem, 2007. **387**(5): p. 1649-56.

224. Maheedhar, K., et al., *Diagnosis of ovarian cancer by Raman spectroscopy: a pilot study.* Photomed Laser Surg, 2008. **26**(2): p. 83-90.

225. Mahadevan-Jansen, A., et al., *Near-infrared Raman spectroscopy for in vitro detection of cervical precancers.* Photochem Photobiol, 1998. **68**(1): p. 123-32.

226. Mahadevan-Jansen, A., et al., *Development of a fiber optic probe to measure NIR Raman spectra of cervical tissue in vivo.* Photochem Photobiol, 1998. **68**(3): p. 427-31.

227. Utzinger, U., et al., *Near-Infrared Raman Spectroscopy for in Vivo Detection of Cervical Precancers.* Applied Spectroscopy, 2001. **55**: p. 955-959.

228. Robichaux-Viehoever, A., et al., *Characterization of Raman spectra measured in vivo for the detection of cervical dysplasia.* Appl Spectrosc, 2007. **61**(9): p. 986-93.

229. Wood, B.R., et al., *Shedding New Light on the Molecular Architecture of Oocytes Using a Combination of Synchrotron Fourier Transform-Infrared and Raman Spectroscopic Mapping.* Anal Chem, 2008.

230. Maquelin, K., et al., *Raman spectroscopic method for identification of clinically relevant microorganisms growing on solid culture medium.* Anal Chem, 2000. **72**(1): p. 12-9.

231. Everitt, B., S. Landau, and M. Leese, *Cluster analysis*. 4th ed. / Brian S. Everitt, Sabine Landau, Morven Leese. ed. 2001, London: Arnold ; New York : Oxford University Press. viii, 237 p.

232. Krzanowski, W.J., *Principles of multivariate analysis : a user's perspective*. Revised ed. Oxford statistical science series ;. 2000, Oxford: Clarendon. xxi, 586 p.

233. Ivleva, N.P., et al., *Towards a nondestructive chemical characterization of biofilm matrix by Raman microscopy.* Anal Bioanal Chem, 2009. **393**(1): p. 197-206.

234. McCreery, R.L., *Raman spectroscopy for chemical analysis*. 2000, New York ; Chichester: Wiley. xxiv, 420 p.

235. Pommier, C.J.S., et al., *Array detectors for Raman spectroscopy*, in *Handbook of vibrational spectroscopy: Theory and instrumentation*, J.M. Chalmers and P.R. Griffiths, Editors. 2002, Wiley: Chichester. p. 507-521.

236. Tsuboi, M., et al., *Raman spectrum of [5'-^{13}C]thymidine: vibrations of its 5'-end atomic group.* Spectrochimica Acta Part A, 1999. **55**: p. 1887-1896.

237. Hugo, W.B. and A.D. Russell, *Chapter 2: Types of antimicrobial agents*, in *Principles and practice of disinfection, preservation, and sterilisation*, A.D. Russell, W.B. Hugo, and G.A.J. Ayliffe, Editors. 1999, Blackwell Science: Oxford. p. 5-94.

238. Lebrun, N., et al., *Raman analysis of formaldehyde aqueous solutions as a function of concentration.* Journal of Raman Spectroscopy, 2003. **34**: p. 459-464.

239. Monni, J., et al., *Online monitoring of synthesis and curing of phenol-formaldehyde resol resins by Raman spectroscopy.* Polymer, 2008. **49**: p. 3865-3874.

240. Qin, C., J. Xu, and Y. Zhang, *Spectroscopic investigation of the function of aqueous 2-hydroxyethylmethacrylate/glutaraldehyde solution as a dentin desensitizer.* Eur J Oral Sci, 2006. **114**(4): p. 354-9.

241. Benevides, J.M., et al., *Polarized Raman spectroscopy of double-stranded RNA from bacteriophage phi6: local Raman tensors of base and backbone vibrations.* Biophys J, 1997. **72**(6): p. 2748-62.

242. Notingher, I., et al., *In situ characterisation of living cells by Raman spectroscopy.* Spectroscopy, 2002. **16**: p. 43-51.

243. Ebner, T., M. Moser, and G. Tews, *Possible applications of a non-contact 1.48 microm wavelength diode laser in assisted reproduction technologies.* Hum Reprod Update, 2005. **11**(4): p. 425-35.

244. Hollis, A., et al., *Zona pellucida microdrilling with a 1.48 microns diode laser.* IEEE Eng Med Biol Mag, 1997. **16**(3): p. 43-7.

245. Douglas-Hamilton, D.H. and J. Conia, *Thermal effects in laser-assisted pre-embryo zona drilling.* J Biomed Opt, 2001. **6**(2): p. 205-13.

246. Mariani, M.M., et al., *Impact of fixation on in vitro cell culture lines monitored with Raman spectroscopy.* Analyst, 2009. **134**(6): p. 1154-61.

247. Bacallao, R., S. Sohrab, and C. Phillips, *Chapter 18: Guiding principles of specimen preservation for confocal fluorescence microscopy*, in *Handbook of biological confocal microscopy*, J.B. Pawley, Editor. 2006, Springer: New York, NY. p. 368-380.

248. Wood, B.R., et al., *Shedding new light on the molecular architecture of oocytes using a combination of synchrotron Fourier transform-infrared and Raman spectroscopic mapping.* Anal Chem, 2008. **80**(23): p. 9065-72.

249. Synytsya, A., et al., *Raman spectroscopic study of calf thymus DNA: an effect of proton- and g-irradiation.* Journal of Raman Spectroscopy, 2007. **38**: p. 1406-1415.

250. Wilding, M., et al., *Mitochondrial aggregation patterns and activity in human oocytes and preimplantation embryos.* Hum Reprod, 2001. **16**(5): p. 909-17.

251. Van Blerkom, J., et al., *Domains of high-polarized and low-polarized mitochondria may occur in mouse and human oocytes and early embryos.* Hum Reprod, 2002. **17**(2): p. 393-406.

252. Turner, K., D.J. Goldstein, and A.W. Rogers, *Variation in the dry mass of mouse embryos throughout the preimplantation period.* Hum Reprod, 1992. **7**(1): p. 112-6.

253. Gardner, R.L., *Scrambled or bisected mouse eggs and the basis of patterning in mammals.* Bioessays, 1999. **21**(4): p. 271-4.

254. Brinster, R.L., *Protein content of the mouse embryo during the first five days of development.* J Reprod Fertil, 1967. **13**(3): p. 413-20.

255. Nagy, A., et al., *Chapter 2: Summary of Mouse Development*, in *Manipulating the Mouse Embryo: A Laboratory Manual*. 2003, Cold Spring Harbor Laboratory Press: Cold Spring Harbor, N.Y. p. 31-140.

256. de Grauw, C.J., et al., *Axial resolution of confocal Raman microscopes: Gaussian beam theory and practice.* Journal of Microscopy, 1997. **188**(3): p. 273-279.

257. Everall, N.J., *Modeling and Measuring the Effect of Refraction on the Depth Resolution of Confocal Raman Microscopy.* Applied Spectroscopy, 2000. **54**: p. 773-782.

258. Moon, J.H., et al., *Visualization of the metaphase II meiotic spindle in living human oocytes using the Polscope enables the prediction of embryonic developmental competence after ICSI.* Hum Reprod, 2003. **18**(4): p. 817-20.

259. Griffin, J., et al., *Comparative analysis of follicle morphology and oocyte diameter in four mammalian species (mouse, hamster, pig, and human).* J Exp Clin Assist Reprod, 2006. **3**: p. 2.

260. Sathananthan, A.H., *Ultrastructural changes during meiotic maturation in mammalian oocytes: unique aspects of the human oocyte.* Microsc Res Tech, 1994. **27**(2): p. 145-64.

261. Niimura, S., S.-Y. Kawakami, and H. Takano, *Changes in the amount of cytoplasmic inclusions in mouse oocytes during meiotic maturation in vivo and in vitro.* Reproductive Medicine and Biology, 2004. **3**: p. 231-236.

262. Borini, A. and G. Coticchio, *The human oocyte: controlled rate cooling*, in *Textbook of assisted reproductive technologies: laboratory and clinical perspectives*, D.K. Gardner, et al., Editors. 2009, Informa Healthcare: London. p. 255-274.

263. Hosmer, D.W. and S. Lemeshow, *Applied logistic regression*. 2nd ed. ed. 2000, New York ; Chichester: Wiley. xii, 373 p.

264. Albert, A. and J.A. Anderson, *On the existence of maximum likelihood estimates in logistic regression models.* Biometrika, 1984. **71**(1): p. 1-10.

265. Notingher, I., et al., *Multivariate analysis of Raman spectra for in vitro non-invasive studies of living cells.* Journal of Molecular Structure, 2005. **744-747**: p. 179-185.

266. Combelles, C.M., et al., *Assessment of nuclear and cytoplasmic maturation in in-vitro matured human oocytes.* Hum Reprod, 2002. **17**(4): p. 1006-16.

267. Kim, D.H., et al., *Comparison of maturation, fertilization, development, and gene expression of mouse oocytes grown in vitro and in vivo.* J Assist Reprod Genet, 2004. **21**(7): p. 233-40.

268. Kastrop, P.M., et al., *Protein synthesis and phosphorylation patterns of bovine oocytes maturing in vivo.* Mol Reprod Dev, 1991. **29**(3): p. 271-5.

269. Trounson, A., C. Anderiesz, and G. Jones, *Maturation of human oocytes in vitro and their developmental competence.* Reproduction, 2001. **121**(1): p. 51-75.

270. Gilchrist, R.B. and J.G. Thompson, *Oocyte maturation: emerging concepts and technologies to improve developmental potential in vitro.* Theriogenology, 2007. **67**(1): p. 6-15.

271. Schultz, R.M., M.J. LaMarca, and P.M. Wassarman, *Absolute rates of protein synthesis during meiotic maturation of mammalian oocytes in vitro.* Proc Natl Acad Sci U S A, 1978. **75**(9): p. 4160-4.

272. Murray, A.A., et al., *Role of ascorbic acid in promoting follicle integrity and survival in intact mouse ovarian follicles in vitro.* Reproduction, 2001. **121**(1): p. 89-96.

273. Harris, S.E., et al., *Carbohydrate metabolism by murine ovarian follicles and oocytes grown in vitro.* Reproduction, 2007. **134**(3): p. 415-24.

274. Ibanez, E., et al., *Genetic strain variations in the metaphase-II phenotype of mouse oocytes matured in vivo or in vitro.* Reproduction, 2005. **130**(6): p. 845-55.

275. Vergara, G.J., et al., *In vitro fertilization in mice: Strain differences in response to superovulation protocols and effect of cumulus cell removal.* Theriogenology, 1997. **47**(6): p. 1245-52.

276. Baker, S.J. and N. Spears, *The role of intra-ovarian interactions in the regulation of follicle dominance.* Hum Reprod Update, 1999. **5**(2): p. 153-65.

277. Spears, N., J.P. de Bruin, and R.G. Gosden, *The establishment of follicular dominance in co-cultured mouse ovarian follicles.* J Reprod Fertil, 1996. **106**(1): p. 1-6.

278. Murray, A.A. and N. Spears, *What makes a good egg?*, in *Implantation and early development*, H.O.D. Critchley, I.T. Cameron, and S.K. Smith, Editors. 2005, RCOG Press: London. p. 103-118.

279. Miao, Y.L., et al., *Oocyte aging: cellular and molecular changes, developmental potential and reversal possibility.* Hum Reprod Update, 2009. **15**(5): p. 573-85.

280. Byers, S.L., S.J. Payson, and R.A. Taft, *Performance of ten inbred mouse strains following assisted reproductive technologies (ARTs).* Theriogenology, 2006. **65**(9): p. 1716-26.

281. Nagy, A., et al., *Chapter 3: Production of Transgenic and Chimeric Mice*, in *Manipulating the Mouse Embryo: A Laboratory Manual*. 2003, Cold Spring Harbor Laboratory Press: Cold Spring Harbor, N.Y. p. 141-160.